Experimental study and prediction of microstructures and internal stresses during heat treatment of carburized and carbonitrided low-alloyed steels

Karthikeyan Jeyabalan

Thèse

Présentée et soutenue publiquement pour l'obtention du titre de

DOCTEUR DE l'UNIVERSITE DE LORRAINE

Mention " Sciences des Matériaux"

par **Karthikeyan JEYABALAN**

Experimental study and prediction of microstructures and internal stresses during heat treatment of carburized and carbonitrided low-alloyed steels

Soutenance le 14 décembre 2022

Member du jury:

Rapporteurs:	**Laurent BARRALLIER**	**Professeur, Arts et Métiers, Aix en Provence, France**
Rapporteurs:	**Sophie BERVEILLER**	**Maître de Conférences, Arts et Métiers Paris Tech, Metz, France**
Président:	**Manuel FRANCOIS**	**Professeur, U.T.T. , Troyes, France**
Examinateur:	**Pascal LAMESLE**	**Directeur Scientifique et Technique, IRT-M2P, Metz, France**
Directeur(s) de thèse:	**Sabine DENIS**	**Professeur, UL, Nancy, France**
Codirecteur(s) de thèse:	**Julien TEIXEIRA**	**Chargé de Recherche CNRS, IJL, Nancy, France**
Membres invités:	**Marc COURTEAUX**	**Ingénieur Expert Stellantis, Voujeau-court- France**
Membres invités:	**Jacky DULCY**	**Ingénieur de Recherche CNRS, IJL, Nancy, France**

Institut Jean Lamour (IJL), UMR CNRS-UL 7198, 54000 NANCY France

Acknowledgements

I am immensely grateful to everyone who has contributed to this project, scientifically, administratively, and emotionally. Therefore, I want to express my gratitude to all the individuals who contributed to the completion of this work, from near or far.

My deepest thanks go to Sabine Denis, who played a crucial role in my PhD journey. Her encouragement and confidence in my work have been invaluable, and I will never forget her support during difficult situations both professionally and personally. Her knowledge, generosity, and willingness to share have been an inspiration to me, and she has always supported me effectively and without hesitation. I appreciate the confidence she has had in my research, and her guidance throughout my thesis has been invaluable. She has always been supportive and kind in the best possible way, and I will always be grateful for the trust she has shown in me.

I would like to acknowledge Julien Teixeira for his valuable assistance in jointly directing this research. Since my very first day in Nancy, he has provided me with the moral support that has allowed me to feel at home in the international environment. His dedication and hard work were crucial in developing the valuable model, and without his expertise, critical insights, and encouragement, the rigor and accuracy of the interpretations would not have been possible. I am especially grateful for his mentorship in fostering my problem-solving, analytical, and reporting skills.

Jacky Dulcy's energy and knowledge were crucial in laying the foundation for this work. Without him, this thesis would not exist, and I will always remember the days we spent in front of the thermobalance to achieve our goals. His support and determination have been invaluable to me, and I am grateful for his contribution to this work. Beyond scientific collaboration, I cherish the friendship that has grown between us.

I am also deeply grateful to Guillaume Geandier for his guidance on residual stress measurement and determination, as well as his support in exploring new avenues during this work. His valuable support, feedback, and suggestions have immensely contributed to the quality of my research work. I am also grateful to the entire team at IRT M2P, especially Pascal Lamesle and Grégory Michel, for their funding and support, which have been essential. I would also like to thank the entire TTA team for their involvement and support.

I would like to extend my sincere thanks to Marc Courteaux, Simon Catteau, and Andrea Puech whose critical, constructive, and applicable feedback on all the results and issues we encountered during this project have been invaluable. I would like to express my gratitude to Mr. Manuel FRANCOIS for chairing the thesis jury, and to Mr. Laurent BARRALLIER, Mrs. Sophie BERVEILLER, and Mr. Pascal LAMESLE for reviewing this work. Their involvement in the evaluation of the work has given me a new gain of confidence in the usefulness of the proposed results. Their expertise and feedback have been invaluable in improving this thesis.

I would like to thank Benoit Denand for his unwavering support in producing and discussing the thermomechanical experimental results that constituted a part of this research work. I would like to acknowledge the members of the 303 team, with whom I had the honor of working during my doctoral period. I am very grateful to Mrs.Christine Gendarme for her involvement in microprobe measurement. I would also like to thank the MET observations team for the quality and degree of confidence in the results from my work. I cannot forget to acknowledge Mr. Erwan Etienne, in charge of the metallography department, who has always been there to find solutions to the practical issues.

Lastly, I would like to thank my loved ones, family, and friends for their unwavering support throughout this journey. Your presence and support, even across great distances, have meant the world to me.

I dedicate my PhD to my wife Durga, who has shown incredible patience and understanding during the final stages of this journey. Your unwavering support and encouragement, even when progress seemed slow, have been a constant source of strength. Thank you for standing by my side and believing in me. This 'Ph.D' achievement is as much yours as it is mine.

Completing a thesis is not only an academic achievement but also a shared life experience.

Résumé étendu en français

Introduction

Les traitements thermochimiques de cémentation et carbonitruration sont notamment utilisés dans l'industrie automobile pour conférer aux pièces (pignons…) résistance à la fatigue et à l'usure. En effet, les gradients de composition chimique dans la zone superficielle des pièces obtenus lors d'un traitement d'enrichissement en phase austénitique (gradients de teneur en carbone pour la cémentation et carbone + azote pour la carbonitruration) permettent de générer au cours de la trempe à la fois des microstructures conférant des propriétés mécaniques élevées et des contraintes résiduelles de compression. Alors que les traitements de cémentation sont bien maîtrisés, les traitements de carbonitruration requièrent encore des travaux de recherche pour comprendre de manière approfondie et modéliser les phénomènes physiques complexes et rendre le procédé robuste à l'échelle industrielle. Ainsi un « grand » projet visant une meilleure compréhension et l'optimisation des traitements de carbonitruration d'aciers faiblement alliés du point de vue du procédé, des microstructures et propriétés mécaniques ainsi que des contraintes résiduelles a été lancé dans le cadre de l'IRT M2P (Institut de Recherche Technologique « Matériaux, Procédés, Métallurgie). Ce projet intitulé TTA (« Traitements thermiques Avancés » a associé 10 partenaires industriels et l'Institut Jean Lamour (IJL).

Une première thèse (Walter Dal'Maz Silva) a principalement porté sur le procédé d'enrichissement en carbone et en azote et sa modélisation (cinétiques de décomposition des atmosphères gazeuses et diffusion dans la pièce). En parallèle, le travail de thèse de Simon Catteau initié dans le cadre d'une collaboration PSA-IJL était centré sur l'étude expérimentale et la modélisation de la formation des microstructures lors de la décomposition de l'austénite au cours du refroidissement après enrichissement. S.D. Catteau a notamment étudié in situ (par dilatométrie et diffraction des rayons X synchrotron) les cinétiques de transformations de phases pour différentes teneurs en carbone et en azote (échantillons enrichis de manière homogène) et développé un modèle de prévision de ces cinétiques ainsi que des microstructures finales et duretés.

Dans la continuité des travaux de S.D. Catteau, notre étude a été centrée sur la genèse des contraintes internes et la formation des contraintes résiduelles en relation avec les transformations de phases dans des échantillons à gradients de carbone et d'azote à la fois du point de vue expérimental et du point de vue de la prévision par calcul.

Chapitre I: Etude bibliographique

L'étude bibliographique est centrée sur les effets des enrichissements en carbone et en azote sur la genèse des contraintes internes au cours du refroidissement et sur les distributions des contraintes résiduelles après refroidissement.

La première partie du chapitre concerne les résultats expérimentaux et la deuxième partie la prévision des contraintes résiduelles. Après avoir rappelé une approche qualitative qui permet de mettre en exergue les principaux phénomènes à l'origine des contraintes internes au cours du refroidissement, i.e. les gradients de température et les transformations de phases, un état de l'art des modèles numériques couplés thermique-transformations de phases-mécanique est effectué avec des exemples de résultats de calcul pour des traitements de cémentation et de carbonitruration.

Nous retiendrons essentiellement que du point de vue expérimental, seules les contraintes résiduelles (i.e. après traitement) ont été déterminées généralement par

diffraction des rayons X. Les profils de contraintes résiduelles après les traitements de carbonitruration + trempe sont similaires à ceux obtenus après une cémentation suivie de trempe : ils présentent des contraintes de compression dans la zone superficielle enrichie en carbone et en azote avec un maximum de contraintes de compression sous la surface, à l'endroit où la fraction de martensite est maximale ; la diminution des contraintes résiduelles lorsqu'on s'approche de la surface est généralement reliée à l'augmentation de la teneur en austénite résiduelle.

Du point de vue expérimental, il n'existe pas d'étude permettant d'analyser la formation des contraintes internes au cours du refroidissement et de les quantifier. Ainsi le premier objectif de la thèse est de déterminer expérimentalement les contraintes internes au cours du refroidissement in situ par diffraction des rayons X haute énergie sur synchrotron en simultané avec les évolutions microstructurales.

Du point de vue de la simulation numérique, de nombreux auteurs ont simulé les contraintes résiduelles après des traitements de cémentation + trempe et les ont validés expérimentalement.

Pour des traitements de carbonitruration + trempe, seule une équipe au monde montre des résultats de calculs couplés thermique-transformation de phases-mécanique. Dans ces travaux, les effets du carbone et de l'azote sur les cinétiques de transformations de phases sont pris en compte mais sans donner de détails sur les hypothèses et les données d'entrée. Par contre, leurs effets sur les propriétés mécaniques des différentes phases ne sont pas pris en compte. Un enjeu de notre travail sera de déterminer expérimentalement et de prendre en compte dans les simulations les effets du carbone et de l'azote sur le comportement thermomécanique de l'acier. De plus, l'objectif sera de valider expérimentalement les simulations non seulement en fin de refroidissement mais tout au long du refroidissement, ce qui n'a jamais été fait auparavant.

Chapitre II: Méthodes expérimentales

Après avoir présenté le matériau de l'étude (l'acier 23MnCrMo5), nous décrivons d'abord les procédés d'enrichissement en carbone et en azote des échantillons dans une thermobalance de laboratoire. En effet, une étape essentielle pour notre étude est l'obtention d'échantillons enrichis en carbone et en azote (plaquettes d'épaisseur 3 mm) avec des gradients représentatifs des couches carbonitrurées réalisées sur pièces industrielles. D'autre part, il est aussi nécessaire d'élaborer des échantillons avec des teneurs homogènes en carbone et en azote (plaquette d'épaisseur maximale 1 mm) pour les caractérisations thermomécaniques et thermophysiques de l'acier nécessaires pour les simulations numériques. Les méthodes de caractérisation des échantillons enrichis sont aussi décrites (mesures de composition chimique en carbone et en azote à la microsonde, analyses microstructurales (MEB), mesures de microduretés).

Puis, nous détaillons la mise en œuvre des essais thermomécaniques avec la prise en main de la machine de traction/compression à chaud nouvellement acquise par l'équipe de recherche. Du fait de la faible épaisseur de nos échantillons (1 mm) nous avons conçu une nouvelle géométrie d'échantillons de traction et de mors spécifique. Un plan d'expériences comportant des essais de traction des différentes phases/constituants (austénite, ferrite, bainite, martensite) pour différentes températures (entre 900°C et 20°C) et pour différentes teneurs en carbone et en azote a été réalisé. Des essais à différentes vitesses de déformation (2.10^{-4} et 2.10^{-3} s^{-1}) ont aussi été effectués pour caractériser le comportement visqueux des phases. Des essais de transformation de phases sous contrainte de traction ont aussi été réalisés pour quantifier la plasticité de transformation.

Les méthodes de caractérisation des propriétés thermophysiques sont également décrites : mesure de chaleur spécifique en fonction de la température et d'enthalpie de transformations de phases (par DSC et MultiHTC), mesures de diffusivité thermique (méthode flash laser) pour différentes compositions en carbone et azote.

Dans la dernière partie du chapitre, la méthodologie des expériences de diffraction

des rayons X à haute énergie (HEXRD) réalisées à l'ESRF est détaillée. Le dispositif expérimental original est décrit : le four transportable développé au laboratoire a été installé sur la ligne de lumière; il permet un déplacement vertical de l'échantillon (cylindre de diamètre 5mm et d'épaisseur 3mm) instrumenté de thermocouple qui est traversé par le faisceau de RX permettant de suivre in situ au cours d'un refroidissement continu et dans l'épaisseur tout au long des gradients de carbone et/ou d'azote les diagrammes de diffraction (détecteur 2D). L'acquisition (fréquence 50 frames/s) et le traitement des grandes quantités de données expérimentales pour obtenir simultanément les évolutions des fractions de phases (méthode de Rietveld) et les contraintes internes moyennes dans les phases ferritiques (ferrite, bainite, martensite) et austénitiques (méthode des $\sin^2 \psi$) sont ensuite détaillées.

Chapitre III: Analyse des contraintes internes par HEXRD

Dans ce chapitre, nous présentons les résultats expérimentaux de cinétiques de transformation de l'austénite et de formation des contraintes internes au cours du refroidissement dans des échantillons à gradients de carbone et d'azote ainsi que les profils de microstructures et duretés finales et de contraintes résiduelles.

Dans la première partie du chapitre, pour mieux comprendre les évolutions microstructurales dans les échantillons à gradients, nous résumons les résultats obtenus dans des études antérieures pour les cinétiques de transformation de phases de l'austénite au cours du refroidissement dans des échantillons enrichis de manière homogène en carbone, azote et carbone + azote. Il est notamment rappelé que l'enrichissement en azote conduit, contrairement à l'enrichissement en carbone, a une accélération des cinétiques de décomposition de l'austénite pour les transformations à plus haute température ainsi que pour la transformation bainitique (en dessous de la température Bs). Un affinement des microstructures avait aussi été mis en évidence associé à des duretés élevées.

De plus, au-dessus de la température Bs, une nouvelle microstructure appelée « Constituant Haute Température » (CHT) avait été mise en évidence : elle est constituée majoritairement de grains fins de ferrite équiaxe et de différentes populations de nitrures (micrométriques et nanométriques) et de carbures.

Puis, dans une deuxième partie, nous présentons successivement les résultats obtenus lors des essais in situ par HEXRD d'abord dans les échantillons à gradients de carbone (échantillon cémenté) puis dans les échantillons à gradients d'azote (échantillon nitruré) et à gradients de carbone + azote (échantillon carbonitruré) pour bien mettre en évidence le rôle de l'azote. Dans chaque cas, les profils de microstructures finales, duretés et contraintes résiduelles seront aussi comparés à ceux obtenus pour des essais ex situ avec des conditions de refroidissement plus rapides après l'enrichissement : refroidissement air dans la thermobalance et trempe à l'huile.

Pour l'échantillon cémenté (environ 0,55%C en surface et 0,25%C à cœur) et l'expérience in situ (figure 1), il est clairement mis en évidence que la transformation de l'austénite se produit d'abord à cœur (zone non enrichie en carbone) avec la formation de ferrite proeutectoïde puis de bainite et en dernier dans la zone superficielle enrichie en carbone avec la transformation martensitique. Les teneurs en austénite résiduelle sont relativement faibles (maximum 10% en surface).

Les mesures de contraintes in situ permettent de montrer pour la première fois que cette chronologie de transformations de phases induit d'abord des contraintes de compression dans la zone non enrichie et de la traction en surface puis de la compression en surface lorsque cette zone se transforme en martensite et de la traction dans la zone non enrichie. En fin de refroidissement, les profils de contraintes résiduelles (figure 3) montrent des contraintes de compression dans la martensite dans la zone enrichie avec une contrainte maximale sous la surface (-200 MPa) pour une teneur en carbone d'environ 0,4% et des contraintes faibles dans l'austénite. A cœur, les phases ferritiques

comme la phase austénitique sont en traction (environ 200 MPa). Le profil de contrainte dans les phases ferritiques est similaire à ce qui est généralement observé dans la littérature.

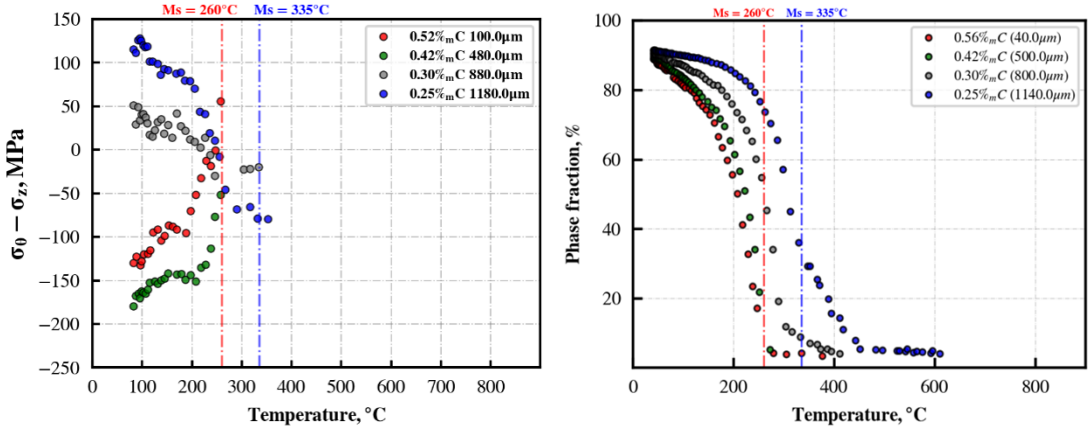

Figure 1: Echantillon cémenté, expérience in-situ. Evolutions en fonction de la température en 4 positions (profondeur) dans le gradient de teneur en carbone a) contraintes dans les phases ferritiques et martensitiques b) fractions massiques des phases ferritiques et martensitiques

Dans le cas d'un refroidissement plus rapide (trempe huile), la microstructure finale est complètement martensitique et le profil de contraintes résiduelles dans la martensite est similaire avec une contrainte de compression maximale en sous couche plus élevée (-300 MPa) et une contrainte de traction plus faible à cœur (100 MPa). Il est à noter que l'austénite résiduelle en surface (environ 10%) est soumise à une contrainte de traction élevée (supérieure à 200 MPa) inexpliquée à ce jour. Dans les deux cas, les profils de microstructures finales sont cohérents avec les duretés mesurées.

Pour l'échantillon nitruré (0,4%N et 0,18%C en surface; profondeur nitrurée environ 400 µm), le profil de contraintes résiduelles mesuré dans les phases ferritiques est complètement différent de celui de l'échantillon cémenté avec une zone superficielle en traction (+500MPa) une zone en compression sous la couche nitrurée (-200MPa) et des contraintes faibles à cœur. L'analyse in situ des contraintes et des fractions de phases permet de corréler ce profil des contraintes résiduelles à la chronologie des transformations de l'austénite dans l'échantillon. En effet, la zone superficielle enrichie en azote se transforme en premier au cours du refroidissement (formation du Constituant Haute Température) puis le cœur se transforme en ferrite et bainite et la zone sous la couche nitrurée (plus riche en carbone) est la dernière à se transformer (formation de bainite/martensite).

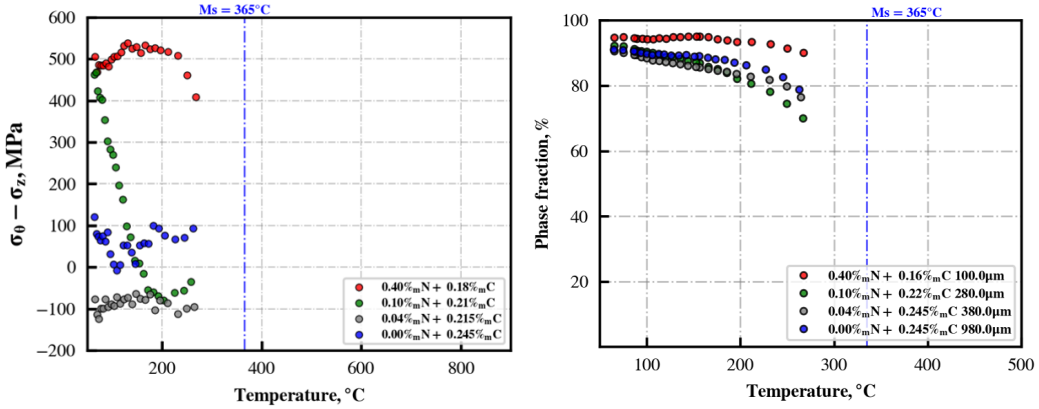

Figure 2: Echantillon nitruré, expérience in situ. Evolutions en fonction de la température en 4 positions dans le gradient a) contraintes dans les phases ferritiques et martensitiques b) fractions massiques des phases ferritiques et martensitiques.

Même si nous ne disposons pas de beaucoup de résultats dans le cas de l'expérience in situ sur échantillon carbonitruré lié à des difficultés expérimentales, la chronologie des transformations de phases et ses conséquences sur la formation des contraintes internes et des contraintes résiduelles peuvent être analysées de la même manière que pour l'échantillon nitruré. Le profil de contraintes résiduelles (figure 4) montre aussi des contraintes résiduelles de traction dans la couche nitrurée (qui varie en fonction de la teneur en carbone locale) et des contraintes de compression sous la couche nitrurée où la teneur en carbone est élevée.

Par contre dans le cas d'un échantillon carbonitruré trempé à l'huile, nous retrouvons un profil de contraintes résiduelles plus « classique » avec néanmoins des contraintes de traction en proche surface. Le refroidissement plus rapide permet d'obtenir une transformation martensitique dans la couche superficielle enrichie en carbone et azote qui se transforme en dernier par rapport au cœur non enrichi sauf en proche surface où la teneur en azote est la plus élevée.

Chapitre IV: Modélisation, simulations numériques et validation expérimentale

Ce chapitre vise à établir des simulations couplées thermique-mécanique-métallurgie, afin de comprendre plus avant les évolutions des contraintes internes en relation avec les transformations de phases au cours du refroidissement dans des échantillons à gradient enrichis en carbone, azote ou carbone + azote. Pour les échantillons enrichis en azote, l'enjeu est d'appréhender des évolutions qui n'avaient pu être suivies intégralement au cours des expériences de DRXHE in situ. Il s'agit aussi de considérer les échantillons qui ont été caractérisés ex situ (trempes huile, refroidissement air). Enfin, l'objectif de ces simulations est de parvenir à des prédictions quantitatives des contraintes et des profils de microstructure et de dureté.

1. Modèle couplé métallurgique, mécanique et thermique

La première partie de ce chapitre rappelle les approches utilisées pour modéliser les différents phénomènes (thermiques, métallurgiques et mécaniques). Le modèle métallurgique a été développé au cours d'études précédentes. Basé sur des lois de Johnson-Mehl-Avrami-Kolmogorov (JMAK) pour les transformations avec diffusion et Koistinen-Marburger pour la martensite, il permet de prédire la cinétique de formation des différents constituants issus de la décomposition de l'austénite pendant le refroidissement (ferrite, perlite, bainite et martensite), en tenant compte de la concentration locale en carbone et en azote. Les lois JMAK sont établies de manière empirique à partir de cinétiques obtenues en conditions isothermes sur l'acier de base (non enrichi en carbone ou en azote). Les cinétiques en conditions anisothermes sont obtenues par une somme de Scheil pour l'incubation et une hypothèse d'additivité modifiée pour l'avancement de la transformation. L'effet de la concentration en carbone est prédit à l'aide de lois à base physique et de données thermodynamiques, tandis que l'effet de la concentration en azote est prédit de manière empirique. Le manuscrit présente des comparaisons entre simulation et expérience illustrant l'aptitude du modèle à prendre en compte l'effet d'un traitement anisotherme ainsi que l'effet de la concentration en carbone et en azote.

Le modèle thermomécanique tient compte de la température, de la microstructure (proportion des différents constituants) et de la teneur en carbone et en azote. Une loi de comportement thermo-élasto-visco-plastique additive est utilisée. On considère l'élasticité isotrope, un critère de Von Mises et une loi d'écoulement de Prandtl Reuss pour la plasticité/viscoplasticité et un écrouissage isotrope. Les paramètres de la loi de comportement sont établis pour chaque constituant de la microstructure, et une moyenne sur ces paramètres est faite pour obtenir la loi de comportement associée à

la microstructure multiphasée. La déformation thermique (isotrope) est calculée par une loi des mélanges des coefficients de dilatation des différentes phases et le modèle tient compte des déformations de transformation (variation de volume et plasticité de transformation).

A partir de notre campagne de caractérisations, nous avons montré que les effets de la teneur en carbone sur le comportement thermomécanique sont en accord avec des travaux précédents sur des alliages similaires. Un enrichissement en azote tend à augmenter les propriétés (limites d'élasticité, contraintes d'écoulement). L'ensemble des paramètres des lois de comportement ont été identifiées à partir de nos résultats expérimentaux et de données issues d'études précédentes du laboratoire ou de la littérature. Les variations de volume associées aux transformations de phases et les coefficients de dilatation ont été établis par dilatométrie. Les déformations de plasticité de transformation ont été établies à partir de nos essais et de données disponibles au laboratoire.

Les évolutions de température sont prédites à partir de l'équation de la conduction de la chaleur. On tient compte d'un terme source lié aux transformations de phases exothermiques. En surface, on considère un transfert convectif. Les données thermophysiques par phase sont obtenues à partir des expériences mentionnées précédemment (chapitre 2) complétées par des données de la littérature ou bien de calculs thermodynamiques. L'aspect multiphasé est pris en compte par une loi des mélanges.

2. Simulation des évolutions couplées métallurgiques, mécaniques et thermiques au sein des échantillons à gradient

Le modèle couplé thermique, mécanique et métallurgique a été implémenté dans le logiciel Eléments Finis Zebulon (Mines Paris-PSL), en s'appuyant sur une version précédente (trempe martensitique, sans effet du carbone). On considère pour le maillage une géométrie 2D axisymétrique, celle des échantillons cylindriques à gradient utilisés pour les expériences in situ (diamètre 5 mm, épaisseur 3 mm). Le maillage consiste en une section rectangulaire contenant 200 éléments bi-dimensionnels cylindriques axisymétriques avec 8 points d'intégration.

L'étude de simulation aborde successivement les expériences présentées au chapitre précédent. On considère ainsi trois types d'enrichissement : cémentation, nitruration et carbonitruration et trois cycles thermiques avec, par ordre croissant de vitesse de refroidissement : le cycle thermique appliqué lors des expériences de DRXHE in situ, un refroidissement air (dans l'enceinte du four à thermobalance) et une trempe huile à température ambiante.

Pour l'échantillon cémenté et le cycle thermique correspondant à l'expérience in situ, la simulation métallurgique prédit, comme attendu, que les transformations de phases sont plus lentes et sont décalées vers de plus basses températures lorsque la concentration en carbone augmente. Il en résulte la chronologie observée expérimentalement, avec la transformation du cœur dans un premier temps, suivi de la surface. Le gradient de microstructure final est dominé par la martensite mais avec une fraction importante de bainite et faible de ferrite proeutectoïde à cœur. L'accord entre simulation et expérience sur les cinétiques et les profils finaux de dureté et de microstructure est satisfaisant (figure 3a). Un écart important concerne cependant la fraction d'austénite résiduelle en fin de refroidissement, qui est sous-estimée. La simulation d'une trempe huile (refroidissement plus rapide) conduit à la même chronologie des transformations de phases (cœur suivi de la surface), mais à une microstructure entièrement martensitique. La fraction d'austénite résiduelle est une nouvelle fois sous-estimée. Pour les deux refroidissements, la surface de l'échantillon (enrichie en carbone) subit successivement des contraintes de traction puis de compression (le centre subit des évolutions inverses). Les profils de contraintes résiduelles sont relativement bien prédits par la simulation sauf dans la zone superficielle

où le calcul ne traduit pas la décroissance de la contrainte de compression (figure 3b). Ce point est abordé dans la discussion ci-dessous.

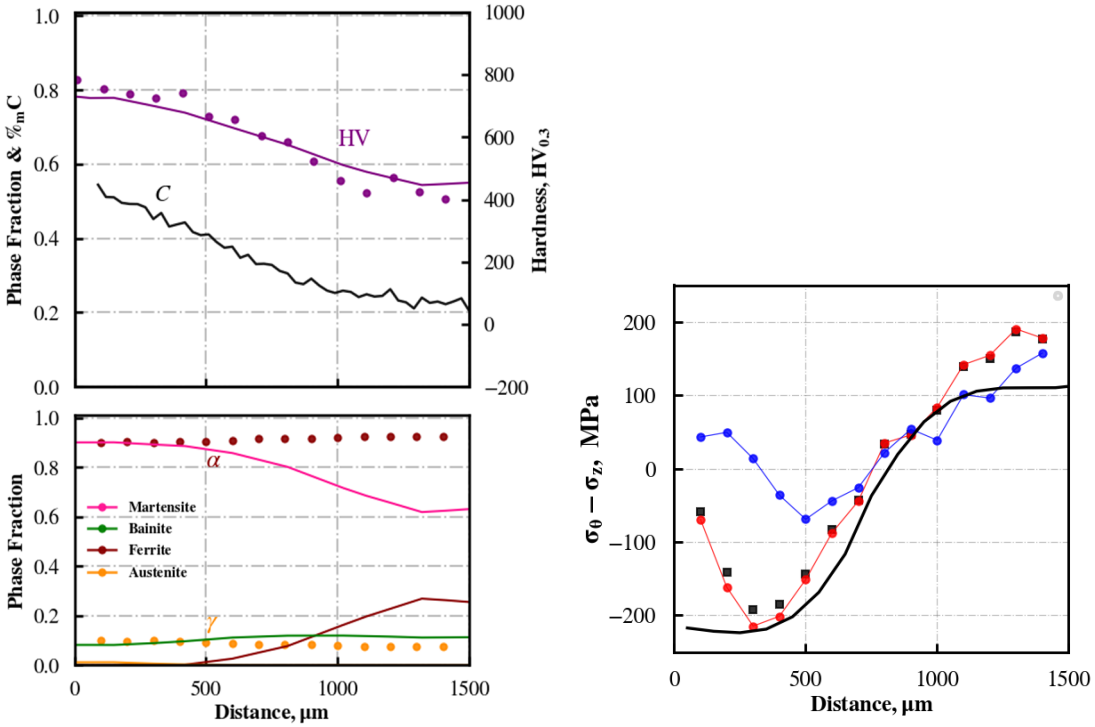

Figure 3 : Echantillon cémenté, expérience in-situ. a) profils de microstructures et de duretés finales calculés (lignes) et mesurés (points) b) profils de contraintes résiduelles calculé (ligne noire) et mesurés dans les phases ferritiques et martensitiques (points rouges et noirs) et dans l'austénite (points bleus)

Pour les échantillons enrichis en azote (nitruration, carbonitruration), la simulation prédit, pour la thermique correspondant à l'expérience DRXHE in situ, la chronologie inverse de celle des échantillons cémentés : transformation de la surface suivie du cœur, en accord avec les expériences. C'est le cas également pour l'échantillon carbonitruré refroidi à l'air. Pour ces échantillons, la simulation prédit la formation du constituant haute température (CHT) au-dessus de Bs. Sous la couche enrichie en azote, les évolutions microstructurales sont déterminées par la concentration locale en carbone (décomposition plus lente de l'austénite et à plus basse température lorsque la concentration locale en carbone augmente). Comme pour les échantillons cémentés, la fraction d'austénite résiduelle est largement sous-estimée. C'est le cas en particulier dans les couches nitrurées (figure 4a). Le modèle prédit en effet une formation trop rapide de CHT, alors qu'une partie de la décomposition de l'austénite s'est vraisemblablement produite aussi sous Bs, avec la formation de bainite et de martensite. De plus, la formation préalable de CHT a probablement stabilisé l'austénite. Du fait des faibles déformations de transformations de phases associées au CHT, la couche nitrurée subit en fin de refroidissement des contraintes de traction. Le modèle prédit que ces dernières sont étroitement corrélées avec la présence d'azote, en accord avec les expériences (figure 4b). Au cours du refroidissement, le modèle prédit les évolutions atypiques de contraintes qui avaient été observées expérimentalement, mais partiellement seulement, par DRXHE in situ.

En revanche, dans le cas d'un refroidissement plus rapide par trempe huile, on n'obtient que de la martensite dans toute l'épaisseur de l'échantillon. On retrouve alors les effets attendus de l'azote : diminution de Ms, augmentation des duretés et de la déformation de transformation (variation de volume). On observe pour la trempe huile la chronologie usuelle (cœur suivi de la surface), des profils de contraintes résiduels conventionnels (compression en surface, traction à cœur) et des profils de dureté corrélés

aux profils de concentration en carbone et en azote.

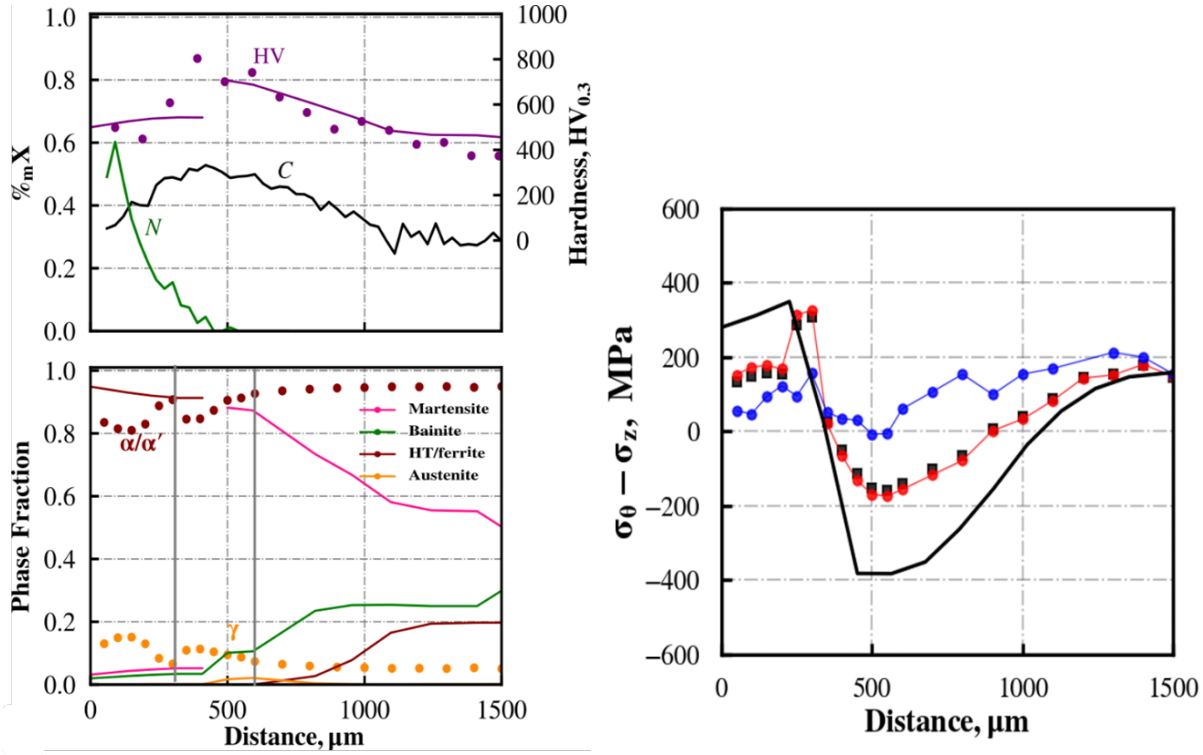

Figure 4 : Echantillon carbonitruré, expérience in situ a) profils de microstructures et de duretés finales calculés (lignes) et mesurés (points) b) profils de contraintes résiduelles calculé (ligne noire) et mesurés dans les phases ferritiques et martensitiques (points rouges et noirs) et dans l'austénite (points bleus)

3. Discussion

L'ensemble de ces simulations représente pour le modèle métallurgique un test supplémentaire par rapport aux études précédentes, du fait de l'étude nouvelle d'échantillons à gradient au lieu d'échantillons à concentration homogène. Les comparaisons entre simulation sont satisfaisantes, aussi bien concernant les cinétiques de transformations de phases que les profils de dureté et de microstructure (mais ces dernières n'ont été observées que pour l'échantillon carbonitruré refroidi à l'air). En revanche, un écart récurrent avec l'expérience est la sous-estimation de la fraction d'austénite résiduelle. Cet écart est observé pour tous les échantillons, quelle que soit la concentration locale en carbone et en azote et pour toutes les vitesses de refroidissement. On attribue cet écart à la non prise en compte par le modèle de la stabilisation de l'austénite au cours des transformations bainitique et martensitique.

Les prévisions de contraintes sont en bon accord avec l'expérience pour les échantillons cémentés, en partie grâce aux modèles métallurgique et mécanique qui sont déjà bien établis concernant les effets du carbone. En revanche, pour les échantillons nitrurés et carbonitrurés, le modèle métallurgique actuel prédit avec des lois empiriques l'influence de la concentration en azote. Quant aux lois de comportement, davantage de caractérisations seraient nécessaires pour bien rendre compte de l'influence de la concentration en azote. Un écart récurrent avec l'expérience concerne une sous-estimation de la contrainte résiduelle près de la surface, lorsqu'il s'agit de contraintes de compression. On peut l'attribuer à la sous-estimation de la fraction d'austénite, bien que les fractions mesurées par DRX soient trop faibles pour que cette explication soit suffisante. Une autre origine possible de ces écarts réside dans l'incertitude sur les profils de carbone et d'azote qui se sont révélés hétérogènes pour une profondeur donnée, d'après certaines mesures.

Pour toutes les simulations présentées dans cette étude, les évolutions de contraintes

ont pour unique origine les déformations de transformations de phases (variations de volume, plasticité de transformation), tandis que les gradients thermiques sont trop faibles pour induire des déformations plastiques, du fait des petites dimensions des échantillons. Les variations de volume ont une influence prépondérante dans l'évolution des contraintes, par rapport aux déformations de plasticité de transformation. Cependant, ces dernières ont un impact significatif sur les niveaux de contraintes résiduelles et ne peuvent être négligées, comme le mettent en évidence des comparaisons entre des simulations avec et sans prise en compte de la plasticité de transformation.

Perspectives

Cette étude ouvre la voie à des travaux futurs. Les limites actuelles des modèles mécanique et métallurgique ont été mentionnées, notamment sur l'influence de l'azote et la stabilisation de l'austénite. La nouvelle méthode DRX in situ ouvre la voie à l'étude d'alliages multiphasés, en donnant accès aux contraintes par phases et la modélisation des contraintes par phase pourrait être développée. Les développements futurs (nouvelles sources synchrotron, nouveaux détecteurs) devraient permettre d'aborder des vitesses de refroidissement plus élevées. L'outil multiphysique peut être utilisé pour simuler des pièces industrielles de plus grandes dimensions et de géométrie complexe, au sein desquelles les gradients thermiques seront significatifs et pourront induire des déformations plastiques. Une étude systématique de l'effet de différents paramètres de traitements (profondeurs enrichies, concentration C/N, vitesse de refroidissement) pourra être menée. Enfin on pourra considérer le revenu après le refroidissement, voire des traitements innovants de trempe interrompue, qui visent à remplacer l'étape de revenu.

Introduction

Steel plays a significant and critical role in the automotive industry, whose performance keeps improving with the latest discoveries to hold the prime position. It has countless microstructures and properties, making it one of the most versatile alloys. The automotive industry has been continuously optimizing fatigue life and reducing distortion of powertrain steel components such as gears, hubs, etc.. These components are often treated to achieve these properties by thermochemical processes. Carburizing and carbonitriding are important thermochemical treatments widely practiced in industries. The treatment aims to generate gradients of carbon or carbon + nitrogen composition in the surface area of the piece by diffusion in the austenitic field, and it is followed by quenching to obtain the desired gradients of microstructures, mechanical properties, and compressive stresses on the surface to improve the fatigue and wear resistance. These last years, due to more severe mechanical and environmental constraints, a new process of low pressure carburizing with gas quenching has been largely developed in the industry. Low pressure carbonitriding with gas quenching develops too, but this process still needs research work to understand deeply the complex physical phenomena involved and also to develop models and numerical tools for better optimizing and ensuring the robustness of the process in industrial applications.

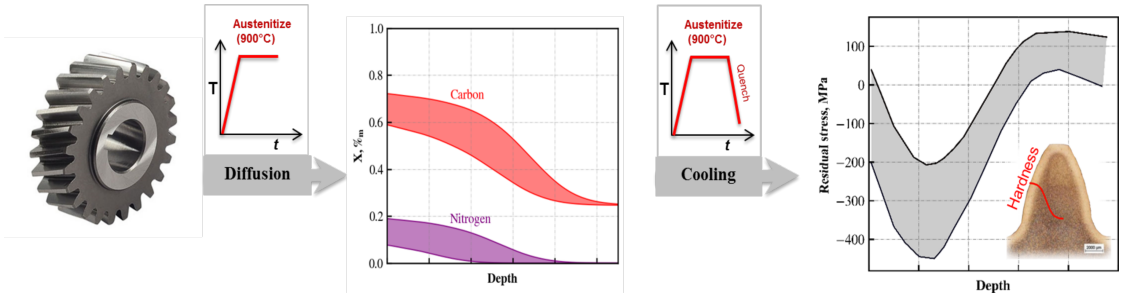

Figure 1: Powertrain component undergoes the thermochemical and quenching process resulting in the microstructure and residual stress distributions along the gradients.[1]

It is the reason why a large program aiming better understanding, control, and optimization of carbonitriding treatments of low alloyed steels from the point of view of the process, the generated microstructures and mechanical properties, as well as the residual stresses has been launched in the frame of IRT M2P (Institut de Recherche Technologique “Matériaux Métallurgie Procédés.” This program called TTA (Traitements Thermiques Avancés) gathered 10 industrial partners and IJL as an academic research laboratory. At first, the Ph.D. work of Walter Dal’Maz Silva [2] was mainly dedicated to the experimental analysis and modeling of the carbonitriding process itself, i.e., the decomposition kinetics of different gas atmospheres and the diffusion kinetics leading to the carbon and nitrogen enrichment profiles.

In parallel, in the frame of his Ph.D. initiated by a collaboration between IJL and PSA, Simon Catteau [3] focused on the experimental study and modelling of the effect of carbon and nitrogen concentrations on the microstructure evolutions associated with austenite decomposition during cooling after the enrichment treatment of low alloyed steel (23MnCrMo5). The experimental study was based on homogeneously enriched samples in carbon, nitrogen, and carbon+nitrogen. In situ techniques (dilatometry, in situ synchrotron X-ray diffraction) were used to determine the phase transformation kinetics as well as post-mortem ones (SEM, TEM) for analyzing the final microstructures and hardnesses. These experimental studies served as a basis for developing a

global phase transformation model to predict kinetics during continuous cooling, final microstructures as well as hardnesses in carbon and nitrogen enriched specimens. In addition, deeper microstructural analyses by TEM have been performed during the post doc of Hugo Van Landeghem [4] in the frame of Labex DAMAS.

On the basis of S. Catteau's work[3], our Ph.D. was launched with the focus on residual stresses generated after the carbonitriding treatment. The aim is to understand how internal stresses are generated during the cooling in relation with the phase transformations in carbon and nitrogen gradient specimens. For that purpose, on the one hand, advanced *in situ* characterizations by synchrotron X-ray diffraction have been implemented, and on the other hand, a coupled model for predicting temperature evolutions, kinetics of phase transformations, and internal stresses.
The manuscript is divided into four chapters.

In the first chapter I, we present the literature studies on residual stresses in carburizing and carbonitriding processes starting with the experimental studies and then the numerical predictions with coupled thermo-metallurgical-mechanical models. We also include a qualitative approach that helps to introduce the complex phenomena that must be modeled.

The second chapter II describes the studied steel and the experimental methods used. One crucial aspect is to elaborate samples: on the one hand, samples homogeneously enriched with carbon, nitrogen and both for the thermomechanical and thermophysical characterizations, and on the other hand, samples with controlled carbon and nitrogen gradients which are representative of the gradients present in industrial parts. This needs to master the enrichment process on a laboratory thermobalance as it will be described.

Another key point of our study was to characterize the thermomechanical and thermophysical behaviour of the steel in order to build the whole set of input data for the numerical simulations. Particularly, we will describe the new thermomechanical device acquired in the lab and its complex handling.

Finally, special emphasis will be given to the in situ High Energy X-Ray Diffraction (HEXRD) technique and to the transportable setup on the synchrotron beamline for measuring mean internal stresses in the phases during cooling.

Chapter III will be devoted to the in situ experimental analyses by High Energy X-ray diffraction (HEXRD) in the carburized, nitrided, and carbonitrided samples that allow to get simultaneously and quantitatively the phase fractions formed and the internal stresses that develop during cooling throughout the chemical composition gradients. The three types of enriched samples will allow to conduct a deep analysis of the role of nitrogen gradients.

Chapter IV concerns the coupled thermal metallurgical thermomechanical modelling and the numerical simulations. First, we recall the main features of the models that are generally used for the prediction of internal /residual stresses during heat treatments. Then, the metallurgical model developed in the thesis by Simon Catteau for the prediction of transformations kinetics in carbon and nitrogen enriched steels is recalled. The full coupled model and sets of input data are implemented in finite element code Zebulon.

Finally, the simulation results (transformation kinetics and internal stresses evolutions) are analyzed and validated through the comparison with the experimental results obtained by in situ HEXRD. Additional experimental validations are performed by comparing post-mortem results (final microstructures and residual stresses) for different cooling conditions of enriched samples.

Contents

Chapter I

Bibliography study

The bibliographic study presented here focuses on the studies of the effects of carbon and/or nitrogen enrichment of steels on the residual stress distributions during cooling. We consider here macroscopical residual stresses (Type I) (see Appendix A) even if stress measurements by X-ray diffraction give access to mean stresses in the analyzed phases.

This review is detailed in two main sections: firstly, we present the experimental studies. Then, a qualitative approach will address the main phenomena of internal stress formation during cooling. Finally, an overview of the numerical models that couple thermal, metallurgical, and mechanical phenomena during the heat treatment process will be given and examples of carburizing and carbonitriding results.

I.1 Effects of carbon and nitrogen enrichment on residual stresses: Experimental studies

I.1.1 Carburizing

For carburizing, a lot of experimental studies have been performed. In the early 1930s, Bühler and Buchholz[5] determined the residual stress distributions of carburized steels experimentally and linked the origin of compressive stresses in the surface area to the volumic variation as austenite transforms to martensite, this volumic variation being larger as the carbon content is higher. Then, several authors[6, 7, 8, 9] pointed out that the chronology of phase transformations along the thickness of the carburized part plays an important role in the residual stress patterns. The outcome of these studies is that in case-hardened steel, the austenite decomposition during quenching proceeds progressively from the case/core interface towards the surface component to form the compressive stress at the surface. Koistinen[10] noted that for the carbon content profiles studied, the maximum compressive stress corresponds to an average carbon content of 0.5%C, the position where the martensite fraction is maximum, as martensite fraction decreases towards the surface because retained austenite increases. Other authors also related the decrease of compressive residual stresses to the increase of retained austenite content. For example, Genzel et al.[11] showed residual stress profiles obtained after carburizing with either oil quenching or liquid nitrogen quenching (see Figure I.1). Higher compressive residual stresses are obtained after liquid nitrogen quenching due to the transformation of retained austenite into martensite.

From the bibliographic review of A. Mey[12] different authors showed that the magnitude and distribution of residual stresses are linked to the rate of austenite decomposition, which depends on the severity of quenching conditions, the case depth, and the carbon content profiles. For example, Burnett et al.[13] observed that increasing cooling rates lead to higher compressive stresses.

Concerning the effects of different quenching conditions on residual stress

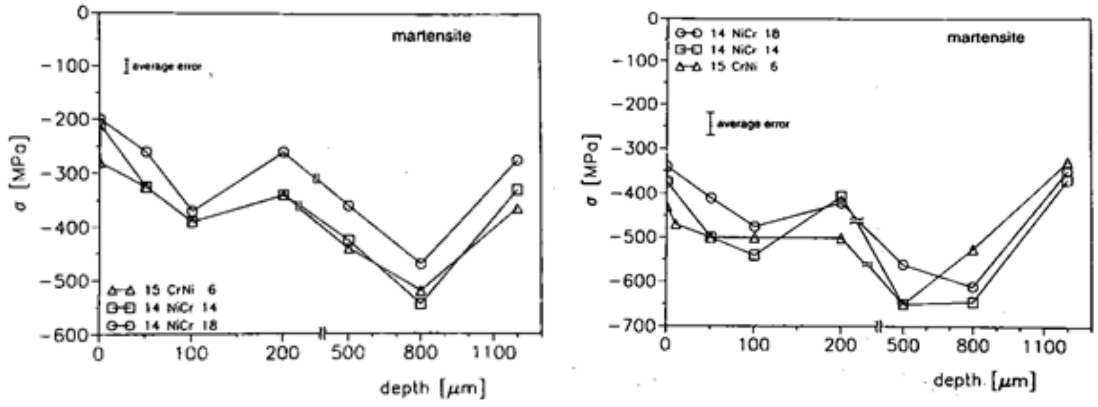

(a) (b)

Figure I.1: Residual stress versus depth for different carburized steels a) quenched in oil (at 60°C) b) quenched in oil (at 60°C) and in liquid nitrogen.

distributions in the carburized specimen, we can also add the experimental work of C. Aubry[14]. Residual stress distributions have been measured after carburizing a 27MnCr5 steel and quenching in different media (cold oil, hot oil, gas quenching). Results are shown further in the simulation part in Figure I.12 and did not evidence a large effect of quenching media in the case studied.

I.1.2 Carbonitriding

Much less experimental results exist for carbonitriding. In early work, Arkhipov et al.[15] investigated the residual stresses distribution in carburized and carbonitrided gear teeth. The authors consider that the residual stresses result from phase transformations alone since thermal stresses are absent due to the moderate cooling rate. They concluded that the surface tensile stresses (see Figure I.2) are due to the effect of the internal oxidation on the transformation sequence of the austenite. They also emphasized that the lowest carbon content results in tensile stresses throughout the entire case depth and an excess of retained austenite in the carbonitrided case changes the surface stresses. The authors also added that nitrogen has almost no effect on internal stresses, i.e., in carbonitrided steel, the stress distributions are similar as in carburized steel.

Today a renewed interest for carbonitriding can be noticed due to the potential gains in mechanical properties (mainly fatigue properties) in comparison with carburizing[16]. For example, experimentally, Katemi et al.[17] investigated the influence of carbon and nitrogen contents on compressive residual stresses. Two carbonitriding experiments were performed with different carbon and nitrogen contents and quenching into oil at 60°C. Residual stress depth profiles were determined using the $sin^2\,\psi$ method, as shown in Figure I.3a and I.3b. In the 50-400 µm depth range, the compressive residual stresses in specimen CN1 are higher than in specimen CN2 due to the lower amount of RA (around 15%) due to less interstitial content. The authors also emphasized that measuring residual stresses in both phases (martensite and retained austenite) is essential for determining the macroscopic residual stress when the retained austenite content is more than 15%. It has also been shown[18] that the position at which the maximum (peak) compressive stresses occurs has a (carbon + nitrogen) content of about 0.5 %wt, corresponding to about 80% martensite.

For the same steel, Katemi et al.[19] also investigated the effect of cryogenic treatment and tempering on residual stresses and retained austenite distributions after carbonitriding and quenching. It was concluded that the cryogenic treatment increases the compressive residual stresses and shifts the maximum compressive residual stress position towards the surface (Figure I.5) due to the transformation of retained austenite into martensite (volumic variation). At the opposite, as expected, tempering relaxes

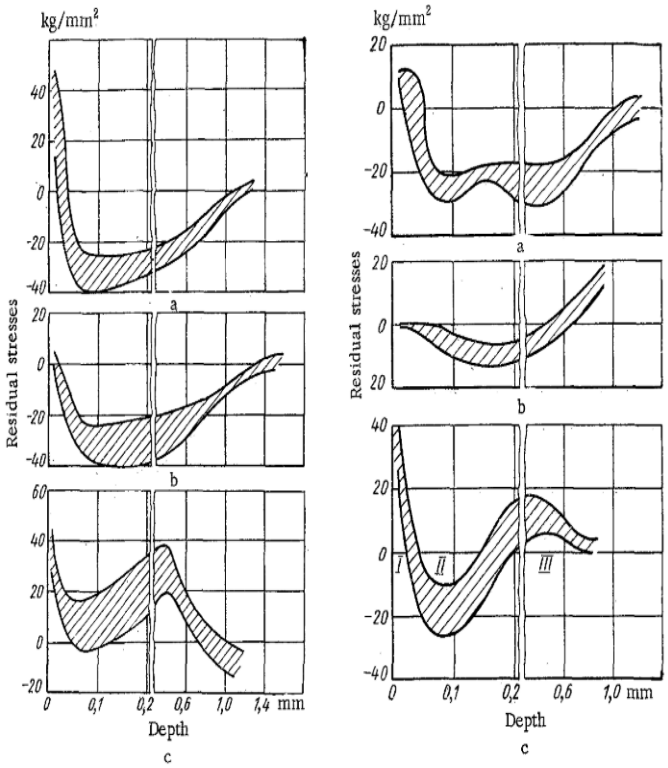

Figure I.2: Residual stresses at the base of the teeth in carburized gear (left) a) 0.87%C at the surface check b) 1.02%C c) 0.73%C and carbonitrided gear(right) with 0.8%C a) 0.52%N b) 0.3%N c) 0.49%N.

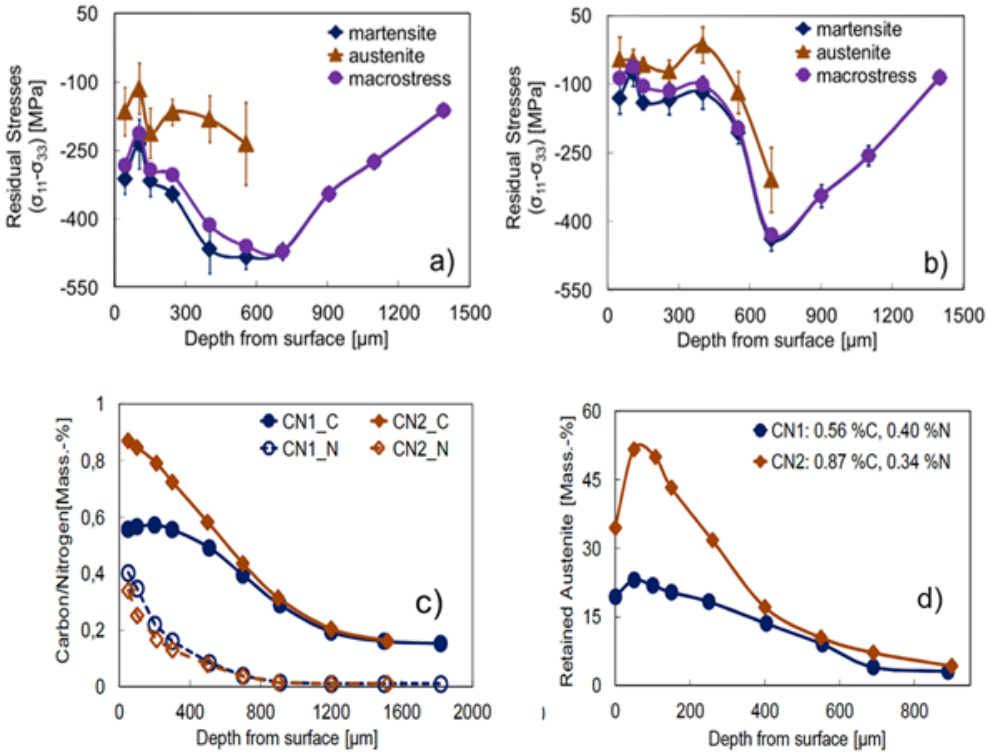

Figure I.3: Carbonitriding of two 18CrNiMo7-6 steel specimens CN1 and CN2 (diameter 34mm, thickness 8mm)[17] a) and b)in-depth residual stress profiles for CN1 and CN2, respectively, c) Carbon and nitrogen profiles d) retained austenite profiles.

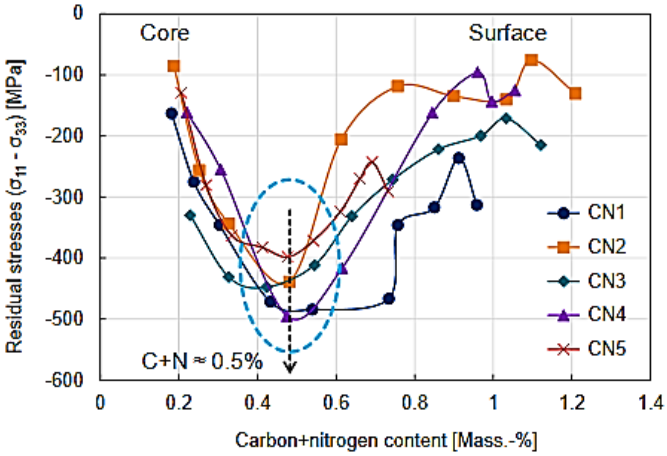

Figure I.4: Residual stresses in martensite as a function of (C+N) content for carbonitrided specimen quenched in oil and untempered.(Cabon and nitrogen contents at the surface are given in the table).

Table I.1: Cabon and nitrogen contents at the sample surface.

S/No.	Carbon [Mass.-percent]	Nitrogen [Mass.-percent]
CN1	0.56	0.40
CN2	0.87	0.34
CN3	0.77	0.36
CN4	0.86	0.20
CN5	0.59	0.18

the residual stresses due to the decrease of the yield stress. Let us mention that very recently[20], the authors also performed in situ X-ray analysis to follow the residual stress evolutions at the surface during tempering.

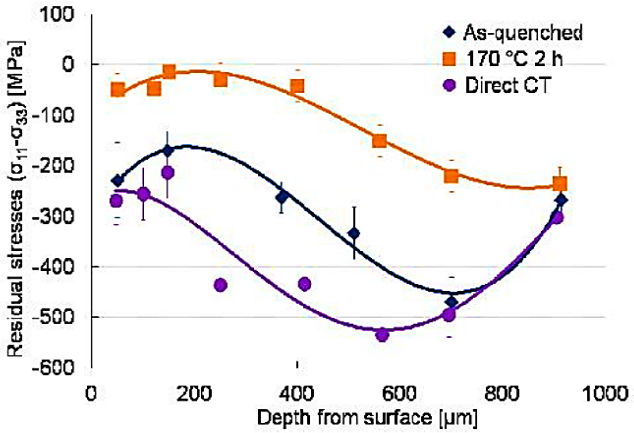

Figure I.5: Residual stresses profiles in martensite after carbonitriding: as-quenched state, after cryogenic treatment and after tempering.

I.2 Predictions of residual stresses

Generally, the residual stresses are characterized experimentally at the end of the quench, and therefore, to understand precisely the residual stress formation, i.e., the internal stress evolutions during the quenching, numerical simulation tools which take into account the complex interactions between mechanical, thermal, and microstructural

evolutions have been developed. Before establishing the computer numerical models, a qualitative analysis was proposed by Bühler and Rose [5] in the early 1950s and followed by other authors[6, 7, 8, 10] to demonstrate the origin of macroscopic internal stresses and tend to explain the final residual stress distribution in parts. In this section, before recalling the present numerical models, we wish to address this very early work of Bühler and Rose[5].

I.2.1 Qualitative analysis of residual stress formation

We take two examples of these approaches[21]: the first is a martensitic quenching of a cylinder, and the second concerns quenching after carburizing. For martensitic quenching, two cases are considered a pure ideal linear elastic material (Figure I.6) and an elastoplastic material Figure I.7a to show the stress evolutions with and without plastic deformation.

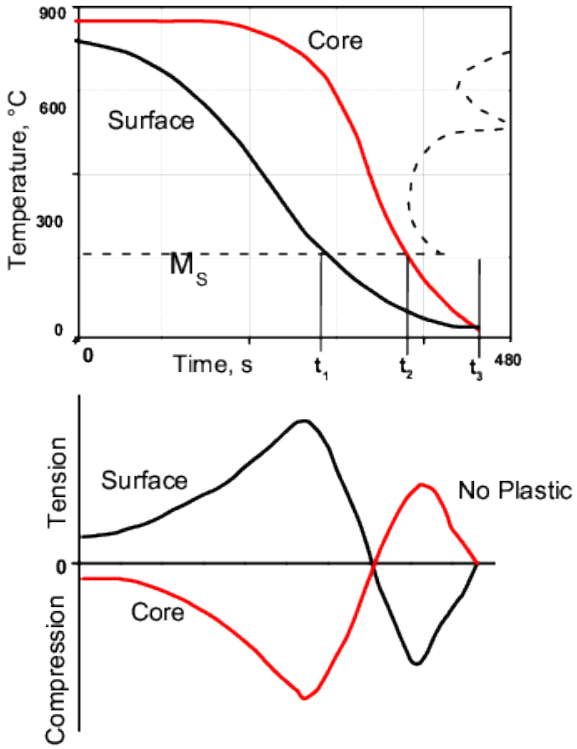

Figure I.6: Evolution of temperature and longitudinal stresses at surface and core in a cylinder for an ideal linear-elastic material that only transforms in martensite during rapid cooling.[21]

The cooling laws of the surface and center are given in Figure I.6 and Figure I.7. In both cases, as the surface temperature decreases more rapidly than the core temperature, it results in thermal gradients between the core and the surface. The thermal stresses increase in tension at the surface and compression at the core. As the martensitic transformation occurs at the surface, the volumic expansion decreases the tensile stresses at the surface and, consequently, decreases compression in the center. As transformation progresses towards the inside of the piece, stresses increase in compression at the surface and in tension in the center. As the martensitic transformation occurs in the center, the tensile stress decreases, as well as the compressive stress at the surface. In the case of an elastic material (Figure I.6), as no permanent deformations remain at the end of cooling, no residual stresses exist.

For an elastoplastic material (it is generally the case), Figure I.7a. shows that the internal stresses during quenching reach the material's yield stress. Consequently, heterogeneous deformations (plastic strains and/or phase transformation strains) remain in the piece after cooling, and residual stresses exist. In their analysis, Rose and Bühler[22]

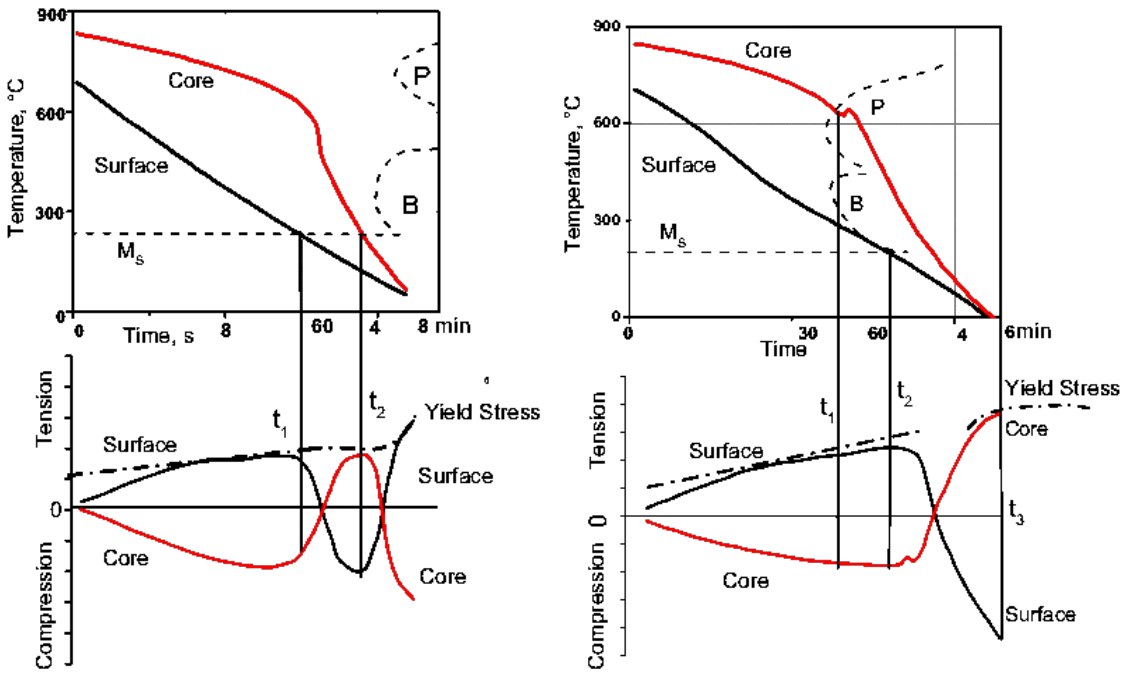

Figure I.7: a) Evolution of thermal and phase transformation stresses on the surface and core of a) an elastoplastic material that only transforms in martensite during rapid cooling b) a carburized cylinder when ferritic-pearlitic transformations occur first in the core and are followed by martensitic transformation in the surface.[21]

assumed that plastic strains occur during cooling as the material is in maximum tension at the surface and in the center, resulting in residual tensile stresses at the surface and compressive stresses in the core after martensitic quenching. Let us mention that is not always the case for the martensitic quenching of a piece.[23, 24, 25] (See the example given in Appendix B)

For quenching after carburizing, Figure I.7b[22] shows the case where a ferrite-pearlite transformation occurs earlier in the core (due to low carbon content in the core), and later on, a martensitic transformation takes place at the surface with the higher carbon content. Due to the latent heat, pearlitic transformation induces recoalescence on the cooling curve. But the effect of the volumic variation on the stress evolution is small. At time t_2, due to the volumic expansion associated with martensitic transformation, a compressive residual stress state is expected at the surface and a tensile stress state in the core. Of course, plastic strains can be generated too during cooling.

Even if these qualitative approaches are very interesting because they evidence the major factors (thermal gradients and phase transformations) that cause residual stresses after heat treatment of metallic alloys and also the complexity of the genesis of internal stresses, they are of course not sufficient to predict quantitatively residual stresses. The quantitative prediction will need to quantify all the deformations of the material (elastic, plastic, thermal, phase transformation, and transformation plasticity strains) in order to calculate the resultant residual stresses states precisely at the different locations in the piece after heat treatment. Thus, the stress states must be predicted all along the treatment, and it is highly complex because they depend on the temperature evolutions at the different locations in the piece as well as on the kinetics of phase transformations. Thus, predicting stress development during heat treatment by considering all these effects was challenging and required coupled finite element models.

I.2.2 Coupled metallo-thermomechanical models

Metallo–thermomechanical coupling models have been developed largely in literature since the 1980s for quenching, surface heat treatments, and thermochemical treatments,

and there is plenty of literature. In this section, firstly, the main features of this model and related literature are briefly reminded (more details can be found in review papers as [26, 27]. Then, we will focus on the results of the calculation of residual stresses for carburizing and carbonitriding treatments.

The triangular schematic diagram (Figure I.8) gives the main features of a metallo-thermomechanical coupling model. The three main models necessary to perform the calculation of the residual stress distribution are the thermal model, the phase transformation model, and the thermomechanical model. For thermochemical treatments (carburizing, carbonitriding), in addition, the effects of carbon and nitrogen on the former models have to be taken into account. One major feature is the couplings between temperature evolutions, stress field, and phase transformations in a material, as shown in Figure I.8. Thus, temperature evolutions will induce phase transformations, and the latent heat produced during phase transformation as well as the changes in thermophysical properties, affect the temperature distribution. The heat generation due to mechanical energy dissipation is small in comparison with heat transfers and is commonly neglected[26].

The thermal stress field is due to inhomogeneous thermal dilatations/contractions in the piece. When the phase transformation occurs, the associated deformations (volumic variation, transformation plasticity) and changes in the thermomechanical behavior must be taken into account[28]. Under the stress field, phase transformation kinetics gets also altered.

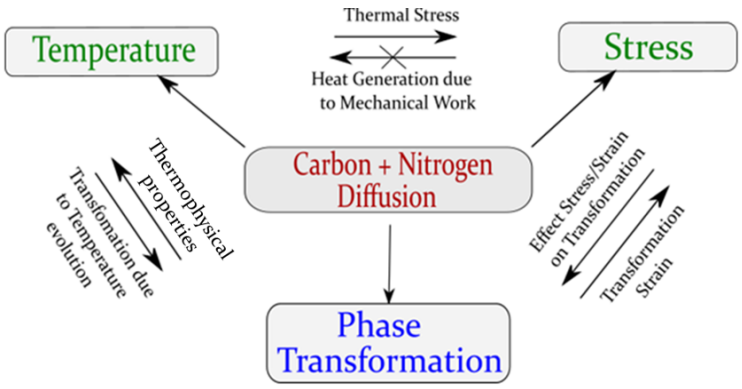

Figure I.8: Diagram of thermal, mechanical, and metallurgical interaction during heat treatment processes[26]

In the 1980s, researchers such as Denis et al.[24], Inoue et al.[29], Sjöström et al.[8], Reti et al.[30], and Leblond.[31], among others, have done significant work in that field. Models for predicting phase transformation kinetics in steels during heat treatment based on global approaches have been developed for the residual stress calculations. These global models take into account temperature time effects, and some authors take into account as well austenitic grain size[32, 33] and stress effects[34]. We will describe further in detail (Chapter IV) the models developed at IJL. Some nucleation and growth models have also been taken into account in residual stress calculations[35].

In their early works, the authors described the material behavior with thermoelastoplastic laws with isotropic or kinematic hardening taking into account the transformation strains (volumic variations and transformation plasticity). In these models, all material properties are temperature and phase fraction dependent. Assumptions on the hardening memory through phase transformations have also been included [36, 37]. In more recent years, thermoelastoviscoplastic laws have also been taken into account[38, 39].

In the early decades, due to the complexity of computer calculations, the authors focused on simple geometry, such as simple 1-D and 2-D shapes such as infinitely long cylinders and cylinders of finite height [36, 40, 41] or large plates served as a simplified model for gear components, with simple thermo elastoplastic behavior[42]. Later on, the

complexity of studies increased by taking into account actual two-dimensional or three-dimensional geometry[43, 44, 45, 46], such as gear profile for studying and controlling, for example, the gear distortion during induction hardening[47]. These complex geometry simulations have included almost all aspects of the material behavior, such as thermo elasto-viscoplastic behavior with the effects of phase transformation, transformation plasticity, and also variable heat transfer coefficients are taken into account. Today, there are several commercial Finite Element software packages like LAGAMINE, SYSWELD, ASTER, FORGE, HEART, GRANTAS, DANTE, DEFORM-3D, and HT-MOD, which are available to simulate a wide variety of heat treatment processes by taking into account all available aspects of material behavior, design, and process parameters. Some general FE software packages, such as ABAQUS and ANSYS are also used for heat treatment calculations. A powerful finite element in-house software, ZEBULON, was developed by Ecole des Mines de Paris to investigate the material behavior in a flexible user-defined environment[48] and will be used in our study.

All these models (thermal, phase transformation, thermomechanical) need numerous input parameters, mostly determined by experimental methods. Specific experimental devices and associated experimental procedures needed to be developed in parallel to the computer codes, as we will show in Chapter II.

It is also important to validate the results of computer simulations by using experimental methods. Classical validation involves comparisons between calculated and measured temperature evolutions during the heat treatment, final microstructures, hardness, residual stress distributions after the heat treatment, and the deformation of the piece. More advanced validations consist of developing new experiments to follow, for example, in situ the deformations of a massive specimen during cooling (see, for example,[49, 50, 51]). But as far as we know, in situ analysis of internal stresses during cooling in specimens with gradients in order to validate the calculated internal stresses evolution does not exist.

I.2.2.1 Quenching of carburized steel

Several authors dealt with the numerical predictions of residual stresses during carburizing treatments. We have chosen to present only a few examples from the very early studies and from the more recent ones. The precursors were the Swedish[8, 52, 53], Japanese[54], German[55], and French groups[12, 14]. Hildenwall and Sjöström[36] have performed the prediction of residual stresses in carburized cylinders via an in-house computer model, including calculations of the temperature gradients during cooling (with thermophysical properties depending not only on temperature and fractions but also on carbon), the kinetics of phase transformations depending on carbon gradients and the internal stresses evolutions during cooling. They considered the thermoelastoplastic behaviour of the steel, including the transformation strains (volumic variations and transformation plasticity). In addition, all the material parameters are dependent on the carbon content. They have particularly analyzed the effects of different carbon gradients in cylindrical pieces on the residual stress states and showed that the comparisons with experimental results work quite well. These authors showed for the first time the large effect of transformation plasticity on the calculated residual stresses in the carburized specimen, as illustrated in Figure I.9 and that this phenomenon must be taken into account for achieving good agreement between calculations and experiments.

Hildenwall[52] and Hoferer[55] also showed, thanks to the simulation, that when the carburized depth increases, the maximum compressive stress is shifted towards lower depths. With their model, Hildenwall et al.[6, 41] were also able to predict residual stresses in the soft pearlite layer that can appear in carburized steels due to surface oxidation. First, they predicted the microstructure distribution versus depth within the pearlitic layer (see Figure I.10a) that leads to an unusual residual stress distribution, as shown in Figure I.10b with tensile residual stress in the pearlitic surface layer and compression

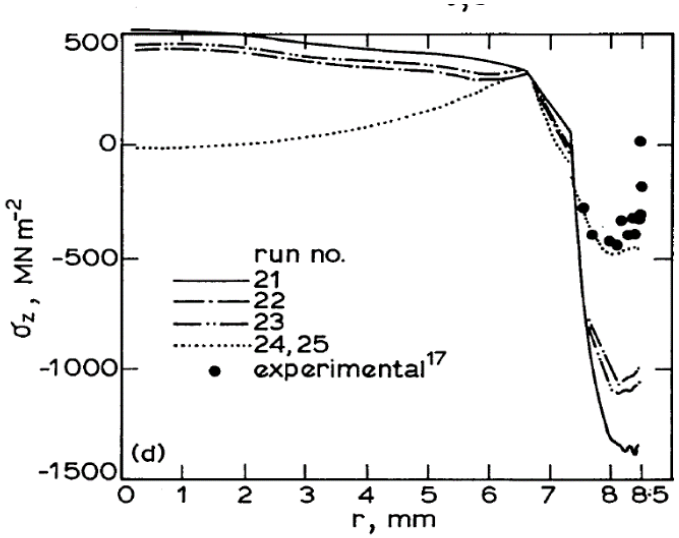

Figure I.9: The effect of transformation plasticity on the residual stress prediction in a carburized cylinder of SIS2511 steel quenched in oil at 60°C [36] and runs 24 and 25 with transformation plasticity included.

in the underlying martensite. Early formed pearlitic layer becomes strained in tension during the martensite formation of the case, and tensile residual stresses arise during the cooling.

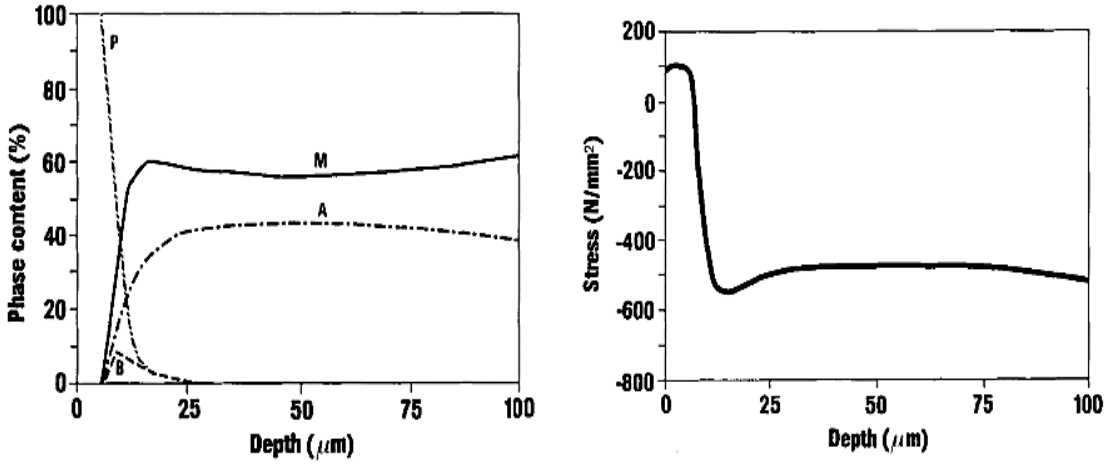

Figure I.10: Calculated a) phase content (P pearlite; M martensite; Austenite; B bainite) and b) residual stress vs. depth below the surface of a carburized plate (thickness 40mm)quenched in oil (60°C).[41]

Burnett et al.[13], using an elastic-plastic finite-element program, also predicted the final residual stress patterns in carburized cylinders during the water and oil quenching (martensitic quench) and systematically traced the entire stress history (see Figure I.11a). The numerical model neglects the effect of transformation plasticity. However, a reasonable agreement with measured XRD results is obtained, as shown in Figure I.11b. The authors show that not only the volumic variations due to phase transformations impact residual stresses but also the plastic deformations generated in the austenite during the cooling, which depends on the severity of the quench: higher cooling rates (i.e., higher temperature gradients) lead to higher plastic strains and thus increase the final residual compressive stress.

Inoue[56] also developed a software to simulate the carburizing process in pieces with also an elastoplastic constitutive behavior law of the material. In particular, the carbon content gradients are predicted in the piece (solution of diffusion equation) and the resulting phase transformations during cooling. The authors were able

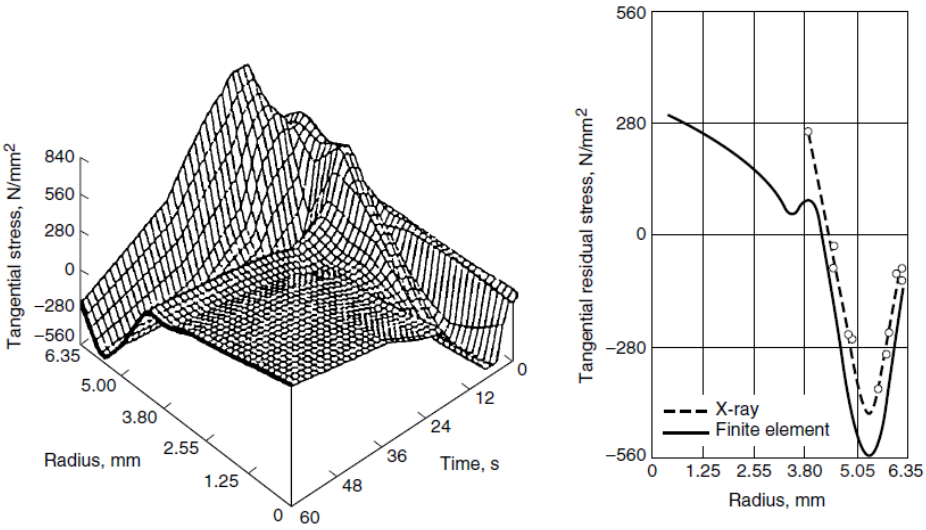

Figure I.11: a) 3D history of tangential stress b) calculated and experimental tangential residual stress profile in an oil-quenched carburized steel cylinder.[13]

to predict microstructures and residual stresses in carburized and quenched gears. Nevertheless, little information is given on the input data and assumptions behind the different models. In Nancy (at LSG2M that became IJL), the former in-house coupled thermal-metallurgical-mechanical calculation model[12, 14, 27, 57] has been further developed in order to predict microstructures and residual stresses after carburizing. A previously existing model for the prediction of anisothermal transformation kinetics from isothermal kinetics Fernandes[58] has been developed to include the effects of carbon gradients[59]. Thermophysical and thermomechanical material parameters have been considered as carbon content dependent too. The transformation plasticity and the effects of stresses on phase transformation are also taken into account. An example of simulated results[25] is given in Figure I.12 for the gas quenching process of an infinitely long cylinder: the final microstructure and hardness profiles (Figure I.12a) and the internal stresses evolutions as well as the permanent strains (Figure I.12b). These simulated results have allowed to understand the effects of phase transformations on internal stress evolutions. As expected, the martensitic transformation at the surface leads to the compressive residual stresses. In Figure I.12b, it can also be clearly seen that during the martensitic transformation (that occurs under stress), relatively high transformation plasticity strains, as compared with the plastic strains are generated in the austenite before the transformation and impact the final residual stress level. In addition, in that study, three different quenching treatments (gas, cold oil, and hot oil) have been performed experimentally and simulated numerically [25]. The shapes of the residual stress profiles are similar. Again, the decrease of compressive stresses in the surface area has been linked to the increase of the retained austenite fractions. The numerical simulation results show higher compressive residual stresses for gas quenching as compared with cold oil quenching (Figure I.12c. It was attributed to the chronology of phase transformations in the specimen: for gas quenching, the phase transformations in the non-enriched areas (mainly bainitic transformation) are completed as martensitic transformation occurs at the surface whereas, for cold quenching, the martensitic transformation continues in the non-enriched area as the surface transforms. The authors point out that due to the experimental errors, residual stress measurements are not able to discriminate the different quenching conditions.

A more complex case has been addressed by A.Mey[12] for a combined treatment: carburizing followed by induction hardening (rapid heating followed by water cooling). The microstructural evolutions on heating and cooling in the carbon gradients and the associated mechanical evolutions are so complex that only the simulation can help to understand what happens in the carburized layer as rapid heating and cooling are applied (Figure I.13). It was shown that the combined treatment allows to double the

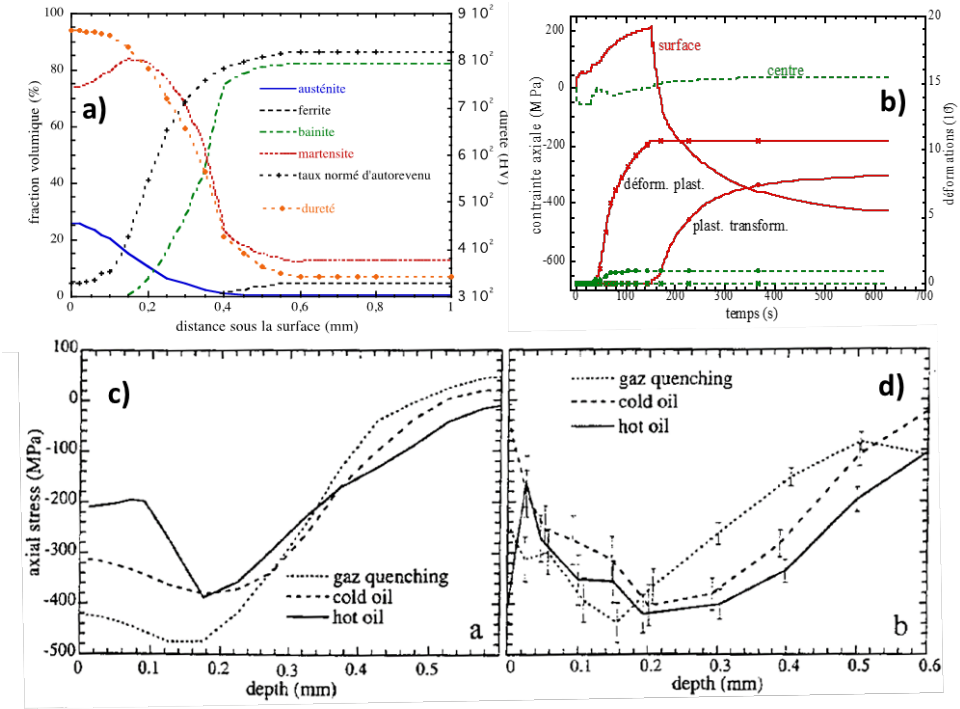

Figure I.12: Simulation of quenching after carburizing of the cylindrical specimen (diameter length) of steel 27MnCr5 a)Calculate final microstructures and hardness profiles after gas quenching b)Evolution of internal stresses and permanent deformations (plastic and transformation plasticity strains) versus time c)Simulated and d)experimental residual stress profiles for quenching in different media[14, 25].

maximum level of compressive residual stresses in comparison with carburizing alone, which could be very beneficial as far as fatigue properties are concerned. It was shown that this increase in compressive stresses is again related to the plastic strains that occur in austenite due to the high thermal gradients on cooling.

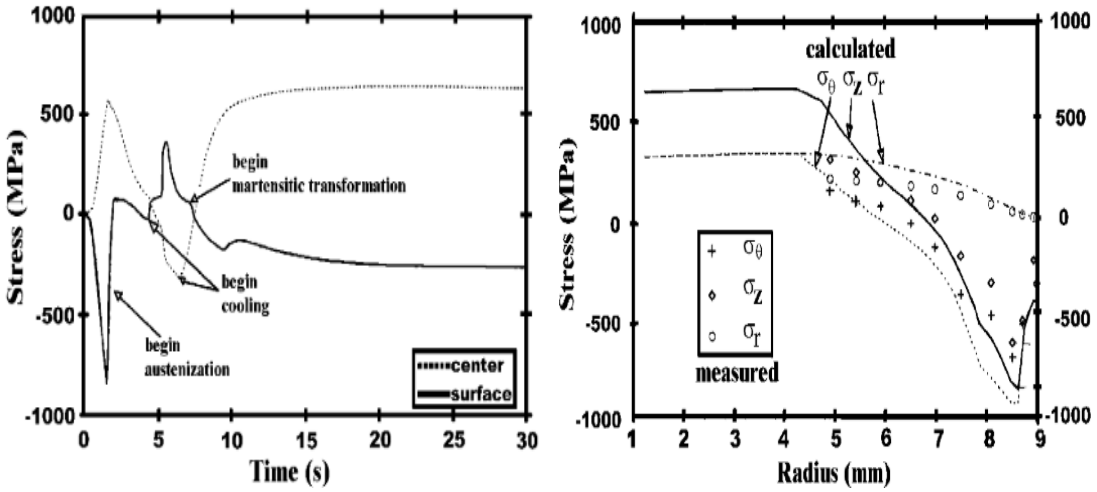

Figure I.13: a)Axial stress evolutions versus time during rapid heating and cooling of a carburized steel (15CrMo4) cylinder and b) calculated and measured residual stress profiles.[12]

In more recent years, the studies rely mainly on the previously developed thermal-metallurgical-mechanical models and mainly address more complex geometries[43, 44, 45, 47, 60, 61, 62]. As far as we know, except for the early work of Inoue[42], only one study[61] takes into account viscoplastic effects in the constitutive behavior law of the material. This evolution towards industrial applications is mainly linked to the development of computation power in later years. Thus, Ferguson et al.[60] studied the development of internal stresses and geometric distortion in carburized and quenched notched coupons for further fatigue resistance studies. An example of residual stress

simulation on carburized and quenched gears were done by Song [63] and Inoue[64], as illustrated in Figure I.14. Sugianto et al.[45] and Decroos et al.[62] have also modeled a more complex helical gear and, in addition, have included gravitation effects during quenching. Indeed, their weight often causes a stress concentration for large and heavy components and is expected to influence the deformation behavior in the region close to the hanging points.

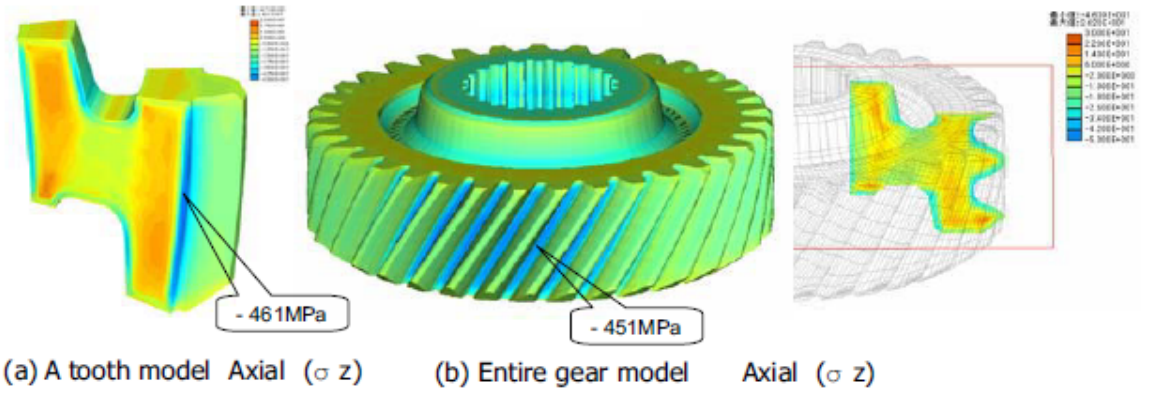

Figure I.14: Calculated axial residual stresses in gear after carburizing and quenching. (a) tooth model, and (b) the entire gear model. [64]

I.2.2.2 Quenching of carbonitrided steel

Only a few authors have addressed the prediction of residual stresses for carbonitriding. Degallaix et al.[65] calculated the residual stresses due to carbonitriding using a simplified approach. The residual stress profile is obtained from the different volumic variations associated with the different phase transformations that occur at different depths that depend on C and N profiles. The phase fractions at different depths are estimated from hardness measurements. An example of the results is shown in Figure I.15. The authors conclude on good agreement between calculated and measured residual stresses. The larger discrepancies at the surface are attributed to oxidation or porosities that make the microhardness measurements difficult and, consequently, the determination of phase fractions.

As far as we know, Liu et al.[66, 67] are the first authors who have performed residual stress calculations using a thermal-metallurgical-thermomechanical model. In addition, they have performed diffusion calculations of carbon and nitrogen profiles in the specimen (Figure I.16a and I.16b). They describe the kinetics of pearlitic transformation by a Johnson Mehl Avrami law. The progress of martensitic transformation depends on carbon and nitrogen contents. The thermomechanical behaviour is considered as thermoelastoplastic, but the parameters do not consider the effects of carbon and nitrogen due to a lack of experimental data. Volumic variations depending on carbon and nitrogen contents are taken into account, but transformation plasticity is neglected. The authors consider a qualitative agreement between the calculated residual stress at the surface and the measured one (Figure I.16d). Let us mention that the paper gives very little information on the input data for the simulations and does not analyze the evolutions of internal stresses during cooling.

A similar approach has been used by Mukai et al.[68]. The carbon steel (JIS-SCM420) ring specimen is subjected to carbonitriding treatment and quenching. The cooling curves of the ring specimen are measured, as well as hardness and residual stresses after the treatment. Figure I.17 represents a comparison of predicted residual stress profiles with the measured profiles in the middle section of the specimen. Here, the discrepancy between measured and calculated values has been attributed to the fact that C and N contents effects are not considered on the thermomechanical behavior, and

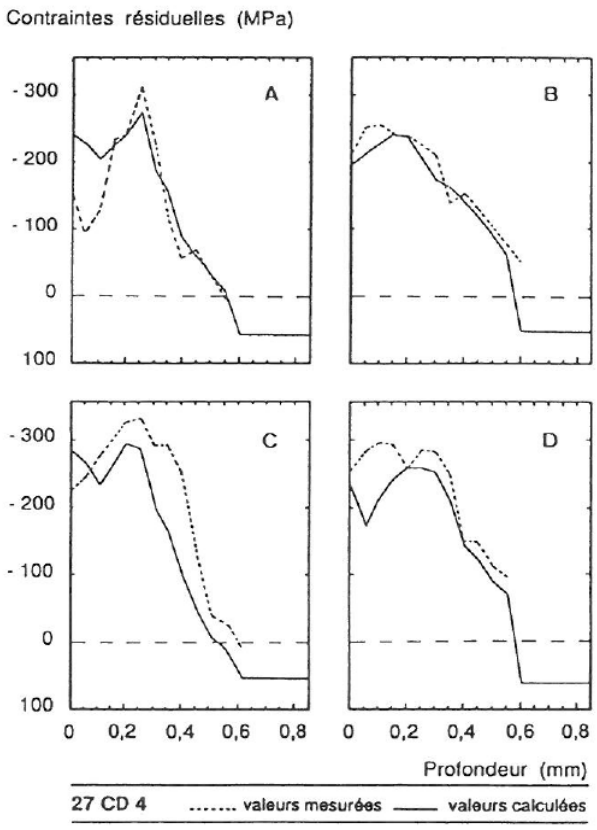

Figure I.15: Residual stress profiles for different carbonitrided specimens A, B, C, and D (base steel 27CrMo4, discs with 5mm thickness.)

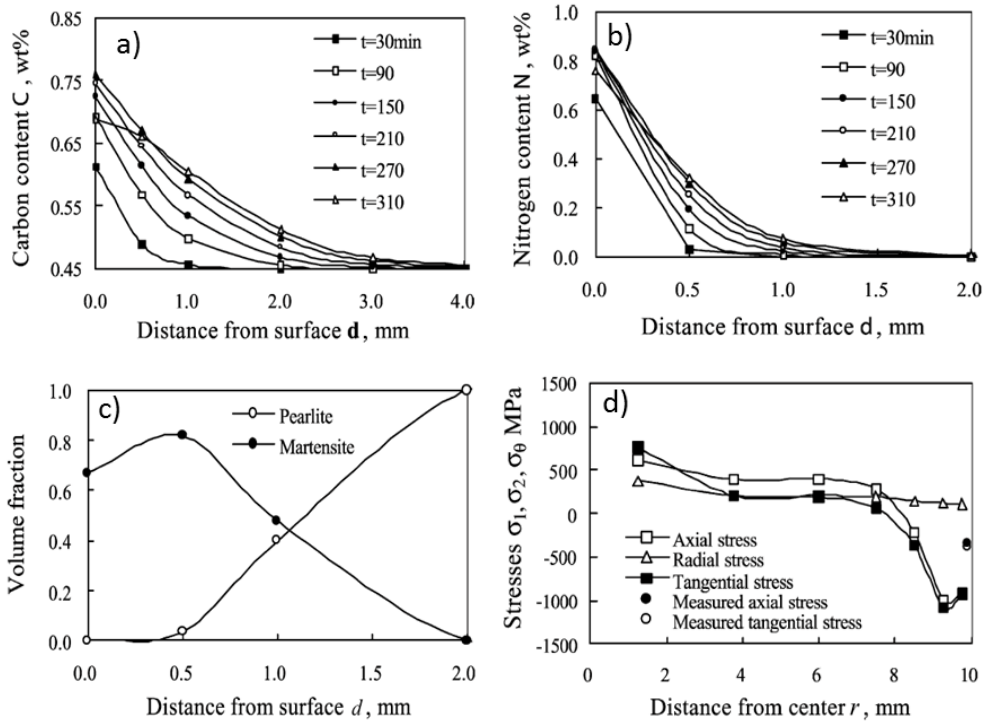

Figure I.16: Carbonitriding of a cylinder of SC45 steel (diameter 20 mm length 60 mm) a) calculated carbon profiles at different times b)calculated nitrogen profiles at different times c) calculated microstructure profiles after quenching in oil at 60°C d) calculated and measured residual stress profiles. [66]

transformation plasticity is not taken into account due to the lack of related experimental results.

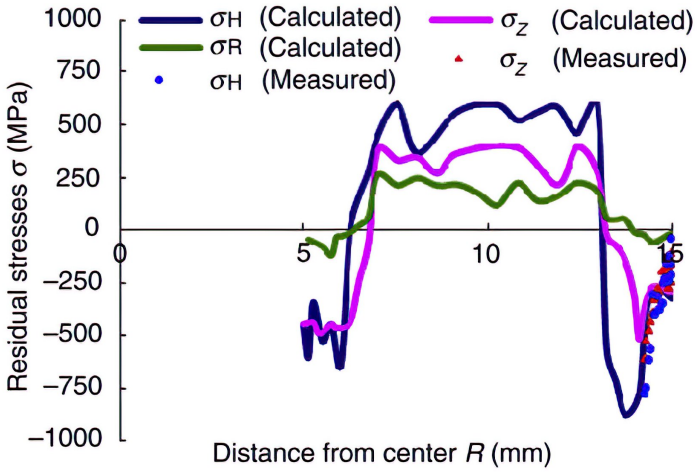

Figure I.17: Residual stress profiles (radial, axial, and hoop stresses)in the middle section of a carbonitrided ring with 30mm diameter (inside diameter 10mm).[68]

I.3 Conclusion

The objective of this literature review was to have a thorough analysis of the existing experimental knowledge and simulation models for predicting residual stresses during the quenching of carburized and carbonitrided steels.

In previous works, the residual stresses distributions were determined experimentally (mainly by X-ray diffraction), exclusively post-mortem. It comes out that the shape of the residual stress profiles after carbonitriding and quenching are similar to the ones observed after carburizing and quenching, as illustrated in the above literature: generally, compressive stresses are observed in the carbonitrided layer with a maximum beneath the surface and tensile stresses in the core as shown in Figure I.18. The maximum compressive stress is linked to a maximum of formed martensite fraction and the decrease towards the surface to an increase of retained austenite. Depending on carbon/nitrogen contents, base steel composition, cooling conditions... even tensile stresses can be observed at the surface.

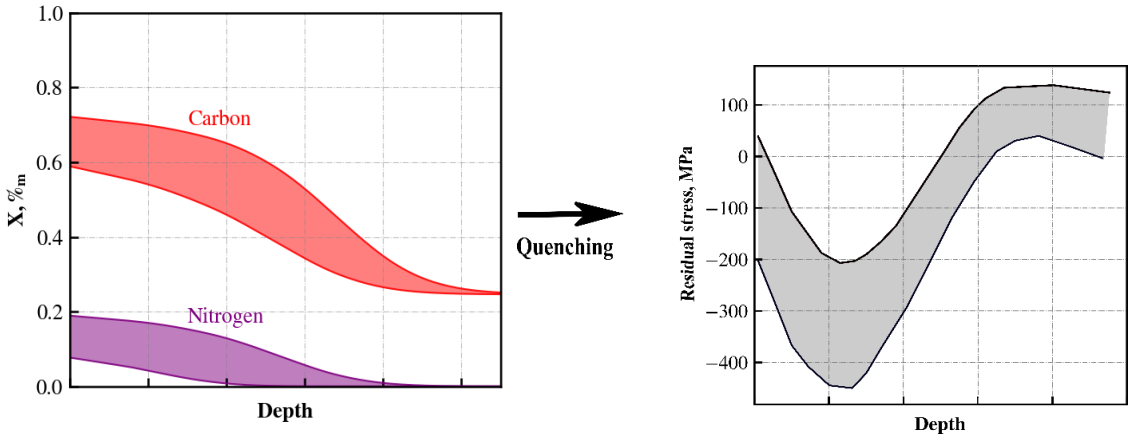

Figure I.18: Schematic representation of the a)carbon and nitrogen and b)typical final residual stresses profiles vs. distance.

Evenif the knowledge of these residual stress profiles is very important, particularly

for the fatigue properties of the pieces, the analysis of how these stresses develop during cooling after carburizing and carbonitriding is lacking. Thus, the first objective of our thesis will be to follow the evolutions of internal stresses experimentally during cooling and simultaneously the microstructural evolutions by in-situ High Energy X-ray diffraction. Indeed, previous work in the lab [69] has shown that with an adequate set-up, it is possible to get the kinetics of phase transformations as well as the internal stresses in the phases during cooling in the specimen without gradients (i.e., without macroscopic internal stresses), but from our knowledge, it has never been attempted in specimen with carbon and nitrogen gradients.

In this review, we have also come across that many authors have dealt with the prediction of residual stresses during quenching developing and using metallo-thermal-mechanical modeling, including the effects of carbon concentration gradients in the carburized layer. Generally, thermoelastoplastic behavior laws of the steel are used; in some cases, thermoelastoviscoplastic behavior has been included.

For carbonitriding, only three authors from the same group (Ju et al.,[66], Liu et al.,[67] and Mukai et al.,[68]) have established coupled analysis of the metallo-thermomechanical behavior during quenching as well as diffusion calculations of carbon and nitrogen.Even if carbon and nitrogen are included in the equations for describing transformations kinetics, no details are given on the assumptions and input data. To the best of our knowledge, no author has included the effect of both carbon and nitrogen contents on mechanical material properties. Thus, an issue of our work will be to get the thermomechanical properties of our steel depending not only on temperature and phase fractions but also on carbon and nitrogen contents using a new in-house device. Thermophysical properties (specific heat, density, thermal conductivity, phase transformation enthalpies) will also be determined as a function of nitrogen.

Of course, the in situ experiments will serve to validate the numerical results not only post-morten but also all along cooling to get a thorough understanding of the origin of the residual stress over the C/N gradients for different thermal cycles and C and/or N contents.

Chapter II

Experimental methods

This chapter features the purpose and benefits of using various techniques. These techniques have assisted in accessing the various parameters and information required to understand better and master the carburized/carbonitriding treatments and the properties of treated steels.

In order to characterize the steel behavior for different carbon and nitrogen contents representative of a carbonitrided layer, an essential step of our study is to produce a specimen with controlled carbon and nitrogen contents. Thus, after a short description of the base steel used in this study, we detail the thermochemical processes developed to enrich the samples with C and/or N homogeneously as well as the process to get gradients of C and/or N. A brief introduction of the heterogeneous gas/solid reaction principle has also been included.

After briefly describing the different methods used to characterize the chemical composition, the microstructures, and the hardnesses of the enriched samples, we will focus on the thermomechanical characterization of our steel.

Indeed, as mentioned before, the prediction of residual stresses needs to get the thermomechanical behavior of the different phases that appear in the steel during cooling after enrichment. The great part of our work involved mastering a new thermomechanical device acquired in the lab. Particularly the design of specimen geometry will be described. In addition, the measurement methods of the thermophysical properties of the steel will also be addressed

In the final section, we describe the techniques used to measure the residual/internal stresses on C and/or N gradient samples, on the one hand, the conventional laboratory X-ray diffraction technique and on the other hand, the synchrotron High Energy X-Ray Diffraction (HEXRD) experiment. Regarding HEXRD experiments, we first describe the dedicated original device and the methodology that allows us to determine the evolutions of internal stresses during cooling and post-mortem residual stress distributions of the heat-treated steels. Then, the focus will be particularly on the acquisition and processing of diffraction data obtained during the HEXRD experiments.

II.1 Description of the steel

The initial/base steel, 23MnCrMo5, is a low-alloyed commercial steel used by the PSA group mainly for the manufacturing of powertrain components. ASCOMETAL® supplied the raw material. Table II.1 shows the chemical composition of the base steel, which belongs to 80428 and R3173-1 casts (steelmaker's code). The base steel was manufactured by continuous casting, and hot-rolled to reduce its diameter to 80 mm. This steel is microalloyed with aluminium, niobium, vanadium and contains nitrogen in significant quantity. The austenitizing step to Ac_3 + 50°C followed by annealing at 625°C allows the aluminum nitride (AlN) to slow-down the growth of austenite grains, thus avoiding the phenomenon of abnormal grain growth during subsequent heat treatment [70].

Table II.1: Chemical composition of base steel (%wt.)

C	Mn	Cr	Si	Ni	Mo	Cu	Al	V	Nb	N	S	P	O
0,246	1,21	1,31	0,237	0,184	0,10	0,23	0,016	0,008	0,003	0,018	0,029	0,015	0,0013

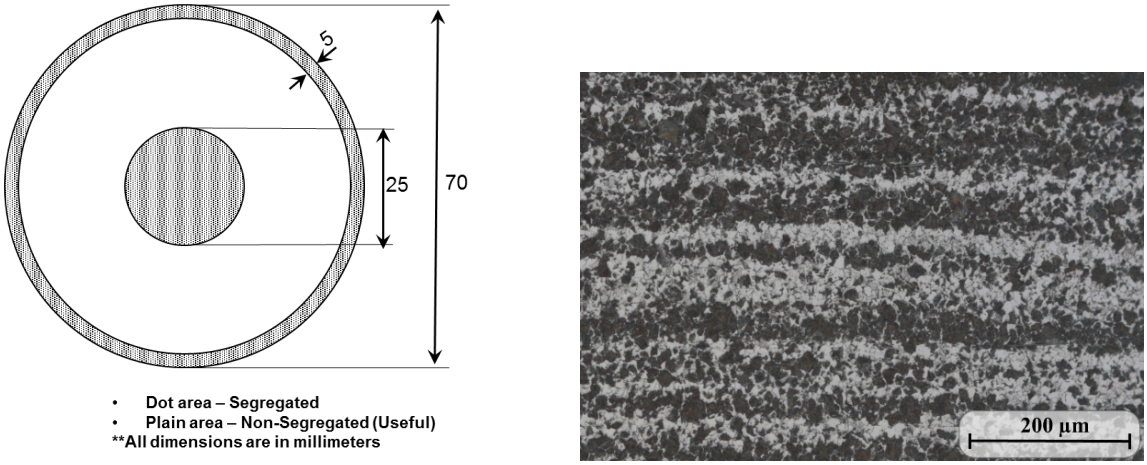

Figure II.1: a) As-received billet illustrating segregated and non-segregated regions. b) The microstructure of 23MnCrMo5 steel in the longitudinal direction of the billets (optical microscope).

In the rolled state, the core and shell regions (dotted area in Figure II.1a) present macrosegregation. The samples were machined out from the non-segregated region along the rolling direction (i.e.,) the longitudinal direction of the billet. The observed initial microstructure of the base steel (Figure II.1b) shows the alternating bands of ferrite (light) and pearlite (dark) with an equal phase fraction of ~50% (using the image acquisition technique). Lamellar specimen with the dimensions of 49 × 10 mm and 1 mm thickness (±0.1 tolerance) were used to be enriched homogeneously with C, N, and C+N contents, whereas specimen dimensions 32 ±1 × 15 ±0.5 with 3.1 ±0.1 mm were used to produce C, N, and C+N gradient specimens. The choice of the specimen dimensions is defined by considering the geometry limitations in other experimental devices, which will be detailed in upcoming sections.

II.2 Thermochemical treatments

Gaseous carburizing or carbonitriding process is a thermochemical process in which steel components are treated at temperatures above the Ac_3 temperature in a controlled atmosphere. This process is a heterogeneous gas-solid reaction, with the absorption of carbon (C) and nitrogen (N) by the surface. These enriching atoms diffuse into the steel leading to a carburized or nitrided layer. Generally, after the enrichment process, the steel component is quenched to transform the enriched austenite(γ) into martensite. Before describing the enrichment process, we recall a previous thermodynamic study [3].

Thermodynamics of Fe-C/ Fe_3C and Fe-N binary systems and multiconstituent system

To design and understand the thermochemical process to enrich the steels with carbon and nitrogen contents, it is essential to know the evolution of thermodynamic phase equilibria [71, 72] and as a starting point the Fe-C/Fe_3C and Fe-N binary phase diagrams, shown in Figure II.2. Two critical lines are important in the austenitic phase to perform this process: first, A_3 temperature decreases more strongly when the carbon content increases than with nitrogen. This critical temperature determines the

minimum temperature to conduct the treatment in the austenitic domain. Then, the A_{cm} equilibrium temperature determines the minimum temperature for which carbon and nitrogen content reaches the saturation of austenite and is therefore linked to the control of enrichment atmospheres. The eutectoid temperature A_1 of the Fe-N system is 590°C instead of 727°C in the Fe-C system. The addition of nitrogen expands the phase field of austenite to lower temperatures.

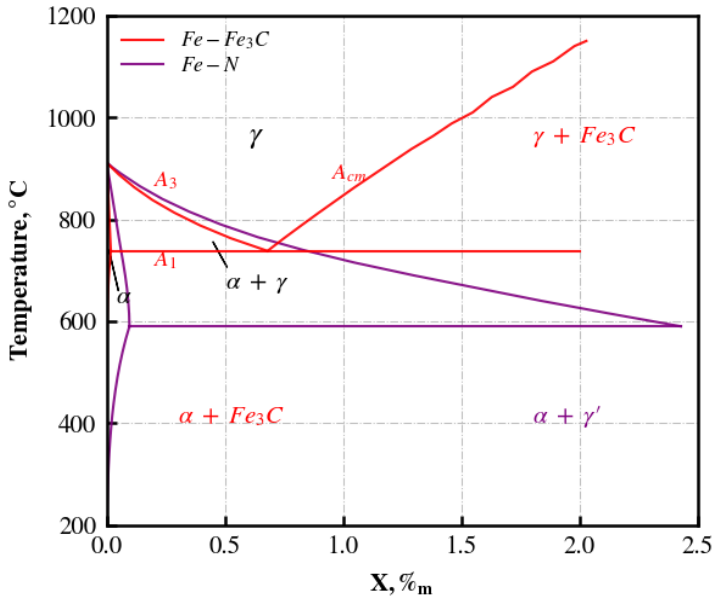

Figure II.2: Fe-Fe_3C and Fe-N binary diagrams calculated using ThermoCalc software®.[73, 74]

In the Fe-N system, nitrogen atoms occupy the octahedral interstices of the FCC and BCC iron lattices; the maximum nitrogen solubility in the γ-Fe lattice at 900°C is 0.088%m. At the eutectoid temperature (A_1), the solubility of nitrogen in the α-phase is 0.11%m and drops to 0.001%m at room temperature, whereas in the Fe-C system, the solubility of carbon in the α-phase is 0.022%m at 725°C, which is lower than the N solubility limit. Below 590°C, the solubility reduction is evident, which will lead to carbide formation in the Fe-Fe_3C system and γ'-Fe_4N nitride formation in Fe-N alloy.

In former studies for our steel composition (23MnCrMo5), a pseudo-ternary cut at the treatment temperature (900°C) using Thermo-Calc® [73, 74] has shown that the carbon solubility limit in nitrogen-free austenite is 0.97%m. This limit tends to be pushed towards higher carbon content with the addition of nitrogen. It has also been shown that austenite without nitrides can only be obtained for low nitrogen content (<0.088%m). We will see later that our enrichment treatments will lead to higher nitrogen contents and, consequently, to the precipitation of nitrides in the austenite.

II.2.1 Laboratory thermobalance

Carbon and/or nitrogen enrichment at high temperatures were carried out in an alumina vertical tubular flow reactor (thermobalance), as shown in Figure II.3, with a dimension of 50 mm diameter, often used in previous studies [2, 3]. The heating system is constructed using two electrical resistors placed around the central zone of the reactor tube over a length of 200 mm. The temperature varies along the reactor length, producing an isothermal zone located halfway in the furnace for a length of 60 mm, limiting the maximum sample height below 50 mm. The samples were suspended in a thermobalance support system located outside of the reactor using nickel wire. During every enrichment process, the samples were positioned in the mentioned isothermal zone in the direction of the reactor axis to ensure its temperature uniformity.

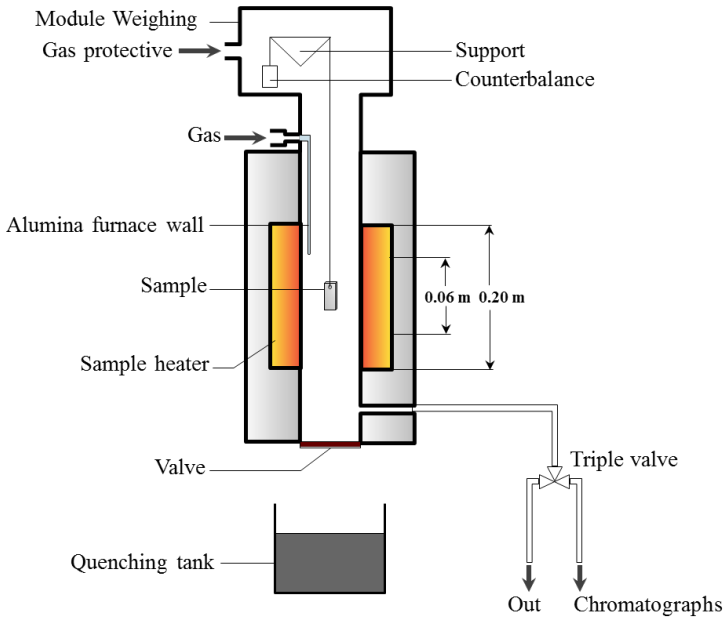

Figure II.3: A schematic diagram of the thermobalance (IJL-Nancy) used for the enrichment process.[2, 3, 75, 76]

The furnace atmosphere consists of the carrier and enriching gases. The injection of each gas species was controlled precisely by several mass flowmeters. The injector made of alumina having an internal diameter of 2 mm is placed 100 mm over the sample and produces a laminar gas flow around the treated part. The gases are supplied uniformly throughout the reactor volume utilizing diaper precursors in a ballast volume of about 1000 cm^3 reactor — the typical flow rate used in the range of 500 cm^3 min^{-1} to 1000 cm^3 min^{-1}. Dedicated studies were performed to determine the behavior of the reactor for different flow rate conditions [2, 3, 75, 76]. Nitrogen molecule (N_2) is injected into the thermobalance as a protective/inert gas to avoid the damage caused by ammonia gas on the measuring system. A hygrometer Dewpro MMY 245 is used for measuring the temperature of the dew point of the carburizing atmospheres. The gas outlet is carried by the lower part of the tubular reactor and exhausts out directly using a triple valve. The chromatographs are placed in series on the exhaust gas line.

II.2.2 Theory of thermochemical treatments

Knowing the necessity of enriching the sample in the controlled atmosphere (T=900° and P=1 atm), Catteau [3] and Dal'Maz Silva [2] determined a protocol to control precisely the gas flow in our reactor in the context of their thesis work. In the section below, we will recall the principle of heterogeneous gas-solid reaction first, and then we will describe the process parameters required to optimize the kinetics of the thermochemical process in this study in order to enrich our low alloyed steel in C, N, or both.

II.2.2.1 Principle of the kinetics of the gas-solid reaction

Globally, this enrichment process is divided into three distinct sub-processes, as shown in Figure II.4. Each sub-process has its kinetics, which has been controlled by the activity gradient (driving force) and the resistance (a reciprocal of mass transfer coefficient) to transfer atom flux between the series of quasistationary states [72]. In such atmospheres, the knowledge of the coupled hydrodynamics, physiochemical, and diffusion phenomenon is essential [72] to enrich C, N, or both homogeneously or to form a gradient in the steel sample. This section aims to illustrate the kinetics parameters

which control each sub-process required to optimize the complete process.

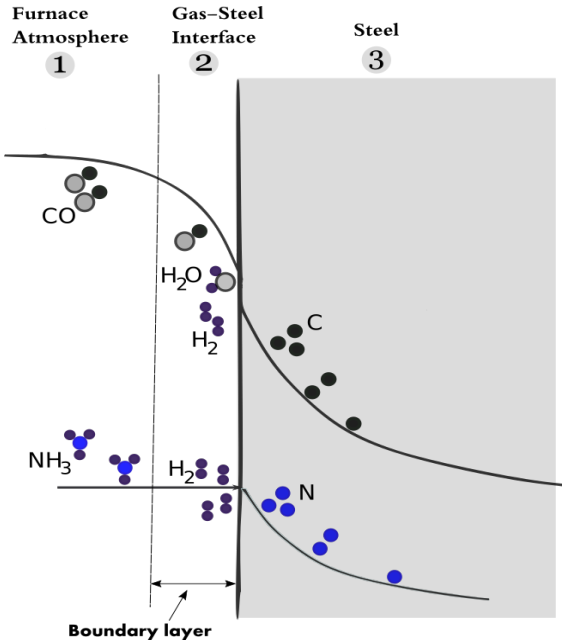

Figure II.4: Schematic diagram of the heterogeneous gas/solid reaction.[72]

In the first stage, the transport of reactive species to the steel surface depends mainly on the thickness of the boundary layer, which is formed due to the velocity gradient between the gas atmosphere and the surface (gas species has zero velocity) of the gaseous molecules. Essentially, the hydrodynamic parameters of the reactor (i.e.,) total gas flow rate and gas agitation (renewal of the reactive species at the surface) need to be observed within the furnace in the enriching conditions, to ensure the transport of species to or away from the steel surface. The active control over these process parameters reduces the resistance and increases the driving force to transfer atom flux to the gas-solid interface. Therefore, to avoid this stage as a rate-limiting step, the overall hydrodynamic behavior of the reactor has been analyzed by determining the residence time distributions of the gaseous molecules in the reactor, especially for the nitriding process, the residence time of the NH_3 molecules is crucial [71, 77, 78]. This parameter has been evaluated to systematize the reactor, which transports the gas molecule to the steel's surface in an ideal manner.

In the second stage, the adsorbed gas molecules on the steel surface are decomposed by the physicochemical reaction, which also activates the diffusion of C/N atoms into the solid solution. The kinetics of this step depends on the thermodynamic parameter of the reaction, such as the reaction rate constant (K_N), which is sensitive to temperature and gas composition [71]. Intend, the kinetics of the reaction depends on the kinetics of the desorption processes of the diffusing atoms on the steel surface. The mass transfer coefficient of enriching gas has been increased to favor the desorption of the species, which are the resultant product of the composition of the gaseous mixture. In the case of carburizing, the presence of hydrogen molecules promotes the desorption of a fraction of the oxygen atoms to form water vapor. Insitu quantitative analysis of actual gas composition with and without the sample are carried out using the chromatography technique [2, 3]. This analysis assists in tracking the kinetics of active gas decomposition and the reaction products during the surface reactions. In particular, this reports the actual value of the K_N of the nitriding atmosphere that allows controlling the rate of enrichment. Besides, better control of the physicochemical phenomena on the sample surface is achieved with the optimized hydrodynamic behavior of the reactor. The detailed study of the pyrolysis of acetylene and ammonia at atmospheric and low pressures conditions has also been done by chromatography [2].The reactor parameters and the kinetics of the first two stages have been studied and designed previously, which

ensure that these steps are not rate-limiting steps [2, 3]. With these well-controlled reactor conditions, the surface reaction quickly raises the saturation level of C/N on the steel's surface, and the only limiting step is the third stage, to diffuse the C/N atoms into the solid lattice.

Finally, the third stage has to be understood, i.e., the diffusion of the atoms (C or N) adsorbed on the surface towards the lattice of the steel effectively. For nitriding, the catalytic ammonia decomposition reaction takes place on the surface of the steel, and the nitriding diffusion reaction co-occurs. Whereas the carburizing process takes place in two stages: the enrichment phase is the stage to saturate the sample surface concentration (boundary condition, C_{sat} ~ 1.1%), and the diffusion stage is to diffuse the carbon atom into the steel with zero flux. Concentration profiles versus time can be obtained by the solution of 2nd Fick's law:

$$\nabla \cdot J = \frac{\partial c_i}{\partial t} = -D_i \left(\frac{\partial^2 c_i}{\partial x^2} + \frac{\partial^2 c_i}{\partial y^2} + \frac{\partial^2 c_i}{\partial z^2}\right)$$

J is the flux of atoms (rate of diffusion), D_i is the diffusion coefficient (or diffusivity) expressed in m^2s^{-1}, c_i is the concentration (atoms/m^{-3}).

II.2.3 Simulation of the enrichment process

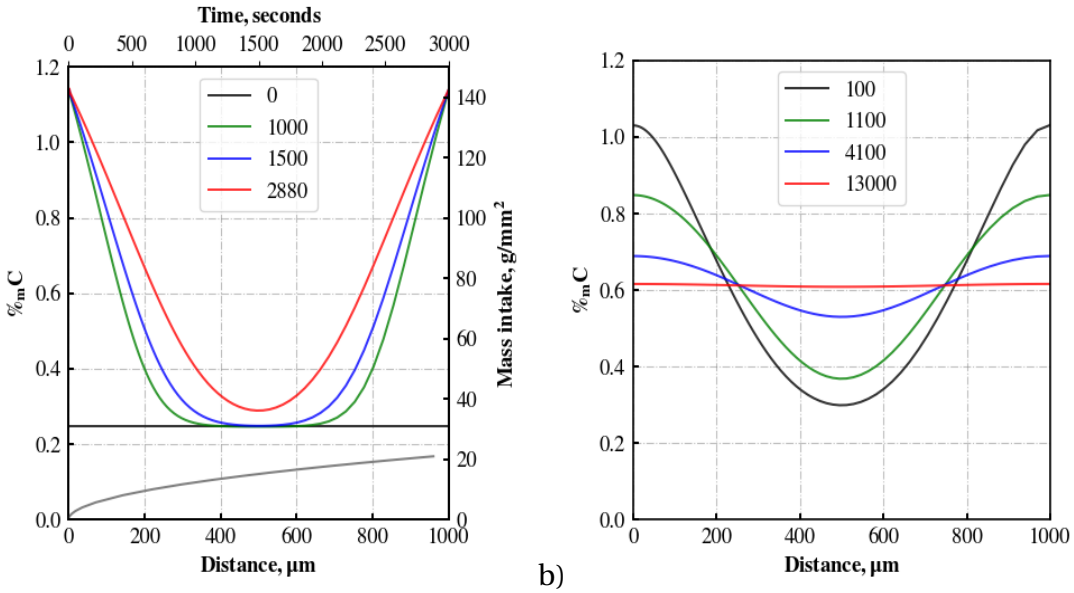

Figure II.5: Evolution of the carbon profiles calculated at different times (in seconds) a) enrichment phase with mass intake versus time in grey and b) diffusion phase.

The thermochemical treatments were designed using DICTRA® software for diffusion calculations to establish the enrichment process with C, N, or both. These simulations were performed by choosing the appropriate boundary conditions, such as the saturation mass fraction of atoms at the surface and diffusion coefficients at 900°C [2, 72]. These simulations allow us to predict the evolution of the C/N content in the austenitic phase field as a function of time and depth, as shown in Figure II.5 and II.6, and to reduce the number of enrichment experiments. We opted for a small thickness sample of 1 mm for these simulations.

Firstly, the enrichment and diffusion conditions required to enrich the sample 0.6%mC homogeneously at 0.6%mC were calculated by considering the constant carbon activity and zero flux, respectively, on both surfaces of the sample. The sample surfaces are super-saturated with 1.1%mC (Figure II.5) at 900°C when the mass gain reaches a sufficient limit (+21mg/mm^2 in total) to enrich the given lamellar sample with 0.6%mC

homogeneously. The calculation predicts ~4.5 hours to complete the carbon enrichment process (includes 45 minutes of enrichment phase and 3 hours and 45 minutes of diffusion phase), as shown in Figure II.5.

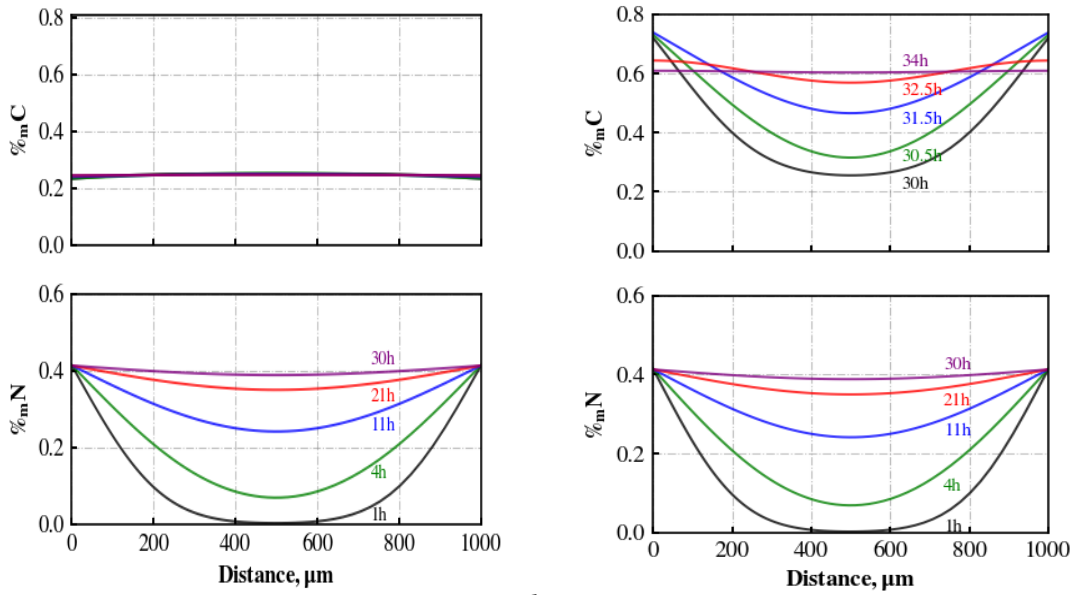

Figure II.6: Evolution of the carbon and nitrogen profiles calculated at different times (in hours) for a) the nitriding process and b) carbonitriding process.

For the nitriding and carbonitriding processes, the calculations were also performed with DICTRA®. The evolution of the carbon and nitrogen profiles at different time steps of nitriding and carbonitriding processes are shown in Figure II.6a and II.6b.

For nitriding, the simulation predicts that for nitrogen it takes a longer time (~30 hours) to achieve homogeneity within the specimen. The carbon enrichment step in the carbonitriding process is similar to the carburizing process. The presence of nitrogen in the sample contributes to a significant increase in the rate of the carbon diffusion process by raising the diffusion coefficient of carbon in austenite. As a result, the superficial concentration of carbon in the sample is achieved within 4 hours, which is less than the carburizing process.

II.2.4 Enrichment process

The target compositions have been chosen to be representative of the carbonitrided layers of gears with the industrial tolerance ranges [1], i.e., for carbon 0.6%m C, for nitrogen 0.4%m N. As our aim will be to obtain the thermomechanical and thermophysical behaviour for different compositions, numerous samples are required: carbon enriched (0.6%m) samples, nitrogen enriched (0.4%m) samples, and samples enriched both in C (0.6%m) and N (0.4%m). The samples have been enriched homogeneously by mastering the thermochemical treatments with the above described process parameters. The thermochemical process begins by heating the samples at a rate of 10°C/s under an inert atmosphere (N_2 + H_2 gases) with a total flow rate of 500 cm^3min^{-1}. The size of the austenitic grains can evolve rapidly as a function of temperature [79, 80]. To keep a homogeneous austenitic grain size with an average diameter of d = 11.8 µm (ASTM 9.5) [3], a temperature of 900°C is selected to carry out the enrichment treatment.

Four samples (thickness of 1 mm) were placed around a meshed cylindrical basket (a diameter of 50 mm) to be homogeneously enriched in C and/or N. The C/N contents in a sample group vary slightly due to the difference in gas flow at the different locations

within the furnace [3]. The samples with the gradient of C, N, or both were produced by placing in the furnace two samples (of 3 mm thickness) parallelly and separated at a distance of 10mm. At the end of the treatment, the samples were manually unhooked to perform oil quenching; the time required to transfer the sample from the furnace to the oil (20°C) quench tank is about a second. During "calm air" cooling, the samples were cooled inside the furnace to room temperature.

The chemical composition profiles of the enriched samples were measured by using a Joel-JXA- 8530F electron probe microanalyzer (EPMA), as will be described later on.

II.2.4.1 Homogeneous sample

II.2.4.1.a Carbon enrichment

Generally, gaseous atmospheres for the carburizing process is produced by using CO-H_2 [72] gas mixture or CH_4 gas. Either of these atmospheres is composed of various gases and results in a complex carburizing atmosphere (i.e., more than 180 chemical reactions co-occur in the atmosphere [81]). Of all these reactions, only limited reactions are essential to determine the rate of carbon transfer from the atmosphere to the steel surface [72]. The carburizing of these atmospheres is mostly driven by gas equilibrium reactions, as illustrated below,

$$CH_4 \rightarrow C_\gamma + 2H_2$$
$$CO + H_2 \leftrightarrow C_\gamma + H_2O$$

where C_γ corresponds to C atom dissolved in solid solution; among these two atmospheres, the *CH_4* gas atmosphere was used in S.D. Catteau's dissertation [3] to avoid oxidation in the thin specimen (500 µm). Carbon enrichment was carried out under an atmosphere composed of CO–H_2–N_2 in W.Dal' Maz Silva's dissertation [2]. The carbon potential of an atmosphere is defined as the C mass fraction of the sample in equilibrium with the gas atmosphere [77]. The partial pressures of carburizing (CO, CH_4) and decarburizing (CO_2, H_2O) gases determine the carbon potential in the gas atmosphere [72]. In the carburizing process used in our study, CO gas flows into the atmosphere (N_2+H_2) heated to 900°C. It is referred to as a boost or enrichment stage that lasts 1.5 hours. The carbon potential is maintained to achieve the desired carbon content (0.6%m) by retaining the dew point (the partial pressure of water vapor) around -15±2°C at an atmospheric temperature of 20°C, where the partial pressure of CO and H_2 remains constant in the carburizing atmosphere. The effective carbon activity has been increased by adding acetylene (C_2H_2 gas) initially. Thus the saturation point is reached in a shorter time. The carbon potential always remains below saturation (C_{sat} ~1.1%m) to avoid the formation of carbides or soot. The diffusion stage, where the surface carbon diffuses into the sample under a neutral atmosphere (N_2+H_2) is 3.5 hours long to achieve the final homogeneous C content (0.6%m) content.

Results of the chemical analyses (Figure II.7a) show the carbon content profiles along the thickness of the sample, which evidences good homogeneity in positions on either side of the middle. It is confirmed by the hardness profiles with an average hardness value of 900 $HV_{0.3}$ (Figure II.7b). The experimental C profiles of the test specimens (1mm thick plates) correlate well with the calculated profiles in Section II.2.3.

II.2.4.1.b Nitrogen enrichment

Ammonia decomposition plays an essential role in the nitrogen enrichment processes and depends highly on surface area and temperature [71, 77]. The used nitriding process begins after the heating phase, as a gaseous mixture (95% N_2+ H_2 and 5% NH_3) flows into the enclosure heated to 900°C at a rate of 500 $cm^3.min^{-1}$. A significant portion (98.5%) [3] of ammonia gas molecules is thermally decomposed into N_2 and H_2 at 900°C

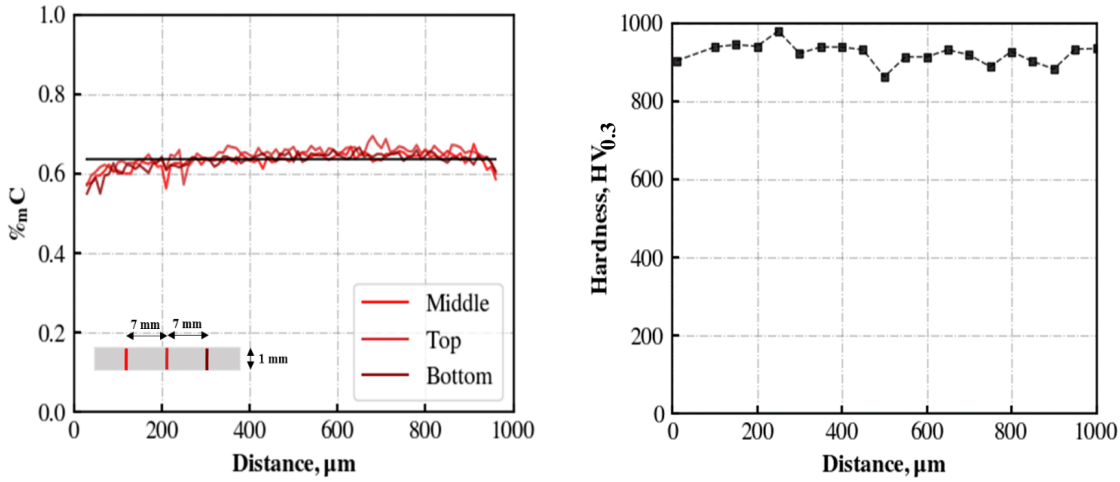

Figure II.7: a) Carbon profiles measured using microprobe along the thickness at three different positions and b) hardness profile along the thickness in the middle of the sample.

[77] after entering the furnace. The inflow rates of atmospheric gases are set to target a predetermined K_N value corresponding to a target final nitrogen content, taking into account the decomposition of the ammonia molecule in the gas phase.

In contrast to the carburizing gas, there is no proper method to control the decomposition of NH_3 accurately [71] to release nascent nitrogen. Therefore one must rely on the relationship of the volumetric flow of the process gas (carrier gas and enrichment gas) to the ammonia. The rate of ammonia decomposition is proportional to the nitrogen activity of the atmosphere. A previous study has used a similar approach to the one used for enrichment in the ferritic phase [2, 3]. It is based on the equilibrium constant of the following reaction.

$$2NH_3 \rightarrow 2\underline{N}_\gamma + 3H_2$$

$$K_N(T) = \frac{a_N^m \cdot P(H_2)^{\frac{3}{2}}}{P(NH_3)}$$

The nitrogen activity (linked to the concentration) in the solid solution for the equilibrium at 900°C was calculated using the ThermoCalc® software and the TCFE7 database. The evolution of nitrogen in solid solution is given as a function of the total nitrogen content in the alloy in Figure II.8. Up to the solubility limit (0.088%m), the curve is linear. The change of slope is due to the precipitation of chromium nitrides in the austenite.

Experimentally, the partial pressure of ammonia is established in 60 minutes after the beginning of the circulation of the gaseous mixture [3]. This pressure is said pseudo-equilibrium and, after that, allows to drive the enrichment of the samples. The significant weight gain in the sample is directly related to the flow of ammonia gas in the first phase and obtained for a relatively shorter time. The establishment of pseudo-equilibrium slows the dissociation of remaining residual ammonia into nascent nitrogen [71] and requires double the time needed to reach a steady state. Hence, the rate of nitrogen transfer into the steel surface depends on the residual ammonia content and not on the percentage of ammonia in the inlet gas [77]. The studies show that a significant amount of residual ammonia remains in the furnace and depends directly on the temperature and the flow rate of NH_3 used, therefore, on the residence time of the molecules in the furnace. In order to reflect these considerations, chromatographic measurements were carried out [2, 3]. The influence of the partial pressure of ammonia on nitrogen enrichment was also put forward [3].

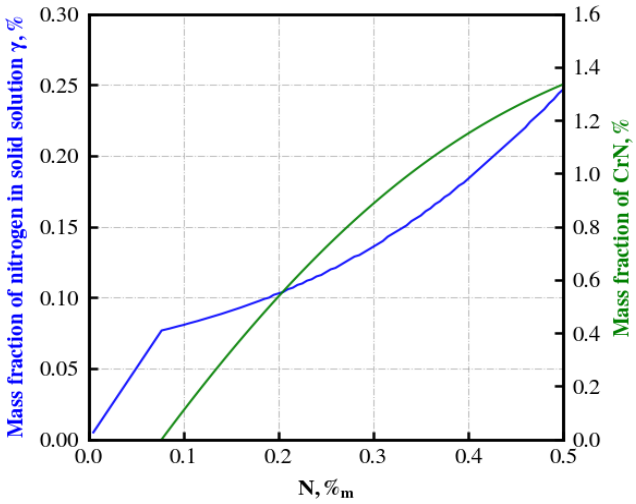

Figure II.8: Thermodynamic equilibrium calculations (TCFE7 database) formation of nitrides at 900°C: (a) N %wt in the solid solution phase (blue curve) and the mass fraction of CrN (green curve) during enrichment your calculation.

Indeed, once the nitrogen content at the surface reaches the value dictated by the gas-solid pseudo-equilibrium, i.e., the content associated with K_N in the enclosure, only the diffusion of nitrogen into the sample limits the enrichment reaction. Meanwhile, the nitrogen content begins to homogenize within the solid phase. The gradual decrease of the enrichment flow is explained by decreasing the amplitude of the nitrogen concentration gradient between the surface and the core of the samples, implying a decrease in the diffusion rate.

The specimens at the end of the treatment have an average weight gain of 20.5 ±0.05mg. The small variations of mass gain between the specimens show a decent homogeneity of the gas mixing in the oven. EPMA measurements (Figure II.10) show the presence of high nitrogen peaks scattered throughout the thickness of the nitrided and carbonitrided samples, which correspond to the presence of nitrides that precipitated in the austenite. Apart from these peaks, the nitrogen concentration is nearly homogenous, with an average concentration of 0.45%m.

EDS observation (Figure II.9) shows the distribution of the CrN nitrides inside the nitrogen-enriched layer. It can be observed that CrN is also agglomerated with other nitrides, $MnSiN_2$ and AlN [3, 4, 82], and other precipitates are also present, like sulfides. Let us mention that AlN nitrides were present before the enrichment.

During nitrogen enrichment, as expected decarburization occurs, as shown in Figure II.10a, where the mean carbon content is 0.1%m instead of the initial carbon content of 0.25%m. Due to the constant supply of hydrogen gas [72] and the repulsive C-N interactions in the austenite [4] at the surface of the steel sample. It can be noticed that the hardness profile (Figure II.10b) was obtained after calm air cooling, confirming the satisfactory homogeneity of the specimen despite a decrease at the edges.

II.2.4.1.c Carbon and nitrogen enrichment

As detailed above, the fully controlled carbon or nitrogen enrichment in the austenitic phase is achieved using process parameters [2, 3]. In previous studies [2, 3], the C+N enrichment is separated into two distinct stages, which is contrary to the single-stage enrichment process using complex atmospheres[77, 78]: first to enrich samples with nitrogen and then successively with carbon by transferring ammonia and methane gases for the respective enrichments. Our study established a new process for combined enrichment C+N on the lamellar specimens (1mm thickness) using carbon monoxide and ammonia gases, respectively. In order to obtain 0.6%C + 0.4%N contents in the austenitic

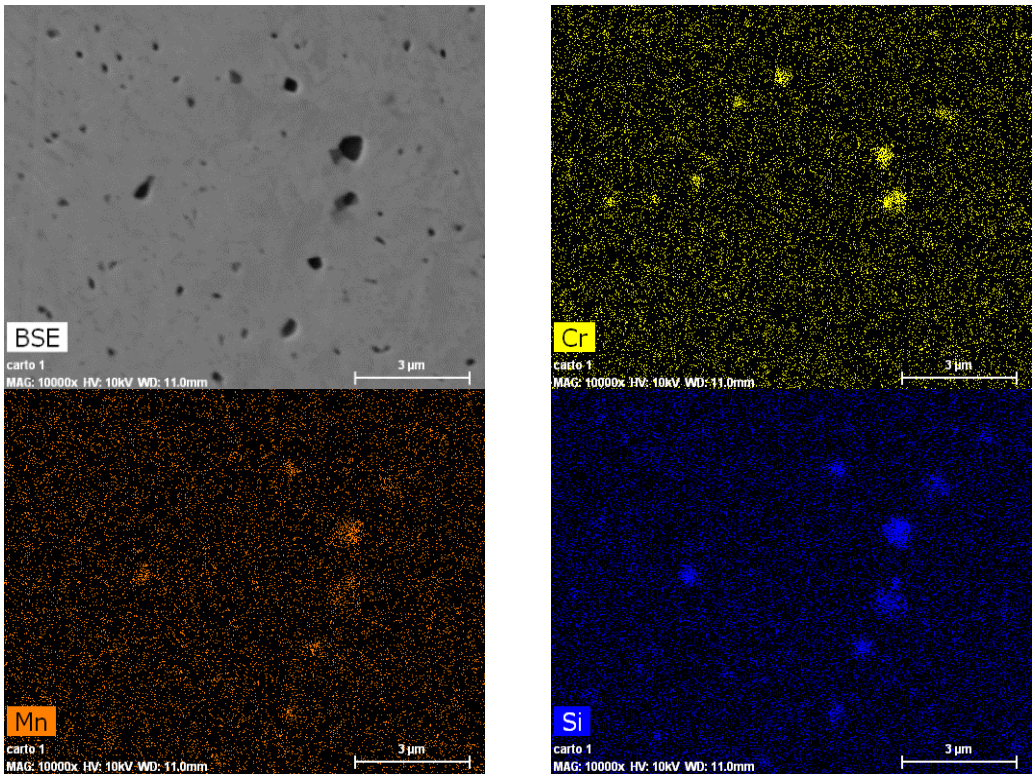

Figure II.9: Characterization of precipitates formed during nitrogen enrichment of steel in the austenitic phase by EDS mapping.

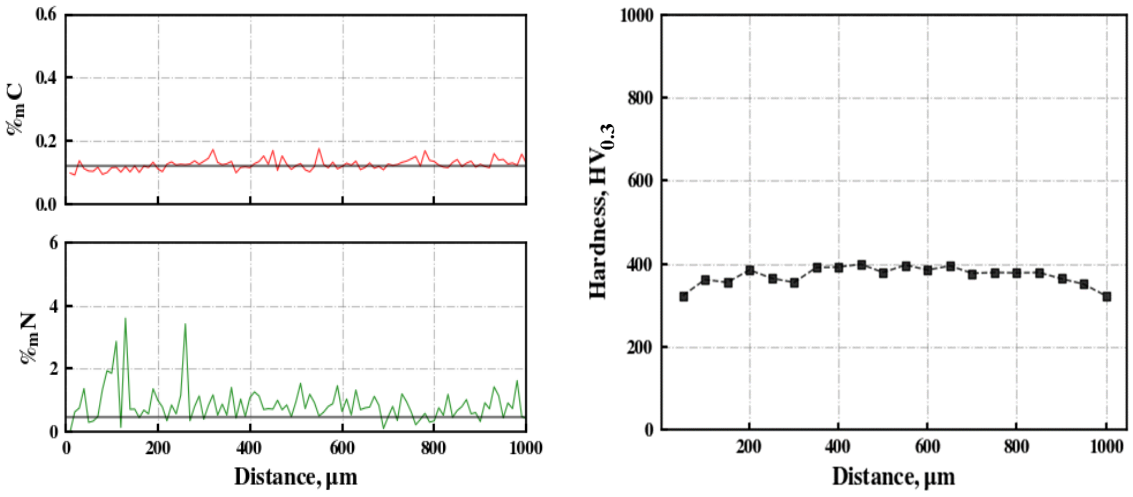

Figure II.10: a) C and N profiles measured along the thickness for nitriding process using microprobe and b) hardness profile (after calm air cooling).

solid solution, two attempts have been made:

Attempt A: During this attempt, after heating and thermal stabilization in an inert atmosphere (H_2 +N_2), the carburizing step begins. CO gas was passed to form an atmosphere composed of 60% H_2, 20% N_2, and 20% CO with a gas flow of 500 $cm^3.min^{-1}$ along with 0.5% O_2 to maintain carbon potential in the reactor for 4 hours. The amount of oxygen was determined from the equilibrium conditions of the carburizing reactions [72]. The addition of 3% NH_3 leads to the nitriding step, which simultaneously takes place for around 24 hours without changing the injection rates of N_2 and H_2. The partial pressure of ammonia was maintained throughout the phase to avoid excessive nitrogen loss and to drive the nitrogen into the specimen. Cooling was done in calm air inside the furnace at the end of the cycle.

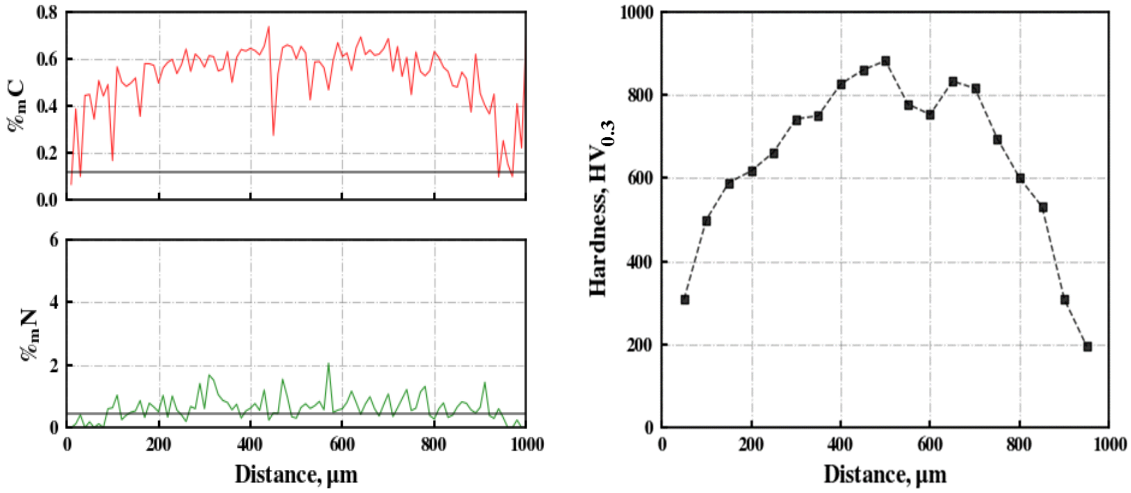

Figure II.11: a) C and N profiles measured using microprobe along the thickness for carbonitriding-A process and b) hardness profile.

Attempt B: Contrary to the previous attempt, for the C + N enrichment, the methodology adopted here was first to enrich samples with nitrogen and then successively with carbon. Ammonia cracked at 900°C, along with N_2 and H_2 gases, for 24 hours to obtain 0.45%N content throughout the thickness of the specimen homogeneously. Successively, CO gas is passed along with N_2 and H_2 gases for 2 hours to enrich with the saturation carbon content of 1.1%C at the surface and followed by a diffusion phase of about 3 hours. Cooling is done by oil quenching at the end of the cycle.

Among the two attempts, the latter is considered to be a better process for achieving homogeneous compositions, as shown in Figure II.12a. In contrast, the former process leads to high decarburization due to less control over the complex atmosphere, as shown by the C and N profiles in Figure II.11a and the hardness profile (Figure II.11b). The insertion of 0.45%m nitrogen in solid solution leads to the decarburization samples at 0.1%C at the end of the enrichment phase. The actual mass gain value due to nitrogen intake is estimated, including decarburization (+23.55 mg). The nitrogen profile presents a solid solution content of 0.45%m with the presence of nitrides distributed in the thickness of the sample. The carbon profile, meanwhile, is rather homogeneous, with a mean value of 0.4%m, which is less than the target carbon content. The carbon potential has been adjusted and corrected for other carbon enrichment experiments to achieve the desired carbon content. The homogeneity of the chemical composition has also been checked by a hardness profile measurement, as shown Figure II.12b.

The present study, along with previous studies [2, 3], has made it possible to control the enrichment process and to obtain homogeneous specimens with carbon and nitrogen

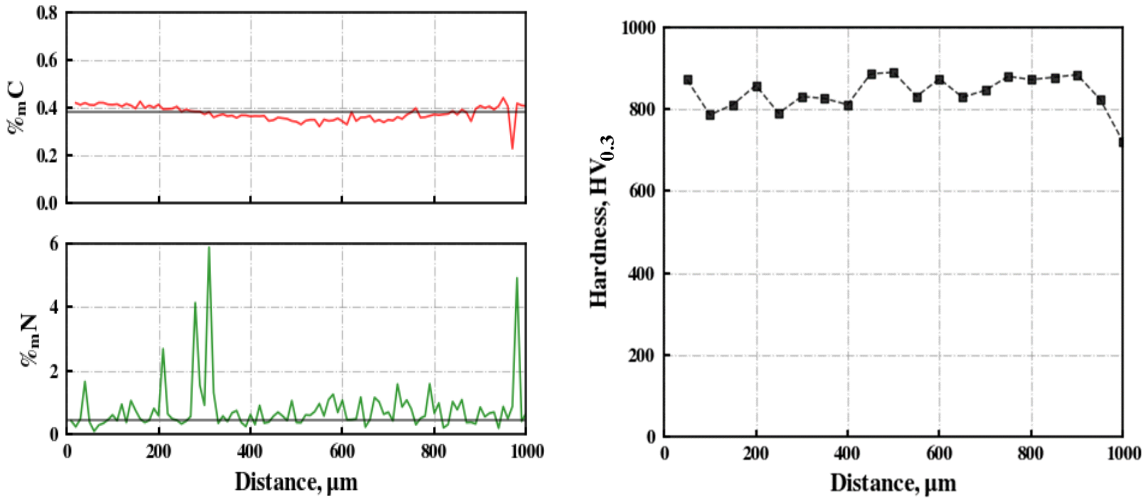

Figure II.12: a) C and N profiles measured using microprobe along the thickness for carbonitriding-B process and b) hardness put $HV_{0.3}$

contents. After each enrichment treatment, the obtained concentration of carbon and nitrogen are not precisely the same in the samples and their compositional ranges.

II.2.4.2 Gradient sample

The reactor was charged with two samples for carbon and/or nitrogen enrichment of samples with gradients. The heating was carried out under an inert atmosphere composed of $0.8N_2$ - $0.2H_2$ (in volume fraction) with a total flow rate of 500 cm^3 per minute. One sample was subjected to in-depth characterization, such as microstructure and associated hardnesses. Another sample was used to perform a post-mortem residual stresses study and in-situ measurements of phase fractions and internal stresses evolutions during cooling throughout C, N, and C+N concentration gradients.

The carburizing was carried out in a *CO* atmosphere chosen to ensure saturation of the carbon content at the surface, thus ensuring a constant surface concentration condition for the diffusion of this element. Nitriding uses an ammonia-based atmosphere. Since NH_3 is very unstable at 900°C, the chemical potential between the residual ammonia fraction at this temperature in the gas and the nitrogen in the steel was used to control the atmosphere. For this purpose, Thermo-Calc calculation [83, 84] was performed to determine the activity of nitrogen in the material, thereby making it possible to generalize the definition of nitriding potential. Details of these approaches to control the process are available in the literature [71, 85]. Rapid cooling and calm air cooling were applied to the samples after carbonitriding, which will allow us to analyze the effect of cooling conditions on phase transformations and internal/residual stresses.

Carbon enrichments, either for carbonitriding or for carburizing, have been made for 2 hours. In the case of nitriding and carbonitriding, the enrichments in nitrogen were carried out for 3 hours. Contrary to carbonitriding for homogeneous samples, carburizing is followed by nitriding to produce gradient samples, as shown in Figure II.13. It implies imposing a zero flux diffusion interval of 3 hours after carburizing. The nitriding takes place in a single enrichment step of 3 hours. The diffusion time, furnace atmosphere, and cooling medium for generating the gradient samples are summarized below in Table II.2.

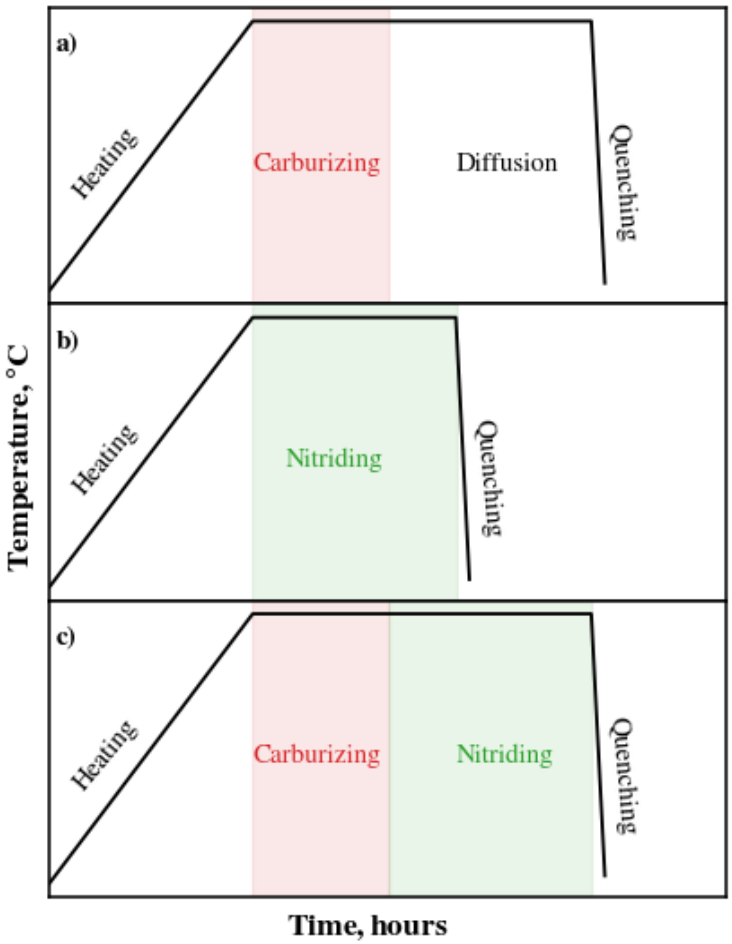

Figure II.13: Thermochemical treatments of carburizing, nitriding, and carbonitriding process.

Table II.2: Processing conditions and limits for carburizing, nitriding, and diffusion of the different cycles of thermochemical treatments

Treatment	**Duration at 900°C**	**Furnace Atmosphere**	**Boundary Conditions**
Carburizing	Enrichment – 2 hrs	N_2, 0.4H_2,0.2CO	Dew point, T_r = -10°C
	Diffusion - 3hrs	N_2, 0.4H_2	No flux
Nitriding	Enrichment – 3 hrs	N_2, 0.72H_2, 0.04NH_3	$K_N = 8.6 \times 10^{-3}$ $atm^{-0.5}$ [2]
Carbonitriding	Carburizing – 2hrs	N_2, 0.4H_2,0.2CO	Dew point, T_r = -10°C
	Nitriding - 3hrs	N_2, 0.72H_2, 0.04NH_3	$K_N = 8.6 \times 10^{-3}$ $atm^{-0.5}$ [2]

II.3 Microstructural and chemical composition characterizations

II.3.1 Optical microscope

Zeiss Axioplan 2 is an optical microscope equipped with AxioVision acquisition software, which enables us to obtain microstructures up to x1250 magnification. All the samples were sequentially polished with silicon carbide (SiC) abrasive paper. A typical polishing procedure is followed by decreasing the size of the SiC paper (46.2, 30.2, 21.8, 15.3, 6.5, 2.5, 1 µm) to obtain perfectly flat and contamination-free samples. Then, polished samples are etched with 4% nital solution (4 cm^3 of HNO_3 + 96 cm^3 of CH_3OH) for approximately 5-8 seconds.

II.3.2 Vickers microhardness

Vickers micro-hardness of the various steels is determined using the Matsuzawa MXT50 device available at IJL-Nancy. The Vickers hardness test method consists of indenting the enriched steels (metallographically prepared) with a diamond indenter in the form of a right pyramid with a square base and an angle of 136° between opposite faces subjected to a load of 300g. The full load was typically applied for 5 seconds. The average length of two diagonals of the indentation left on the surface of the material after unloading is proportional to the Vickers hardness value ($HV_{0.3}$). The hardnesses of the carburized, nitrided, and carbonitrided steels have been determined along the thickness/depth in which enrichment takes place, and each measurement point is spaced out 100 µm apart.

II.3.3 Scanning electronmicroscope

We used a Jeol Quanta 600-F equipped with a field emission gun (FEG) system. Spot size (current) that ranges from 1 to 7 unit for each voltage, from 200V to 30kV, allows the acquisition of high-resolution images. Secondary electrons (SE) generates images with a topography contrast of the specimens. A thin layer of copper coating is applied to the specimen to reduce the surface charging, which can result in distorted images. Backscattered electrons (BSE) allow getting images with a composition contrast (A higher atomic number leads to a brighter image). Hence, the chemical composition can be analyzed semi-quantitatively using energy dispersive spectroscopy (EDS) with a Brücker detector SDD (Silicon Drift Detector) coupled to the acquisition software Spirits at IJL-Nancy.

II.3.4 Microprobe analyzer

Jeol-JXA-8530F electron probe microanalyzer (EPMA) was used to determine the carbon and nitrogen concentrations along the enriched direction of the samples. A field emission electron gun capable of producing a stream of electrons, which interacts with the target element of the sample to emit the characteristic X-rays. Based on WDS (Wavelength-Dispersive X-ray Spectrometry, the lighter elements, such as C and N in our enriched steels were analyzed quantitatively.

The samples were mounted in a Bismuth based alloy (Bi-Sn-Cd) to avoid contamination. The standard procedure was followed to polish the samples. The final chemical polishing was also done with colloid alumina (Al_2O_3) suspensions, which have a particle size of 0.1 µm, and then rinsed with methanol and dried under blower at 70°C. Before placing in the analysis chamber, the samples were cleaned in a plasma cleaner Gatan Solarius 950, for 4 minutes.

The local carbon concentration was measured by comparing the obtained curve for the C Kα line intensity of the sample with the calibration curve of reference steel samples.

Nitrogen concentration measurements were calibrated by using a pure stoichiometric Fe_4N reference sample. The precision of the concentration measurements was estimated to be ±0.04 wt% and ±0.07 wt% for carbon and nitrogen, respectively. More details regarding EPMA can be found in [3].

II.4 Thermomechanical study

The thermomechanical study was performed to determine the thermo-elasto-viscoplastic behavior and the interactions between stresses and phase transformations in the enriched steels. For the thermo-mechanical characterization, tensile and relaxation tests were performed for the different phases/constituents, namely austenite, ferrite, pearlite, high temperature constituents (present in N enriched specimen), bainite, and martensite as a function of temperature, strain rate, C, and N contents, to determine thermo-elasto-viscoplastic behavior at high temperatures and thermo-elastoplastic behavior at lower temperatures. A long experience in the characterization of the thermomechanical behavior of metallic alloys at various temperatures with controlled or evolving microstructures (even in metastable states) exists in Nancy (LSG2M first and then IJL) using in-house built DITHEM (Thermomechanical Dilatometer) [86, 87, 88]. Recently, an original new thermomechanical simulator allowing both tensile and compressive testing was established at IJL-Nancy.

II.4.1 Tensile and Compressive machine - overview

High temperature tensile-compression machine (*french acronym* - MTCC) is primarily intended to study the thermomechanical behavior of metallic alloys and the microstructural evolution under the influence of stresses or plastic deformations.

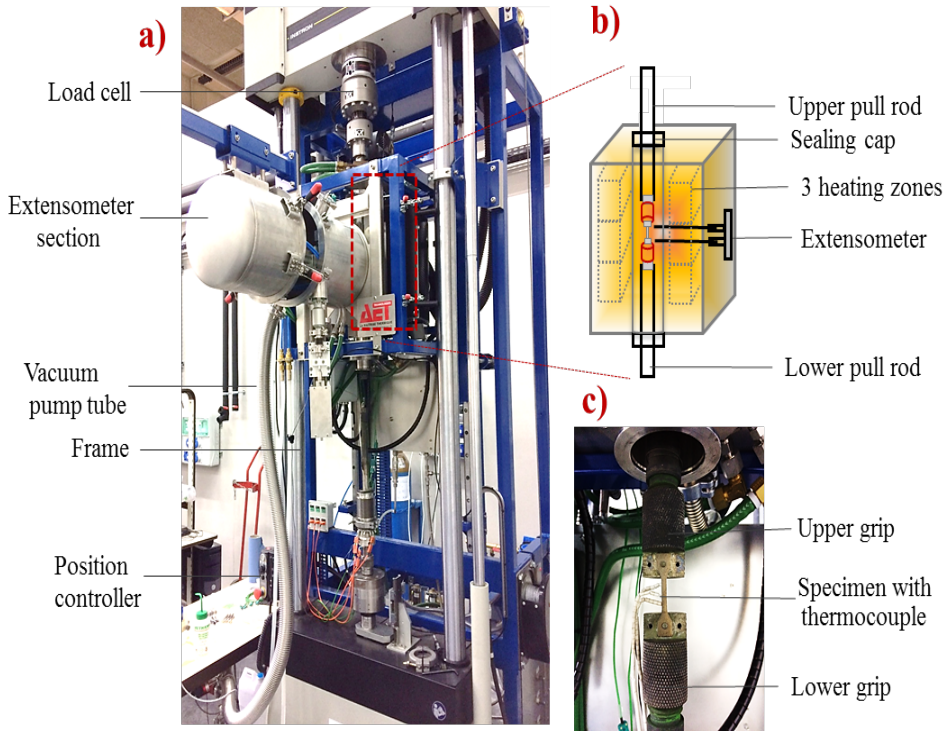

Figure II.14: a) Thermomechanical Simulator (IJL), b) a side view of the furnace and extensometer system, and c) Cylindrical specimen instrumented with 3 Thermocouples & a high-temperature extensometer.

MTCC (Figure II.14a) mainly consists of a furnace chamber, a load cell, high stiff load

frames as the mechanical platform, extensometers, cooling systems, mechanical and thermal control systems. A servo-hydraulic mechanical testing machine (Instron 8802) equipped with a radiation furnace (AET Technologies®) of approximately 30 kW makes it possible to carry out tensile, compression tests, or both during a controlled complex thermal cycle under a low pressure atmosphere (or under vacuum). Loads applicable between 1 N to 5 kN can be applied, and strain rates can be varied between 10^{-4} s^{-1} to 10^{-2} s^{-1}. The maximum load capacity of 5kN was used for our study. During testing, the specimen is manually clamped in the grip heads (top and bottom) by three M3 bolts. The furnace has three-zone heating with embedded heating elements (a series of lamps). These lamps heat the sample using radiation and enable heating rates up to 50°Cs^{-1} to a maximum specimen temperature of 1100°C. By the way, Figure II.14b shows the chamber with the previously listed elements. The temperature control system has three controllers in a *master-slave configuration* capable of following single or multi-ramps.

Spot welding of three K-type thermocouples to the specimen surface along the gage length (one at the center and the other two at the ends of the gauge length), as shown in Figure II.14c provides the user with an indication of temperature gradient during the calibration process (See details in Appendix D). The cooling system consists of four feedthroughs: a water cooling system for the sample grips and grips arms, one for the inlet gas nozzle, and another for outlet gas. Two vacuum pumps (primary and secondary) pump down to 6.3×10^{-3} mbar vacuum, and then inert gas (nitrogen/argon) was injected into the chamber to avoid oxidation at high temperature.

High temperature tensile tests were carried out at different strain rates, and the deformation was measured using a high temperature extensometer. Precise high temperature (~1100°C) and clip-on contact extensometers at room temperature (~20°C) allow accurately controlling strain and strain rates. The separate cooling system avoids the overheating of the extensometer above 160°C. These gauge extensometers were utilized to control strain during strain-controlled tests and for data acquisition during stress-controlled tests. The extensometer gauge length is adjustable between 12.5 and 25 mm with a maximum and minimum travel of +20% and -10%; we have chosen a minimum gauge length according to our sample geometry. The extensometer legs are made of alumina chisel end rods and attached to the specimen. The extensometer is held in place using a mounting kit (Figure II.14b), which ensures that a low contact not greater than 300g was applied on the extensometer legs to the side of the sample (along the thickness side) to make sure the extensometers tightly attached to the sample.

Two modules, namely Console and Wavematrix, were utilized to control the thermomechanical tests. The console module is an interface to control the position of the actuator before/after tests or during specimen installation. 'Sample protect' is an essential safety feature to limit the breakage or overload of the sample. The Wavematrix module is an interface used to construct and maintain all the thermomechanical testing methodologies, execute the test itself, and acquire data. An interaction between the controlled thermal and mechanical cycles is established using the Wavematrix module. The thermal cycle is programmed using the AET® furnace module by dividing into a series of segments defining the start and end temperatures and the duration of each segment. The amount of gas flow (percentage of valve opening), the heating (input voltage), and PID coefficients (Proportional-Integral-Derivative) allow us to regulate the temperature of each segment and are also used to optimize the temperature gradients within the sample.

II.4.2 Design of thermomechanical specimens and grips

As already mentioned, we have to determine the thermomechanical behavior of steel as a function of C, N, or both contents using the thermomechanical test machine. Our specific issue is the small sample thickness (1 mm) afforded by the thermochemical enrichment process, as we needed homogeneous samples (details given in Section II.2.3). The length, width, and gauge length of the tensile test specimen should not exceed 60

mm, 10 mm, and 12.5 mm, respectively. These geometry limitations arise from the dimension allowances of the thermobalance and the tensile test extensometer. The minimum dimension of a dog-bone tensile test specimen as per ASTM E8M-04 standard is 6 mm gauge width (W), useful gauge length (G) greater than 1.5 cm, and a total length varies between 8 to 10 cm. This standard dimension of the tensile sample is large compared to our requirements; None of the standard geometries for the miniature test pieces proposed by ASTM [89, 90] meet our requirements. Thus, a non-standard dog-bone tensile specimen with a rectangular cross-section (see Figure II.15a) was designed, taking the above dimensional limitations as a reference. A series of finite element analyses were performed by varying the dimensions of gauge width (W), the distance between the center of the hole and the edge of the sample (A), and fillet radius (R) to analyze the Von Mises stress distributions of the sample as will be shown beneath.

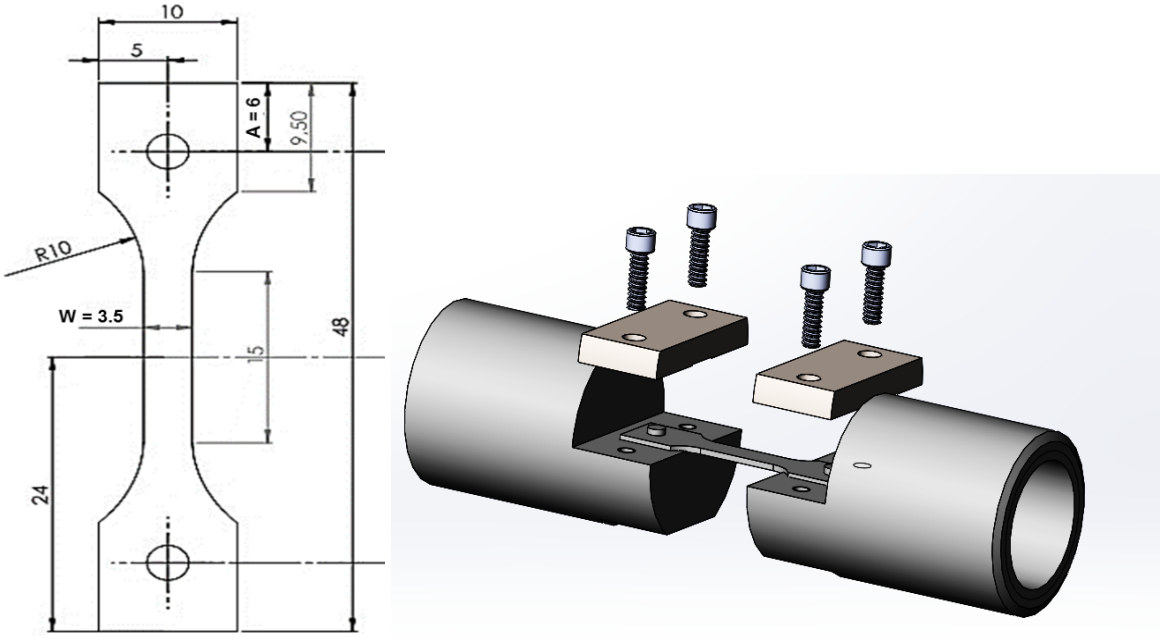

Figure II.15: a) Geometry of the tensile test specimen and b) grip assembly.

Various types of gripping devices are used to transmit the force applied by the testing machine to the test specimens. Usually, a pinned grip is adapted to this specimen type and the thermomechanical device (see Figure II.15b). It was designed using SolidWorks Version-23, the CAD commercial software. Gripping is ensured mainly by the pins. The grips are made of cobalt-based alloy to withstand high temperatures and loading. To ensure axial tensile stress within the gauge length, the axis of the test specimen should coincide with the centerline of the heads of the testing machine.

II.4.2.1 Simulation verification

Finite element software ABAQUS V.13.0 was used to simulate the tensile test of our flat specimen considering half symmetry. Reduced integration is afforded by meshing with hexahedral C3D8R elements. The total nodes and elements are 33121 and 28380, respectively (see Figure II.16a). A rigid analytical body was used to represent the loading pin, as shown in Figure II.16b. Aligning the pin to the center of the loading hole ensured that the loading would be symmetric. The loading was applied in displacement control to a displacement of 0.25mm on the top edge of the analytical rigid pin towards the longitudinal direction (see Figure II.16b). All DOF (degree of freedom) of one node of the sample and one node in the pin are arrested. Constitutive material model data were obtained from uniaxial tension tests at room temperature: Young's modulus of 210 GPa and Poisson ratio of 0.3 were assumed for the material. The plastic behavior was assumed

to be isotropic and the Von Mises yield criterion was used. The final Von-Mises stress and equivalent plastic strain distributions along the gauge length and hole regions for the given geometry were analyzed, as shown in Figure II.17. Low-stress concentration at the loaded hole section, homogeneous stress, and plastic strain distributions along the gauge length were obtained, which make this tensile specimen geometry fit for the tensile test experiments.

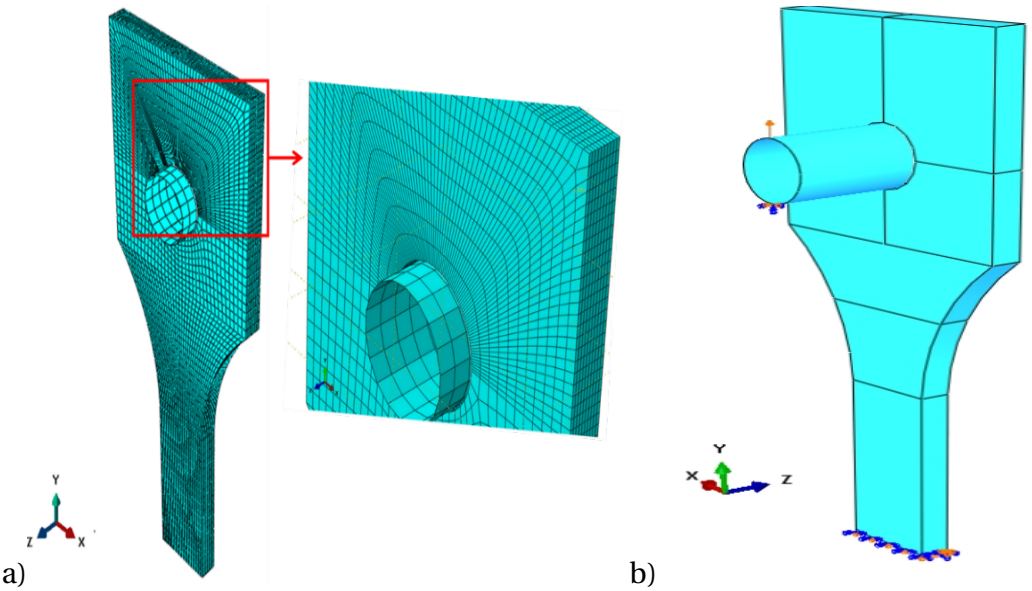

a) b)

Figure II.16: a) Mesh geometry and b) boundary conditions used for the tensile test FEM simulations.

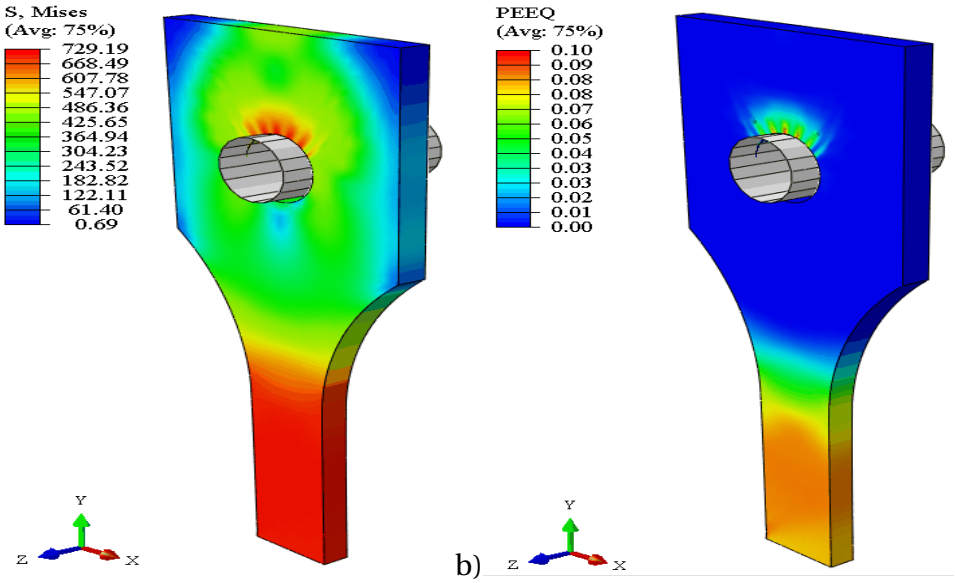

a) b)

Figure II.17: a) Von-Mises stresses and b) Equivalent plastic strains distributions in the tensile test specimen (FEM simulation).

II.4.2.2 Experimental verification

Before performing the experiments with our specimen, tensile tests were carried out on another steel to verify the correct “management” of the new MTCC machine and test the performance of the newly designed tensile grips and specimen geometry. The tensile specimens were made up of bainitic steel, which behavior is known from previous studies

(DITHEM experiment) [91]. A tensile test was performed at room temperature (25°C) on a specimen along its longitudinal axis, with a small initial load (10% of yield stress) to maintain the specimen. In Figure II.18, the measured elastic modulus on the MTCC machine is lower than the one of the reference test (154 GPa instead of 195 GPa), but on unloading, the elastic modulus is comparable to reference values (201 GPa). Even though yield strength and ultimate tensile strength show deviations of 6% from the strengths of the reference test [91], it can be considered acceptable considering the difficulty of performing tests on very small specimens. (It has to be mentioned that the bainitic reference steel specimen [91] has a cylindrical geometry of 5mm diameter compared to our 1mm thick sample).

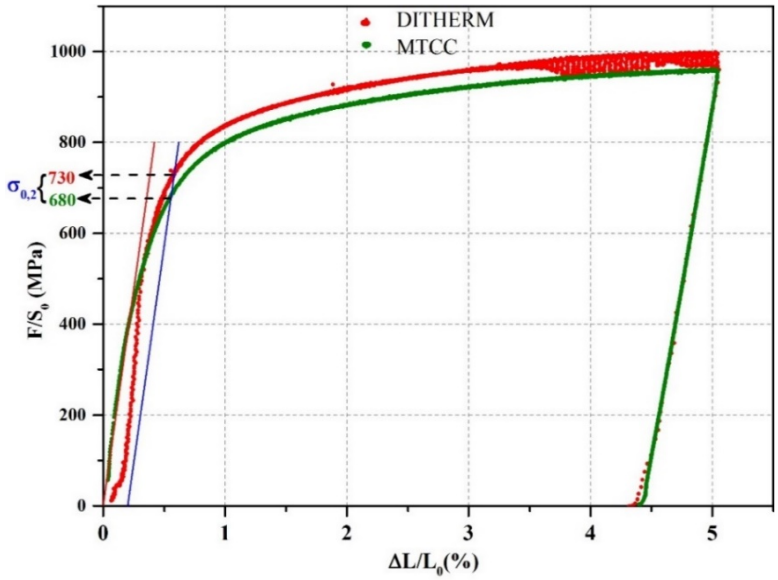

Figure II.18: First thermomechanical test performed on a newly designed tensile test specimen and grips.

II.4.3 Thermomechanical tests

II.4.3.1 Tensile and relaxation test

With the new MTCC device, tensile specimen, and grips, it is possible to perform well-controlled tension and relaxation tests at various temperature ranges between 900°C (where austenite is stable) and lower temperatures where austenite is metastable, and different phase transformations will occur. As an example, we have shown first in Figure II.20 a typical thermal cycle that is applied for characterizing bainite formed at 400°C. The sample was heated up to 900°C at a rate of 2°Cs^{-1}. Then the sample is cooled down to 400°C at a mean cooling rate of 60°C/s and maintained at 400°C. Through the instrumentation of the sample with 3 thermocouples along the gauge length, temperature differences along the gauge length are evidenced. These differences increase during heating, reaching 30°C between the center and the bottom at 900°C, but the temperature becomes homogeneous during the holding at 900°C. During cooling, gradients increase (they reach 30°C between the top and the center of the gauge length but remain low (12°C) during the isothermal holding. It can be noticed that the control of the transition from rapid cooling to isothermal holding is quite good (small overshoot). Figure II.19 shows the results of a complete thermomechanical test at 900°C of the austenite comprising tensile and relaxation tests. The stress and deformation of the sample were followed throughout the whole treatment. On heating, the thermal expansion coefficient of the ferritic phase is similar to the results obtained in the dilatometry (12°C/s). However, the

contraction between Ac_1 temperature and A_{C3} shows a variation of ±15% if compared to the dilatometric results. It could be due to the thermal dilatation of the grip plates.

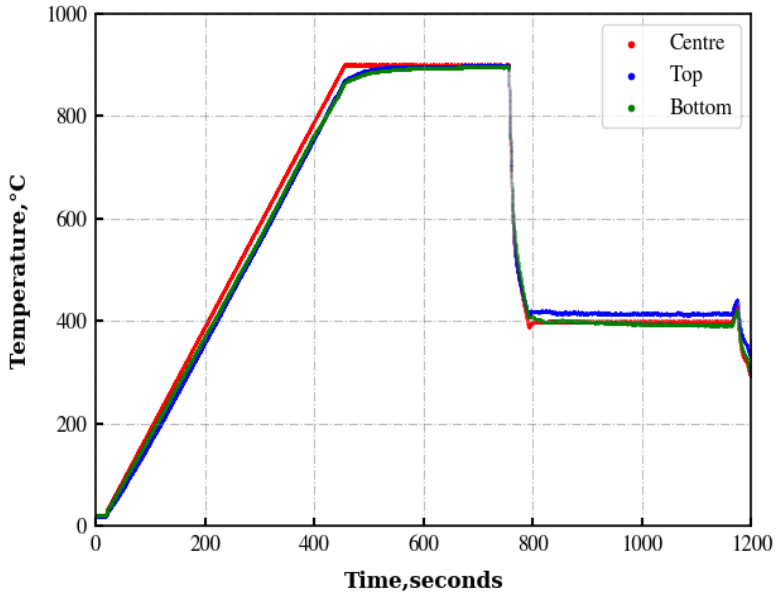

Figure II.19: Temperature evolution during bainitic transformation.

A small constant load (10N) was applied all along the treatment to maintain the specimen before the tensile test. The specimen was deformed at a constant rate of $2x10^{-4}$ s^{-1} and interrupted at 5% plastic strain. Then the deformation is maintained constant for the relaxation test. Evenif the control of the deformation rate is correct, at a high temperature (900°C), the response of the material is very sensitive to variations in deformation rate and leads to variations in the flow stress. We also encountered difficulties to control perfectly the constant deformation for the relaxation test.

We have encountered other experimental difficulties, especially during the high-temperature thermomechanical tests, that are summarized here:

During rapid cooling, the difference in thermal dilatation between the tensile specimen and the grip plates causes a localized stress distribution in the neck region of the specimen. All high temperature experiments (> 550°C) were executed by maintaining a gap tolerance between the support plates and the testing specimen to avoid this localized stress concentration at the neck region. However, the localized stress built-up when the cooling continues below 550°C. This issue challenges the thermomechanical studies of bainite and martensite phases (phase transformation occurs < 550°C). Thus, we have chosen to obtain the desired microstructures (particularly bainite) using rapid cycling in-house dilatometer (DCR) (See Section II.4.4). The sample with the desired microstructure was then tested thermomechanically (on MTCC) to determine the thermomechanical behavior of the formed microstructure.

The second difficulty is related to the measurement of the deformation using a high-temperature extensometer, mainly to track the elastic strain of the sample. The defect in the extensometer alignment on the specimen was adjusted before each test to avoid the bending stresses, which affect the elastic modulus. Nevertheless, elastic modulus will be generally underestimated at higher temperatures.

Horizontal, vertical, and angular alignments of the specimen, the positioning of the extensometer, PID configurations of thermal and mechanical systems, and some precautious measurements before and after the experiment (see Appendix D) are essential to the generation of accurate, repeatable, and reproducible thermomechanical results.

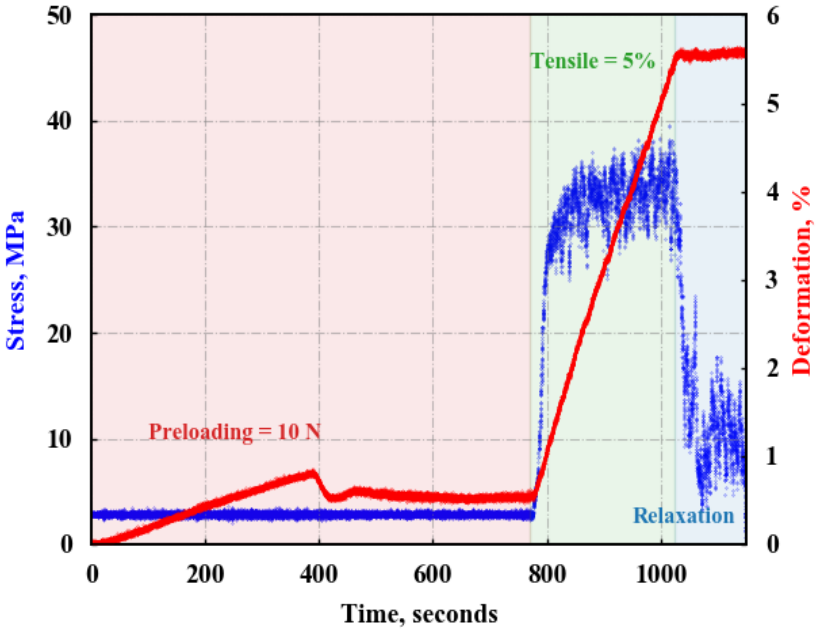

Figure II.20: An example of a complete thermomechanical cycle applied for an isothermal transformation.

II.4.3.2 Scheduled experiments

Our objective is to quantify the variations of the thermomechanical properties as a function of the test temperature, interstitial chemical contents (C, N, and C+N), phase/constituents, and strain rates. Various thermomechanical tests were scheduled and performed, as shown in Table II.3. For the reasons of experimental limitations, the minimum and maximum temperatures for different phases/constituents were selected. We chose two strain rates, $2x10^{-3}$ $s^{-1,}$ and $2x10^{-4}$ $s^{-1,}$ which correspond to the interval of strain rates that occur during the heat treatment. The effect of the strain rates has been quantified only at 900°C and 600°C, and the tensile tests were followed by relaxation tests to quantify the viscous effects at higher temperatures. The obtained experimental results and their analyses are presented for the temperature range between 25°C and 900°C in Chapter IV.

For austenite, complete thermomechanical tests comprising tensile and relaxation tests are performed, as shown in Figure II.21a. For the base and carburized steels, the thermomechanical behavior of austenite was obtained at 900°C and 700°C. Rapid cooling at a rate of 60°C/s from the austenitization temperature down to 700°C may ensure that the austenite decomposition is avoided and allows to get the behaviour of the metastable austenite.

For the nitrogen-containing steels, the thermomechanical test for the austenite phase is possible only at 900°C. Indeed, it has been shown in previous studies that enrichment in nitrogen induces a strong acceleration of the isothermal austenite decomposition kinetics [3]. This faster kinetics makes the thermomechanical test for the austenite phase at 700°C impossible. Very fine ferrite microstructure containing nano precipitates (CrN) are formed during the thermal treatment [3, 4, 92] that lead to higher hardnesses at room temperature. Thus, the thermomechanical behavior of this constituent (called 'high temperature constituent') at 600°C and room temperature once the transformation is completed has been determined, as shown in Figure II.21b. The specimen is deformed plastically up to 2% at a strain rate of $2x10^{-3}s^{-1}$.

For bainite, we need the thermomechanical behaviour not only as a function of temperature but also depending on the temperature at which the bainite is formed. For our tests, the isothermal transformation temperatures 400°C and 350°C were chosen to

Table II.3: Schedule of thermomechanical studies.

Steels	T (°C)	Phase	Strain rate, 1/s	
			0.002	0.0002
23MnCrMo5 Base	20/200	Ferrite + Pearlite	X	
	900/700	Austenite	X	X
	400/20	Bainite	X	X
	20/200	Martensite	X	
23MnCrMo5 Carburized 0.6%C	900/700	Austenite	X	X
	350/20	Bainite	X	
	20	Martensite	X	
23MnCrMo5 Carbonitrided 0.6%C & 0.45%N	900	Austenite	X	X
	600/20	Ferrite/CrN	X	
	350/20	Bainite	X	
	20	Martensite	X	
23MnCrMo5 Nitrided 0.1%C & 0.45%N	20	Ferrite/CrN	X	
	20	Bainite	X	
	20	Martensite	X	

produce a fully transformed bainitic microstructure. The bainitic tensile test samples were obtained using the dilatometer (DCR) (as mentioned in Section II.4.4), and these samples was reheated in the thermomechanical machine to the corresponding isothermal transformation temperature (400°C for the base steel and 350°C for carburized and carbonitrided steels) as shown in Figure II.21c.

The thermomechanical behavior of martensite was characterized at 20°C (on martensitic samples obtained by dilatometry) and at 200°C after reheating the martensitic sample (see Figure II.21d).

The plastic deformation was limited to 2% for all phases except the austenitic phase (5% plastic strain). Indeed, during heat treatment, only small plastic strains are generated during cooling.

II.4.3.3 Effect of stress on phase transformation

As mentioned in chapter 1 and as it will be detailed in chapter 4, the simulation of residual stresses needs to take into account the effect of stresses on the phase transformations that are based on experimental results. The main purpose of these experiments is to determine the transformation plasticity strain as a function of applied stress. They will also give access to the acceleration of the kinetics due to the applied stress.

The effect of stress on bainitic transformation is measured for an isothermal transformation by applying a constant tensile stress at the beginning of the isothermal holding (in the austenite), as shown in Figure II.22a. For martensitic transformation that occurs during continuous cooling, the stress is applied above Ms temperature (taking into account that Ms increases with applied tensile stress) and maintained constant down to room temperature, as shown in Figure II.22b. The applied stress ranges from 0 MPa to

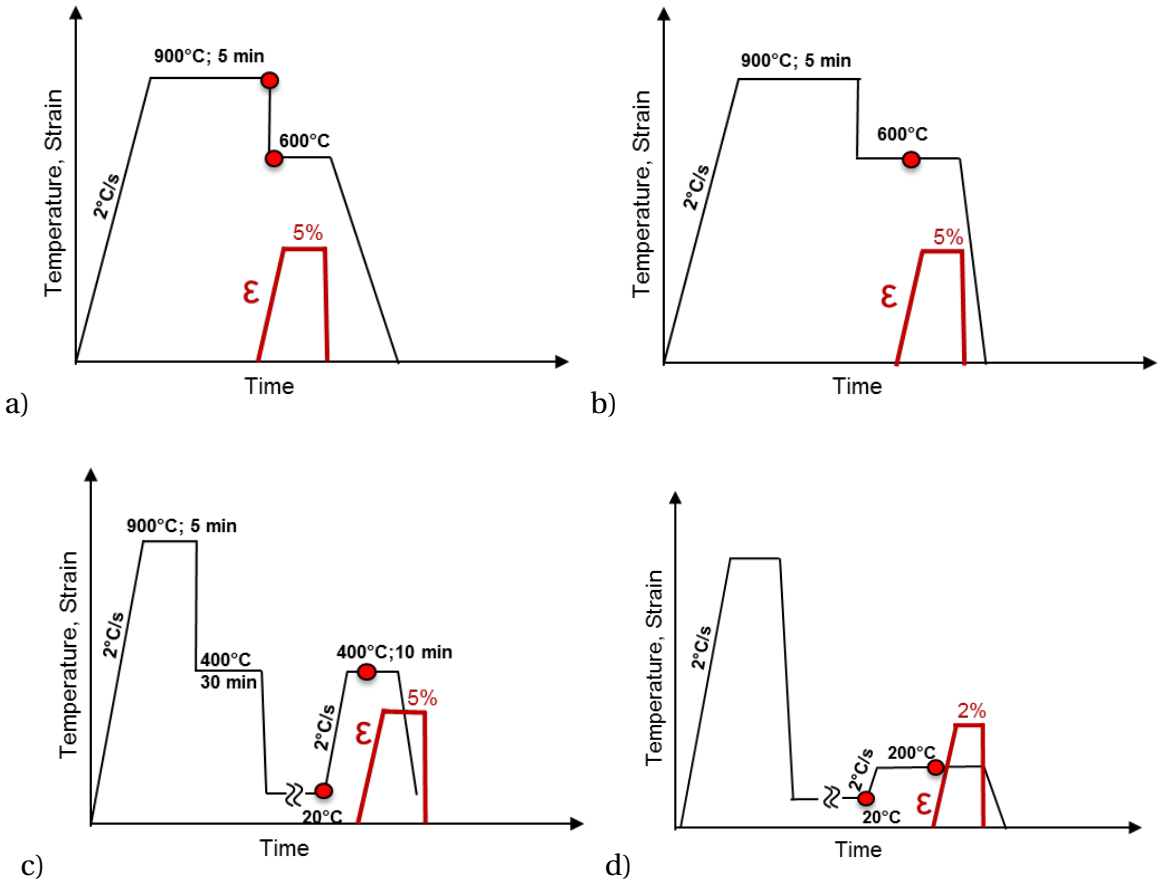

Figure II.21: Thermomechanical tests performed for a) austenite(top left)700°Cb) high temperature constituents (top right) c) bainite (bottom left) d) martensite (bottom right).

half of austenite yield stress MPa (at the considered temperature). Nevertheless, as the maximum cooling rate is 60°C/s (average between 900°C and 350°C) that can be reached experimentally, it will not be possible to reach bainitic and martensitic transformation for all steel compositions. Particularly, in the nitrided specimen, the incubation time of the high temperature constituent is approximately 20s at 600°C, and isothermal HT constituents and bainitic transformations could not be reached.

II.4.4 Dilatometry

As mentioned before, the in-house dilatometer for rapid thermal cycling (DCR) was used to generate the microstructures in the tensile test samples, which have been later on used for the thermomechanical test. Dilatometric tests were also performed in order to obtain the thermal expansion coefficients of the different constituents, the transformation strain (volumic variation) [3, 86, 93] for the different phase transformations as well as the overall kinetics of phase transformations. On this device, the sample is held vertically between two silica rods in a chamber under a high vacuum (5.10^{-4} mbar). The heating is done under the N_2/Ar atmosphere, and the cooling is controlled by blowing helium gas to the sample surface (helium for the highest cooling rates). The sample temperature during the treatment is measured using K type thermocouple (chromel/alumel) welded at the center of the sample. The thermal treatment is divided into a series of segments, in which the process parameters such as temperature, voltage, and gas flow rate are defined. The deformation is obtained by measuring the displacement of the upper rod silica using the LVDT (Linear Variable Differential Transform) sensor.

It should be noted that no appropriate support system was available for the lamellar

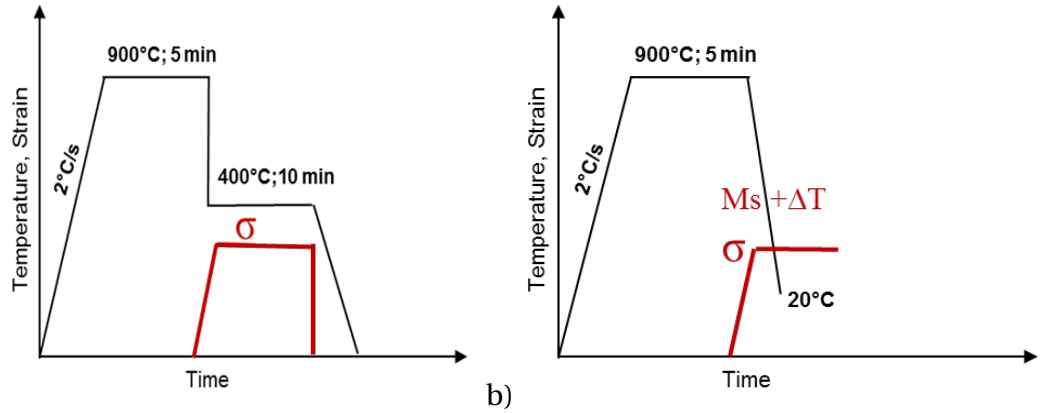

Figure II.22: Stress-phase interaction tests performed during a) bainite and b) martensite formations.

tensile sample. Therefore, to avoid the specimen shift or detachment from the notch during rapid cooling, it was fixed at both ends of the notches by means of a platinum wire. This setup allows the specimen to displace along with the upper rod with less noise.

II.5 Thermophysical study

II.5.1 Specific heat and enthalpy measurements

Specific heat is the amount of stored heat in a unit temperature range. To determine the specific heat precisely in a wide range of temperatures (20 - 1000°C), the use of two devices of calorimetry is required:

- **Multi HTC** (Multi High Temperature Calorimeter),
- **DSC** (Differential Scanning Calorimeter),

DSC allows accurate measurements until 800°C, while Multi HTC enables us to reach higher temperatures (up to 1600°C). However, sensitivity is less in the temperature range of 20 - 500°C. Both devices (i.e.,) DSC and Multi HTC were used for measurements in the range of 20 to 800°C and 400 to 1200°C, respectively, to get full temperature range data.

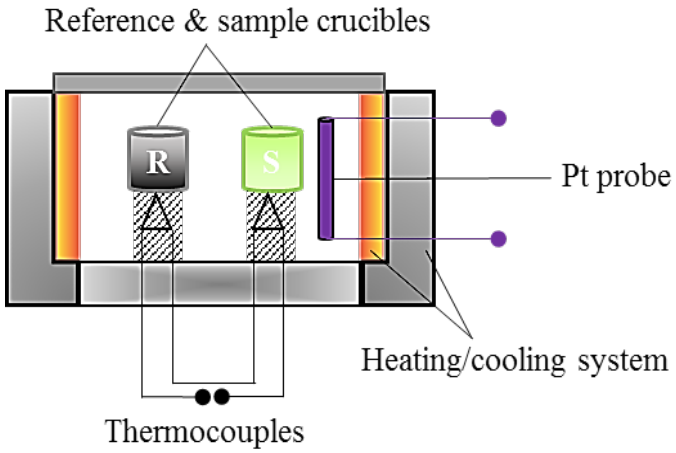

Figure II.23: Scheme of the differential scanning calorimeter (DSC) apparatus.

The system consists of a furnace with a protective Ar atmosphere (an adiabatic enclosure is assumed) and two crucibles equipped with thermocouples. Specific heat

is determined based on the comparative method, where three measurements are run consecutively with one empty crucible always: the first one with the other crucible without sample, the second one with a reference sample (here pure alumina), and the third one with the target sample. Specific heat measurements were done on three samples: base steel, carburized, and carbonitrided homogeneous steel samples. The standard geometry of 3 x 3 x 18 mm was used for the *Cp* measurements of the base steel. Our 1 mm thick enriched samples prevented us from choosing the standard sample geometry; instead, a non-standard sample composed of three sliced pieces of 1 x 3 x 18 mm was used, which satisfies the necessity of having a consistent mass for all enriched samples. All the measurements were performed during heating in a stepped mode: continuous heating (with a rate of 10°C/min) is imposed between a succession of isothermal steps every 20°C for 30 minutes. The transmitted signals correspond to the heat flux (mW) into the sample and the reference, and the difference in heat flow at an isothermal segment is obtained by integrating over time. The thermal imbalance between the two crucibles is due to the specific heat of the sample, which is given by:

$$m * Cp = \frac{\Delta H}{\Delta T} \tag{II.1}$$

where ΔH is the area under the signal resulting from the weighted imbalance of the mass of the sample. The enthalpy of phase transformation was also determined using differential scanning calorimetry (DSC) at a constant controlled heating and cooling rate. Here, the sample was heated up to 1000°C at a rate of 5°C/min and then cooled to room temperature at the same rate. This determination generally requires two tests: without and with the sample and the reference (pure alumina) sample. The crucible holds about a few mg of the steel.

II.5.2 Thermal diffusivity measurements

The thermal diffusivity measurements were performed on a laser flash apparatus (LFA 427, Netzsch). In turn, the thermal conductivity will then be calculated, as shown in Chapter IV.

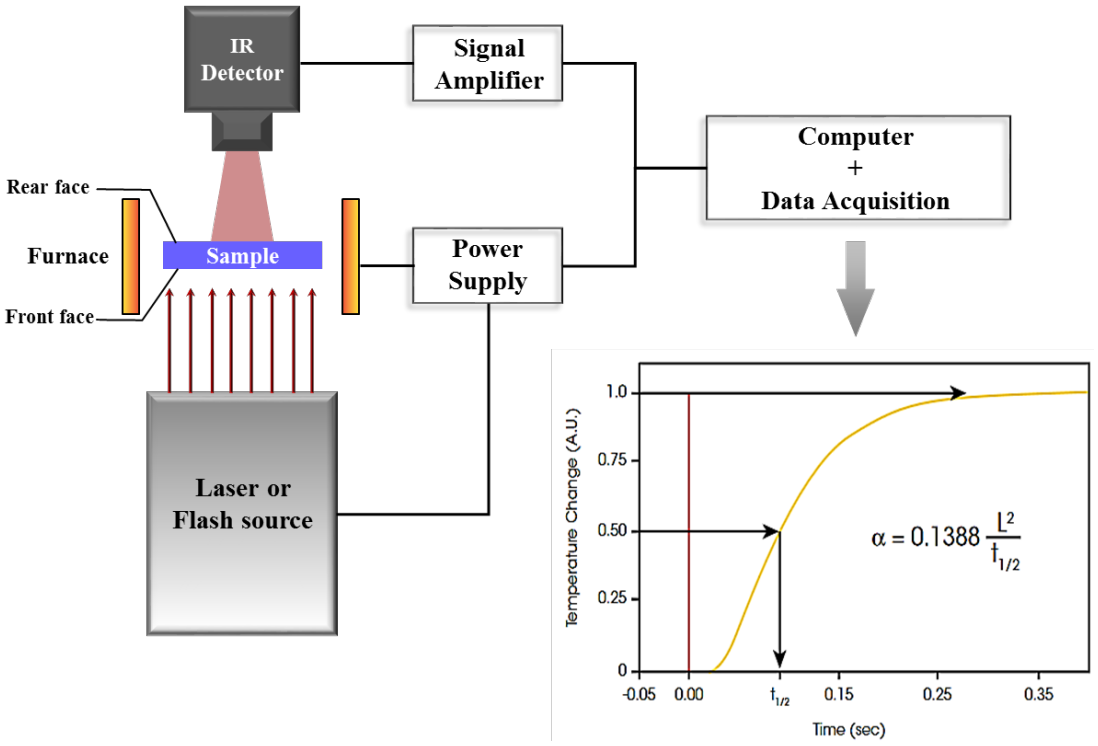

Figure II.24: The scheme of the thermal diffusivity measurement setup (Netzsch LFA 427).[94].

The scheme of the measuring device is given in Figure II.24. This device consists of a high temperature furnace, which operates between 25 and 1100°C under an argon atmosphere. The heat pulse was provided by a laser operating at a wavelength of λ = 1064 nm and delivering a maximum power of 20 J/pulse. Two thermocouples were used to regulate the oven temperature and to measure the sample temperature. Base steel, C, and C+N homogeneous enriched lamellar samples (49 × 10 × 1 mm) were processed into a perfect square-shaped sample (10 x 10 x 1mm) for cross-plane thermal diffusivity measurement. Both sides of the sample were polished up to 800 grit sandpaper and sandblasted in order to avoid the effects of reflection due to the metallic shine and to have better laser beam absorption and an excellent emission to the detector. The volumetric mass density was determined at room temperature, neglecting any temperature dependence.

In the flash method, the front surface of a sample is thermally excited by a laser energy pulse, and the rise of rear face temperature is measured by an infrared detector (InSb with Ge filter) in a particular time interval. The diffusivity was calculated using in-built software models. In the automatic mode, the software manages the input parameters: sample dimensions, temperature steps (25 °C), heating ramp (5°C/min), pulse width (0.3 ms), duration in between the pulses (1 min), laser power (420 V) and ensures excellent reproducibility of the measurements.

II.6 X-ray Diffraction

In this study, the main aim was to track simultaneously the phase transformation kinetics and internal stress evolutions of the carburized, nitrided, and carbonitrided steels during cooling along with the carbon and/or carbon+nitrogen gradients using High-energy X-ray diffraction (HEXRD) available at a synchrotron radiation source. Residual stresses profiles in depth have also been measured post-mortem. In addition, we have performed some laboratory X-ray diffraction experiments. Hereafter we describe the laboratory X-Ray device shortly, and we detail the HEXRD device and methodologies afterward.

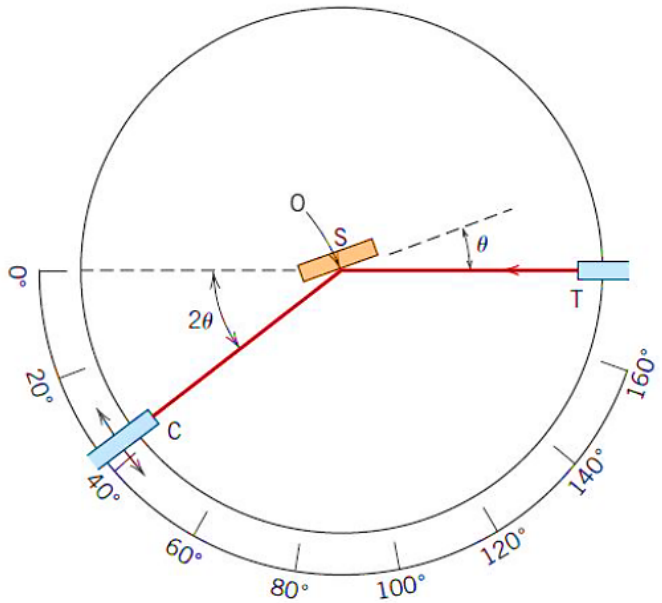

Figure II.25: Diffractometer with sample (S), X-ray source (T), and detector (C).

II.6.1 Low energy X-ray diffraction (Laboratory scale)

Brücker D8 Discover consists of an X-ray source (Co-kα_1) producing monochromatic radiation with a wavelength of 1.78897 Å that has a depth of penetration of about 11.5µm. The scintillation (detector) detects the diffracted X-rays. The diameter of the collimator is 0.5mm. The specimen was mounted on a goniometer, which can be turned around two axes ϕ and ψ while the detector can be moved around the 2θ axis.

Laboratory XRD was used to investigate and quantify mainly the presence of retained austenite and residual stresses at the surface of the lamellar samples for the four different thermochemical treatments: carbonitriding-oil quenching or air cooling, carburizing-oil quenching and nitriding-oil quenching. The crystallographic plane {211} of ferrite/martensite was used (it is typically used for residual stress measurements in steels), its Bragg angle being $2\theta = 99.70°$. The measurement of residual stresses was performed using the conventional $\sin^2\psi$ method (as will be described in Section II.6.2.2.a). The measurements are made by tilting the samples for different ϕ angles and by varying ψ angles from 0 to 90°. Three phi angles (0°, 45°, and 90°) and ψ angles (±71.57, ±60.00, ± 50.77, ± 42.13, ± 33.21, ± 22.79, ± 0.00) have been used. The software PANalytical X'Pert Stress is used to perform the residual stress analysis.

II.6.2 High energy X-ray diffraction (Synchrotron Radiation)

Laboratory X-ray generators are characterized by relatively low intensities giving rise to slow rates of data acquisition and low penetrating depth; thus, it is possible to analyze only the near-surface of the sample[95]. By contrast, synchrotron sources (Figure II.26) provide high photon fluxes and high energy X-ray beams that allow to analyze a large volume of the sample with a high temporal resolution. There are several facilities around the world for HEXRD, and we have conducted our measurements at the ESRF (European Synchrotron Radiation Facility) in Grenoble, France). The experiments were carried out using the most appropriate beamlines ID11 and ID15B with a monochromatic beam of ~87 keV.

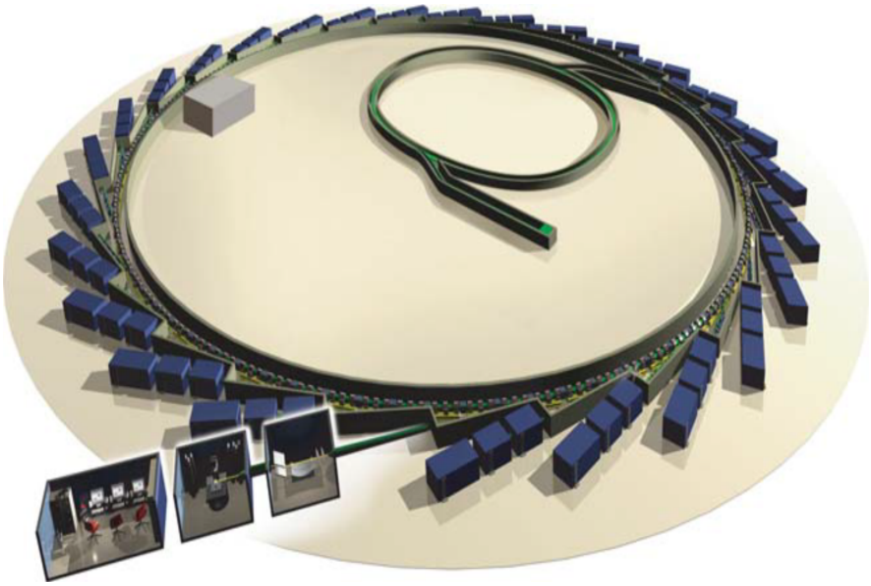

Figure II.26: Insertion devices (magnets) are used to deflect the electron beam in the storage ring of a synchrotron creating an intense beam of X-rays substantially tangential to the ring. The beamlines are located along these tangents and include optical elements to control the wavelength, beam dimensions, and focus[96].

II.6.2.1 Experimental setup

Figure II.27 shows the photograph of the in-house furnace installed on the beamline at ESRF for the experiments. The setup scheme shows that the high energy beam passes through the slits and is transmitted through the sample radially, as shown in Figure II.28a. The very high penetration depth of HEXRD allows scanning a large sample volume, thus being representative of the bulk and lessening the surface effect [97]. For post-mortem studies, the beam aperture was limited to a section of 100 µm (along the sample axis) by 400 µm (lateral to the sample axis using a slit system (Table-II.4). It allows obtaining the desired beam dimension for the size of the enriched layer to get a reasonably good resolution. For the *in situ* experiments during cooling, the beam size along the sample axis was reduced to 20 µm so that the beam could scan the smallest enriched layer as possible (as shown in Figure II.28c). The transmitted signal was collected by a large-area bidimensional (2D) detector located at a distance of ~1.1 m. The entire Debye–Scherrer (DS) rings with a maximum 2θ angle of 12° offer large mappings of reciprocal space that are projected onto the detector plane perpendicular to the through transmitted beam, as shown in Figure II.30. Cylindrical samples of 5 mm diameter and 3.2 mm height were machined out (as shown in Figure II.28b) from a lamellar gradient sample[1] (with a dimension of 32 x 10 x 3.2 mm) using a some wire cutting technique. *In situ* in-depth internal stress evolutions during cooling for carburized, nitrided, and carbonitrided steels were performed using this specimen geometry. In-depth residual stress measurements at room temperature for carburized and two carbonitrided samples (oil quenched and air-cooled) were also performed.

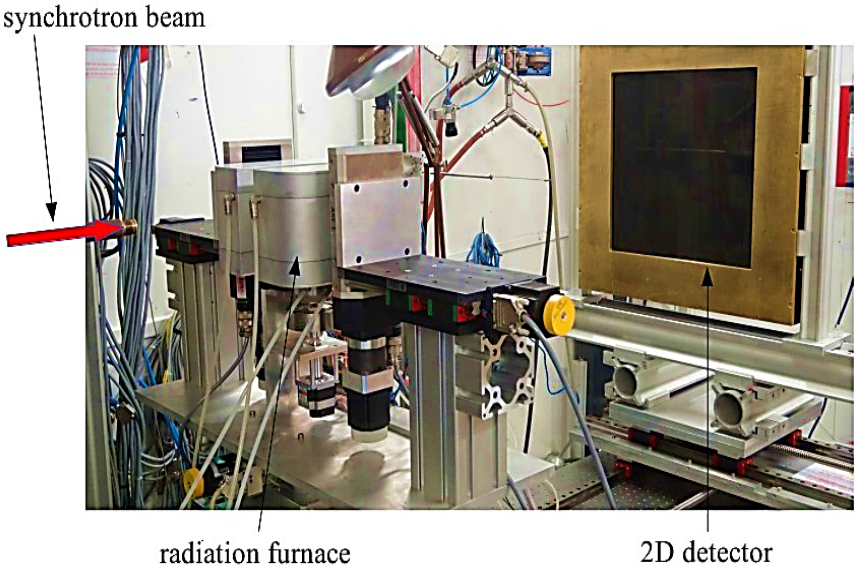

Figure II.27: Experimental setup of high energy diffraction with the in-house furnace [98] placed on the beamline before the detector.

With the in-house experimental device (Figure II.28) [98], controlled heating and cooling can be performed. During *in situ* studies, the sample was placed in a tubular furnace and austenitized at 900°C for 5 min using a lamp heating furnace with an environmental chamber (Ar circulation) to prevent oxidation and decarburization. This furnace consists of two halogen lamps (with a power of 1000 Watts each) placed opposite to each other. The distance between the lamps and the sample position was optimized to have homogeneous temperature distribution on the sample. The temperature was controlled by using S-type thermocouple spot welded on the sample surface. The thermocouple is placed on the other side of the beam path to avoid diffraction signals

[1]The lamellar specimen were C and/or N enriched on the thermobalance and quenched as described previously and also used for laboratory-scale residual stress determination.

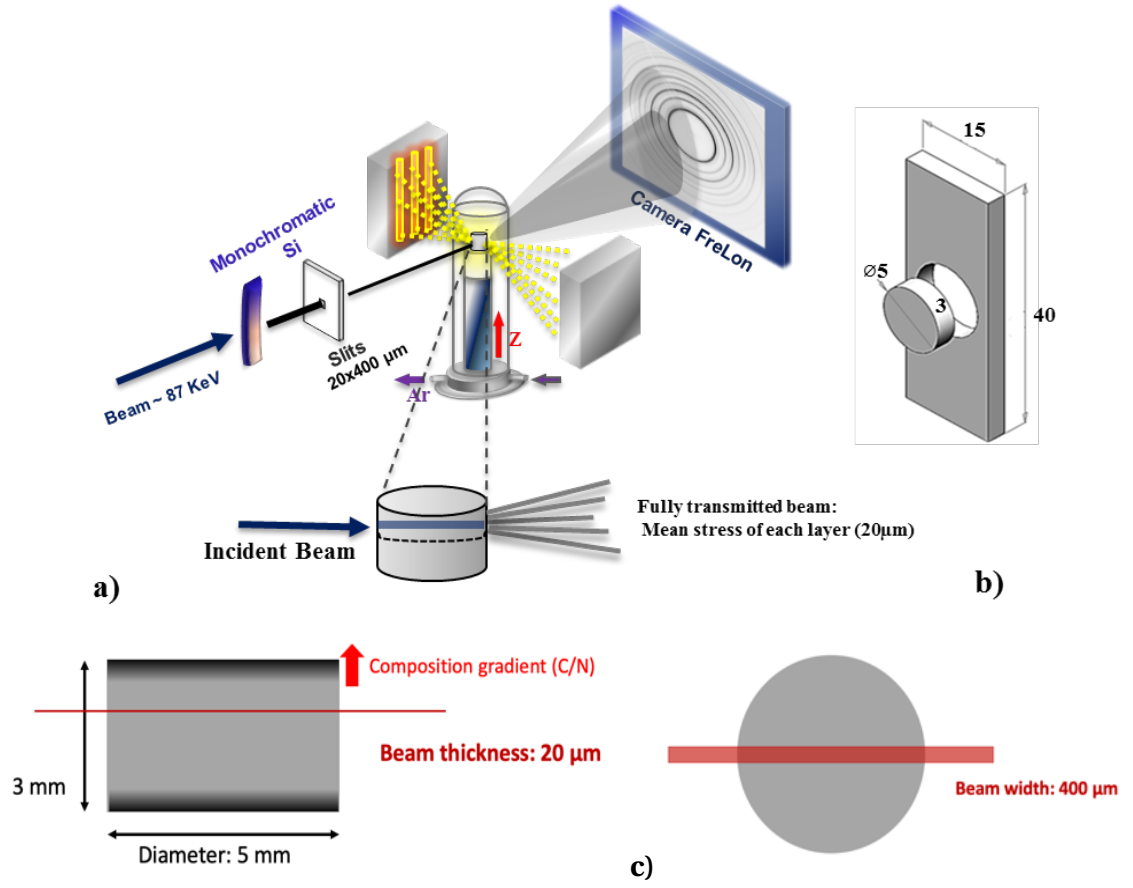

Figure II.28: Schematic setup of Synchrotron X-ray and furnace setup(during insitu study), b)cylindrical sample is machined out of lamella, and c) Scheme of the specimen illustrating the gauge volume.

of the thermocouple. The sample was cooled with gas (Ar) blowing at a controlled rate 2°C/s between 900°C and 550°C, and then the furnace lamps were switched off allowing the sample to cool naturally until room temperature. The thermal cycle (Figure II.29a) was programmed by dividing it into different segments, which are representative of each stage of treatment (heating, austenitization, gas cooling, and controlled cooling without gas). The main inputs are the voltage and the duration of each segment.

The diffraction frames have been acquired at different rates using different detectors (see Table II.4). The maximum acquisition rate was limited to 50 frames/s. Special care was taken to ascertain that the beam was entirely inside the sample at all times, so that edge effects would not influence the measurements. Some other sources of experimental errors will be addressed later on (Section II.6.2.2).

For post-mortem studies, the sample mounted on a ceramic head and rotated around its axis by steps of 90° By placing the sample on a computer-controlled translation table, the sample was translated in a z-direction to scan every 100µm. This configuration allows us to obtain the DS rings of each layer in the composition gradient within a short time interval. In this way, a map of the stress gradients along the C and/or N gradients was built up.

For the case of *in-situ* measurements, the DS rings were obtained without the rotation of the sample. Before the cooling phase, the beam was fixed at a distance of 500 µm from the top of the sample. (These recorded diffraction patterns are not used for the analysis). In the cooling stage, the sample begins to move up and down vertically to scan *in situ* the sample half-thickness, including the C/N enriched case, thanks to a table with controlled axial movement provided by ESRF, Grenoble. Each cycle lasted about 6.65s. The sketch of

Table II.4: Diffractometer with sample (S), X-ray source (T), and detector (C).

Parameters	**Post-mortem study**		**Insitu study**
	After Thermochemical Treatment	**After Insitu Treatment**	
Wavelength (Å)	0.0141	0.0141	0.0141
Beamline	ID11	ID15B	ID15B
Gauge volume μm^3	100 x 400 x5000	100 x 400X5000	20 x 400X5000
Acquisition rate	2 frames/sec	2 frames/sec	50 frames/sec
Detector/ size	CCD	FRELON camera	Perkin Elmer XRD1621
Rotation	360°	360°	No rotation
Exposition time per layer (seconds)	2	2	0.7

*gauge volume is reduced to 20x400x5000 μm^3 in the N-enriched layers.

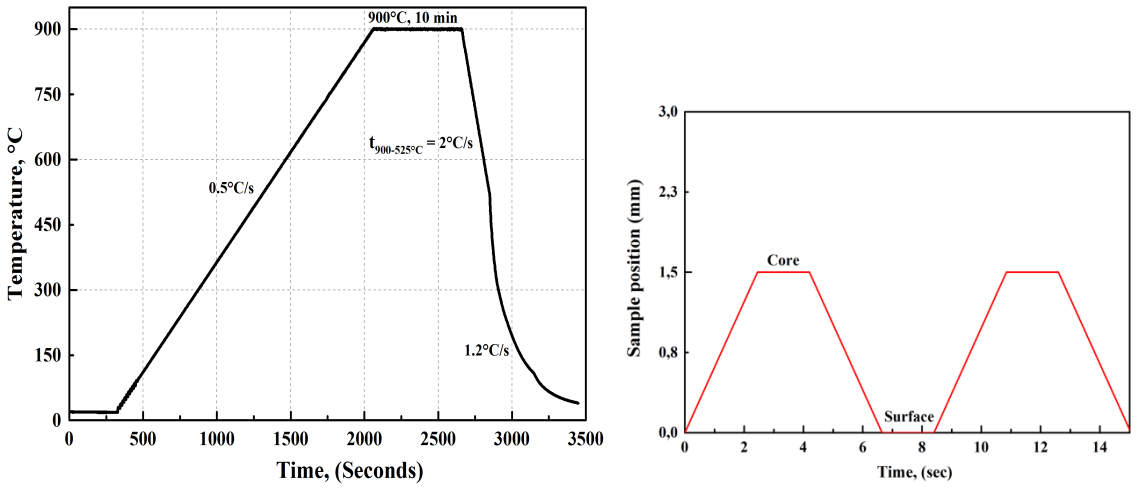

Figure II.29: a) Thermal treatment applied during the in-situ study and b) Sample movement along the z-axis with a fixed beam position.

the sample movement cycle is shown in Figure II.29b. Finally, the *in-situ* measurement of a gradient sample for the thermal cycle generates around 14,000 diffraction frames.

II.6.2.2 Diffraction patterns processing

II.6.2.2.a Quantitative Phase Analysis

The DS rings were integrated circularly or reduced to extract average phase fractions and lattice parameters using Fit2D software [99] and PyFai [100]. The latter has been designed to integrate images taken with 2D area detectors like CCD or pixel detectors. The diffractograms were then subjected to a full Rietveld refinement procedure using the Fullprof software [101, 102] in the 2θ range from 2.50° to 9.0° with a step size of 0.0071°. Both *in-situ* and post-mortem measurements were submitted to this same refinement process by knowing the wavelength of the radiation and the crystallographic nature of each phase. The refinement was performed by simultaneously fitting the whole 1D spectra using pseudo-Voigt functions (Appendix C). Mathematically, the best-fit approximation was obtained by the least-squares method. For all considered spectra, the confidence factor χ^2 was inferior to 1.5. No texture was taken into account in the analysis; for more details on this standard procedure and the adjustment criteria. (see Appendix C).

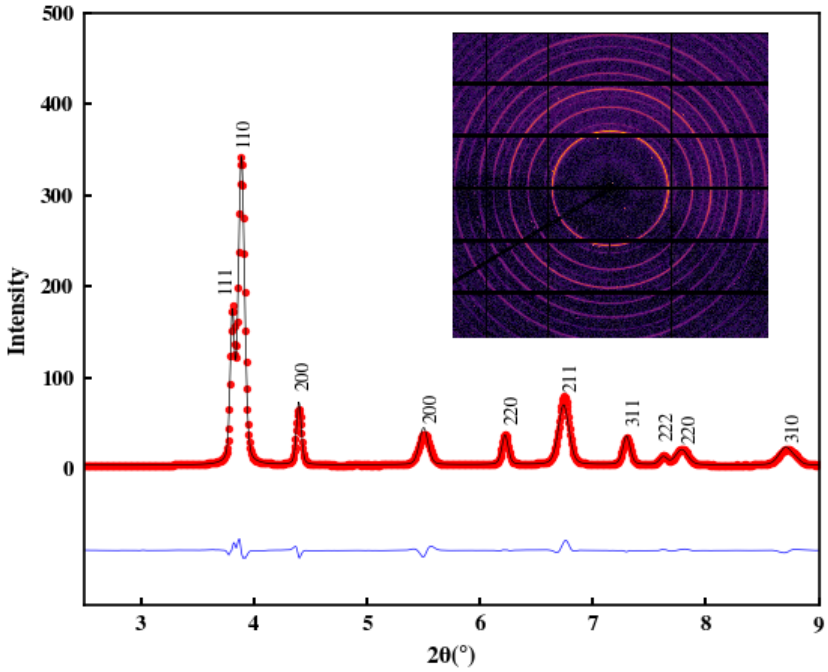

Figure II.30: Diffraction intensity of the carburized sample is plotted against the scattering vector.

The average lattice parameter and phase fraction of each phase was determined by summing one or more profile peak fitting functions, which are more likely to represent the bulk behavior of an enriched layer. For example, the diffraction patterns of carburized gas cooled samples obtained from the measurements at 600°C are shown in Figure II.30.

For all the experiments, two phases were identified on diffraction patterns: a face-centered cubic (FCC) phase corresponding to austenite and a body-centered (BCC) phase. In our experiments, the martensitic phases exhibit no tetragonal unit cell (c/a ratio) as well as ferritic bainite. Thus in our analysis, ferrite, bainite, and martensite were referred to as "ferritic" phases. Nevertheless, we observed that the diffraction peaks obtained for the martensite are broadened in comparison with ferrite, as generally observed [103].

The surface layers of the enriched steels contain not only major phases (ferritic and austenite phases) but also small carbides and nitrides. We detected diffraction patterns for these constituents, but these could not be quantified due to their small intensities. The

uncertainty associated with the phase fractions was more pronounced for the fractions of less than 10% (approximately 5%). An automated mode option, 'cyclic refinement' in FullProf, was used to analyze many diffractograms obtained during the in-situ or post-mortem experiments.

II.6.2.2.b Quantitative Stress Analysis

First, we will recall the classical $\sin^2\psi$ method for determining residual stresses. Then we will address the specific aspects linked to the use of synchrotron and 2D detector.

Classical method of stress determination Here, we will briefly recall the classical $\sin^2\psi$ method for determining residual stresses using laboratory X-ray and high energy X-ray diffractions.

When the X-ray beam passes through the sample, the crystals/grains with a specific orientation relative to the sample surface, θ_0 diffracts the incident beams as shown schematically in Figure II.31 according to Bragg's law [104]:

$$n\lambda = 2d_{hkl}\sin\theta_{hkl} \tag{II.2}$$

By knowing λ is the x-ray wavelength, n is an integer (typically 1), θ_{hkl} is the diffraction angle of the hkl plane; this law allows us to determine the lattice spacing d_{hkl}, of the crystals of a selected phase. When the material is strained, the lattice spacing for a given reflection {hkl} is changed, inducing a shift of the diffraction peaks, as shown in Figure II.31. By precise measurement of this shift, the change in the inter-planar spacing, δd_{hkl}, and then the strain, ε, in the material, can be evaluated using Eqn. II.3. The stress tensor can be determined using generalized Hooke's law [104].

The normal strain along the crystallographic plane normal direction can be measured by the 2θ shift of the diffraction pattern. The full stress/strain tensor in the measurement point can be determined by measuring the normal strains in various directions in the sample coordinates.

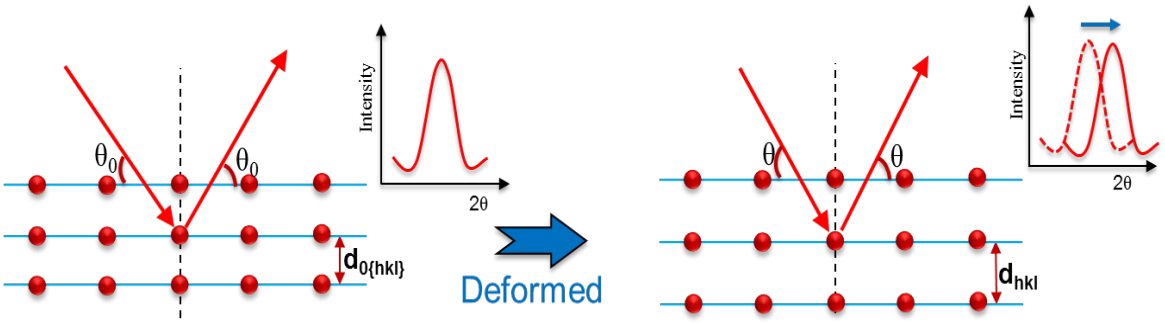

Figure II.31: X-ray diffraction within a crystal structure, d = interplanar lattice spacing, θ = Bragg angle

To represent the stress and strain are tensorial quantities, it is convenient to consider two different cartesian frames of reference: the sample frame of reference, S, and the laboratory frame of reference, L. The S_3 axis is oriented perpendicular to the specimen surface, and the S_1 and S_2 axes lie in the surface plane. The sample reference frame is chosen in such a way that the L_3 axis coincides with the diffraction vector. For the relative orientation of laboratory and sample frames of reference and the definition of angles (as in Figure II.32), consider frames coincide, which is detailed by Nye [105].

2θ is the angle between the incident (transmitted) and diffracted X-ray beams. ω and χ are the sample rotational angles along the axial and radial axes of the cylindrical sample. The coordinate systems S_i and L_i are related through the (rotation) angles ϕ and ψ. The vector $\vec{n}$ is the bisector of the angle formed by the incident beam and the diffracted beam.

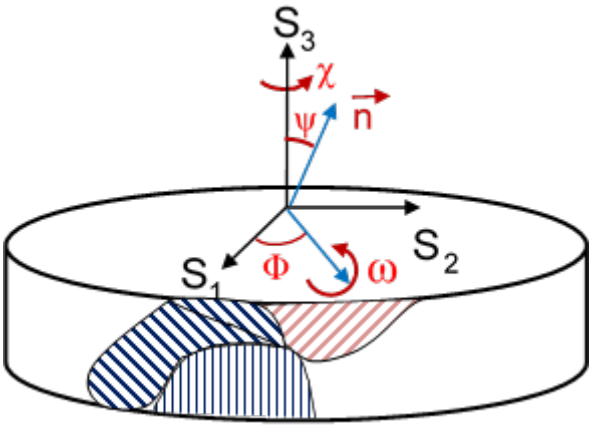

Figure II.32: Coordinate systems used to measure stresses with diffraction. The S_i coordinate axes are the sample coordinate system. Oriented by the angles ϕ and ψ with the sample coordinate system is the L_3 axis of the laboratory coordinate system — the relation between the direction of the measured normal strain and the sample coordinates.

The measurements are made by tilting the samples for different ϕ angles and by varying ψ angles from 0 to 90°. The strain $\varepsilon_{\phi\psi}$ along the direction normal $\vec{n}$ (or L_3 coordinate axis) to the diffracting planes is expressed below by considering the components of the strain tensor ε_{ij} in the sample reference system:

$$\varepsilon_{\phi\psi} = \ln\left(\frac{\sin\theta_0}{\sin\theta}\right) \cong \frac{d_{hkl} - d_0}{d_0}$$

$$\varepsilon_{\phi\psi} = (\varepsilon_{11}\cos^2\phi + \varepsilon_{22}\sin 2\phi + \varepsilon_{22}\sin^2\phi - \varepsilon_{33})\sin^2\psi + (\varepsilon_{13}\cos\phi + \varepsilon_{23}\sin\phi)\sin 2\psi + \varepsilon_{33} \quad \text{(II.3)}$$

For a homogeneous and isotropic material, using generalized Hooke's law, the expression of the deformation $\varepsilon_{\varphi\psi}$ versus the stress components is obtained,

$$\varepsilon_{\varphi\psi} = \frac{1}{2}S_2\left[(\sigma_\varphi - \sigma_{33})\sin^2\psi + \sigma_{33} + (\sigma_{13}\cos\varphi + \sigma_{23}\sin\varphi)\sin 2\psi\right] + S_1(\sigma_{11} + \sigma_{22} + \sigma_{33})$$

with:

$$\sigma_\varphi = \sigma_{22}\sin^2\phi + \sigma_{11}\cos^2\phi + 2\sigma_{12}\cos\phi\sin\phi$$

S_1 and S_2 are the radio crystallographic elastic constants. For a triaxial stress state, $\varepsilon_{\phi\,\psi}$ versus $\sin^2\psi$ for a given angle is an ellipse (Figure II.33).

The slope of the ellipse axis allows us to obtain the stress difference $(\sigma_\phi - \sigma_{33})$. The opening of the ellipse is proportional to the shear component of the stress tensor. The stress differences $(\sigma_\phi - \sigma_{33})$ are mean values inside the considered phase. For ϕ = 0°, the stress difference $(\sigma_{11} - \sigma_{33})$ is obtained, as well as σ_{33},

For ϕ = 90°, we obtain $(\sigma_{22} - \sigma_{33})$ and σ_{23}. In multiphase materials, the stress component in the direction normal to the surface is $\sigma_{33} \neq 0$. To get all the components of the stress tensor, it is necessary to determine σ_{33} that requires the knowledge of the lattice parameters of an unstressed specimen, i.e., d_0 for each phase. [2]

[2]The stress determined by lab XRD in α/α' phase can be compared to the tangential stress (*In-situ* HEXRD). HEXRD gives an estimate of the stress difference (σ_{11}-σ_{33}). One can assume that, at the sample's surface, σ_{33} is close to zero in α/α' phase. Indeed, this α/α' is the preponderant phase and the stress in α/α' is thus close to the macroscopic stress (the average in α/α' and γ), which is equal to zero, due to the boundary condition. In that case the slope of the ellipse axis gives directly σ_{11} and σ_{22} for ϕ = 0° and ϕ = 90°

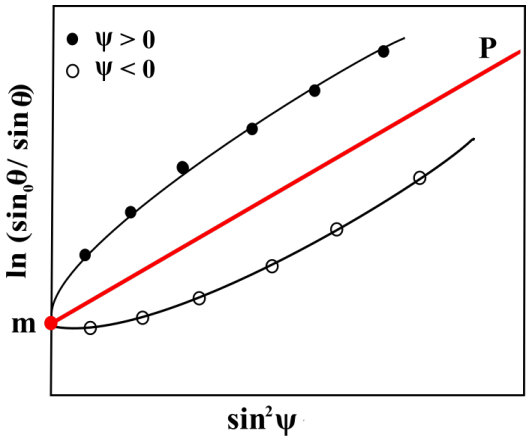

Figure II.33: Schematic curves ln(sin θ_0/sin θ) versus $\sin^2\psi$ for a triaxial stress state. P: the slope of the ellipse axis, m: intercept.

Specific aspects related to synchrotron XRD and 2D detector The use of a high energy beam (E > 80 keV) makes it possible to cross the sample and to make an analysis of the stresses within the gauge volume, contrary to the experiments realized in the laboratory where the analysis can only be carried out at the surface. Besides, the advantage of using a 2D detector is to collect diffractograms I = f (2θ) in several directions (ϕ, ψ) on a single image because the detector can record complete rings from Debye-Scherrer. Thus 2D images with Debye-Scherrer rings were collected according to different orientations (ϕ) (Figure II.34). The specificity of the images obtained requires appropriate exploitation to extract the stresses.

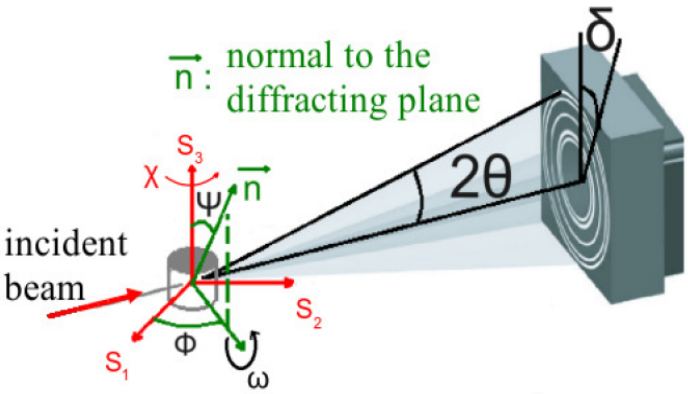

Figure II.34: Angles definition from setup configuration: (S_1, S_2, S_3) is the sample reference system, and ϕ and ψ define the direction normal to the diffracting plane{hkl}.[69]

First, the image must be integrated for each azimuth, δ, to obtain the diffractograms I = f (2θ). The whole diffraction rings (360°) are 'sliced' into a 1° sector; thus, we obtain 360 diffractograms (intensity, 2θ) per ring. This line profile was sufficient enough to produce a smooth profile with a flat background. When a 1° sector line profile is not good enough to have smoothened fitting, a perfect fit profile can be obtained by slicing the rings with higher angular sectors (2° - 5°). This higher angular sector eliminates the uncertainties by averaging the spectra spots to form smooth line profiles.

For the stress analysis, we have chosen {311} planes of γ and the {200} planes of α/α'. Individual diffraction peaks were selected as they do not overlap with other peaks. To determine the θ position (scattering angle) peaks were approximated by a Pearson

respectively.

VII function that allows reproducing of the shape of our peaks. A source of errors in the determination of peak position, may come from variations of the beam position in time.The center of the Debye Scherrer rings might not be identical with the position of the transmitted beam. By averaging 2θ positions of two opposite azimuths, i.e., δ and δ + 180°, the uncertainties in the 2θ position [97] have been avoided.

With this fit function of the peak, we could also characterize the mean full width at half maximum (FWHM) for each phase. These operations are repeated for all diffractograms collected during the thermal treatment.

In post-mortem stress analysis, we have considered two specific ϕ orientations (0°, 90°) corresponding to the χ orientations (0°, 180°) and (90°, 270°). Thus we use a rotating specimen, and it was evidenced that the position of the specimen changes during the rotation (small tilt relative to the axis of rotation), as illustrated in the photo (Figure II.35). It leads to variations in the diffraction angles. It is illustrated in Figure II.36 shows, for example, the variations of the lattice parameter of austenite during the rotation (here, we give the image numbers). We can see a "zig-zag" lattice parameter variation with an envelope around an average position, as shown in Figure II.36b. It is possible to distinguish the four orientations where the sample rests, which enables us to determine the strains from the known position of the sample. These evolutions of the diffraction angles have been taken into account for correcting peak positions.

For *in situ* measurements, no rotation was applied to the specimen. Indeed, the first experiments with rotation of the specimen around its axis showed that measured stresses were very close showing that axisymmetry is verified. Thus, for further experiments, no rotation was applied.

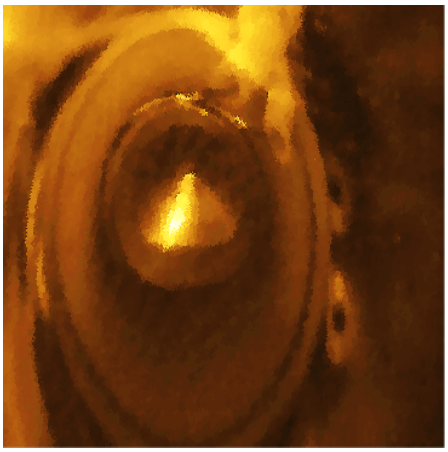

Figure II.35: A photographic image of the tilted sample during sample

Finally, in order to apply the $\sin^2\psi$ method (see Section II.6.2.2.a), it is necessary to convert the configuration with the 2D detector (Figure II.34) to the classical (ϕ, ψ) configuration. Indeed each azimuth corresponds to a pair of angles (ϕ ψ) that are calculated by using the expressions below,

$$\cos\psi = \cos c\left(\left(1-\frac{\sin^2\theta\sin^2\delta}{1-\cos^2 c}\right)\left(1-\frac{\sin^2\omega\sin^2\delta}{1-\cos^2 c}\right)\right)^{1/2} - \frac{\sin\omega\sin\theta\sin^2\delta}{1-\cos^2 c}$$

$$\Phi = \chi + \arccos\theta\left(\frac{\sin(\theta-\omega)}{\sin\psi}\right)$$

where

$$\cos c = \cos\theta\cos\omega + \sin\theta\sin\omega\cos\delta$$

It can be seen that almost the full range of ψ angle is scanned (from ca. 5° to 90°) on a single image; the angle ϕ is not constant but close to 90°(for an orientation χ = 0°) for azimuths varying from 0° to 70° and from 110° to 180°.

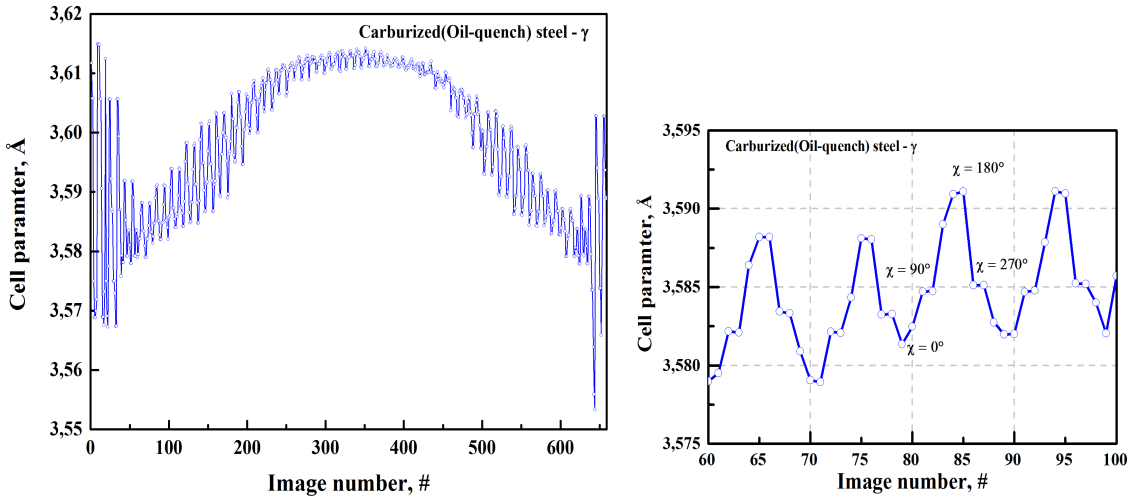

Figure II.36: Evolution of peak position over image number and a zoomed view of the image numbers 60–100.

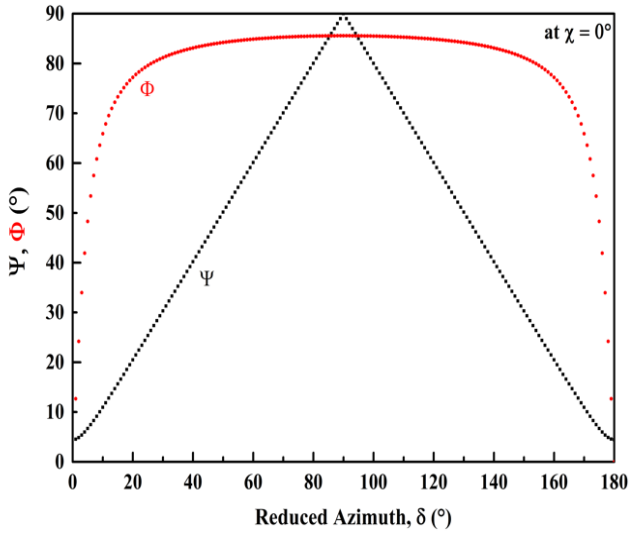

Figure II.37: Evolution of ϕ and ψ angles versus azimuth.

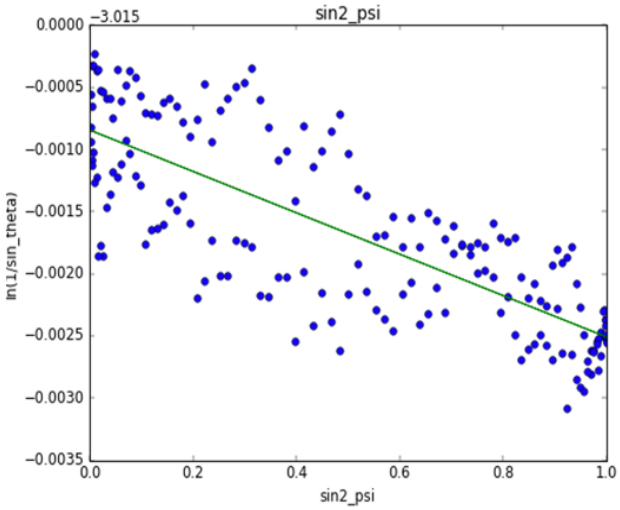

Figure II.38: $\sin^2\psi$ plot for martensite at the carbon enriched surface of a carburized specimen.

In our specific configuration (Figure II.28), in cylindrical coordinates (r, θ, z) (r for radial, θ for tangential, and z for axial) of the sample, we will get only ($\sigma_{\theta\theta} - \sigma_{zz}$) called later on ($\sigma_\theta - \sigma_z$). As mentioned before (Section II.6.2.1), this stress difference will be a mean value in the gauge volume defined in Table II-4). From our experimental results, the shear stresses are generally negligible, as shown in Figure II.38.

For our stress analysis, we used the isotropic elastic constants S_1= - ν/E and $1/2S_2$= 1+ ν/E with Young's modulus, E, and Poisson's ratio, respectively ν. At 20°C, we used 210 GPa and 0.3 for E and ν, respectively, for all phases [104]. The evolutions of E and ν as a function of temperature have been extracted from the literature [14, 93] and have been considered the same for all the phases.

A mean error for the measured stress values is evaluated at 50 MPa. From the mean stresses determined in the phases by X-ray diffraction (for ferritic and austenite phases) and the measured phase fractions and we got the macroscopic stress. The whole experiment generates a large volume of data. Indeed, recording all the data necessary for determining the stress component during the cooling. Gas cooling of each enriched steel generated more than 15,000 2D images representing more than 150 Gb of raw data. The whole analysis leads to determining the position of 10 million diffraction peaks for the two phases present in the enriched steels. Several scripts in python language were developed to automate the data processing.

Chapter III

Analysis of internal stress - HEXRD

The main objectives of this chapter are to analyze and understand the origins of the residual stresses formed in the carburized, nitrided, and carbonitrided gradient samples with respect to phase transformation kinetics. High-energy synchrotron X-ray diffraction (HEXRD) technique has been used as a primary technique to characterize quantitatively the fractions of phases formed and the internal stresses evolutions during cooling through the gradients.

The first section of this chapter summarizes previous experimental analysis of the phase transformation kinetics of the austenite on cooling and the formed microstructures in homogeneously enriched samples with carbon (C), nitrogen (N), and carbon + nitrogen (C+N) [3, 106, 107]. These analyses will help to understand better the results obtained in the gradient samples.

The second section describes the gradient samples i.e. the carbon and nitrogen profiles as well as the heat treatments applied.

The following section is focused on the analysis of the phase transformation kinetics and internal stresses evolutions during cooling in the gradient specimen : firstly in carburized specimen and then in nitrided and carbonitrided specimen in order to study the influence of nitrogen.

In each case, the final microstructure, hardness and residual stress profiles will also be compared to the ones obtained for different cooling conditions after enrichment to assess the role of different transformation kinetics on the residual stresses.

III.1 Summary on effects of C/N on austenite decomposition in 23MnCrMo5

This part presents a summary of previous investigations regarding the effects of enrichments in carbon and nitrogen on the austenite decomposition in 23MnCrMo5 steel. In these previous studies [3, 4], the experiments were carried out with laboratory samples having a homogenous composition in C/N. These results (microstructural observations, measurements of transformation kinetics, measurements of hardness) will serve as a guide to interpret the results regarding gradient samples, which will be presented in this chapter. The phase transformations were studied in steel samples having the homogeneous compositions shown in Table III.1. After austenitization at 900°C, the samples were submitted to isothermal treatments or continuous cooling.

In base steel (I) and carburized steel (C), the usual products of the austenite decomposition are observed. For decreasing isothermal treatment temperature or for increasing cooling rate: proeutectoid ferrite, pearlite, bainite, martensite. Enrichment in carbon leads to slower phase transformation kinetics and to lower temperature ranges

Table III.1: Carbon and nitrogen contents of investigated steels.

Steel	**Enrichment**	**$\%_m$C ±0.04**	**$\%_m$N ±0.07**	**B_s (°C)**	**M_s (°C)**
I	Initial	0.23	-	550 ± 25	385
C	Carburized	0.57	-	500 ± 25	260
N	Nitrided	0.07-0.13*	0.27-0.39	400 - 500	**
C+N	Carbonitrided	0.59-0.68	0.31-0.41	400 - 500	205

*Nitrided steel underwent decarburization during enrichment; ** hardenability was too low to determine the M_s.

(lower Bs and Ms), as expected. The latter temperatures are shown in Table III.1. Carbon and nitrogen contents of investigated steels. The hardness of martensite (Figure III.1) was measured as well as for the different products of austenite decomposition. For the latter, it was measured after isothermal treatments up to phase transformation completion followed by quench to room temperature shows the measured hardness. For base and carburized steels (blue and red symbols), the hardness increases for decreasing transformation temperature, and it is higher for bainite than for products formed above Bs.

More original effects were observed regarding the effects of enrichment with nitrogen of the austenite. Firstly, it drastically accelerates the kinetics of austenite decomposition. This is illustrated in Figure III.2a, which compares the kinetics of bainitic ferrite formation during isothermal treatment at 400°C, for the different steel compositions. Comparing e.g. C and CN steels, the latter has more interstitials (C, N) but faster kinetics, although C and N are expected to stabilize thermodynamically the austenite. These kinetics effects were also observed above the Bs temperature.

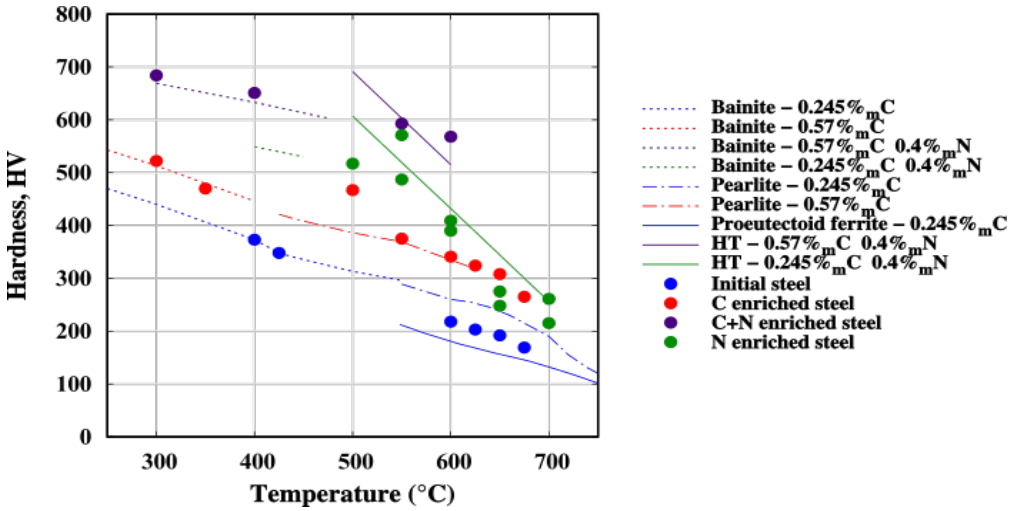

Figure III.1: Vickers microhardness measurements (load 100 g, at room temperature) after IT vs. IT temperature for C, N, C + N steels, and I. ITs with incomplete transformations ($T > Ae_1$ range or bainite range close to Bs) are not represented. Dashed and continuous lines: empirical functions employed in the model.

Another consequence is the formation of new microstructures, especially above Bs, where a microstructure that was termed a "High Temperature Constituent" (HTC) is obtained (Figure III.2b). It is dominated by fine equiaxed ferrite grains (a few µm), the absence of any remaining austenite, and the presence of different populations of nitrides and carbides. (Nanosized CrN nitrides inside the ferrite grains were also observed by TEM). Other observations and discussions on possible mechanisms for HTC formation

are presented in [3, 4]. Similar effects of microstructure refinement were observed in the temperature domain of bainite transformation. These finer microstructures are associated with high hardness (Figure III.2b). Whatever the temperature of the isothermal treatment, the hardness is higher for the nitrided steel (green symbols) than in carburized steel, although the latter has more interstitial elements. The carbonitrided steel shows the highest hardnesses.

Both effects of nitrogen enrichment (acceleration of kinetics, refinement of microstructures) have been ascribed to the precipitation of nitrides (CrN, $MnSiN_2$), which would stimulate the nucleation and growth of ferrite. These mechanisms are still being investigated.

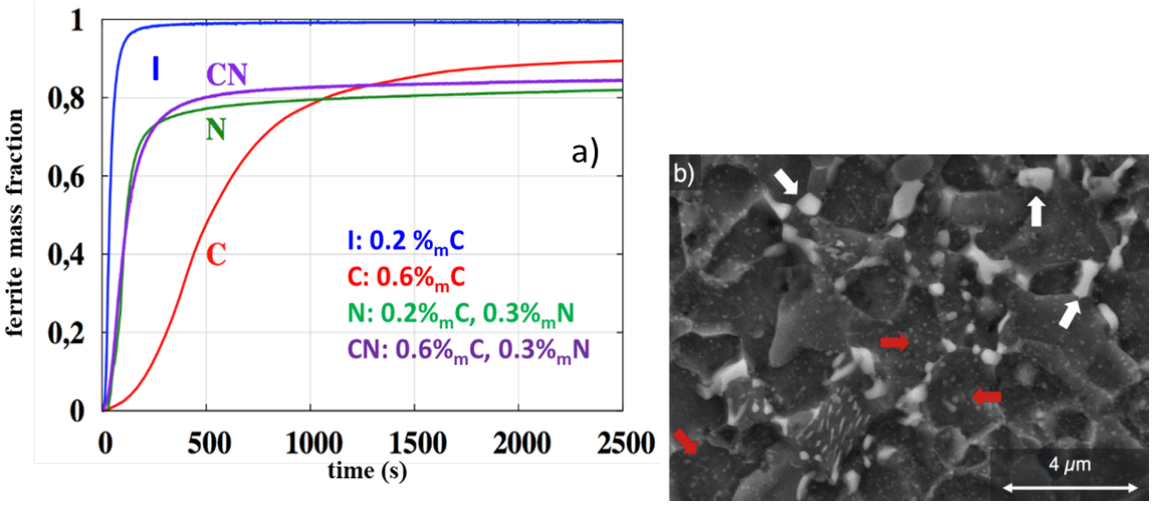

Figure III.2: a) Isothermal transformation kinetics established by HEXRD in I, C, N and C+N steels at 400°C (directly reproduced from [92]). b) SEM micrograph (SE) of the High Temperature Constituent obtained in nitrided steel after 3h isothermal hold at 650°C.

III.2 Experimental

In this section, we present the gradient samples which will be considered in this chapter, as well as the thermal treatments investigated. The experimental methods related to electron microscopy, hardness measurements, and *in-situ* High Energy Diffraction experiments have been presented in Chapter II.

The purpose of the gradient samples is to investigate the influence of carbon and/or nitrogen composition gradients, primarily on the formation of internal/residual stresses, as a consequence of the different local transformation kinetics and of the different phase transformation strains throughout the sample thickness. Our analysis will be based on our previous studies of phase transformations inside homogeneous samples, summarized in the previous section. The microstructures resulting from austenite decomposition will also be examined in the gradient samples.

In line with the previous studies on homogeneous samples, three types of enrichment are considered for the gradient samples: carburized, nitrided, and carbonitrided, as shown in Figure III.3. These composition profiles will be presented in more detail in the next section. The profiles have been designed to be representative of industrial treatments, and the compositions correspond to those of the homogeneous samples (Table III.1). The main features are a surface composition of 0.6wt.%C and 0.4wt.%N in the case of carbon and nitrogen enrichment and a depth of enrichment of about 1 mm and 0.5 mm for carbon and nitrogen, respectively.

Different thermal cooling laws are considered in order to make vary the nature of the austenite decomposition products and the chronology of the phase transformations

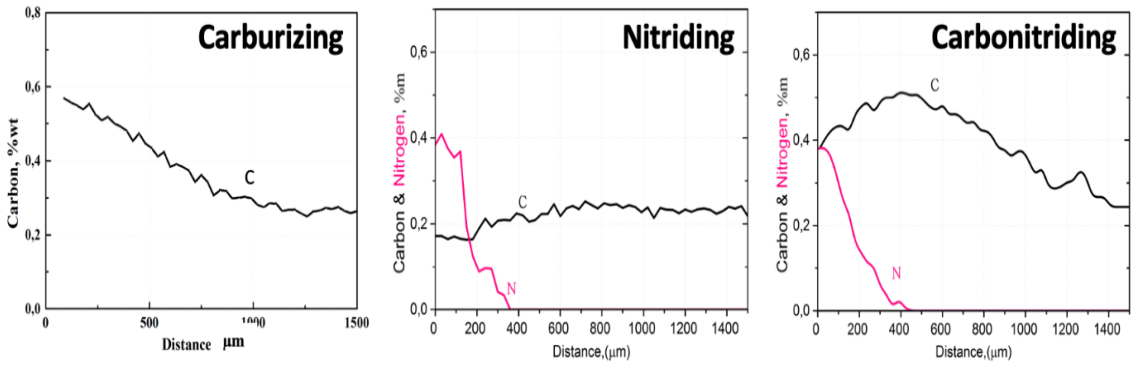

Figure III.3: Profiles of composition in carbon and nitrogen measured by EPMA in carburized, nitrided and carbonitrided gradient samples. (Representation limited to samples' half thickness).

throughout the sample thickness and to see the consequences on the formation of internal stresses. The HEXRD experiments were carried out in three stages, as schematized in Figure III.4:

- After the enrichment treatment at 900°C followed by cooling for *ex situ* analysis, two cooling laws are considered: cooling in air or quenching into the cold oil. The measured temperature evolutions are plotted in Figure III.4b.
- During cooling after re-austenitization at 900°C for 10 min, inside the mobile furnace presented in Chapter II, for the *in-situ* analysis. The samples are cooled at a controlled rate of 2°C/s down to 500°C (regulation by controlling the power of the lamps), followed by gas blowing (Figure III.4b). The *in- situ* experiments were stopped when the sample temperature reached 80°C. Before re-austenitization, the samples were quenched, after enrichment, into cold oil.
- After the *in-situ* experiments, the samples were examined thoroughly *ex situ* by HEXRD for a precise determination of residual stresses and phases' fractions.

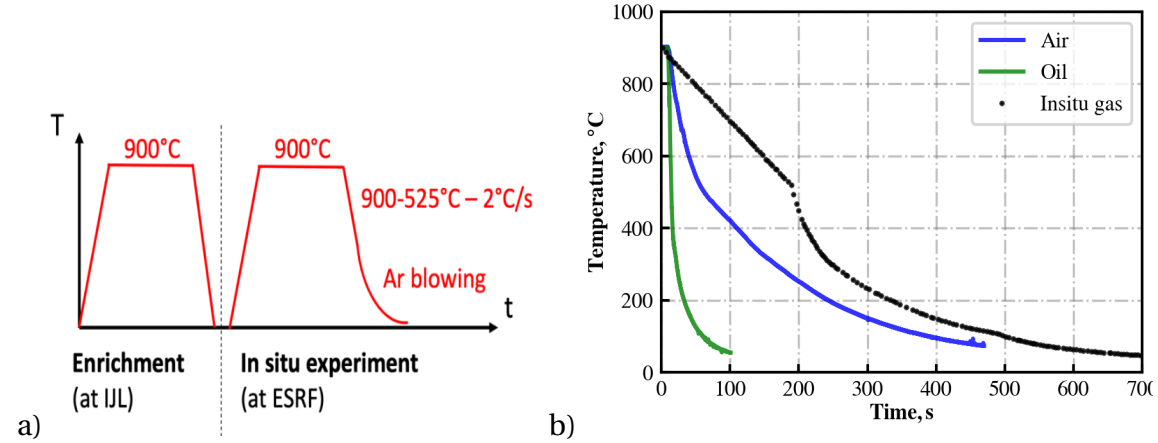

Figure III.4: a) Schematic of thermal treatments investigated. b) Measured temperature evolutions during cooling in air and quench into cold oil right after enrichment at 900°C or during the in-situ experiment.

III.3 Carburized specimen

In this part, the carbon composition of the gradient samples measured by EPMA will be presented first before showing the results regarding the phase transformation kinetics

and, finally, the internal stress evolutions. In both latter parts, the results of *in-situ* and *ex situ* experiments will be presented together, and the effect of the cooling rate will be analyzed. As carburizing treatments have been investigated in previous experimental and simulation works [25] these experiments give the possibility to assess our new experimental method based on *in-situ* HEXRD, as will be seen in the following.

III.3.1 Composition profile

Figure III.5 shows three carbon composition profiles established by EPMA on a carburized gradient sample, after enrichment at 900°C and oil quench. The profiles were measured through the thickness (ca. 3.1 mm) at three different positions of the lamellar sample (see Figure II.7). These profiles are in agreement with the ones targeted for the study: the center kept the composition of the initial steel (0.25wt.%C) and the surface composition ranges between ca. 0.45 and 0.65wt.%C. The depth of enrichment is about 1 mm. However, one can see that the three profiles are not identical. For one given position, the measured values can be scattered over a range of up to ca. 0.15wt.%C, especially near the surface of the right-hand side. This non-perfect distribution of carbon concentrations at the scale of the gradient sample (of dimensions 40x15x3.1 mm^3) will be considered in the following when interpreting the phase transformation kinetics and the stresses evolutions. Another heterogeneity of the sample regards the shape of the composition profile near the surface. The three profiles show steep gradients on the left-hand side, whereas flatter profiles are observed on the right-hand side. One of the profiles even suggests a decrease of the carbon content near the surface.

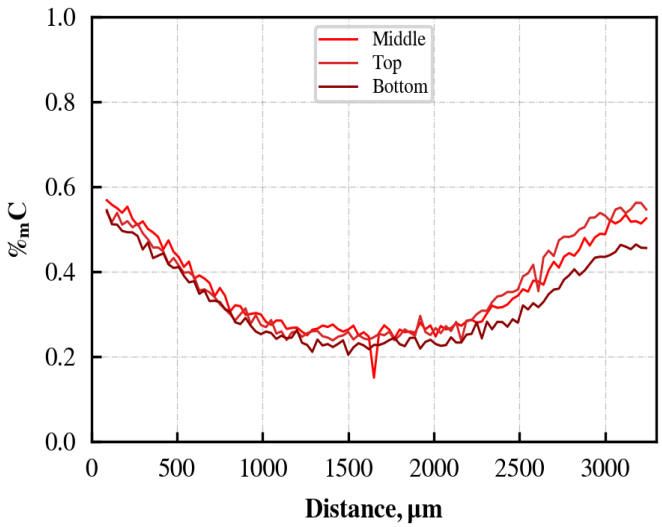

Figure III.5: Three carbon composition profiles along the thickness of a carburized gradient sample obtained by EPMA and at three different positions.

III.3.2 Phase transformation kinetics

The evolutions of α/α' phase mass fractions inside the carburized gradient sample are presented in Figure III.6a as a function of the temperature. For clarity reasons, only four positions inside the enriched case are presented. These positions are indicated with respect to the depth and the local carbon composition. During cooling, the austenite starts to decompose firstly in the core at 600°C because of the lower carbon concentration. The regions closer to the surface transform in later stages, because of the higher carbon concentration. In the center of the sample (depth 1.2 mm, blue curve), the different stages of the austenite decomposition are visible: formation of proeutectoid ferrite above Bs, then bainite transformation starting at about 450°C and martensitic transformation

starting at 330°C. The Ms of the steel with initial carbon composition is actually equal to 385°C (Table III.1) [3]. The decrease of the actual Ms temperature comes from the prior formation of proeutectoid ferrite and bainite, which stabilized the austenite against the martensitic transformation. At depth 0.88 mm (grey curve) the sequence of bainite followed by martensite is also visible (Ms ca. 310°C). At depths 0.1 mm and 0.4 mm, the transformation is mostly martensitic.

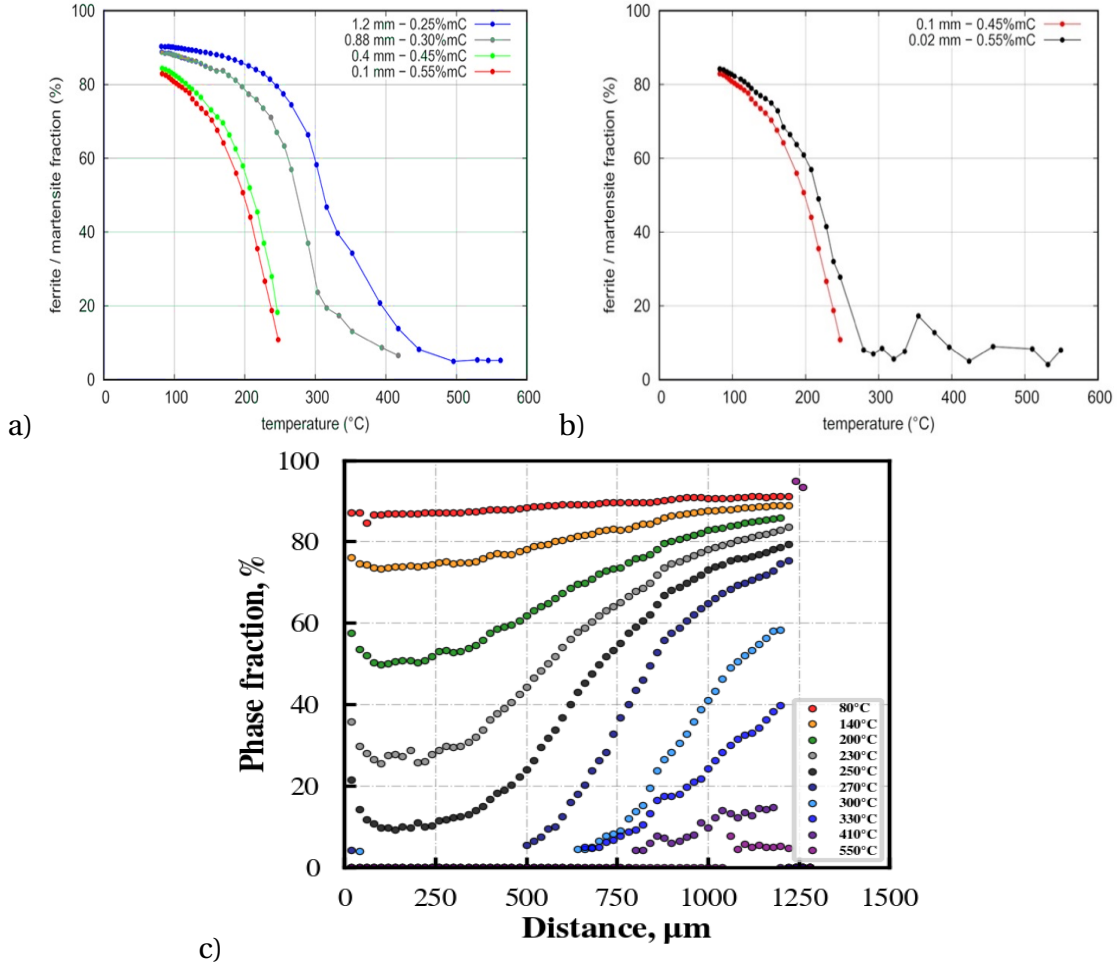

Figure III.6: Carburized gradient sample, in-situ experiment: austenite decomposition kinetics measured in-situ by HEXRD. Ferrite/martensite mass fraction: a,b) as a function of temperature at different depths; c) depth profiles (distance from the C-enriched surface) at different temperatures.

Figure III.6c shows profiles of α/α' fraction, which are plotted as a function of the depth under the surface, at different temperatures. These profiles are in agreement with the chronology mentioned above: the C-enriched surface transforms after the center. This chronology is the one expected, as it is known that for the investigated steel, enrichment in carbon leads to slower austenite transformation kinetics [3]. However, the profiles also show that the regions closest to the surface (depth lower than ca. 100 µm) transform faster than the regions underneath. For example, Figure III.6b compares the respective kinetics at depth 20 µm and 100 µm. The faster kinetics near the surface is unexpected, but it may be interpreted by considering the carbon profiles established by EPMA on the gradient samples (Figure III.5). The carbon concentration at 100 µm under the surface ranges between 0.45wt.%C and 0.65wt.C. Although these profiles were not established on the disc-shaped sample which served for the *in-situ* experiment, they show that, near the surface, the X-ray beam could cross regions of the sample which are heterogeneous in carbon concentration. Locally, the carbon content could be as low as 0.45wt.% which would explain the phase transformation starting earlier than in inner

regions. Another possible origin of the faster kinetics near the surface could be the effect of stresses on the phase transformation kinetics.

By interpreting the kinetics curves such as in Figure III.6a, it is possible to estimate (with some uncertainty though) the fraction of proeutectoid ferrite, bainite and martensite for each position in the composition profile. The corresponding profiles are plotted in Figure III.7a, while Figure III.7b shows the profile of hardness and recalls the carbon composition profile. The fraction of austenite at room temperature was measured by XRD. At room temperature, the final microstructure consists mostly of martensite in carbon-enriched regions with a small amount of retained austenite (maximum 10% at the surface). Hardness is about 780 $HV_{0.3}$ at the surface, which is in agreement with the local carbon concentration of 0.55%$_m$ and with a martensitic microstructure. Below the carbon-enriched case, the microstructure is a mixture of bainite and martensite and the fraction of bainite increases with the depth. Near the center, between a depth of 1 mm and 1.2 mm, there is up to 10% of proeutectoid ferrite. The hardness in the center is equal to 400 $HV_{0.3}$, which is consistent with the estimated composition of the microstructure. Let us mention that no microstructural observations were carried out to confirm or not the presence of proeutectoid ferrite.

It is also possible to plot the Ms temperature as a function of the depth. The experimental profile of Ms is plotted in Figure III.8. As expected, the Ms temperature decreases when approaching the surface, because of the higher carbon concentration. The figure also shows the Ms value expected as a function of the local concentration in carbon. It was calculated with our empirical formula (Eqn. III.1).

$$\mathrm{Ms}(\%\mathrm{C}) = 390 - 492 \times (\%\mathrm{C} - 0.25) \tag{III.1}$$

It can be seen that, except near the surface, the accounting of the carbon content is not sufficient to interpret the variations of Ms. One should also consider the effect of prior bainite transformation on the stabilization of austenite against the martensitic transformation. To this aim, we used our empirical formula (Eqn. III.2).

$$\Delta\mathrm{Ms}(\%\mathrm{C}) = \{ \begin{matrix} -168.8 \times y_b & .....y_b < 60\% \\ -205 + 507.4 \times y_b & .....y_b > 60\% \end{matrix} \} \tag{III.2}$$

The corresponding curve is plotted in Figure III.8. One can see that important discrepancies of about 40°C remain, except near the surface and in the center. This can be ascribed to the lack of precision in the determination of the bainite fraction and the accuracy of our empirical formula. Another origin of the discrepancies could be the effect of stresses on the martensitic transformation.

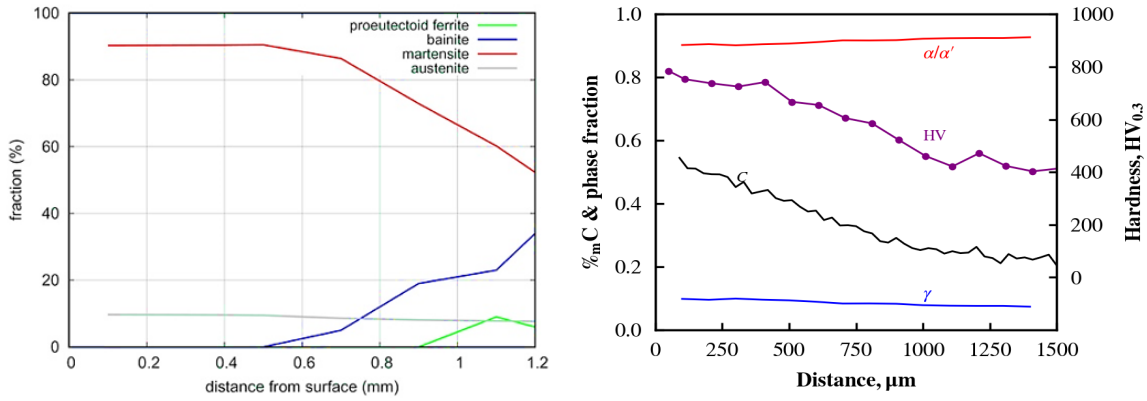

Figure III.7: Carburized gradient sample, in-situ experiment. Profiles at the end of the cooling of: a) fraction of austenite phase and austenite decomposition products (proeutectoid ferrite, bainite, martensite). b) α/α' phases mass fractions measured by XRD and hardness, along with the carbon composition.

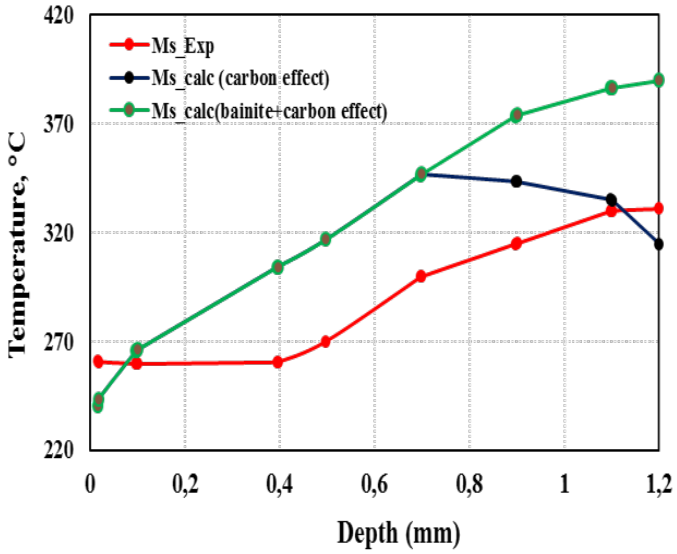

Figure III.8: Profile of Ms temperature according to the experiments, calculated as a function of the carbon concentration according to empirical formula Eqn. III.1, and with the accounting of the effect of prior formation of bainite (Eqn. III.2).

Figure III.9 shows the profiles of hardness and phase fraction (α/α', γ) for a similar carburized gradient sample, but for which the measurements were done after enrichment at 900°C and quench into oil. Hence, the cooling was faster than the one applied during the *in-situ* experiment. As will be seen in the simulations of phase transformations (Section IV.2.2), one expects a full martensitic microstructure throughout the thickness of the sample. Regarding the austenite fraction, the presence of austenite in the center of the sample (ca. 5%) is unexpected in view of previous experiments on dilatometry samples [3] which showed that for the corresponding carbon composition (the one of the initial steel, 0.25wt.%C), one should expect a full martensitic transformation, without residual austenite. The presence of residual austenite may be ascribed to the cooling slower during the quench into cold oil than during the dilatometry experiment (gas blowing), which could have favored austenite stabilization.

The hardnesses measured for this sample are in good agreement with a microstructure composed mostly of martensite. A hardness of about 800 $HV_{0.3}$ is indeed expected near the surfaces enriched to about 0.6 wt.%C (see Figure III.9). In the center, the hardness measured (ca. 500 $HV_{0.3}$) is also in good agreement with the value expected for a martensitic microstructure with the initial steel composition. One can see that the hardness decreases near both surfaces of the sample. This comes in part from the increase of the retained austenite fraction when approaching the surface. But this may also be ascribed again to the heterogeneities in carbon concentration established near the surface by EPMA (Figure III.5), as discussed above. Figure III.9 shows also hardness profiles established at different positions of the lamellar gradient sample. It can be seen that the hardnesses present some scatter (up to ca. 100 $HV_{0.3}$) which can be ascribed to the scatter in carbon concentration, whose range is about 0.1wt.%C (see e.g.Figure III.9).

III.3.3 Internal stress evolutions

As mentioned in Chapter II, the method used to determine the stresses by HEXRD allows to obtain the difference between the tangential stress and the axial stress, which is averaged inside the volume sample by the beam. Hereafter, this stress difference will be referred to as 'the stress'. Due to experimental difficulties, it was not possible to determine the stresses in the austenite phase with the same accuracy as in α/α' phases. Also, reliable data could be obtained only below ca. 350°C in the latter phase. Hence, we will present

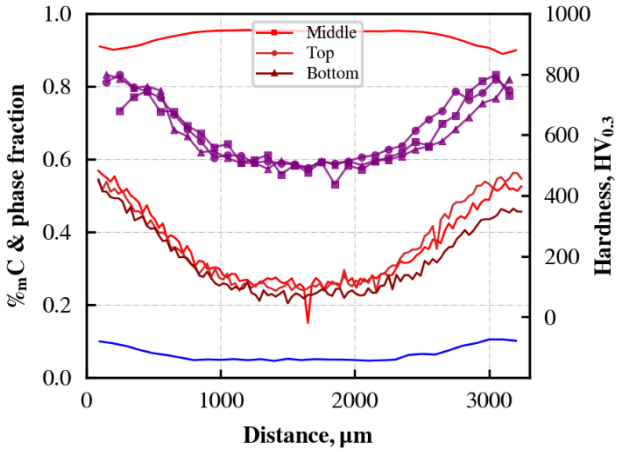

Figure III.9: Carburized gradient sample after enrichment at 900°C and quench into cold oil: profiles of α/α' and γ mass fraction measured by XRD, of hardness and of carbon concentration.

only the stresses evolutions which occurred in α/α' and in this temperature range.

The evolution of the stress inside the α/α' phases is plotted in Figure III.10a as a function of the temperature, at four representative positions (depth under the surface) of the gradient sample. At the centre (blue curve), the α/α' phase goes first into compression, because of the volume expansion associated with the phase transformation. These evolutions are similar farther from the centre (grey curve). The regions closer to the surface transform later, because of the higher carbon concentration. When these regions undergo the martensitic transformation, a compressive stress state is established in martensite (red and green curves). To maintain the mechanical equilibrium, the inner regions go into tension.

Figure III.10b and III.10c show stress profiles in α/α' phases at four different temperatures. At 330°C and 265°C, all the α/α' phase present in the sample is under compression. This is due to the phase transformation strain. The curves corresponding to temperatures 215°C and 85°C confirm that once the regions near the edge undergo a martensitic transformation, a profile of stresses with compression near the surface and tension in the centre, is generated. The magnitude of the stresses increases during the cooling. This is due to the progression of the phase transformation, mostly near the surface, under 215°C.

Figure III.10d shows the profiles of residual stresses determined at room temperature in α/α' and γ phases. A rotation of 90° was applied to the disc-shaped sample around its axis, in order to check the cylindrical symmetry of the stress distribution. The corresponding curves are nearly superposed, which confirms (partly, at least) that the stresses are distributed following an axial symmetry. The profile of residual stresses in α/α' phases is close to the one established at 85°C, with a slightly higher magnitude of the stresses for the latter temperature.

The residual stresses in the γ phase are lower than in the α/α' phases. The formation of the residual stresses in austenite is more difficult to interpret in the absence of reliable data coming from the *in-situ* experiment for this phase. The behavior of the two/three-phases α/α'+γ the material should also be considered (e.g. [92]). At room temperature, the fraction of γ phase is lower than 10%. Hence, the macroscopic stress (the average among the phases) is nearly equal to the one in the α/α' phase. As classically observed in the framework of carburizing [25], the residual stresses are compressive near the surface and tensile near the centre. (The compressive stress is maximum below the surface for carbon content of about 0.4%$_m$). This distribution of the stresses is due in large part to the chronology of the phase transformations taking place throughout the gradient sample, with the centre transforming first, followed by the surface. This will be discussed more in the simulation section.

One can see that the magnitude of the compressive residual stresses decreases when

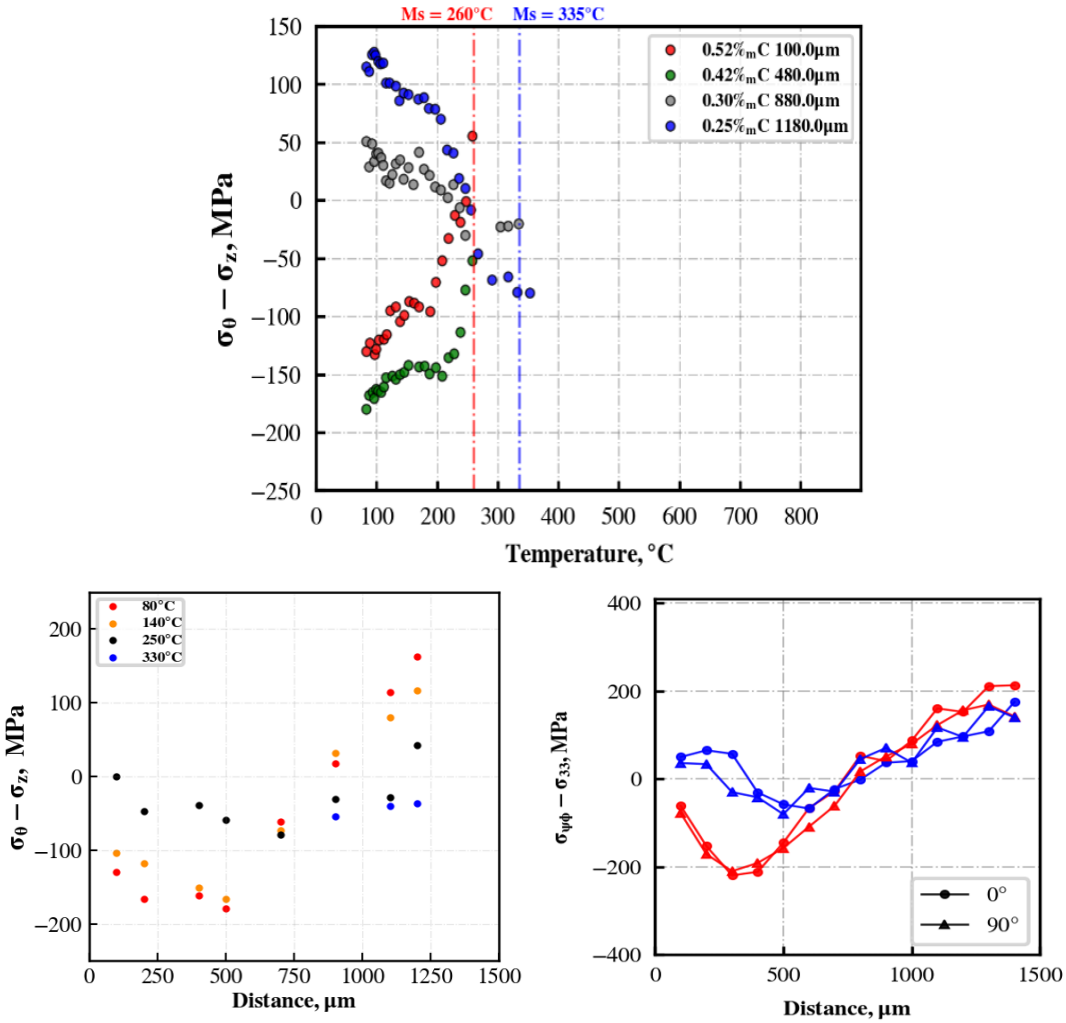

Figure III.10: Carburized gradient specimen, in-situ experiment. a) Evolution of the stress in α/α' phases as a function of the temperature at four different positions in the gradient sample. b) Profiles of the stress in α/α' at different temperatures. c) Profiles of residual stress in α/α' and γ phases, at room temperature after the cooling and for two rotations of the disc-shaped sample around its axis.

approaching the surface. This may be ascribed first to the increase of the fraction of residual austenite near the surface (Figure III.9), which means that less martensite has formed, thereby reducing the volumic expansion. Another origin can be the faster phase transformations which occurred close to the surface, as shown in previous section. This modified chronology could have drastic consequences on the formation of residual stresses.

Figure III.11 shows the profile of residual stresses established by HEXRD in another carburized gradient sample, after enrichment at 900°C and quench into oil. Compared to the *in-situ* experiment (with lower cooling rate) the residual stress in α/α' is higher beneath the surface and lower in the centre. The magnitude of the compressive residual stress in α/α' decreases when approaching the surface, as it was also the case for the *in-situ* experiment. The austenite phase shows high tensile stresses (about 300 MPa) near the surface, whereas it was not the case for the *in-situ* experiment. Let us mention that the residual stress in α/α' at the surface was also determined by laboratory XRD (Chapter II). This stress can be compared to the stress difference plotted in Figure III.11. A value of -167 MPa was determined, which is close to the result from HEXRD.

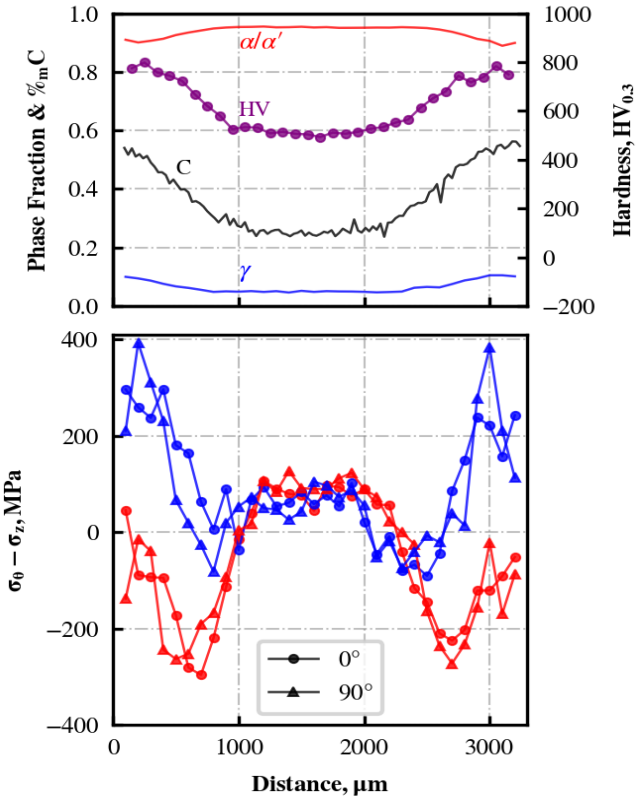

Figure III.11: Profiles of residual stress difference established by HEXRD in a carburized gradient sample, after enrichment at 900°C and quench into oil.

III.4 Nitrogen-enriched gradient specimens

This part focuses on the effects of enrichment in nitrogen, by considering the nitrided and carbonitrided composition gradient samples. After having presented the C, N concentration profiles established by EPMA on both samples, a second part will focus on the microstructural gradient which was observed in the carbonitrided sample after enrichment followed by cooling in air. As will be seen, unusual gradients of microstructure will be obtained, because of the effects of N enrichment on austenite decomposition recalled in Section III.2. This will help to better understand the results related to different cooling rates and to stresses evolution presented in third part for the nitrided specimen and in fourth part for the carbonitrided specimen.

III.4.1 Composition profiles

Figure III.12 shows the carbon and nitrogen composition profiles established by EPMA in the nitrided gradient sample (after oil quench). One single profile was established for this sample along its thickness, 3.1 mm. Hence, its homogeneity along its length was not verified, contrary to the case of the carburized gradient specimen (Section III.3.1). At both edges, the maximum nitrogen concentration is about 0.4 wt.% and the depth of enrichment is about 400 µm. Some decarburization occurred, mostly in the nitrogen-enriched cases, but also underneath (depth down to ca. 600 µm). The carbon concentration decreased down to about 0.1 wt.% at the surface on the right-hand side. In the centre, the sample kept the carbon concentration of the initial steel, 0.25 wt.%.

Composition profiles were measured by EPMA inside two carbonitrided specimens. The first one underwent a quench into oil after enrichment, whereas the second one was air-cooled and also served for the *in-situ* experiment. Composition profiles of carbonitrided air cooled specimen is shown (Figure III.13), and composition profiles of oil quench specimen is also similar. Some decarburization occurred during the enrichment,

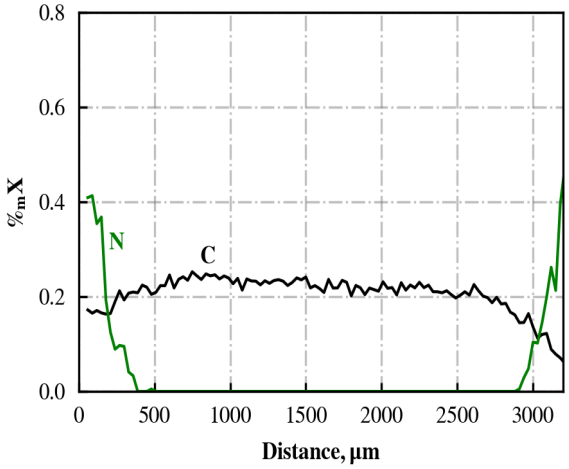

Figure III.12: Carbon and nitrogen composition profile in the nitrided gradient sample (oil quench).

leading to a maximum carbon concentration of 0.5%m at a depth of 400 µm. The centre of the samples kept the carbon composition of the initial steel. The depth of the nitrogen-enriched layer is about 0.5 mm and the concentration of nitrogen at the surface is in the range 0.4-0.6 wt.%N. One can see significant differences in the concentrations between both profiles. For example, the maximum carbon concentration (at about 400 µm) depth ranges between 0.4wt.% and 0.55wt.%. These differences among two lamellar samples suggest that similar spread of the composition profiles may exist inside the cylindrical samples which were used for the HEXRD experiments, as it was also the case of the carburized specimens (Section III.3.1).

III.4.2 Influence of nitrogen enrichment on the microstructure profile after cooling in air of a carbonitrided gradient specimen

The carbonitrided gradient sample cooled in air is considered here to illustrate the effects of a nitrogen enrichment on the microstructure profile. The corresponding composition profile is presented in Figure III.13b. The microstructure profile differs strongly from the more classical case of a carburized specimen which would have underwent the same cooling. Most important difference concerns the N-enriched case. At 100 µm under the surface (Figure III.13a), the microstructure contains a majority of HTC (Section III.1). It consists of a majority of equiaxed ferrite grains with less than 5 µm size. The bright contrast in the SEM micrograph corresponds to CrN nitrides with different morphologies: cuboidal/spheroidal (arrowed A, B) or lamellar (C) inside the ferrite grains [3]. The former morphology corresponds to CrN nitrides which were formed during the enrichment treatment. The latter forms together with the ferrite transformation. TEM observations also revealed the presence of nano-sized coherent precipitates inside the ferrite grains, which increase the hardness. According to the EBSD phase map (Figure III.13b), smaller ferrite grains are also present; these may have formed under the Bs temperature. A significant amount of blocky retained austenite is also detected, in agreement with the HEXRD measurements (Figure III.13f).

Below the N-enriched case at 700 µm depth (Figure III.13c), there is a mixture of bainite and martensite. The amount of the latter decreases towards the core of the sample where more (coarser) bainite is formed (Figure III.13d), due to the lower C concentration. The amount of retained austenite ranges from ca. 30% at the surface to 10% in the core according to *ex-situ* HEXRD. Three zones can thus be distinguished in the case, as illustrated by the hardness profiles: hardness decreases towards the surface with increasing N content, it is maximum beneath the N-enriched layer, where C content and martensite fraction are the highest and it decreases towards the center.

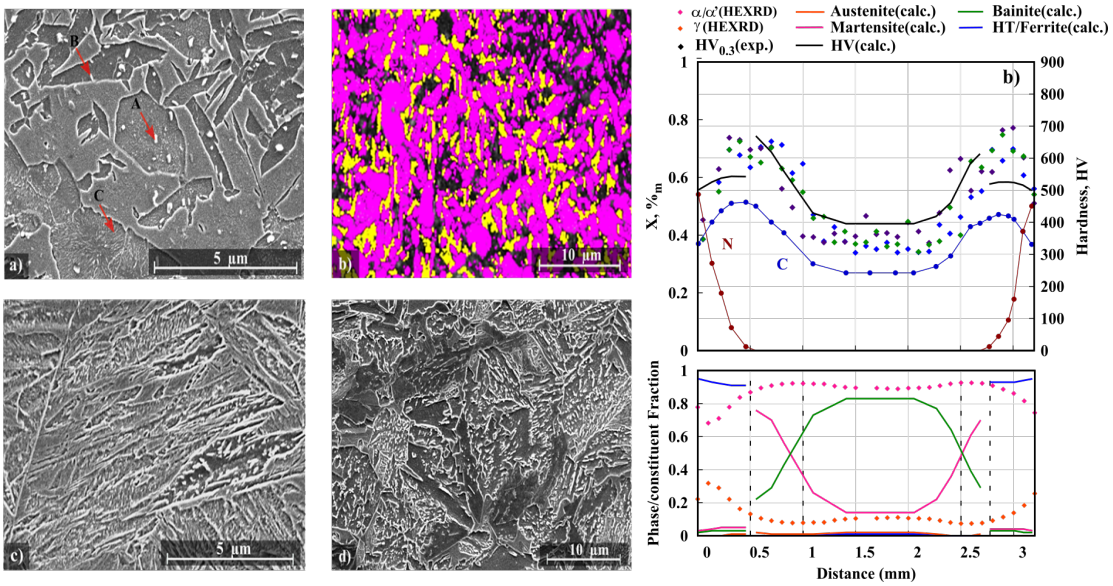

Figure III.13: Air-cooled carbonitrided gradient sample. a-b-c-d) Microstructural observations at various depths below the surface. a-b) at 100 µm by SEM and by EBSD (phase identification with ferrite in pink and retained austenite in yellow); c) at 700 µm; d) in the center. e) Carbon and nitrogen concentration profiles and hardness profiles (solid black line: calculation; points: measurements according to three profiles spaced 7 mm apart, each represented by a color code). f) Calculated phase/constituent fractions and experiment (HEXRD: retained austenite or phases identified as cubic centered: ferrite, bainitic ferrite or martensite).

In addition to modifying the microstructure profile, the enrichment in nitrogen modifies the chronology of the phase transformations throughout the case. From previous works, it is known that an enrichment in nitrogen induces a strong acceleration of the isothermal austenite decomposition kinetics, [3, 4, 106], Section III.1. Hence, contrary to an enrichment in carbon, an enrichment in nitrogen leads to a strong loss of hardenability near the surface, which will tend to transform at first (instead of at last, in more usual cases). In next sections, the consequences on microstructural and internal stresses evolutions will be examined *in-situ*. The comparison with calculated results will be discussed in Chapter IV .

III.4.3 Nitrided gradient specimen: *in-situ* phase transformation kinetics

As explained in Chapter II, the presence of bright spots at high temperature in the recorded 2D diffraction patterns (Debye-Scherrer rings) prevented their analysis to determine the phase transformation kinetics, as well as the stresses. Compared to the carburized specimen, an additional issue was the probable loss of stability of the austenite grains during the austenitization at 900°C. As a result, the recorded diffraction patterns were not exploitable above 275°C for the nitrided specimen. At this temperature, the austenite decomposition was already well underway throughout the thickness of the sample, as will be seen.

Figure III.14a shows the kinetics of austenite decomposition in the nitrided specimen established *in-situ* by HEXRD. The α/α' mass fraction is plotted as a function of temperature at four representative points located at depths 100 µm, 280 µm, 380 µm and 990 µm. Although only the last stages of the austenite decomposition are visible, these curves provide an overview of the chronology of the phase transformations inside the nitrided gradient sample. It can be seen that the point closest to surface transformed at first, followed by the regions underneath. The profiles of α/α' mass fraction plotted in

Figure III.14b confirm this chronology, characterized by the surface transforming at first. As mentioned above, the fast decomposition of austenite near the surface is ascribed to the presence of nitrogen and to the presence of CrN nitrides which precipitated during the enrichment. These nitrides would stimulate the formation of ferrite.

Under the nitrogen-enriched case (below ca. 400 µm), the fraction of α/α' phases is nearly uniform, as expected because of the homogeneous carbon concentration. Indeed, one can expect that the austenite decomposition kinetics was uniform, if one neglects possible effects of stresses on the phase transformation kinetics. Nevertheless, in the profile at 275°C, the fraction of α/α' is lower between ca. 200 µm and 400 µm. This may be due to the fact that in this region, the nitrogen concentration was too low to trigger the effects of nitrogen accelerating the austenite decomposition. Indeed, from previous work, it is thought that these effects only exist when CrN nitrides precipitate during the enrichment at 900°C. These nitrides may be absent in this region, because the nitrogen concentration was below its solubility limit with respect to the precipitation of CrN (0.1wt.%N) in austenite. On the other hand, the amount of interstitial elements (C,N) is locally higher, which may have slowed down the austenite decomposition, according to the usual effect of the interstitials stabilizing the austenite.

Hence, in the nitrided sample, the chronology is reversed compared to the usual one associated with carburizing (core followed by surface). The surface (down to 200 µm) transforms first due to the concentration of N higher than 0.1%mN. The core (below ca. 400 µm) transforms in second and finally the intermediate region, which transforms at last, because it has the highest amount of interstitial elements, but without CrN nitrides. But this latter region is actually not clearly put into evidence.

The profile of γ and α/α' phases at the end of the cooling is shown in Figure III.15a. The fraction of austenite is lower in the N-enriched case, which indicates that the austenite may have decomposed at high temperature (above Bs). The hardness close to the surface is lower than 300 $HV_{0.3}$, which is in agreement with the formation of the "High Temperature Constituent" (Section III.1), above Bs. In the centre, the fraction of austenite is higher, which means that bainite and/or martensitic transformations occurred. Accordingly, the hardness in the centre (ca. 400 $HV_{0.3}$) is in agreement with a martensitic microstructure for the base steel, or to bainite formed at low temperature. In the intermediate region, the hardness is slightly higher, which may be ascribed to the formation of bainite/martensite, in presence of higher concentration of interstitial elements than in the centre.

This envisaged profile of microstructure (which could not be assessed by microstructural observations) has to be considered with care, because of the lack of exploitable experimental data at high temperature during the *in-situ* experiment. Due to this lack of data, the exact temperature range at which the phase transformations occurred is unknown. The simulations of phase transformations in Chapter 4 will help to clarify what is the probable profile of microstructure in this specimen.

Figure III.15c also shows the hardness profile obtained in another nitrided gradient specimen enriched in the same conditions, but after quench into cold oil, hence after faster cooling than during the *in-situ* experiment. (For this specimen, the profile of α/α' and γ phases fractions was not established by HEXRD). The microstructure consists of a mixture of bainite and martensite in the N-enriched layer (Figure III.15b) and mostly martensite in the non- enriched area (0.245%mC), in view of the measured hardness. The hardness is uniform in the non-enriched area, and it slightly increases with the nitrogen content towards the surface of the specimen. One can notice that this increase of hardness is much smaller as compared to carburized gradient sample (Figure III.11), mainly because of a decrease in carbon content and the presence of bainite. Hence, it is shown that nitriding is less efficient than carburizing in terms of surface hardening.

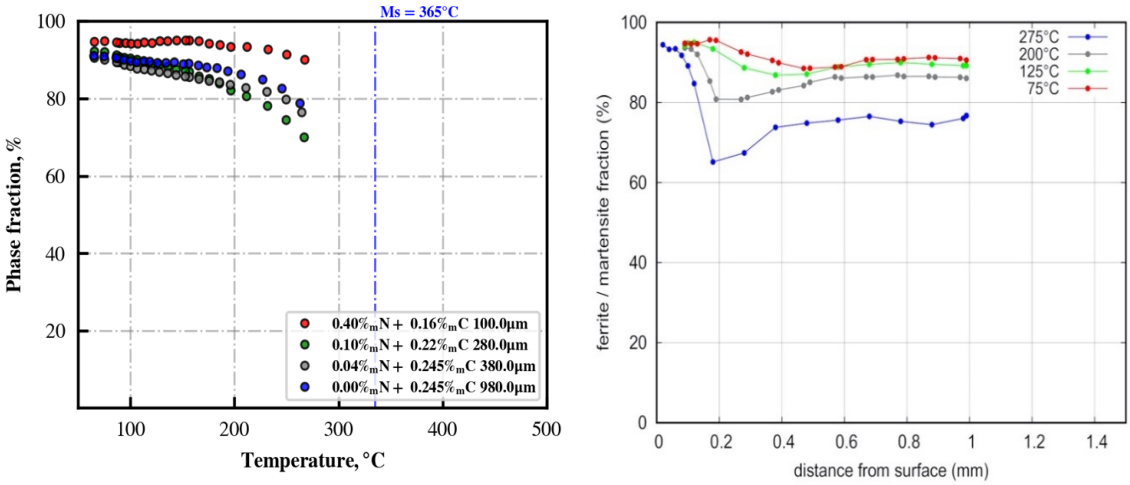

Figure III.14: Nitrided gradient specimen, in-situ experiment: austenite decomposition kinetics measured in-situ by HEXRD. Ferrite/martensite mass fraction: a) as a function of temperature at different depths; b) profiles along the sample thickness (distance from the C-enriched surface) at different temperatures.

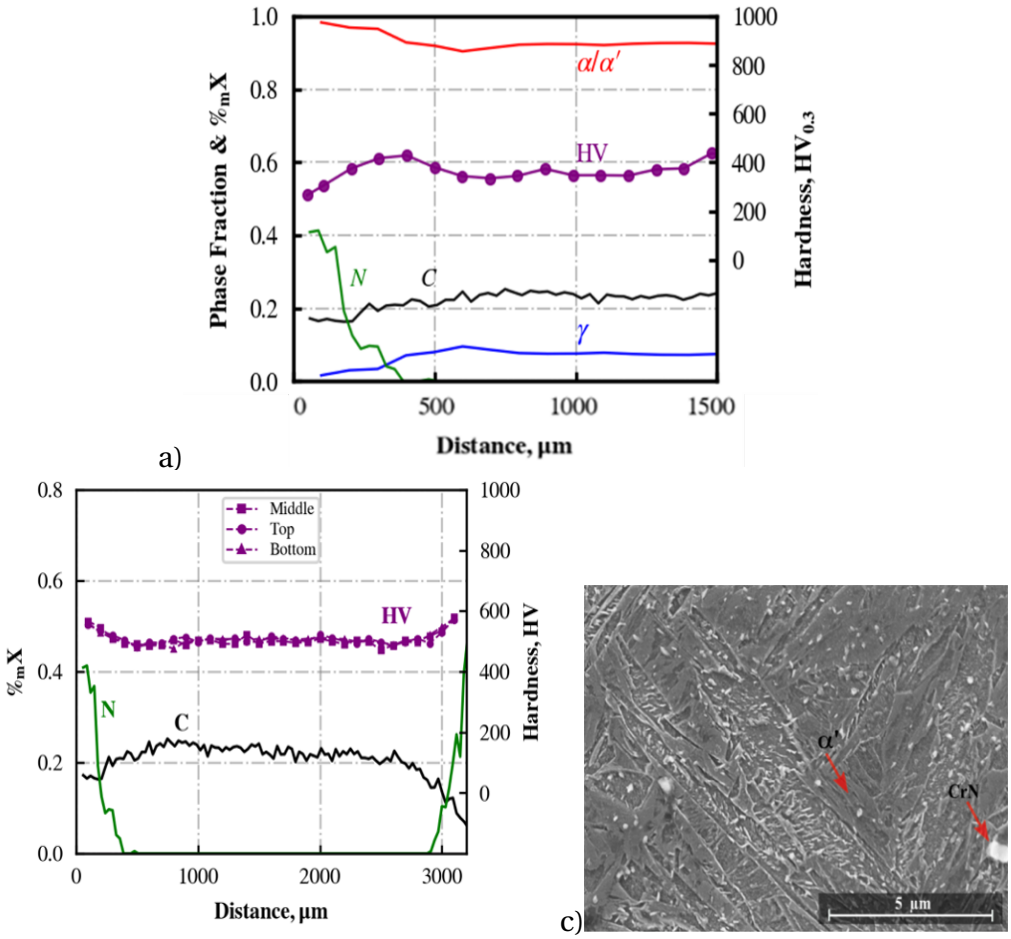

Figure III.15: Nitrided gradient specimen, profiles of α/α' and γ mass fraction measured by XRD, of hardness and of carbon concentration a) in-situ experiment. profiles at the end of the cooling, b) Microstructural observations below the surface at 100 µm by SEM c) sample after enrichment at 900°C and quench into cold oil.

III.4.4 Internal stress evolutions

Figure III.16a shows the evolution of the stress in α/α' phase as a function of the temperature established *in-situ* by HEXRD during the cooling of the nitrided gradient sample. Four representative points inside the sample are represented. Like for the phase transformation kinetics, the stresses could not be determined above 275°C. Despite this lack of data, one can clearly see the consequence of the modified chronology of the phase transformations in the presence of nitrogen: both points closest to the surface and located inside the nitrogen-enriched layer end up with tensile stress, instead of compressive stress which were obtained in the more classical case of carburized specimen (Section III.3.3). Inner points end with lower stress.

Figure III.16b shows the profiles of the stress in α/α' phase obtained at different temperatures. For all temperatures, the profiles show a similar shape: high tensile stress (up to 600 MPa) down to ca. 300 µm, low compressive stresses (less than 100 MPa) between 300 µm and 600 µm and low tensile stresses (less than 100 MPa) below 600 µm. This shape is directly related to the chronology of the austenite decomposition throughout the sample's thickness, which was mentioned in the previous section. The first region to transform (near the surface) has tensile stresses and the last (intermediate) has compression stresses. The profiles plotted in Figure III.16b show the end of the internal stress evolutions. At 275°C, the stress near the surface has not yet reached its final value, because a significant fraction of austenite has still not yet decomposed (see Figure III.14). In inner regions, the evolutions of the stress profile are less clear and remain inside the experimental uncertainty.

Figure III.16c shows the profiles of residual stresses at room temperature in the same sample, obtained by HEXRD in α/α' and γ phases. A rotation about 90° was done to check the homogeneity of the stresses, which is put into evidence by the good superposition of the curves. The residual stress profile of α/α' phase has an unusual shape with high tensile stresses near the surface. These are correlated with the nitrogen-enriched case. In this region, the austenite is also in tension. In the inner regions, the residual stress in α/α' phase is compressive over a larger depth than obtained during the *in-situ* experiments. The intermediate region (between depth ca. 400-600 µm) is again observable, having higher compressive stress. The residual stress in austenite is tensile throughout the thickness of the sample.

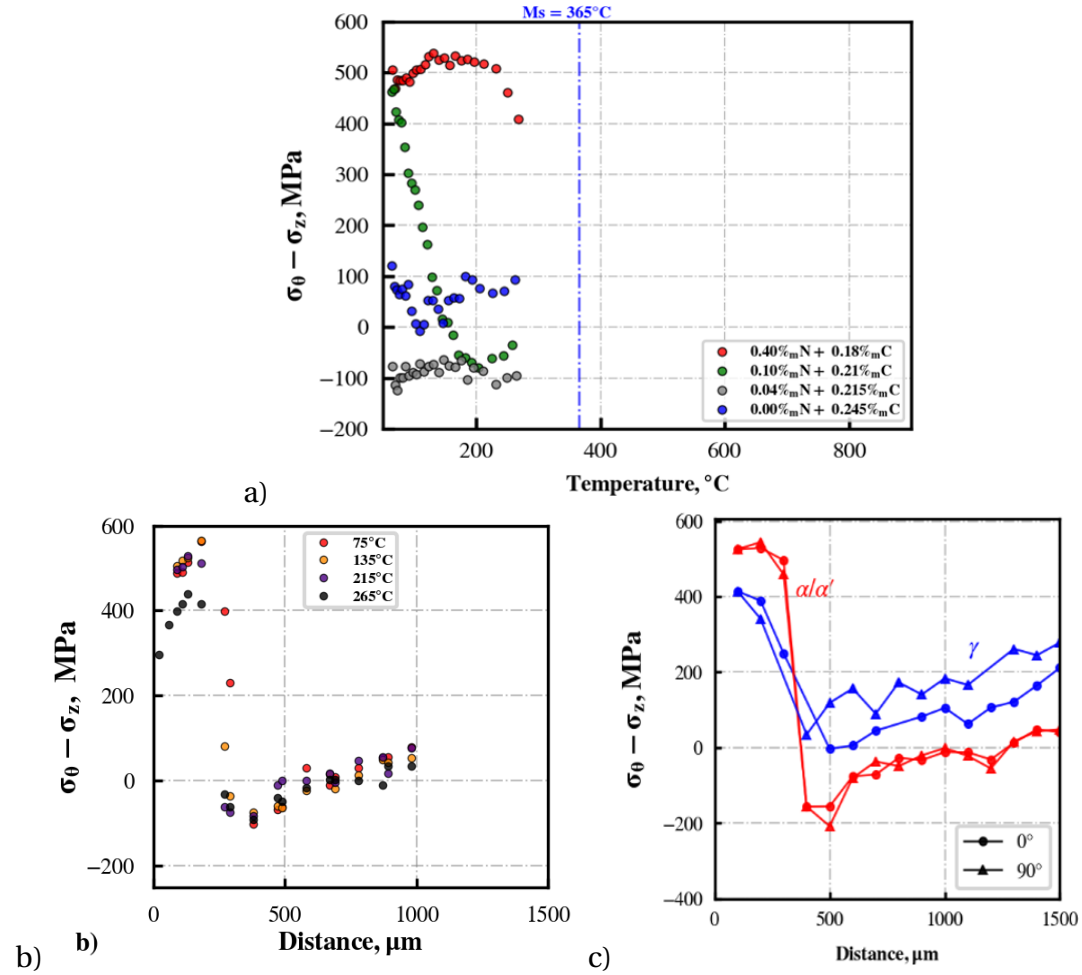

Figure III.16: Nitrided gradient specimen, in-situ experiment. a) Evolution of the stress in α/α' phases as a function of the temperature at four different positions in the gradient sample. b) Profiles of the stress in α/α' at different temperatures. c) Profiles of residual stress in α/α' and γ phases, at room temperature after the cooling and for two rotations of the disc-shaped sample around its axis.

III.5 Carbonitrided specimen

III.5.1 Phase transformation kinetics

The same experimental difficulties as for the nitrided sample prevented the complete *in-situ* monitoring of the α/α' and γ phase fractions and of the internal stresses. For the carbonitrided gradient sample, almost no experimental data could be recorded during the cooling. These evolutions are therefore not presented. A few successful acquisitions during cooling allowed, however, to obtain a partial view on the chronology of the phase transformations, but mostly inside the nitrogen-enriched case. Figure III.17 shows profiles of α/α' phase fraction which were obtained from the surface down to a depth of 0.6 mm, at temperatures 464°C and 593°C. The nitrogen-enriched case decomposed before the core of the sample, like for the nitrided sample, but the decomposition of the austenite started below the surface (at ca. 250 µm depth), followed by the surface and finally by the core. Hence, this chronology differs from the case of the nitrided sample, for which the surface transformed at first. The faster austenite decomposition at about 250 µm depth is unexpected in view of the measured C and N composition profiles. According to previous works (see Section III.1), the austenite closer to the surface should have decomposed faster, because the carbon and nitrogen concentrations are respectively lower and higher (Figure III.13b). One possible explanation could be that

the compositions in C and N which were measured by EPMA may not be representative of the actual ones in the carbonitrided sample used for the *in-situ* experiment. As shown by Figure III.13, the profiles of composition in C and N may differ from one sample to another.

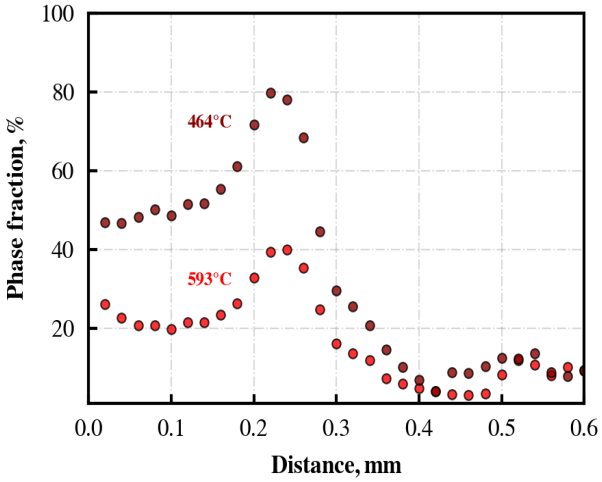

Figure III.17: Profiles of α/α' phase fraction from the surface up to a depth of 0.6 mm, obtained at 464 and 593°C.

Figure III.18a shows the profiles of α/α', γ and CrN phase fractions obtained at room temperature by HEXRD, after the *in-situ* experiment. In the nitrogen-enriched case (depth down to 500 µm), the fraction of austenite goes up to 20%. This suggests that a significant fraction of bainite and martensite formed in this region. According to the profiles in Figure III.17, the fraction of "High Temperature Constituent" (HTC) is about 40% in the nitrogen-enriched case (mostly down to 300 µm depth). Indeed, the Bs temperature is estimated to be in the range 400-500°C (Table **??**). The decomposition above Bs of the austenite is more pronounced at depth about 250 µm, which would explain the lower fraction of austenite. (As recalled in Section III.1, the HTC does not contain austenite). Below the nitrogen-enriched case, the fraction of austenite is nearly uniform. The CrN nitrides mass fraction could also be established inside the nitrogen-enriched case. These nitrides formed both during the prior enrichment treatment and during the decomposition of the austenite.

Figure III.18a also shows the profile of hardness. In the centre, where the gradient sample has the composition of the initial steel (0.25%mC), the hardness (400 HV) is consistent with a microstructure composed of martensite or bainite formed at low temperature. Under the N-enriched case, (ca. 600 µm depth), the hardness (ca. 700 HV) corresponds to a fully martensitic microstructure (plus residual austenite). Inside the nitrogen-enriched case, the hardness is about 800 HV at the bottom of the N-enriched layer and it decreases down to about 450 HV when approaching the edge. These values of hardness are consistent with the microstructure expected in this region of the gradient sample: a mixture of high-temperature constituent, bainite and martensite. The decrease of the hardness near the edge is due to the decrease of the carbon concentration, which makes decrease the hardness of all of these constituents (see Figure III.1). As for the effect of the nitrogen concentration on the hardness, it could not be established from previous works.

Hence the microstructural profile inside the carbonitrided gradient sample after the *in-situ* experiment is similar the one presented in Section III.4.2 after a cooling in air. One can identify three regions: the nitrogen-enriched case, which contains a mixture of martensite, bainite and high-temperature constituent, the region beneath (down to ca. 1 mm) inside which martensite is preponderant and finally the centre with possibly a mixture of bainite and martensite. There is residual austenite throughout the sample

thickness, with increasing amount when the austenite decomposed below Bs and when the C concentration is higher.

Figure III.18b shows the profiles of C, N composition, phase fraction and hardness inside a similar carbonitrided gradient sample, but after a faster quench into oil, applied directly after the enrichment. The values of the hardness show that the microstructure is fully martensitic throughout the thickness of the sample (with some residual austenite), except near the edges (depth ca. 250 µm), where the hardness decreases sharply. This is ascribed to the nitrogen which decreased the hardenability and to the decrease of the carbon concentration near the edges. The mass fraction of austenite ranges between 10% and 5% throughout the sample thickness. It increases when the carbon concentration increases, because of the variation of the Ms temperature. More complex variations occur in the nitrogen-enriched case, but a better knowledge of the microstructure in this part of the sample would be necessary for a complete interpretation.

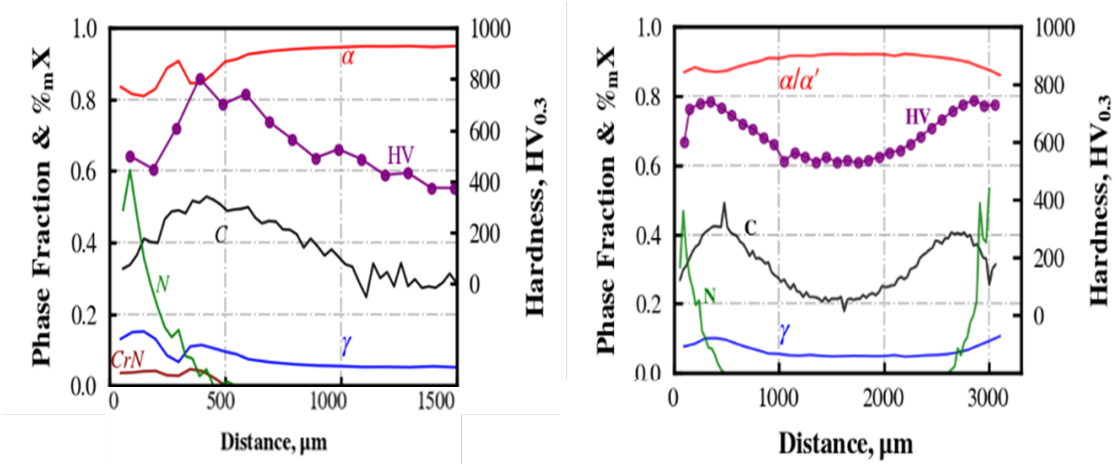

Figure III.18: Carbonitrided gradient samples. Profiles of phase mass fraction obtained by HEXRD at room temperature, of hardness and of composition in C and N. a) After in-situ experiment; b) after enrichment and quench into oil.

III.5.2 Internal stress evolutions

As mentioned in previous section, few acquisitions could be performed during the *in-situ* HEXRD experiment, for the carbonitrided gradient sample. Figure III.19a shows the stress profiles obtained in α/α' phase at 464°C and 593°C. Like for the phase transformations (previous section), these profiles are mostly focused in the N-enriched case. At 464°C, the α/α' phase undergoes low compression stress (less than -50 MPa or close to zero). This can be interpreted by the austenite decomposition which started earlier in the N-enriched case than in the regions beneath. The α/α' phase is under compression because of the phase transformation strains. At 593°C, the stress in α/α' phase is under tension, going from zero at the surface to ca. 110 MPa at depth 350 µm.

Let us mention that at both temperatures, there is still a significant fraction of austenite. The stresses could not be determined *in-situ* in the latter phase, which makes impossible a full interpretation of the stresses evolutions.

Residual stress profiles in α/α' phase and in γ phase are plotted in Figure III.19b. Like for the nitrided gradient sample, three regions can be identified regarding the α/α' phase: the N-enriched case with tensile stresses, the centre (below ca. 800 µm) with lower tensile stress and an intermediate region with compression stresses. As the α/α' phase is preponderant inside the whole sample, this gives an overview of the macroscopic stress. One can assume that a chronology of austenite decomposition similar to the one of the nitrided sample occurred: the N-enriched case, followed by the centre and finally the intermediate region, which is the richest in carbon and without the effects of nitrogen

on the loss of hardenability. Inside the N-enriched case, the stress profile now has a maximum (~ 300 MPa) at a depth which corresponds to the zone which transformed faster. As for the austenite, it shows tensile stresses throughout the thickness of the sample.

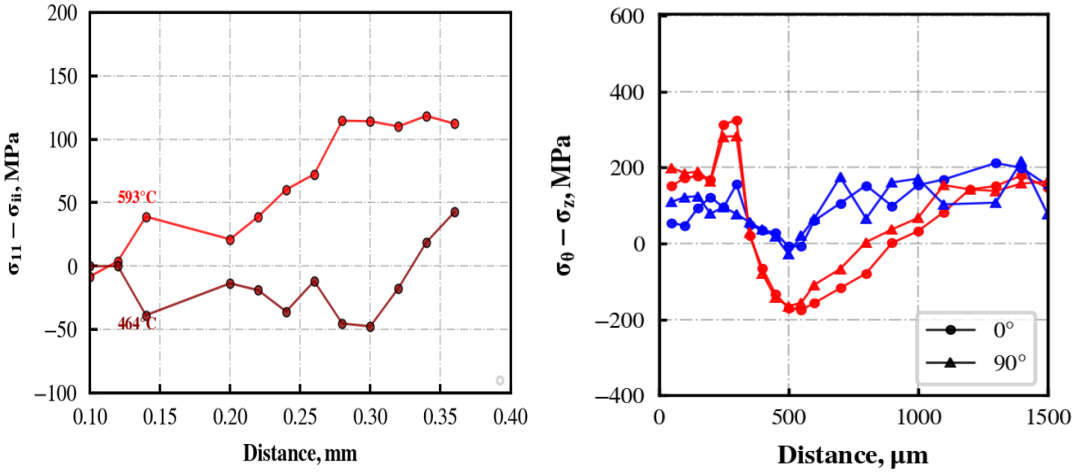

Figure III.19: Carbonitrided sample, in-situ HEXRD experiment. a) Profiles of the stress in α/α' phase obtained at 464°C and 593°C.b) residual stress profiles.

Figure III.20a shows the profile of residual stresses obtained by HEXRD in a similar carbonitrided sample, but after quench into oil following the enrichment treatment (faster cooling than for *in-situ* experiment). As mentioned in previous section, the microstructure is fully martensitic except in the N-enriched case (with less than ca. 15% austenite throughout the thickness of the sample). Like for the *in-situ* experiment, three regions can be identified in the "left part" of the sample: the N-enriched case with tensile stresses, the centre (below 1 mm) with tensile stress (up to 200 MPa) and an intermediate region with compressive stresses. Comparing this experiment with the *in-situ* experiment, main differences regard, first, the shape of the stress profile in the N-enriched case. There is no more a maximum under the surface (see Figure III.20), suggesting that in this sample and inside the N-enriched case, the surface transformed before the regions beneath. In the regions beneath the N-enriched case, the stresses in α/α' (tensile or compressive) are higher. This may be interpreted in part by the higher fraction of martensite, which has higher transformation strain than the bainite. The differences in phase transformation kinetics also come into play, but this cannot be interpreted without *in-situ* data.

Figure III.20b shows the profile of residual stresses obtained by HEXRD in a similar carbonitrided sample, but after cooling in air following the enrichment treatment. The cooling rate is intermediate between the quench into oil and the *in-situ* experiment (Figure III.4). The same three regions as in both previous carbonitrided gradient samples are identified in the stress profile (N-enriched case, the region underneath and the centre). The microstructure present in each of these regions was presented in Section III.4.2 for this sample. Regarding the residual stresses, the most important difference with both previous carbonitrided samples regards the tensile stresses in the N-enriched case, which are much higher (up to 800 MPa). Comparing with the sample which underwent the *in-situ* experiment (slower cooling), the sample cooled in air may have underwent more significant bainite transformation. As the related phase transformation strain is higher for bainite than for products formed at higher temperature, this may explain in part the higher stress in the N-enriched case, in the sample cooled in air. By reaction, the stresses in the regions underneath would be lower. But for a complete analysis, the phase transformation kinetics would need to be known in detail. This will be investigated further in the modelling section.

Let us mention that the residual stress in α/α' at the surface (see Footnote 2 Chapter

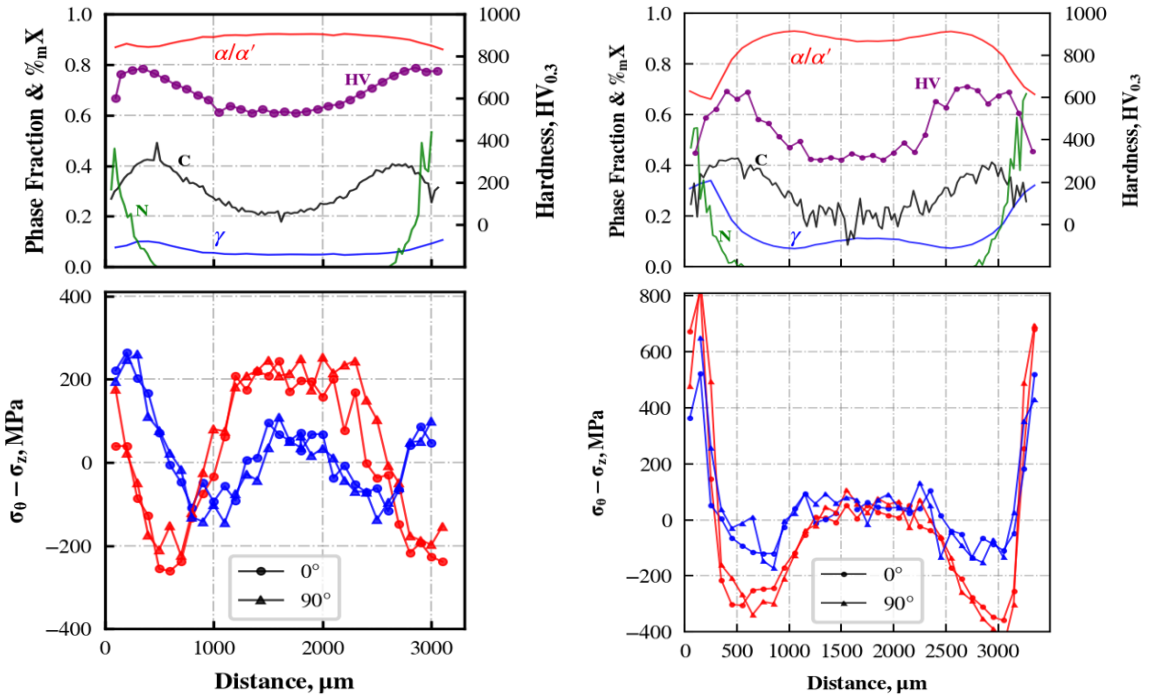

Figure III.20: Carbonitrided gradient samples: profiles of residual stress in α/α' (red) and γ (blue) phases. For each phase, both curves correspond to a rotation of 0° or 90° around the cylinder axis. Profiles obtained at room temperature by HEXRD, after enrichment at 900°C and a) quench into oil; b) cooling in air.

II) was also determined by laboratory XRD, giving -25 MPa and +620 MPa respectively for the quench into oil and the cooling in air, which is in good agreement with HEXRD.

III.6 Conclusion

A methodology was developed to determine by HEXRD simultaneously the phase fractions and the internal stresses evolutions during continuous cooling inside 3 mm-thick samples with carbon and nitrogen gradients. The HEXRD *in-situ* experiments were carried out in transmission mode (powder diffraction), and the thermal treatments were achieved by a portable lamp furnace designed and produced at IJL to be placed at a synchrotron beamline.

The influence of the cooling rate was investigated by examining (post-mortem) similar samples after faster cooling (quench into oil, cooling in the air). The Debye-Scherrer rings produced by the diffracted beams were recorded by a two-dimension detector. After post-treatment, the phase fractions were established as a function of time and temperature by Rietveld analysis, whereas the stresses were determined with the $\sin^2\psi$ method in ferritic (α/α') and austenitic (γ) phases separately.

For the carburized specimen, it is confirmed that the phase transformations occur firstly in the core during cooling and lastly in the carbon-enriched surface layer. By analyzing the kinetics of austenite decomposition throughout the thickness of the sample, the fraction of each product of phase transformations (ferrite, bainite, martensite) could be estimated, and a good agreement was found with the measurements of hardness. In previous works, this analysis was based on a thorough study of phase transformations in the investigated steel.

The chronology of the phase transformations mentioned above (core followed by surface) leads to compressive stresses in the layer enriched in carbon and tensile stresses in the regions beneath, as shown by former numerical simulation studies. As far as we know, it is the first time that the development of internal stresses can be analyzed

experimentally *in-situ*.

This new experimental method investigated nitrogen-enriched samples (nitrided or carbonitrided). As shown in previous works, the enrichment in the nitrogen of the austenite has strong effects on its decomposition: faster kinetics (loss of hardenability), finer microstructures, and higher hardness. We investigated the consequences on the formation of microstructures and stresses in the composition gradient. Unusual microstructure profiles and residual stress have been obtained, with the development of tensile stresses in the nitrogen enriched layer during cooling. The microstructural analysis suggests that it is due to the chronology of the phase transformations in the different layers having different C/N compositions. Three regions are identified in the case: the nitrided layer transforms first during cooling (due to its low hardenability, a large part of the transformation occurs above Bs), the core with the initial composition transforms second, and an intermediate region rich in carbon which transforms later on. Hence, the chronology is reversed compared to the more classical case of carburizing. This was the case for the *in-situ* experiment (cooling by gas blowing) but also for faster cooling in air or by quenching into the oil.

For all investigated cases (type of enrichment, cooling rate), the stresses are due to phase transformation strains (volume change, phase transformation plasticity). Indeed, the temperature gradients are too small in view of the samples' size to induce plastic strains. The experimental analysis carried out in this chapter allowed us to interpret the shape of microstructural and stresses profiles. Modeling and simulation are necessary to go further and investigate more quantitatively the effects of phase transformations chronology, local composition in C and N, cooling rate....

Chapter IV

Modeling, numerical simulations, and experimental validation

This chapter aims to establish the coupled metallo-thermomechanical simulations, to quantitatively understand the internal stresses evolutions in relationship with the phase transformations during cooling in enriched samples with gradients of carbon, nitrogen, and carbon + nitrogen. However, such numerical simulations require adequate modeling of the underlying thermal, metallurgical, and mechanical behavior of C and/or N enriched steels.

The first part of this chapter recalls the modelling of the different phenomena (thermal, metallurgical, and mechanical). Firstly, we make a summary of the metallurgical model developed in a previous study [3, 82, 92] and show its experimental validation for continuous cooling experiments for C and/or N enriched specimen of 23MnCr5Mo [3]. Secondly, we recall the modelling of the thermomechanical behaviour of the steel. We describe the experimental thermomechanical tests' results for different phases/constituents in C and/or N homogeneously enriched steels. Then, we show how the necessary model parameters have been obtained. In a third section, the thermal model is described as well as the thermophysical characterization of the C and/or N homogeneously enriched steels.

In the second part of this chapter, the models and input data have been implemented in the coupled finite element simulation tool (Zebulon). The coupled metallo thermomechanical simulations are performed to predict the genesis of internal stresses with respect to the phase transformation kinetics inside samples with C and/or N composition gradients resulting from carburizing, nitriding, or carbonitriding treatments cooled in different media (furnace-gas, calm air, and oil). Then, the simulation results are analyzed and validated through the comparison with the experimental results obtained by *in situ* HEXRD (slow cooling) of C and/or N gradients samples presented in Chapter II. In addition, the validation of final hardnesses, microstructures, and residual stresses on the C and/or N gradients samples after furnace-gas, calm air, and oil cooling are also included.

IV.1 Coupled thermo-metallo mechanical modeling

The objective of this section begins by recalling all essential physical phenomena during heat treatment and their modelling which were already much-studied to date [26, 59]. These models aim to simulate numerically and predict the evolutions of temperatures, phase transformation kinetics, and stresses/strains evolutions [106] during cooling of a part as well as the final microstructures, hardness, and residual stresses. As mentioned in Chapter I, the existing models mainly take into account mainly the effects of temperature and phase fractions on the model parameters and in some cases the effect of carbon

content. Thus the aim of former studies and present work is to focus on taking into account too the combined effects of carbon and nitrogen to be able to study thoroughly carburizing and carbonitriding treatments.

This reason initiated several studies: the first was focused on the microstructural evolutions after carbonitriding [3, 4, 92, 107] considering 23MnCrMo5 steel. It addressed, in particular, the influence of N on austenite decomposition. Multi-phase transformations are considered for developing a modeling scheme: austenite to ferrite, pearlite, bainite, and martensite transformations. The fraction of carbides or nitrides precipitates have been considered insignificant. Validation of the model has been performed for the prediction of phase transformation kinetics during isothermal holding and continuous cooling at a constant cooling rate of a chemically homogeneous specimen, the former will be recalled in Section IV.1.1.

Second, this present study has been focused on the characterization of thermomechanical and thermophysical behaviors and the determination of their parameters as a function of temperature and phases/constituents, emphasizing the specific effects of C and/or N contents. The development of thermomechanical and thermophysical models uses different laws (constitutive material laws), and we will see that to determine the complete set of input data, to take account of the effect of C and/or N content and microstructures is very complex. These developed models and parameters are then validated by comparison with the different experimental results of the C and/or N homogeneous enriched steels.

IV.1.1 Modeling of phase transformation kinetics

In Chapter III, we have recalled the experimental results on the influence of carbon and/or nitrogen enrichments on the austenite decomposition in terms of kinetics, microstructures, and hardness. This section summarizes the metallurgical model that takes into account C and N concentrations. The model is presented in detail [3, 106]. This global model can predict microstructure evolutions and final hardness in anisothermal conditions and consider C and N from kinetic and microstructural data obtained experimentally in isothermal conditions on homogeneously C and N enriched specimen contents developed, based on an additivity principle. For transformations with diffusion, progressions are described according to Kolmogorov-Johnson-Mehl-Avrami (KJMA) rule [108, 109, 110, 111, 112]:

$$y_k = y_k^{MAX}(T)\,[1-\exp(-k_k\,(t-t_k)^{n_k})] \tag{IV.1}$$

where y_k is the volume fraction of constituent k (pro-eutectoid ferrite (PF) /cementite, pearlite (P), or bainite (B)),$y_k^{MAX}$is the maximum volume fraction at the transformation temperature. n_k and k_k are kinetics coefficients determined for each temperature from isothermal kinetics on initial steel. n_k depends on the transformation mechanism and, for each phase, is supposed constant (no dependence on transformation temperature) while k_k is strongly dependent on transformation temperature. The JMAK parameters were directly established on the basis of these experiments, and the precision was good whatever the IT temperature, as mentioned in Figure III.1. In anisothermal conditions, the calculation of transformation progress by Eqn. IV.1 is preceded by the calculation of incubation period according to Scheil's method:

$$S = f\sum_j \frac{\Delta t_j}{t_k(T_j)} \tag{IV.2}$$

where Δt_j is the increment of time at timestep j, and t_k is the incubation time of the isothermal transformation, which depends on temperature, and f is a heredity factor being introduced in order to take into account non-additivity of incubation at the transition from high temperature (higher than Bs) to the bainitic domain. Transformation

starts when Scheil's sum S Eqn. IV.2 becomes equal to 1. Martensitic transformation progression is described using the Koistinen-Marburger relation:

$$y_M = y_k\,[1 - e^{-\alpha(Ms-T)}] \tag{IV.3}$$

where y_M corresponds to the martensite fraction formed, y_k to the fraction of remaining austenite at M_s temperature, and α is an experimentally determined coefficient.

The accounting of carbon content variations in the austenite is inspired by the approach developed by Mey [12]. It consists of calculating displacements of IT curves along time and temperature axes using the equations of Kirkaldy [113]. These displacements are mainly linked to carbon content dependent undercooling. The thermodynamic approach has been established to predict the equilibrium temperatures A_3, A_1, and T_H as well as the maximum fractions of proeutectoid ferrite. A modification of the additivity principle has also been introduced to take into account the effects of austenite stabilization during cooling on the kinetics of bainite transformation and the M_s temperature. The influence of austenite carbon content on diffusion-dependent transformation kinetics is taken into account using the approach developed in [12, 59]. These authors introduce the shift of isothermal transformation curves in terms of time and temperature defined as:

$$D_{k,\xi} = \frac{\tau_{k,\xi} - \tau^0_{k,\xi}}{\tau^0_{k,\xi}} \tag{IV.4}$$

where $\tau_{i,\xi}$ represents the time needed to form a fraction ξ of constituents k and $\tau^0_{k,\xi}$ is the same time relative to the reference material (initial steel). Characteristic times $\tau_{k,\xi}$ are calculated using Kirkaldy's relations initially dedicated to model IT diagrams as a function of steel composition. Thus, shifts of transformation curves calculated with Eqn. IV.4 are principally due to undercooling variations with the carbon content and are used to calculate kinetics parameters (n_k and k_k) of the JMAK equation Eqn. IV.1

Due to the more complex transformation mechanism after adding nitrogen, a simplified approach has been implemented. Two transformation domains are considered: a domain for the formation of the "high temperature" constituent (for T>Bs) where kinetic parameter k_k depends on carbon content and n_k is constant, and a bainitic transformation domain where kinetic parameters do not depend on composition (by the experimental results from which mean kinetics has been used as input data at the different temperatures). This approach is used only when nitrogen content exceeds $0.1\%_m$ (solubility limit of nitrogen in austenite at 900°C).

Finally, hardness is calculated by averaging the contributions of the different constituents formed during cooling. Each constituent's hardness depends on the temperature at which it is formed and on carbon and nitrogen composition. Indeed, empirical laws were established from experimental hardness measurements on isothermally transformed samples.

IV.1.1.1 Results for homogeneous samples

We recall here the experimental validation of the calculated kinetics during continuous cooling as well as final microstructures and hardnesses considering homogeneous specimens with different C and N compositions from Jeyabalan et al.[106]. For performing these simulations, the isothermal kinetics have been determined in the whole temperature range between Ae_3 and Ms temperature for the different compositions. All the kinetics results have been synthesized on the IT diagram of initial steel, carbon, and nitrogen enriched steels shown in Figure IV.1.

Figure IV.2a gives a synthesis of all the results of initial steel showing the fractions of

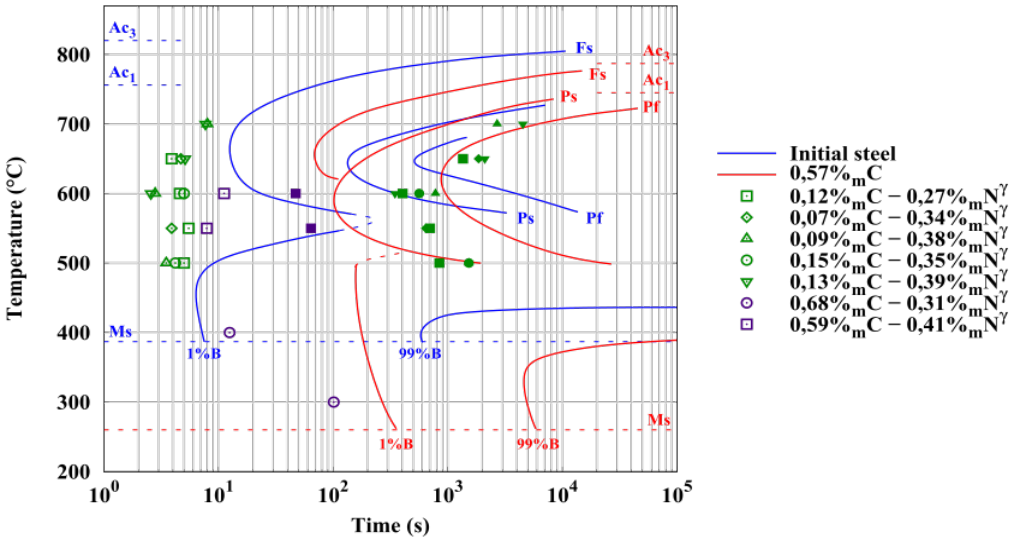

Figure IV.1: IT diagrams of I, C, N, and C+N steels. Scatter for N, and C+N steels come from differences in steel chemical composition. Fs: proeutectoid ferrite start; Ps and Pf: Pearlite start and finish.

the different products (at room temperature) as a function of the cooling rate as well as the associated hardness. Fractions of proeutectoid ferrite and pearlite are higher at lower cooling rates. Increasing the cooling rate makes increases successively the final fraction of bainite and then martensite. Except for the proeutectoid ferrite proportion at 0.5°C.s^{-1}, the difference between the simulation and the experiment does not exceed 10%. The discrepancies regarding the hardness do not exceed 50 HV, except in the case of a fully martensitic transformation (cooling at 50°C.s^{-1}). This discrepancy comes from the empirical relationship relating the hardness of martensite and its composition in carbon following the approach of Krauss [3, 106, 114]. Our formula results from a compromise between different experiments.

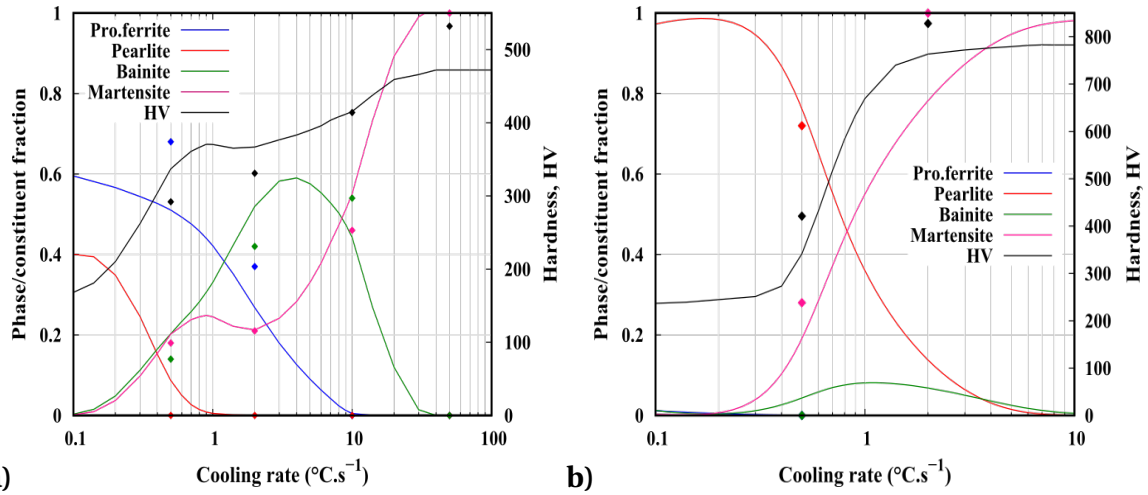

Figure IV.2: Fractions of products and hardness at room temperature for different cooling rates for the a) initial and b) carburized steels; calculated (continuous lines) and experimental (points).

Synthesis of the results for C steel is shown in Figure IV.2b. For both cooling rates considered experimentally, 0.5 and 2°C.s^{-1}, the differences between the calculations and the experiments are limited. compared to the I steel, the higher carbon concentration reduced proeutectoid ferrite and bainite proportions significantly. One obtains in the majority either pearlite or martensite.

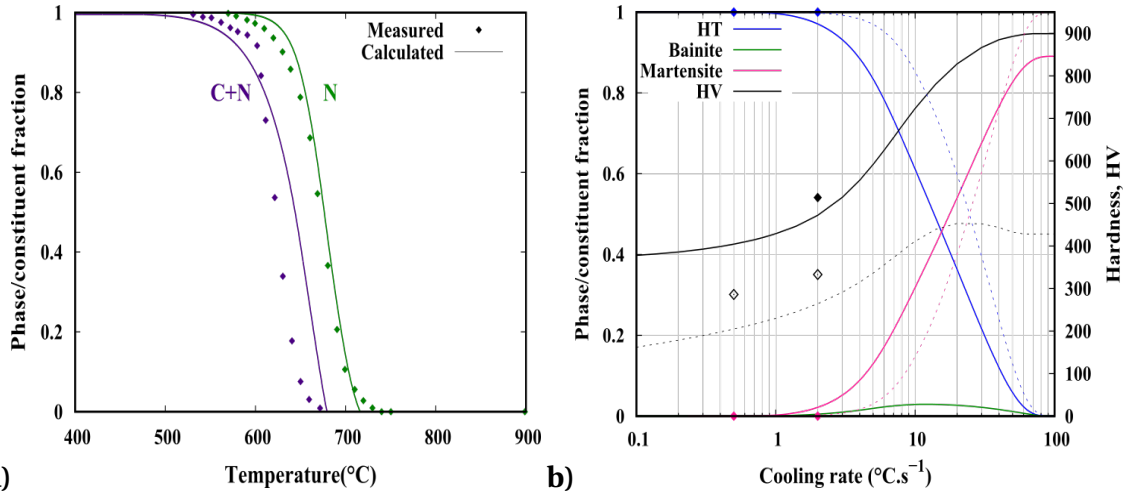

Figure IV.3: a) Experimental and calculated kinetics of austenite decomposition during continuous cooling at 2°C.s^{-1} in N steel (left) and C+N steel (right) b)Fractions of products and hardness at room temperature vs. cooling rate, calculated for the C+N steel (continuous lines) and N steel (dashed lines). Dots are for experiments (C+N steel in black and N steel in white)

For showing the effects of nitrogen, as an example, the simulated kinetics for a 2°C.s^{-1} cooling rate is compared to the experiment in Figure IV.3a on the one hand for the steel enriched in nitrogen (N) and on the other hand for the steel with carbon and nitrogen (C+N). Calculated global kinetics and final microstructures are in good agreement with the experiment. Indeed, one predicts the formation of the high-temperature constituent exclusively, in accordance with the microstructural observations. The temperature of the transformation start is nevertheless underestimated for the nitrided steel. This underestimation comes from the incubation times (t_{HT}) (figure with IT diagram), which are difficult to measure accurately due to the fast kinetics. The simulation for the C+N steel shows clearly the slow-down of the formation of the high-temperature constituent due to the higher carbon concentration, which is accounted in empirical formulae.

Figure IV.3b presents the synthesis of the results for both N and C+N steels. Predominantly formed products are either the high-temperature constituent or the martensite. The amount of bainite never exceeds 2%. The critical cooling rate to form only martensite is 50°C.s^{-1}. As expected, the higher carbon concentration in the steel enriched in carbon and nitrogen (0.63%$_m$ instead of 0.1%$_m$) makes martensite formation at lower cooling rates possible. For the C+N steel, 15% retained austenite is present at room temperature, per our experimental results, which is in good agreement with the simulation (11%). The calculated hardnesses are higher for the C+N steel than for the N steel. Because of the numerous simplifying hypotheses, the comparisons between simulations and experiments for the anisothermal kinetics in nitrided and carbonitrided homogeneous samples are considered as satisfactory [3, 106].

IV.2 Thermomechanical study

The first part of this section recalls the thermomechanical model which is generally used for residual stress calculations and the different material parameters that are necessary. As already mentioned our aim will be to study and introduce the effects of both carbon and nitrogen.

The second part of this section shows some results from the thermomechanical characterization performed by tensile tests on homogeneously enriched specimens either with carbon or nitrogen alone or with both carbon and nitrogen.

The third part of this section describes the strategies and identification procedures to derive the whole set of input data necessary for further simulations on gradient

specimens. The thermomechanical parameters will be identified from the experimental tensile and dilatometry tests. But, as the parameters cannot be obtained experimentally for the whole range of temperatures, carbon contents, and nitrogen contents necessary for further simulations, we have to interpolate and extrapolate on the basis of former knowledge and data.

IV.2.1 Thermomechanical model

On a macroscopic scale, the thermomechanical behavior of metallic alloys during heat treatment (see [26] for a review and references) is calculated by using the constitutive equation in the incremental form [25, 26, 56, 59]

$$d\varepsilon_{ij}^{tot} = d\varepsilon_{ij}^{e} + d\varepsilon_{ij}^{p} + d\varepsilon_{ij}^{th} + d\varepsilon_{ij}^{tr} + d\varepsilon_{ij}^{tp} \tag{IV.5}$$

where $d\varepsilon_{ij}^{e}$ is the incremental elastic strain, $d\varepsilon_{ij}^{p}$ the incremental viscoplastic strain, $d\varepsilon_{ij}^{th}$the incremental thermal strain, $d\varepsilon_{ij}^{tr}$ the incremental volumic strain due to phase transformation, an $d\varepsilon_{ij}^{tp}$ the incremental strain due to transformation plasticity. These different terms are detailed beneath

IV.2.1.1 Elastic strain

Elastic strain is calculated using Hooke's law as given below,

$$\varepsilon_{ij}{}^{e} = \frac{1}{E}(1+\nu)\sigma_{ij} + \delta_{ij}\nu\sigma_{kk} \tag{IV.6}$$

where σ_{ij} are the components of the stress tensor, δ_{ij} is the Kronecker symbol (when i=j, δ_{ij}=1 otherwise δ_{ij}=0),Young's modulus (*E*), and Poisson's ratio (ν). Young's modulus is generally temperature and phase dependent, and Poisson's ratio is assumed constant.

IV.2.1.2 Plastic/viscoplastic strain

$d\varepsilon_{ij}^{p}$ is the plastic strain increment when no viscous effects are considered or the viscoplasticstrain. It is calculated by using the classical theory of plasticity or viscoplasticity with the Von Mises yield criterion and the associated hardening rules (isotropic and/or kinematic). In the following, we will consider isotropic hardening. The plastic strain increment is calculated as,

$$d\varepsilon_{ij}^{p} = \frac{3}{2}\frac{d\varepsilon_{e}^{p}}{\sigma_{e}}\sigma'_{ij} \tag{IV.7}$$

$\sigma'_{ij} = (\sigma_{ij} - \frac{1}{3}\delta_{ij}\sigma_{mm})$ are the components of the stress deviator tensor.
σ_e is the Von Mises equivalent stress,

$$\sigma_{e} = \sqrt{\frac{3}{2}\sigma'_{ij} \times \sigma'_{ij}}$$

$d\varepsilon_{e}^{p}$ is the increment of the equivalent plastic deformation defined as

$$d\varepsilon_{e}^{p} = \sqrt{\frac{2}{3}d\varepsilon_{ij}^{p}d\varepsilon_{ij}^{p}}$$

A specific feature linked to phase transformations concerns the “memory“ of plastic strains as transformation occurs. Here we assume full inheritance by the new phase formed of the plastic strains of the austenite.

We will use an additive law to describe the thermoelastoplastic/viscoplastic behaviour law of the steels. It has been chosen as it allows us to describe the transition easily from the viscoplastic behaviour at high temperature to the elastoplastic behaviour at lower temperatures. Thus, the flow stress of each phase $\sigma_{f,k}$ is the sum of three contributions, as illustrated in Figure IV.4[115].

$$\sigma_{f,k} = \sigma_{0,k} + H_k {\varepsilon_p}^{n_k} + K_k \dot{\varepsilon}_p^{m_k} \tag{IV.8}$$

where $\sigma_{0,k}$ is the threshold stress, $H_k {\varepsilon_p}^{n_k}$ is the hardening due to the deformation, $K_k \dot{\varepsilon}_p^{m_k}$ is the viscous stress. ${\varepsilon_p}^{n_k}$ is the plastic/viscoplastic strain, and $\dot{\varepsilon}_p^{m_k}$ is the plastic/viscoplastic strain rate. n_k *and* H_k are the hardening parameters, K_k is the consistency, and m_k the strain rate sensitivity: all these parameters are temperature dependent and are generally are obtained from tensile tests at different strain rates and relaxation test [86]. From our knowledge (see Chapter I), these parameters have also been taken carbon content dependent but only for (linear) elastoplastic behavior of the steel for performing residual stress calculation for carburizing [12] and never nitrogen dependent for neither nitriding (in the austenitic fields) nor carbonitriding treatments.

The flow stress of the multiphase material is obtained through a mixture rule of the flow stresses of the different phases,

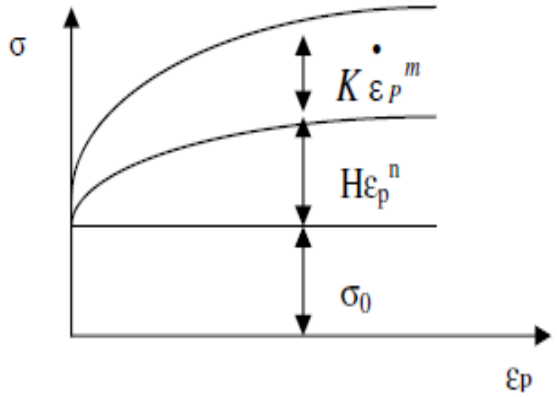

Figure IV.4: Flow stress decomposition for a tensile test.

IV.2.1.3 Thermal strain

The thermal strain increment due to thermal expansion/contraction is defined as,

$$\varepsilon_{ij}^{th} = \sum_k y_k \int_0^T \alpha_k(T) dT \delta_{ij} \tag{IV.9}$$

where $\alpha_k(T)$ is the temperature-dependent thermal expansion coefficient for phase k. This coefficient is derived from the dilatometry tests.

IV.2.1.4 Transformation strain

The transformation strain is due to the volumic variations associated with the phase transformations and can be formulated by,

$$\varepsilon_{ij}^{tr} = \sum_k \varepsilon_{k,0°C}^{tr} y_k \delta_{ij} \tag{IV.10}$$

where $\varepsilon_{k,0°C}^{tr}$ represents the expansion associated with the transformation of austenite to the k^{th}phase at 0°C.

IV.2.1.5 Transformation plasticity

Transformation plasticity is an additional deformation that occurs when phase transformations occur under stress. Two mechanisms are often credited for the explanation of transformation plasticity phenomena, related to either the accommodation of the transformation strain by local plastic deformations (called Greenwood-Johnson mechanism[116]) or by the orientation of the phase transformation product due to the applied stress for transformations with shear deformation (Magee mechanism [117]) or both. Macroscopically, transformation plasticity strain increment, in its most used form, is written [59],

$$d\varepsilon_{ij}^{pt} = \frac{3}{2} K_k f'(y_k) S_{ij} dy_k \tag{IV.11}$$

S_{ij} are the components of the stress deviator tensor, K_k is the coefficient of transformation plasticity, which is generally obtained experimentally. $f(y_k)$ is a function of the transformation fraction; from experiments for ferritic and pearlitic transformations $f(y_k) = y_k$ and for bainitic and martensite transformations $f(y_k) = (2 - y_k) y_k$ [59].

IV.2.2 Characterizations of thermomechanical behavior

In order to determine the parameters of the thermoelastoviscoplastic behaviour law (Eqn. IV.8), tensile tests have been performed following the schedule given in Table II.3. These tensile tests have been performed for the initial steel and C and/or N homogeneously enriched specimens. For confidentiality reasons, we cannot present the results of all thermomechanical tests; only a few examples of tensile tests are illustrated in the first part of this section. In the second part of this section, we present the construction of the set of parameters for the C and/or N enriched steels in relation to the microstructures.

IV.2.2.1 Experimental results of thermomechanical tests

We first present some results at higher temperatures where the phases/constituent show a viscous behavior (austenite, ferrite+pearlite, HTconstituent) and then results at lower temperatures where viscous effects are no longer present (bainite, martensite). We have noted that in our tests the modulus of elasticity is not the same during loading and unloading, and a low modulus of elasticity is also emphasized during loading in some tests. This low modulus of elasticity or "stiffness" results from the faulty placement or slippage of rod-type extensometers on the tensile sample (as discussed in Chapter II), mainly during the elevated temperature tests.

IV.2.2.1.a Thermomechanical behavior of phases/constituents with viscous behavior

Figure IV.5a presents the tensile stress-strain curves of the austenite phase at 900°C for two different strain rates, 2×10^{-3} /s and 2×10^{-4} /s. As expected, the yield strength and the flow stress of the base steel and the enriched steels are higher for a larger strain rate (2×10^{-3} /s), evidencing the viscous effects at higher temperature (above 500°C that corresponds to the generally admitted criterion $T > T_f/3$, T_f being the fusion temperature). It can also be observed that, for a given strain rate, the yield strength and strain hardening increase when the carbon and nitrogen contents increase, which can be linked to the solid solution hardening that increases as interstitial content increases.

Figure IV.5b shows the stress-strain curves of the ferrito-pearlitic mixture (50% ferrite + 50% pearlite) of the initial steel obtained at room temperature (25°C) and at 200°C (after reheating) and the stress-strain curves of the N-rich steels for the high temperature constituents (formed at 600°C temperature after isothermal holding) and tested either at 600°C or at room temperature 25°C. As expected, we observe a decrease in the flow

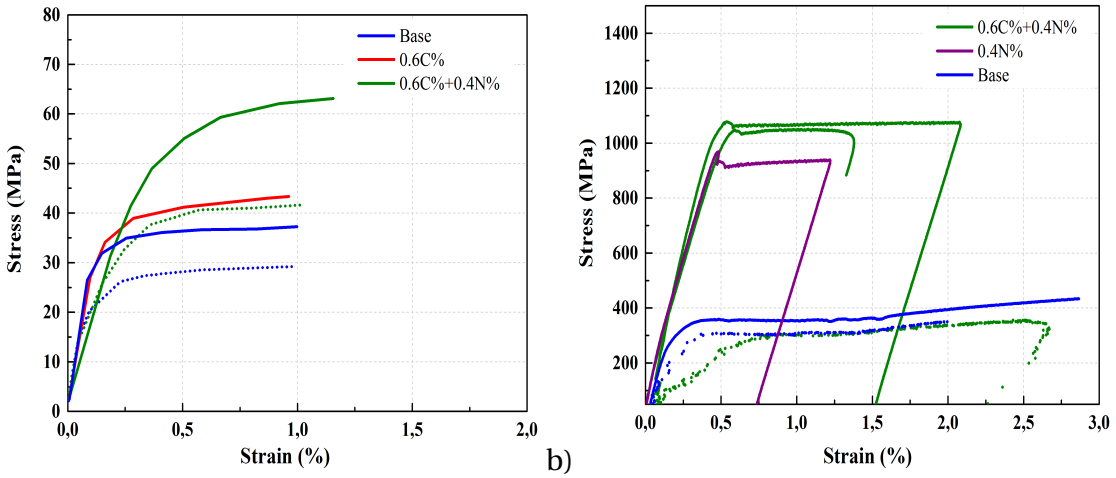

a) b)

Figure IV.5: Experimental tensile test curves of a) austenite at 900°C for different strain rates 2 × 10-3 (solid lines) and 2 × 10-4 /s (dot lines) for initial and different enriched steels and b)ferrite+pearlite mixture at 25°C (solid lines) and 200°C (dotted lines) for initial steel (blue), and HT constituents at 25°C (solid lines) and 600°C (dot lines) for nitrogen enriched steels (green and purple).

stress of the initial steel between room temperature and 200°C. We also observed a strong increase in the yield strength of the HT constituent in C+N steel from 600°C to 25°C.

It is surprising that all the tensile test curves present small strain hardening even at room temperature. Let us mention that the tensile behavior of C+N steel is reproducible, as shown by two tests performed in the same condition at 25°C (green curves in Figure IV.5b).

We can also see higher and lower yield stress on the behaviour of the HT constituent at room temperature (after deformation at 600°C) that could be linked to some aging due to carbon and nitrogen evenif the plastic deformation at 600°C was relatively small (2.5%).

IV.2.2.1.b Thermomechanical behavior of phases/constituents without viscous behavior

Figure IV.6a shows the experimental tensile curves of full bainitic microstructures at 25°C: after an isothermal bainitic transformation at 400°C for the initial steel and after an isothermal bainitic transformation at 350°C for the C enriched and N enriched steels. The tensile test curves performed respectively at 350°C and 400°C at the end of the isothermal holding for the C enriched steel and the initial steel, respectively, are plotted.

As expected, the effect of interstitial contents on the evolution of the yield strength and strain hardening is very clear. However, we have noticed that C steel shows a higher overall strain-hardening capacity of the microstructure than N and C+N steels. In addition, the C+N steel specimens revealed a lower yield strength than the N steel, which could be linked to the transformation at 350°C that was not entirely complete. The results have also shown that the viscous effects are negligible at 400°C.

Figure IV.6b shows the tensile curves of the martensitic phase in the initial, C, and N enriched steels at 25°C. For initial steel, martensitic transformation is completed at room temperature, and the martensitic microstructure shows a high yield strength and strain hardening. For C or N steels, the premature failure of the specimen during the tests hinders to know the tensile behavior. We can mention that the C + N steel microstructure is not fully martensite and contains 8-12% retained austenite.

Figure IV.7 shows a synthesis of the conventional yield strengths at 0.2% plastic strain called $\sigma_{0,2\%}$ for all the presented results above. Generally, the yield strength of steel is affected by different strengthening mechanisms, such as solid solution strengthening owing to interstitial and substitutional atoms, grain boundary

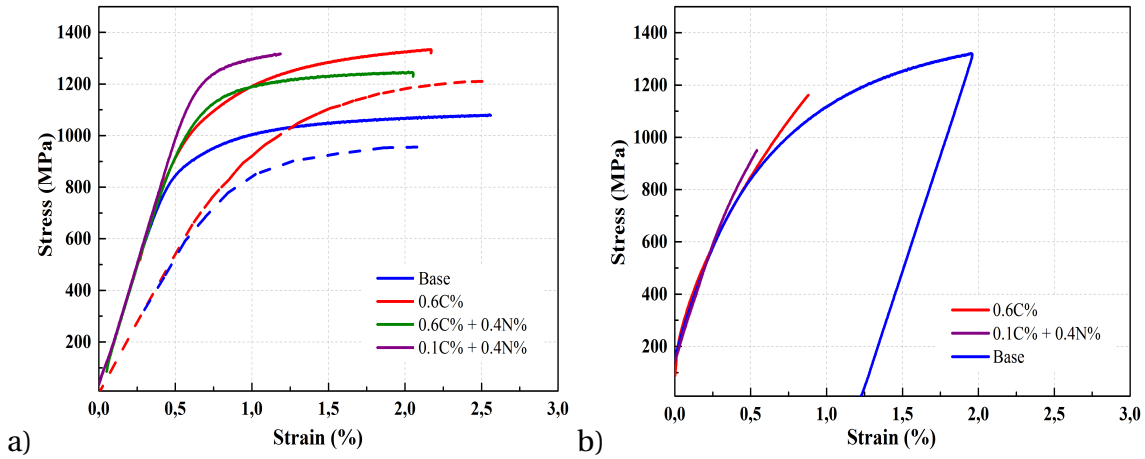

Figure IV.6: Experimental tensile test curves of a) bainite at 25°C (solid lines) and at higher temperatures (400°C for the initial steel and 350°C for C steel) (dot lines) for the strain rate 2 × 10^{-3} /s and b) martensite at 25°C for initial and different enriched steels.

strengthening and/or microstructure size strengthening, dislocation strengthening, precipitation strengthening, etc. [86, 118]. To detail these different contributions in our C and/or N enriched steels is very complex and outside the scope of our study, but some deep microstructural analysis of the nitrogen enriched steels [4, 92] can be recalled and related to the here measured yield strengths.

In Figure IV.7, we can see that N and C+N steel show higher yield strength at room temperature (1240 and 1090 MPa, respectively) for bainitic microstructures formed at 350°C than the initial martensitic steel. For N steel, the yield strength is even higher than for the C enriched steel (for bainitic microstructures formed at 350°C) evenif the interstitial content is lower. It is even higher than the yield strength of C enriched martensite. This high yield strength is linked to a very fine and tangled bainite microstructure [92]. The same tendencies were observed previously from hardness measurements (Figure III.1) [3].

The high temperature constituent in N and C+N steels formed at 600°C also reveals a high yield strength at room temperature (above 1000 MPa for C+N). The C+N specimen shows higher yield strength than the N specimen and is close to the yield strength of martensite in the initial steel at room temperature. For this constituent (formed above Bs), the high yield strength results in large part from the refinement of the microstructure of very small equiaxed ferrite grains (sizes ca. 4microns) and intra-granular nanosized CrN nitrides inside the equiaxed ferrite grains [4, 119]. This effect of refined microstructures can be more significant than strengthening due to the higher interstitial contents [92].

IV.2.2.2 Thermomechanical for C and/or N enriched steels

IV.2.2.2.a Determination of the parameters associated with the plastic/viscoplastic strains

As described previously, the behaviour of our steels is described by an additive thermoelastoviscoplastic law (Eqn. IV.8) where the different parameters (σ_0, H, K, n, and m) have to be determined for each phase/constituent versus temperature and carbon and nitrogen contents. The form of this law and the number of parameters makes it difficult to handle it manually. Thus, the parameters are obtained using the optimizer module in Zebulon software [48], where the difference between the experimental and simulated curves is reduced using conventional iterative algorithms. Manual adjustments are also performed in order to respect physical evolutions of the parameters versus temperature, i.e., when the temperature decreases, the threshold stress and the hardening parameters

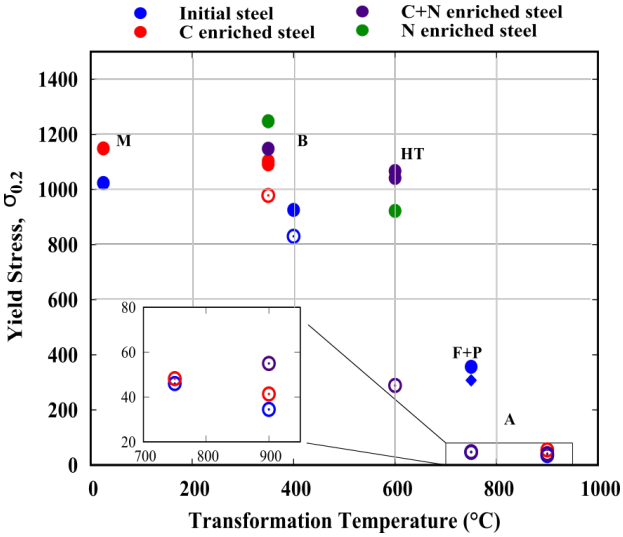

Figure IV.7: Variation of the conventional tensile strength at a strain rate 2 X 10^{-3} /s versus the transformation temperature for C and/or N enriched steel (filled circle represents the tensile test performed at 25°C, the unfilled circle represents tensile and deformation temperatures are the same and filled diamond represents deformation temperature of ferrite+pearlite phase at 200°C).

increase, and the parameters of the viscous stress decrease.

During optimization, available literature data [120] of Young's modulus of ferritic (E_α) and austenitic (E_γ) phases in low alloyed steels, which varies almost linearly with temperature (°C) expressed as below,

$$E_\alpha = (215920 - 0.0268T - 80.98T^2) \times 10^6 GPa$$
$$E_\gamma = (198100 - 0.0244T - 64.94T^2) \times 10^6 GPa$$

Indeed, as previously mentioned in the Section II.4.3.1, the tensile test data for Young's modulus is not used in this study, as it is not precisely determined. From previous work [12, 14], we have assumed that Young's modulus does not depend on chemical composition.

Due to lack of time and technical difficulties, the characterizations were performed only for extreme C and/or N contents, and temperatures and some data are missing. In addition, some data are impossible to measure due to the physics (particularly the hardenability of the steels). Thus, to have a complete dataset for the thermomechanical model, the thermomechanical parameters have to be extrapolated for the intermediate temperatures and C and/or N contents with the help of the literature, as will be described beneath. The resultant thermomechanical parameters variations with C and/or N content and temperature have been described using empirical laws. But these laws cannot be given in the following due to confidentiality reasons. To validate the thermomechanical model with the complete parameter set, the simulated tensile curves are compared with the experimental curves of C and/or N homogeneous specimen.

IV.2.2.2.b Thermo-elastoplastic behavior of phases with viscous effect

In our approach, we have taken into account the temperature effects, the microstructural effects, and the effects of carbon and nitrogen on the threshold stress σ_0 and on the hardening parameter H. Hardening coefficient n is supposed to be constant for each phase/constituent. For the viscous effects (that play a role above 500°C as mentioned before), we assume that K et m parameters are only temperature dependent. They were directly established based on the tensile curves at different strain rates and agreed well with the literature [14].

The general procedure will be to determine for each phase/constituent the

temperature evolutions of the parameters σ_0 and H for the initial steel and add the contribution of carbon and nitrogen. Thus, threshold stress ($\sigma^k_{0,C,N}$) and hardening parameter (H_k) will be written as,

$$\sigma^k_{0,C,N} = \sigma^k_{0,I} + \Delta\sigma^k_{0,C,N}$$
$$H_k = H_{kI} + \Delta H_{k,C,N}$$

threshold stress ($\sigma^k_{0,I}$), and hardening parameter (H_{kI}) of initial steel for the phase or constituent *k* . We have assumed that the variation of threshold stress ($\Delta\sigma^k_{0,C,N}$) and hardening parameter ($\Delta H_{k,C,N}$) increase linearly with carbon and nitrogen. The variations of threshold stress for austenite and hardening parameter above 700°C were established based on the measurements done in the initial steel, the *C* steel (enriched to 0.57%$_m$ C), and the C+N steel (enriched to 0.57%$_m$ C + 0.4%$_m$ N). From the initial steel tensile curves, the temperature evolutions of the parameters are determined and extrapolated to lower temperatures based on the previous studies [14]; from the enriched steel curves, we have assumed that the parameters increase linearly with carbon and nitrogen. Let us mention that in literature, the yield strength of austenite has also been given linearly dependent on carbon and nitrogen [121]. Figure IV.8a shows the comparison of experimental and simulated stress-strain curves for austenite with the determined data set that are in good agreement.

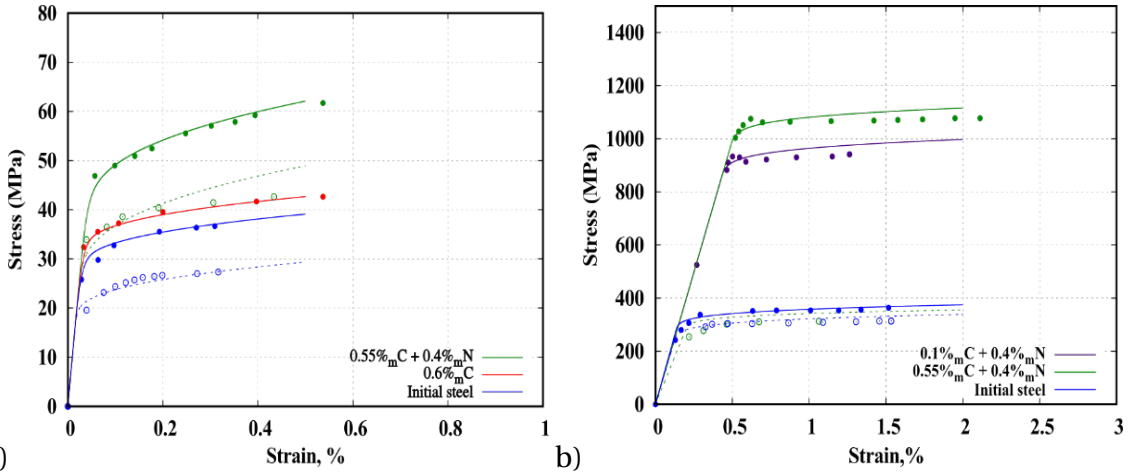

Figure IV.8: Comparison between the experimental tensile test with simulated curves of a) austenite at 900°C for different strain rates 2×10^{-3} (solid lines) and 2×10^{-4} /s (dotted lines) for initial and different enriched steels and b)ferrite+pearlite mixture at 25°C (solid lines) and 200°C (dotted lines), and HT constituents at 25°C (solid lines) and 600°C (dotted lines) for initial and different enriched steels.

Figure IV.8b shows the comparison of experimental and simulated stress-strain curves of the ferrito-pearlitic mixture and the high temperature constituents that are in good agreement too. The thermomechanical parameters of individual proeutectoid ferrite and pearlite products have been determined versus temperature with the two experiments of the ferrito-pearlitic mixture in initial steel and extrapolated over the whole range of temperature where these phases/constituents can be present (i.e.from Ae_3 to room temperature) also using data from previous studies [88]. It is assumed that the ferrite and pearlite parameters do not depend on the carbon content [12]. This assumption seems realistic as the formation of these products is not largely present in our further simulations (Section IV.4.2).

In C+N steels, the threshold stress of HT constituents and hardening parameter temperature dependency is determined from the experimental curve obtained for 0.4%N, and a linear increase with carbon content has been taken into account based on our experimental results (it is assumed that these parameters do not vary with nitrogen in

the range of compositions we study).

IV.2.2.2.c Thermo-elastoplastic behavior of phases without viscous effect

As previously, the temperature dependency of the threshold stress and hardening parameter has been determined from the initial steel tensile test curves and extrapolated in the whole temperature range where the phases/constituents may be present (from Bs to room temperature for bainite and from Ms to room temperature for martensite) also using data from previous studies in the lab [86, 87]. From our experiments on carbon enriched steel, the identified threshold stress and the hardening parameters of bainite and martensite phases agree well with the literature for the effect of carbon that leads to an increase of these parameters which is assumed linear [14, 86]. From our experiments on enriched steels, we have also taken into account a linear dependency of the theshold stress with carbon and nitrogen contents. The hardening parameter H_k is considered only carbon content dependent.

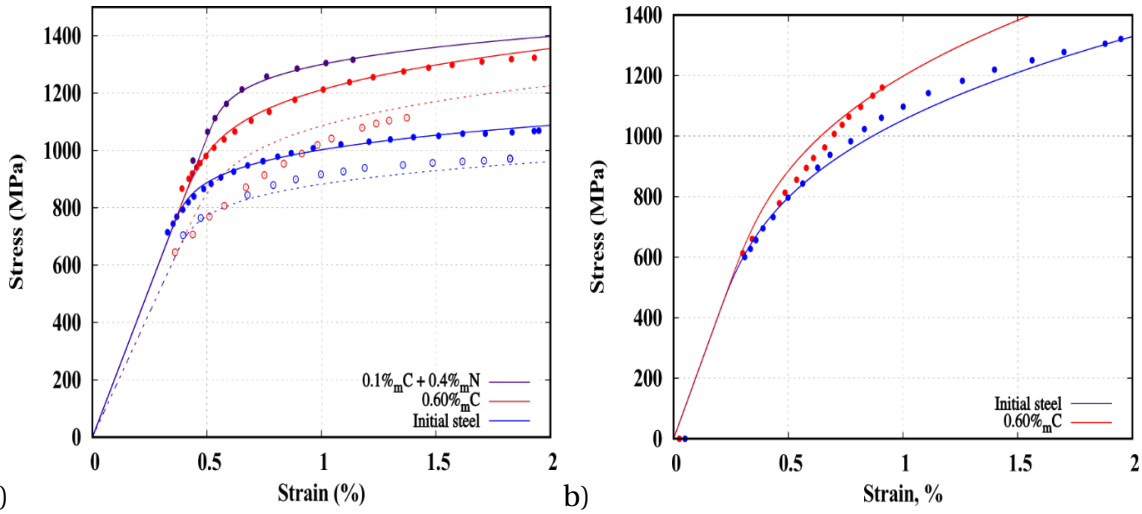

Figure IV.9: Experimental tensile test curves and simulated ones of a) bainitic at 25°C (solid lines) and at elevated temperatures (dotted lines) for the strain rates 2×10^{-3} /s and b) martensite at 25°C for initial and different enriched steels.

The hardening coefficient, n has been assumed constant for bainite as well as for martensite. Figure IV.9a shows a pretty good coherence between the experimental and simulated stress-strain curves of bainitic phases for the enriched steels. The discrepancy on the yield stress and flow stress for the bainite at 350°C in the carbon enriched steel can be related to the constant hardening coefficient assumed for all ferrite, pearlite and bainite phases.

The obtained thermomechanical parameters of martensite in the initial steel also allows a good description of the behaviour at room temperature (Figure IV.9). These parameters are lacking for the enriched steels due to the experimental failures (as discussed in Section II.4.3.1). These parameters have been obtained from literature data. Indeed, it is well known that for martensite carbon and nitrogen lead to solid solution strengthening [114]. In our work, a linear increase of the threshold stress with carbon and nitrogen contents have been used. The dependency with nitrogen is taken into account when N content exceeds 0.1%$_m$ (solubility limit of N in austenite at 900°C. The correlation between experiment and simulation for the C enriched steel is considered as satisfactory in the range of deformation 0-0.75% where we have an experimental result.

IV.2.3 Thermal strains and transformation strains

The mean thermal expansion coefficients for the different phases/constituents in C and/or N steels and the transformation strains are derived from the experimental

dilatometric curves. For example, Figure IV.10 shows the dilatometric curves on heating (heating rate 10°C/s austenitization at 900°C during 30 min) and cooling (rate 55°C/s) in the initial steel and in two enriched steels: 0.57%m C and 0.6%m C + 0.37%m N steels. The cooling rate is high enough (60°C/s) to get martensitic transformation for the three steels. As expected Ms temperature is lower for the more enriched steels and these results are in agreement with the previous results of S Catteau [3]. From that curves we get the mean thermal expansion coefficient of austenite is α_γ= 21.4 x 10^{-6} 1/s and the one of martensite for the initial steel is α_m=12.2 x 10^{-6} 1/s. The transformation strain ($\varepsilon^{tr}_{k,0°C}$ see Eqn. IV.9) for the martensitic transformation can also be measured the reference being the austenite at 0°C. From these results and also previous results from S. Catteau [3], we got the transformation strain evolution versus C+N content (Figure IV.11b) and we derived the following empirical equation relating $\varepsilon^{tr}_{\gamma-\alpha',0°C}$ to the C and N contents for a complete martensitic transformation

$$\varepsilon^{tr}_{\gamma-\alpha',0°C} = 0.0036 \times \%_m(C+N) + 0.0065$$

As expected , this strain increases with C and/or N content.

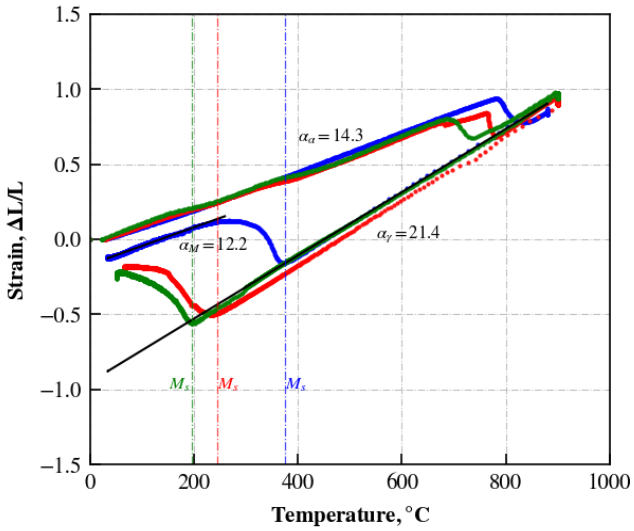

Figure IV.10: Experimental dilatometry curves of martensitic transformation in initial,0.57%mC, and 0.6%mC+0.37%mN steels.

For the other phases/constituents, we have used the dilatometry curves obtained for isothermal treatments. In Figure IV.12a and IV.12b, we can see the dilatometric curves for isothermal bainitic transformation and 'ferritic' transformations respectively.

After austenitization, the specimen is cooled down (we see the thermal contraction of the austenite) to the isothermal holding temperature where the transformation occurs (accompanied by a strain increase due to the volumic expansion). After the isothermal holding, the specimen is cooled down and we see the thermal contraction. (transformations are almost completed after the isothermal holding excepted for the bainitic transformation at 350°C in the carburized steel (0.57%$_m$C where a martensitic transformation can be seen at about 200°C)

The transformation strains obtained for the different transformations are plotted in Figure IV.11a versus the carbon content of the steel. It can be observed that for steels without nitrogen, the strain decreases as carbon content increases for ferrite+pearlite transformation as well as for bainitic transformation. For steels with 0.4%m nitrogen, the strain also decreases as carbon content increases for the HT constituent transformation but changes only slightly for bainitic transformation. It can be noted that the strain associated with the HT constituent transformation is higher than for the bainitic transformation for a same steel interstitial composition. Presently we have no explanation for that behaviour.

Let us mention that the thermal expansion coefficients of austenite and ferritic microstructures are close to the values determined previously for austenite and martensite (Figure IV.11b). One can mention that these mean coefficients of thermal expansion agree also with the HEXRD results. Thus, finally we will consider mean thermal expansion coefficient for austenite as α_γ= 21.4 x 10^{-6} 1/°C for all compositions and the same mean thermal expansion coefficient for the ferritic phases (Ferrite+pearlite, baiite, HTconstituent) as α_m=12.2 x 10^{-6} 1/°C.

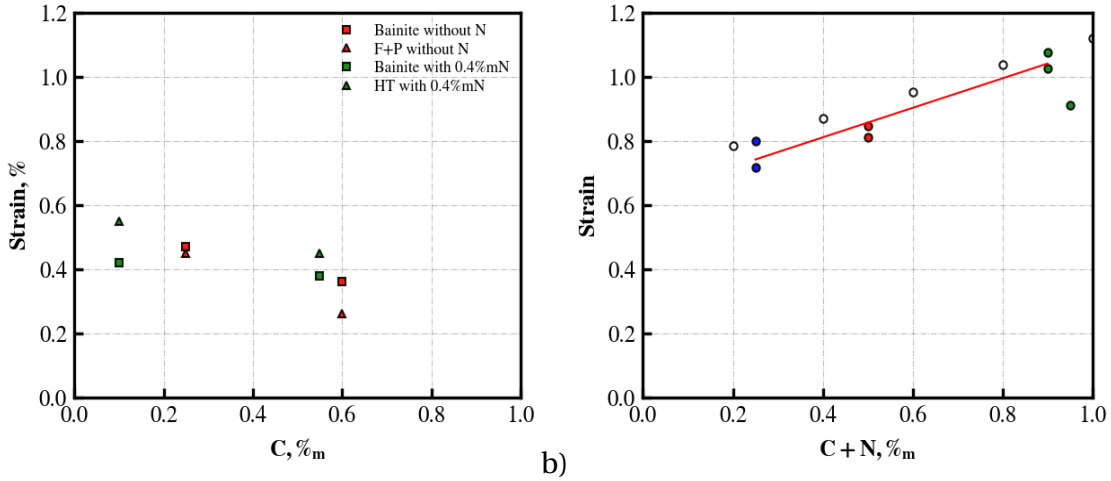

Figure IV.11: Transformation strain due to phase transformation from austenite to decomposition products $\varepsilon^{tr}_{k,0°C}$ a) ferrite + pearlite (triangle), high temperature constituents(triangle), bainite(square), and b) martensite(circle) (which depends on C and/or N contents)

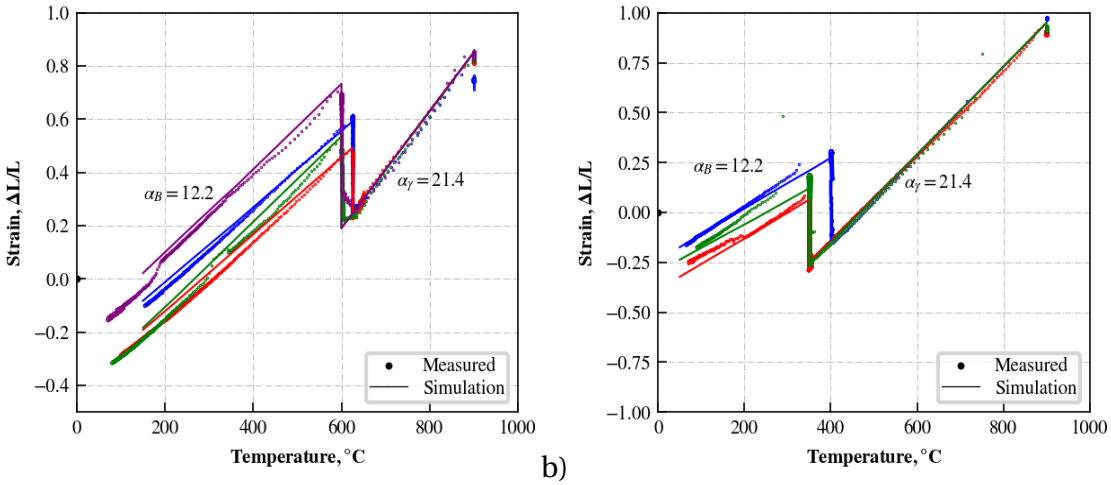

Figure IV.12: Experimental dilatometry curves for isothermal transformations (a) ferrite-pearlite and HT constituent, b) bainite, in initial (blue curve), 0.57%$_m$C (red curve), 0.1%mC+0.4%$_m$N (purple) , 0.57%$_m$C+0.4%$_m$N (green curve) steels.[3]

IV.2.4 Transformation plasticity strain

As described in Chapter II, for diffusion dependent transformations, the test consists after the austenitization to cool the specimen down to an isothermal holding temperature (as quickly as possible) and to apply stress before the transformation starts. For our base steel, these tests were not possible neither for ferrite perlitic transformation neither for bainitic transformation due to the low hardenability of the steel.

For the carbon enriched steel (0.57%mC), a test was performed for the isothermal bainitic transformation at 350°C for an applied stresses of 50 MPa. Figure IV.13 shows

the evolution of the strain versus time during the holding at 350°C for no applied stress and for a stress level (that corresponds approximately to the half of the yield stress of austenite at 350°C). The strain increases rapidly during the transformation and becomes asymptotic as transformation slows down. Final strain is larger when the applied stress increases evidencing transformation plasticity.

The difference in deformation between unstressed and tensile stressed cases allow to determine the coefficient K. Assuming linearity of the deformation with applied stress the values obtained is K = 1.76 x 10^{-4}MPa^{-1}. It appears also clearly that the transformation is accelerated by the applied stress as already observed previously [86, 87]. The progression of the bainite transformation is well described and agrees with experimenta curves.

The obtained K value is higher to the one obtained by [86, 87] for the bainitic transformation of steels (1.6 x 10^{-4}MPa^{-1}). In addition, these authors showed that K value can be well approximated by the K value proposed in the model by Greenwood-Johnson [116].

$$K_k = \frac{5}{6}\frac{\Delta_k}{\sigma_y}$$

where Δ_k is the volumic change associated with the decomposition of austenite into phase *k*, $\Delta_k = \frac{\Delta V}{V}$ where σ_y is the yield strength of parent austenite.

For nitrogen enriched steels, the experiments were also not possible due to a too low hardenability of the steel; as already mentioned the kinetics of the high temperature constituent (Figure IV.1) is very fast (incubation time at 600°C less than 2s) and the required cooling rates to measure the transformation plasticity, could not achieved with our experimental setup.

Thus, we calculated K parameter for the carbon and nitrogen enriched steel using the measured volumic variations and the yield stress of austenite. It comes out that the K values do not vary largely with the carbon and nitrogen contents.

Finally, from gathered experimental data from previous works in my lab for different phase transformations (pearlite [122], bainite [86, 87], martensite) in different steels (see Figure IV.13), mean values of K has been chosen. K = 1.5 x 10^{-4} MPa^{-1} for ferrite, pearlite HTC (High Temperature constituent), and bainitic transformations, and K = 6.5 x 10^{-5} MPa^{-1}, for martensitic transformation.

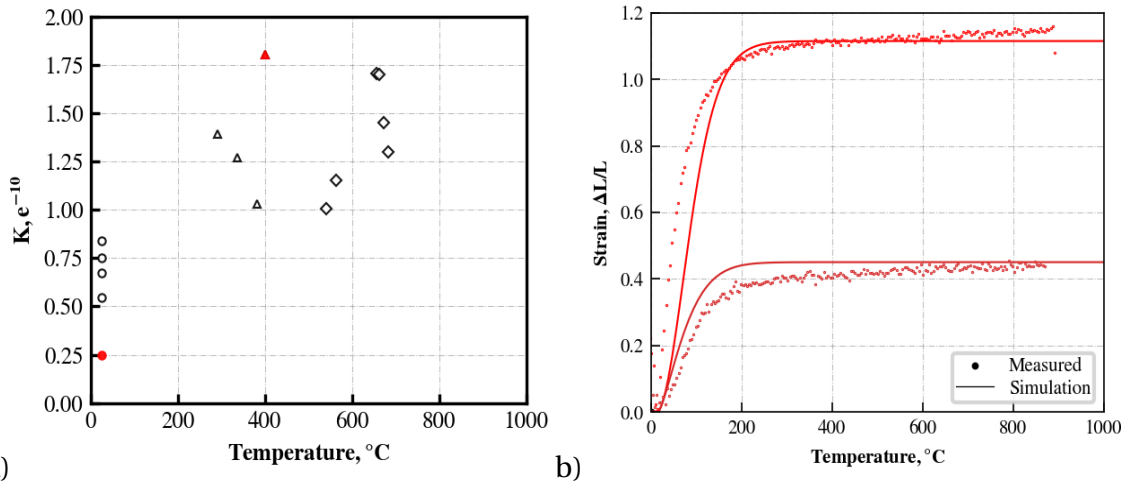

Figure IV.13: a) Effect of constant tensile stress applied to the isothermal baintic transformation of C steel (0,57%m) at 350°C b)Synthesis of transformation plasticity(K parameter) derived from experimental results at LSG2M for different transformations.[37, 86, 87, 116, 123]

IV.3 Thermophysical study

IV.3.1 Thermal model

The numerical simulation of a heat treatment first involves determining the temperature distribution in the part by solving heat conduction equation:

$$\rho C_p \frac{\partial T}{\partial t} = \lambda \left(\frac{\partial^2 T}{\partial x^2} + \frac{\partial^2 T}{\partial y^2} + \frac{\partial^2 T}{\partial z^2}\right) + \dot{q}$$

where T is the temperature, t the time, λ the thermal conductivity, C_p the specific heat,ρ the density, $\dot{q}$ the heat source term that describes the heat released during phase transformation [34, 59, 124, 125] and is written :

$$\dot{q} = \Delta H_k \frac{dy_k}{dt}$$

where $\frac{dy_k}{dt}$is the rate of transformation and ΔH_k is the enthalpy of transformation for constituent k. y_k are the volume fractions of the different phases/constituents, *k*. λ, C_p ,ρ are temperature and microstructure dependent and calculated by mixture laws. For example, for the thermal conductivity, $\lambda = \Sigma y_k \lambda_k$.

For the thermal analysis, the boundary condition at the surface during cooling is stated by Newton's law of convection as below,

$$\lambda \frac{\partial T}{\partial ns} = \Phi_c = h\,(T_s - T_\infty)$$

With Φ_c surface heat flux density, $h(T_s)$ the convective heat transfer coefficient ($W/m^2.°C$) as a function of T_s (surface temperature) and T_∞ is the quenchant temperature. $\frac{\partial T}{\partial ns}$ is the temperature gradient normal to the surface.

IV.3.2 Experimental results and modelling of thermophysical behavior

The thermophysical properties such as thermal conductivity, specific heat, density, and the enthalpy of transformation are determined experimentally, and using Thermocalc® for the different enriched steels as a function of the temperature and the phases/constituents.

IV.3.2.1 Density

The density of the ferritic and the austenite phases are determined for initial, $0.6\%_m C$, and $0.6\%_m C + 0.4\%_m N$ steels as a function of temperature using the Thermocalc® TCFE9 database as shown in Figure IV.14. The densities of ferritic phases and austenite are sensitive to the interstitial contents (C and/or N): density decreases with increasing interstitial contents and N content shows a stronger influence on the ferritic phase's density.

For our simulations, we need data for the density until room temperature, thus an extrapolation has been made using the thermal expansion coefficient. The variation of density as a function of the temperature for the different phases is expressed as below,

$$\rho(T) = \frac{\rho_0}{(1 + 3\alpha T)}$$

where ρ_0, known density at a reference temperature (25°C); Finally, the expression of the evolutions of density over the whole temperature range are expressed as follows,

For ferritic phase:

$$\rho_\alpha\,(kg.m^{-3}) = 7868 - 92.5 \times \%mN - 0.3567 \times T°C$$

For austenitic phase:

$$\rho_\gamma\,(\mathrm{kg.m^{-3}}) \;=\; 8091 - 78.97 \times (\%\mathrm{mC} + \%\mathrm{mN}) - 0.5442 \times \mathrm{T^{\circ}C}$$

Our calculations are consistent with previous studies [12, 25, 86].

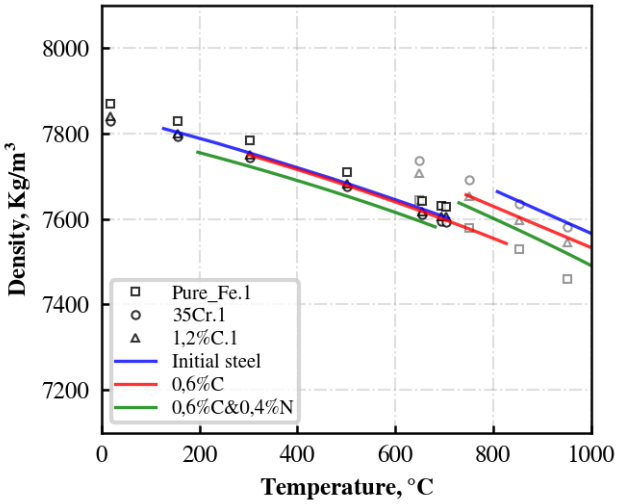

Figure IV.14: the evolution of the density for the ferritic and austenitic phases in the initial (23MnCrMo5), C, and C+N steels as a function of temperature and different steels from various studies.

IV.3.2.2 Specific heat

The specific heat evolution for initial and C and/or N enriched steels were measured using differential scanning calorimetry (DSC) on heating from room temperature to 900°C (heating rate of 5K/min), and also determined using Thermocalc®. A standard sample with 3 mm thickness has been used to assess C_p values for initial steel whereas for C and/or N enriched steels, three sliced pieces (with 1mm thick) are used, equivalent to DSC's standard sample. Nevertheless, the non-homogeneous heat flow between the sliced pieces results in the diverged C_p values for all enriched steel, compared to initial steel (Figure IV.15). We observe classical evolutions of C_p: a monotonous increase of C_p in the ferritic phase up to 700°C and then a sharp increase related to Curie magnetic transition (let us mention that we get an "apparent" C_p since the phase transformation from ferritic phase to austenite which is endothermic occurs in the same temperature interval). Concerning enriched steels C and N Thermocalc® results are superposed. This confirms from previous studies [12, 86, 87] on different low alloyed steels, it has been shown that C_p does not vary much with chemical composition and remains close to the one of pure iron.

Thus,

A fit of C_p evolution for the ferritic domain gives the following regression,

$$\mathrm{C_p}\left(\frac{\mathrm{J}}{\mathrm{kg.K}}\right) = 3.319 \times 10^6 + 8.714 \times \mathrm{T}^2$$

and for the austenitic domain, we assume C_p varies linearly with temperature down to room temperature as below,

$$\mathrm{C_p}\left(\frac{\mathrm{J}}{\mathrm{kg.K}}\right) = 4.455 \times 10^6 + 395.64 \times \mathrm{T}$$

As mentioned before the C_p for a multiphase material is calculated with a linear mixture rule.

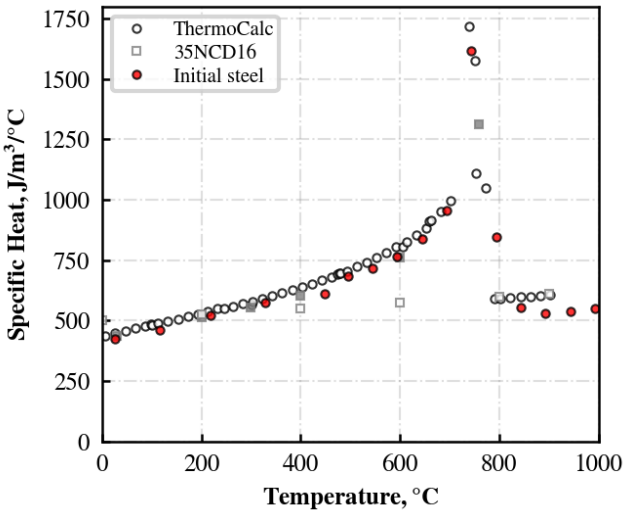

Figure IV.15: the evolution of the specific heat of the initial(23MnCrMo5) steel as a function of temperature, obtained from the experiment, Thermocalc®, and literature[86].

IV.3.2.3 Enthalpy of phase transformation

The enthalpy variation have also been measured using DSC at heating and cooling rates of 5°C/min from room temperature to 1000°C. As can be seen on Figure IV.16, during heating, the endothermic peak represents the austenite transformation from the initial microstructure (ferrite+pearlite) and Ac_1 (723°C) and Ac_3 (826°C) temperatures agree with those measured by dilatometry. Subsequently, during cooling, two convoluted exothermic peaks appear corresponding to the formation of ferrite first (60%) and then to the formation of pearlite (40%). Using the Gaussian integration, the area under the proeutectoid ferrite and pearlite peaks represent the heat flux of 3.388 J/s.°C and 6.063 J/s.°C, for a cooling rate of 5°C/min the energy released during each transformation are 40.67 J and 72.75 J respectively. The enthalpies of formation are given, $\Delta H_{\gamma\rightarrow\alpha}$ = 244.4 MJ/m^3 and $\Delta H_{\gamma\rightarrow(\alpha+Fe_3C)}$ = 655.8 MJ/m^3 for the volume of sample (277.3 mm^3) transformed.

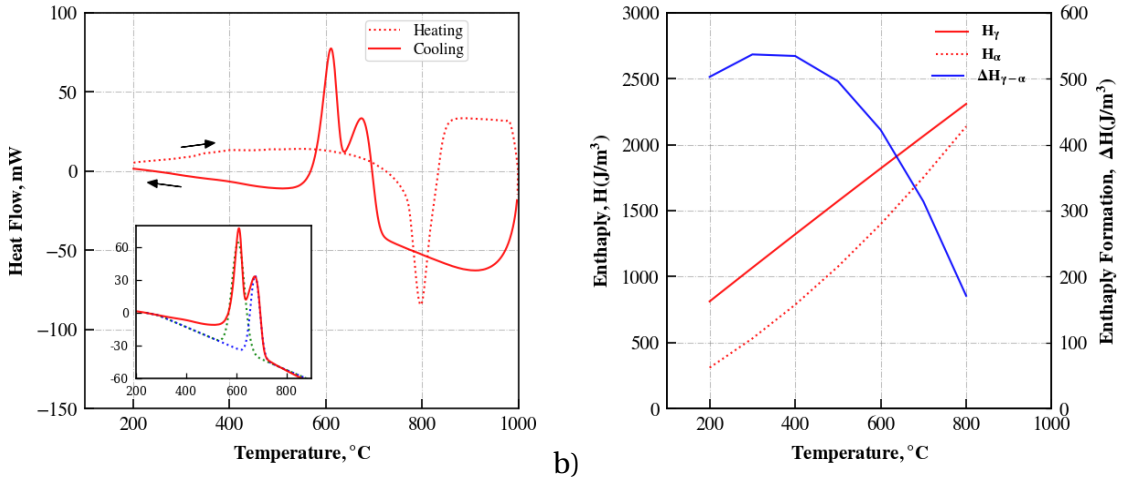

a) b)

Figure IV.16: shows a) the heat flow during heating and cooling at a rate of 5°C/min for the initial steel with an insert plot shows deconvolution of the heat flow during phase transformations during cooling b) the enthalpy transformation of the ferrite and austenite of the 23MnCrMo5 steel as a function of temperature.

The enthalpy of ferrite transformation ($\Delta H_{\gamma\rightarrow\alpha}$) as a function of temperature (Figure IV.16b) has also been calculated by the difference of the enthalpies of the ferrite

(H_α) and austenite (H_γ) phases using ThermoCalc®. The calculated enthalpy of ferrite transformation agrees with the measured one. For the ferritic transformation, this value seems inconsistent with respect to results from the literature [8, 87, 126]. The enthalpies of pearlitic transformation are consistent with the literature results, such as 660 MJ/m^3 at 600°C [8, 127, 128].

We have difficulties determining the enthalpy of the formation using the DSC equipment, with the limited cooling rate to form bainite and/or martensite microstructures. The literature gives the enthalpies of formation from austenite to bainitic transformation, 590 MJ/m^3, and martensitic transformation, 640 MJ/m^3 [36]. We have also assumed that the enthalpies of all phase transformation does not depend on C and/or N contents based on Thermocalc simulations.

IV.3.2.4 Thermal diffusivity and thermal conductivity

As illustrated in Chapter II, the thermal diffusivity measurements were performed using the laser flash method available in the IJL. The measured values of thermal diffusivity of initial steel, 0.45%mC and 0.45%mC + 0.4%mN enriched steels for a heating rate of 5°C/min in a temperature range (25°C - 1000°C) are shown in Figure IV.17 (uncertainty is less than 3%). The thermal diffusivity of ferrite+pearlite (the initial microstructure) in the initial steel decreases linearly during heating up to 750°C. For the carbon enriched steel (0.45%mC) with a martensitic initial microstructure (95±2%) the diffusivity varies slightly until 300°C and then it decreases and reaches the diffusivity of the initial steel at about 550°C. For the carbon and nitrogen enriched steel (0.45%mC+0.4%mN) with a martensitic initial microstructure, diffusivity is higher than the one for the carbon enriched specimen; first it varies relatively slightly and at 400°C it reaches the same values and evolution than the carbon enriched specimen.

Interprtetation of the diffusivity values at the beginning of heating is complex because diffusivity depends on chemical composition but also on the microstructure. The fact that the three curves join at higher temperatures could be related to the fact that the microstructures becomes closer with ferrite and cementite and that the role of chemical composition becomes less. For the austenite phase, the thermal diffusivity of our three steels are close. We have assumed that diffusivity does not depend on the chemical composition and varies linearly with the temperature as proposed below from measurements,

$$\varphi = 3.847 + 0.0021 \times T°C \ (\times 10^{-6} m^2 s^{-1})$$

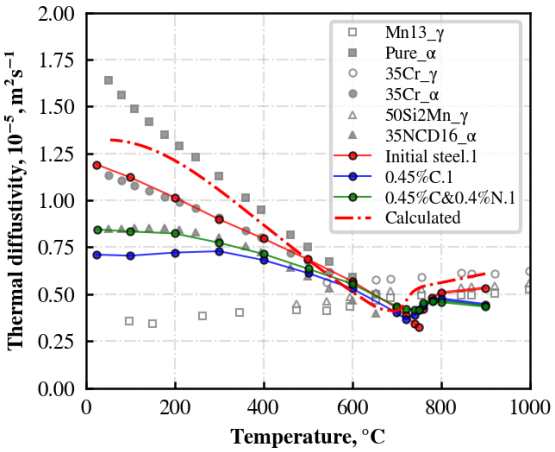

Figure IV.17: Thermal diffusivity as a function of temperature and chemical composition for the ferritic and austenitic phase of initial(23MnCrMo5), C, and CN steels – Data from literature for other steels are also given as well the calculated curve.

The measured values are in the range with the previous studies and literature data of the thermal diffusivity of different phases for different alloy steels, as shown in Figure IV.17. From the diffusivity measurements, we can now determine the thermal conductivity using the definition of the diffusivity, φ

$$\varphi = \frac{\lambda}{\rho C_p}$$

where ρ is the mass density and Cp the specific heat. From the previous determined evolutions of the specific heat (Figure IV.15) and the density (Figure IV.14), we can calculate, the evolutions of the thermal conductivity for the initial steel and of the enriched steels for the ferritic phases as shown on Figure IV.18 and for the austenite Figure IV.19. Finally, we propose following evolution laws for the conductivity that depends both on chemical composition (carbon and nitrogen contents) and microstructure: for ferrite and pearlite microstructures,

$$\lambda_{F+P} = [53.75 + (41.72 \times w_c + 1.7 \times w_n) + ((-8.5 \times w_c + 0.1 \times w_n - 8.0) \times 10^{-5}) \times T^2 + 0.0161 \times T]$$

for bainite and martensite microstructures,

$$\lambda_{B+M} = [32.612 - 23.05 \times w_c + 11.6 \times w_n + 0.0223 \times T]$$

and for the austenite,

$$\lambda_A = [10.36 + 0.0173 \times T]$$

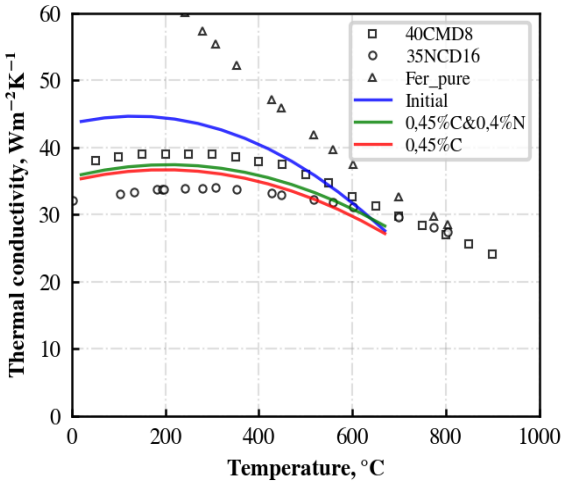

Figure IV.18: Evolution of thermal conductivity as a function of temperature and chemical composition for ferrite and pearlite phase of initial(23MnCrMo5), C, and C+N steels from various studies.

In addition, it seemed interesting to us to recalculate the evolution of thermal diffusivity versus temperature on cooling and also during the phase transformation by using our phase transformation kinetics model. Indeed, during phase transformation, we assume in our approach that the thermophysical parameters are related to the volume fractions of the phases present by a linear mixture law. The comparison between this calculation and the measured diffusivity is shown on Figure IV.17. Small discrepancy exist in austenite, the main discrepancy occurs below 500°C. This difference may be due to the prediction by calculation of 60% ferrite and 40% pearlite during continuous cooling whereas the measured fractions are 50% ferrite and 50% pearlite. On the other hand, the correlation between the calculation and experiments is satisfactory in the transformation field (720°C).

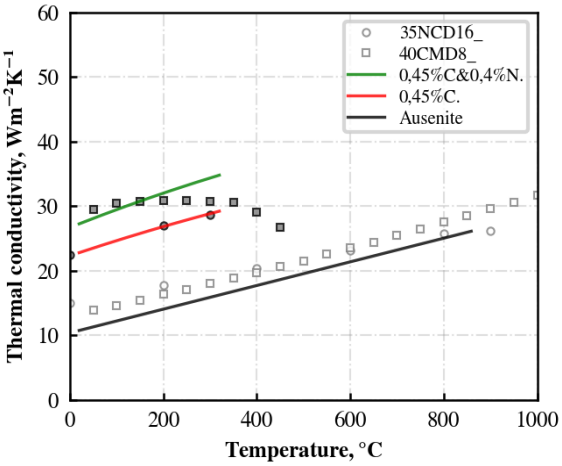

Figure IV.19: Evolution of thermal conductivity as a function of temperature and chemical composition for austenitic and martensite (red and green) phase of initial(23MnCrMo5), C, and C+N steels from various studies.

IV.4 Coupled thermo-metallo-mechanical simulation and validation: Gradient samples

The coupled thermo-metallo-mechanical model was already implemented in Finite Element software Zebulon in previous work [120] for the single (martensite) phase transformation of plain carbon steel during rapid cooling [120]. For carburized/carbonitrided steels, the main issue is to extend the implementation for the multi-phase systems in steels, including the gradients of C and/or N contents (let us mention that a multiphase model has been implemented in Zebulon for titanium alloys [129]). This former test case (fully coupled martensitic water quench) served as a reference to implement our models in Zebulon. As far as we know, very few authors have considered both the effect of carbon and nitrogen in the coupled model. As described above, the determination of the material behavior data as a function of temperature, C, and/or N contents for the different phases/constituents has been fulfilled. The metallurgical model developed previously [3, 106] and recalled Section IV.1.1 simulates the microstructure evolutions inside the samples with gradients [106] and has been implemented in Zebulon for the coupling with the thermal and mechanical models as well as all the necessary data sets.

In the following, *in situ* slow cooling HEXRD experiment results are used to validate the multi-phase system (austenite, ferrite, pearlite, high temperature constituents, bainite, and martensite) and internal stress evolution in C and/or N gradients steels during the cooling. Three types of enrichments were done: carburizing, nitriding, and carbonitriding. The carbon or nitrogen profiles measured by EPMA are given as input data, as shown in Figure IV.33, Figure IV.43, and Figure IV.53. The composition profile is asymmetrical in the carburized samples, as shown in Figure IV.33. The core kept the initial steel composition and at the edges, the carbon content does not exceed 0.65%$_m$ C, which is inside the range of validity of the model. The nitrided samples underwent some decarburization (Figure IV.47), whose depth corresponds to the depth of nitrogen penetration (400 µm). In the carbonitrided samples (Figure IV.57), the profiles of carbon content are again asymmetrical. Due to the decarburization in the nitrogen-enriched layer, the carbon profiles present a local maximum (0.5% C at ca. 0.5 mm check under the surface. The presented profiles for nitrogen correspond to nitrogen in solid solution. Indeed, the peaks corresponding to the nitrides formed at high temperatures have been discarded for better readability.

This section begins with a preprocessing stage of a coupled simulation, including the description of geometry, meshing, and boundary conditions. As we decide to

proceed with the explicit method, the efforts are taken to optimize the timestep. Then, the predictions of the evolutions of phase fractions, and internal stresses of C, N, and C+N enriched specimens will be analysed and compared to the *in situ* experiments. Comparisons between simulation and experiments will also be done for the *ex situ* experiments and different cooling conditions.

IV.4.1 Simulation conditions

For simulating the *in situ* HEXRD experiments of C and/or N enriched steels performed on the cylinders (diameter 5 mm , thickness 3mm) geometry of the samples used for HEXRD experiments. We consider a rectangular section with 2D axisymmetric elements (CAX8r) [48] with reduced integration representing the upper half of the cylindrical sample (inset in Figure IV.20). The simulation always starts at a uniform (austenitization) temperature of 900°C, as depicted in the thermal boundary condition. Z-axis (axe) is the axis of symmetry, and the displacement boundary condition are shown in Figure IV.20.

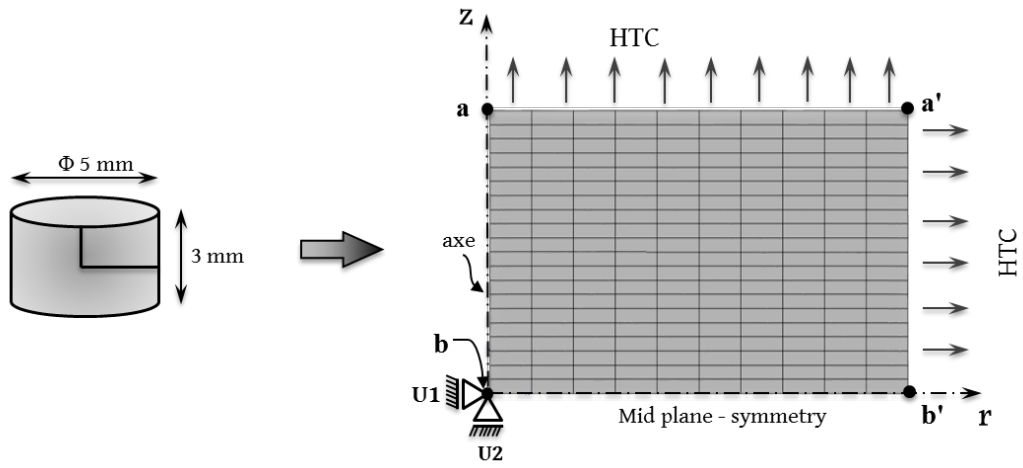

Figure IV.20: Geometry used and finite element mesh

r, θ, and z indicate the radial, circumferential, and longitudinal directions in the cylindrical frame. The nodal locations *a* and *a'* are at the surface and *b and b' are* at the core, as shown in Figure IV.20.

Of course , the simulation will give the stress tensor components distributions along the different directions. In our case, in order to compare with the average values of stress obtained from the HEXRD experiments (σ_θ-σ_z) along the composition gradients, it is necessary to calculate the mean values of the stress component in the gauge volume (see Table II.4). For example, Figure IV.21 shows the radial profiles of the tangential stress along the lines between *aa'* and *bb'*. It can be seen that depending on the position in the thickness, the stress gradients can be large. We have to mention that all specimens have not exactly the same thickness, and this uncertainty in the position of the surface (about 100 µm) can lead to errors of ±50MPa.

As described previously, temperature calculations are performed during cooling with a heat transfer coefficient as boundary condition. Generally, for cooling processes, the heat transfer coefficient along with the surface temperature is obtained from the measured temperature evolutions using the inverse method [26, 130].

Temperature measurements have been performed during the *in situ* experiments as shown in Figure IV.23. The thermal treatment (Figure IV.23) starts with cooling at a controlled rate of 2°C.s^{-1} from 900°C down to 550°C, followed by a second stage with Ar blowing down to room temperature. An iterative procedure that begins with an initial guess and compares successively calculated temperatures with measurements has been used to calculate the temperature-dependent heat transfer coefficient shown on

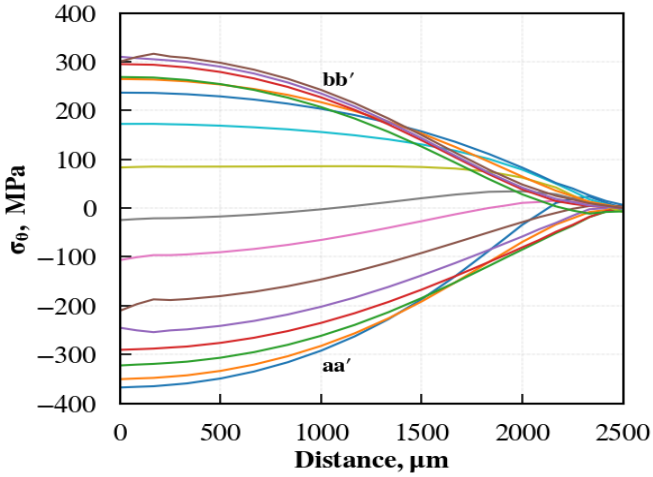

Figure IV.21: Profiles along cylinder radius of predicted tangential stress component $\sigma_\theta$for all line sets of the given mesh geometry for what sample (carburized quench oil).

Figure IV.22 (denoted 'gas'). (The two other cooling conditions will be described later on.)

For the slow cooling of the *in situ* experiments, temperature calculations using the thermal model agree well with experiments (as shown for example for carburizing on Figure IV.23). The temperature predictions show also small thermal gradients in the whole volume of all enriched samples for the entire cooling process (maximum 0.5°C).

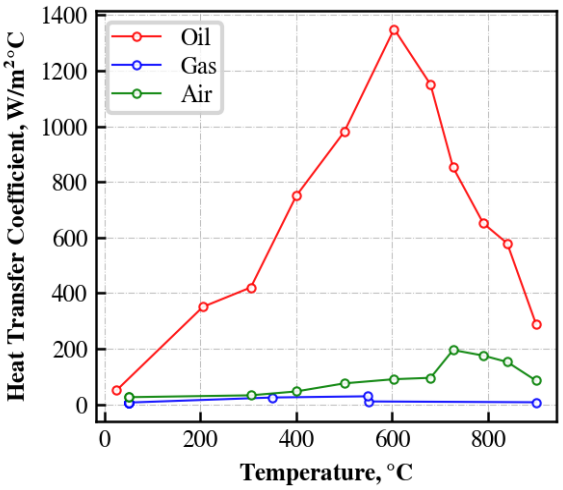

Figure IV.22: Heat transfer coefficient versus surface temperature of the cylindrical specimen for the different cooling media. (gas corresponds to the in situ experiment).

For simulating our "post-mortem" experimental results (i.e. residual stress profiles) obtained on cylindrical specimen machined out from the lamellar sample that have been enriched and cooled down, an appropriate geometry has been used.

Two cooling conditions were applied to the lamellar specimen: oil quench and calm air cooling for carbonitrided samples, and only oil quench for the carburized and nitrided samples. The cooling rate was not controlled, contrary to the *in situ* gas furnace cooling. Temperature evolutions were measured with thermocouples at the surface and at the core of a non-enriched initial steel sample [3] (see Figure IV.24 and Figure IV.25).

Mean cooling rates (between 900°C and 400°C) are respectively 50°C/s for oil quenching and 5°C/s for calm air cooling. From the measurements, the heat transfer coefficients were determined and are shown in Figure IV.22. Obviously, the heat transfer coefficient is much higher for oil quenching.

The thermal model has also been used for predicting the temperature evolutions in

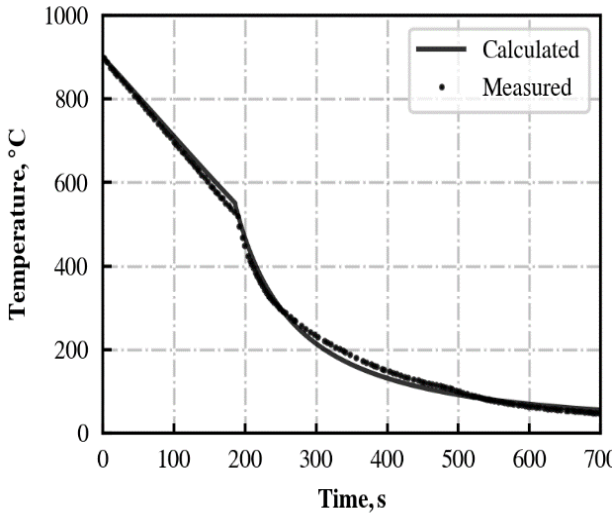

Figure IV.23: Measured temperature evolution at the sample surface during furnace gas cooling under a controlled atmosphere and calculated, considering carburized sample.

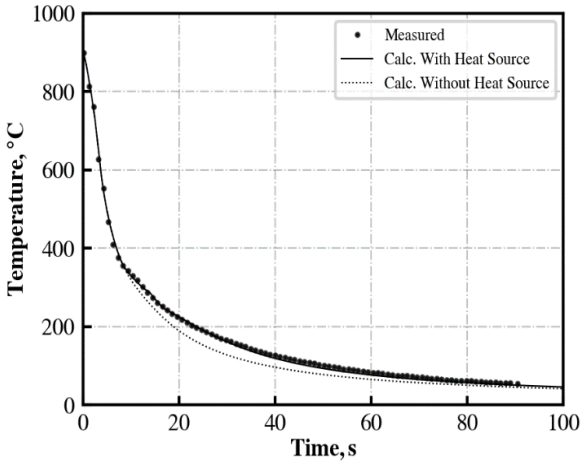

Figure IV.24: Predicted (with and without heat sources) and measured temperature evolution of oil quenched sample. The curves correspond to the average of the thermocouple measurements placed at the center and on the surface of the sample (at mid-height).

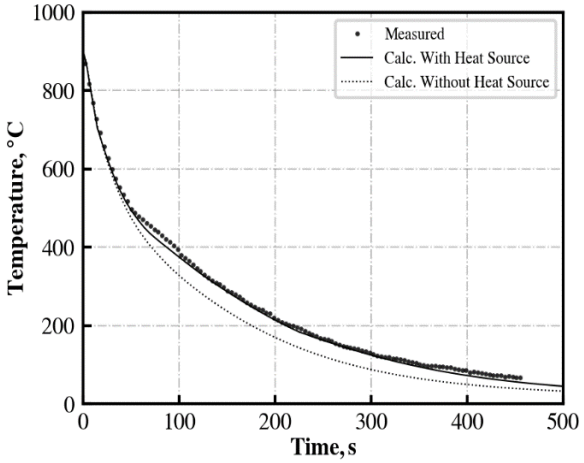

Figure IV.25: Predicted (with and without heat sources) and measured temperature evolution of calm air-cooled sample. The curves correspond to the average of the thermocouple measurements placed at the center and on the surface of the sample (at mid-height).

the sample, including the heat source term that accounts for latent heat release due to phase transformation. Figure IV.24 and Figure IV.25 show good agreement between the measured and the calculated cooling curves. Thanks to a simulation performed without latent heat, we can that its impact on the temperature predictions is not negligible.

The simulation also shows that the temperature gradients in the specimen are relatively small (the maximum difference between core and surface for oil quench is 28.5°C).

IV.4.2 Carburized gradient samples

IV.4.2.1 Phase transformations

Figure IV.26 shows the evolutions of the phase/constituents fractions (proeutectoid ferrite, bainite, martensite, austenite) according to the simulations, considering the *in-situ* experiment (temperature evolutions were presented in Figure IV.23). Two points are represented: the surface and the centre (a and b see Figure IV.20). As shown by the evolutions of the austenite fraction, the centre starts to decompose before the surface, as expected from the profile of carbon composition. Although the two considered points correspond to the largest and lowest carbon concentrations, most part of the respective kinetics are overlapped. In the centre, the simulation predicts the formation of proeutectoid ferrite (26.8%), bainite (36.2%), and martensite (36.8%) successively. At the surface, the formation of only bainite (24.54%) and martensite (72.83%) is predicted. At the end of the cooling, the simulation predicts that there remains no austenite throughout the thickness of the sample, except near the surface (less than 2% of austenite).

The same simulation curves are plotted as a function of temperature in Figure IV.27. (Let us recall that the temperature is almost homogeneous inside the simulated sample, see previous Section IV.4.1). According to the simulations, the centre starts to transform at 700°C, and the surface starts at 450°C. In the centre and at the surface, the Bs is respectively 555°C and 415°C, and the Ms is respectively 365°C and 252°C. The Bs and Ms temperatures are calculated as a function of the local carbon concentration and the effects of prior bainite transformation (Eqn. III.2). The dashed lines in Figure IV.27 show the Ms temperature expected if only the carbon concentration is accounted for, in order to show the effects of prior bainite transformation on austenite stabilization upon martensitic transformation.

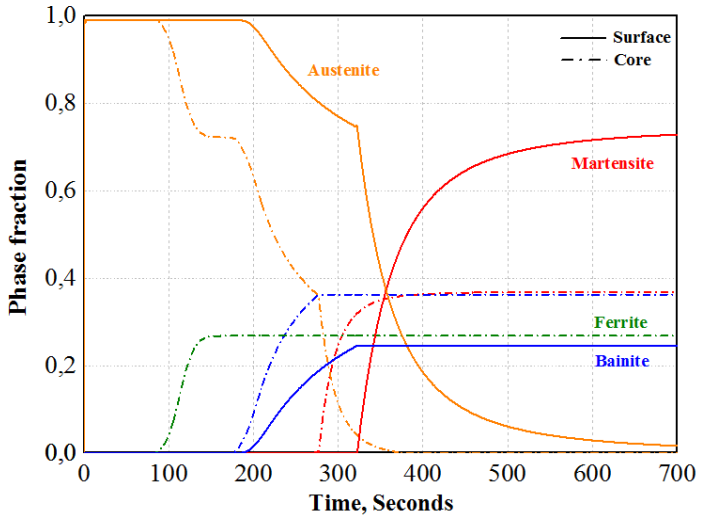

Figure IV.26: Carburized gradient sample, in situ HEXRD experiment: Prediction by the simulation of the phase/constituents fractions evolutions with time, at the surface and in the center.

Figure IV.27 compares the simulations with the kinetics established *in situ* by HEXRD (same curves as in Chapter III). In the center, the simulation overestimates the fraction

of proeutectoid ferrite. Nevertheless, it predicts a plateau of ferrite fraction from 600°C to 500°C. This interruption of the austenite decomposition is in agreement with the experiment, although the proeutectoid ferrite fraction is much lower, according to the latter.

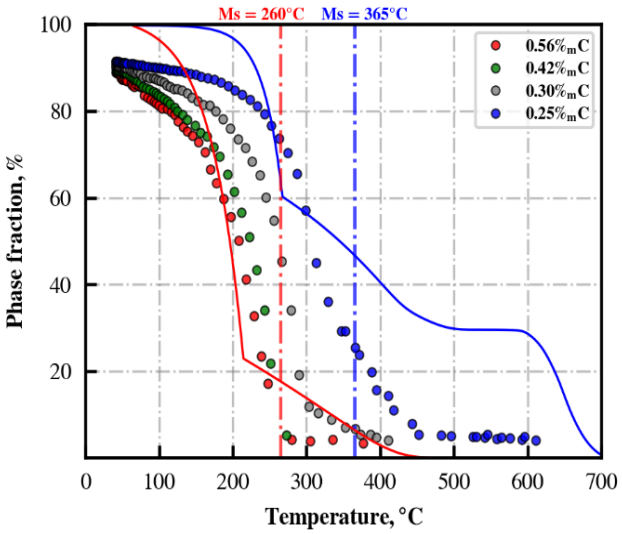

Figure IV.27: Carburized gradient sample, in situ HEXRD experiment: Prediction by the simulation of the phase/constituents fractions evolutions with time, at the surface and in the center.

Despite this discrepancy regarding the proeutectoid ferrite fraction, the start of the bainite transformation is correctly predicted with a temperature of start (Bs), which differs from the experiment by less than 50°C. A higher discrepancy could have been expected because the model takes account of the carbon enrichment of austenite upon proeutectoid ferrite formation, which induces a decrease of Bs (accounted for with Eqn. 27 in [106]). In fact, the bainite transformation starts at a higher temperature according to the simulation than measured experimentally. Besides, the fraction of bainite is correctly predicted.

The martensitic transformation start temperature (Ms) shows a discrepancy between the simulation and experiment, which is higher than 50°C. The predicted Ms is too low, which can be ascribed to the too high fraction of proeutectoid ferrite predicted, and the resulting high carbon concentration in the austenite. As a result, the final fraction of martensite predicted is lower than the experiment. Finally, the simulation predicts that the martensitic transformation eventually consumes all the remaining austenite, whereas the experimental kinetics of martensitic transformation shows a slow-down and, as a result, the presence of retained austenite (about 5%), according to HEXRD.

At the surface, the simulation predicts too fast the kinetics of bainite transformation. Consequently, the Ms temperature predicted is too low by about 40°C (effect of bainite on Ms temperature, Eqn. III.2. The martensitic transformation kinetics is correctly estimated, but, like in the center, its final slow-down is not predicted, as well as the presence of retained austenite (about 10%, according to the experiment).

Figure IV.28 shows profiles of austenite phase fraction according to the simulation and at different temperatures. It shows the sequence of phase transformations starting in the center and finishing at the surface. This is directly related to the profile of carbon composition. One can see a significant overlap of the phase transformation kinetics again throughout the sample thickness. For example, at 250°C, almost the whole thickness of the sample undergoes phase transformations simultaneously. These profiles also confirm that at the end of the cooling (below ca. 140°C), only the regions closest to the surface undergo phase transformations. This will have consequences on the formation of internal stresses, as will be seen later on.

Figure IV.29 shows the microstructural profiles at the end of the cooling according

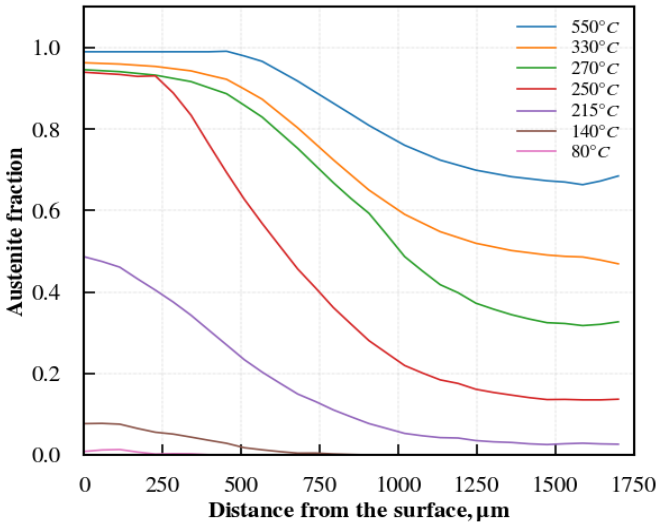

Figure IV.28: Carburized gradient sample, in situ experiment. Profiles of austenite fraction, according to the simulation and at different temperatures.

to experiments and simulation. Despite the discrepancies mentioned above, the profile of martensite fraction is correctly predicted: the fraction of martensite decreases when approaching the centre due to the lower hardenability associated with the carbon composition profile. But the fraction of proeutectoid ferrite is overestimated (see Figure IV.27, chapter III), and not only in the centre, as seen above. Finally, the experiment shows an increase of the bainite fraction towards the centre, whereas the simulation predicts a flat profile. The profile of hardness at the end of the cooling shows good agreement between the simulation and the experiment (Figure IV.30).

This study represents the first assessment of the phase transformations model introduced in [3, 106] with *in situ* tracking of phase transformation kinetics inside a carburized gradient specimen. Let us recall that the metallurgical model was calibrated on isothermal kinetics obtained in the base steel (0.25%$_m$C). We evaluated here the ability of the metallurgical model to take account of the effects of carbon concentration and of cooling are (with methods recalled in Section IV.1.1) inside a gradient sample.

Some discrepancies between simulations and experiments were unexpected. The first one is related to the overestimation of the proeutectoid ferrite fraction in the centre. Indeed, in the previous work [3], a similar condition was investigated experimentally with dilatometry sample: composition in carbon 0.25%m, and cooling rate 2°C/s. For this latter experiment, a fraction of proeutectoid ferrite of about 40% was actually found to form above 625°C. Hence, the differences between simulations and experiments could be ascribed in part to the reproducibility of the experiments. The non-prediction of the slow-down of the martensitic transformation may be related to the stabilization of austenite upon relatively slow cooling. The Koistinen Marburger law, which served to calibrate the model, was estimated on the basis of a dilatometry experiment carried out with a cooling rate of about 55°C/s. According to this dilatometry experiment, the martensite finish temperature (M_f) was equal to 240°C. Let us mention that the presence of austenite was not checked in this sample.

We also considered a carburized gradient sample enriched in the same condition as the previous one but which was quenched into oil after the enrichment treatment. The cooling is thus faster than for the *in situ* experiments (Figure IV.24). As shown in Section IV.1.1.1, the simulation predicts that the sample fully transforms to martensite throughout the sample thickness because of the high cooling rate. As a consequence, the martensitic transformation kinetics simply follows the kinetics given by the Koistinen Marburger law according to the parameters which were identified as a function of the carbon concentration (Eqn.15 in [106]). Figure IV.31 shows shows the time and temperature evolutions of the austenite fraction, calculated at the surface and in the

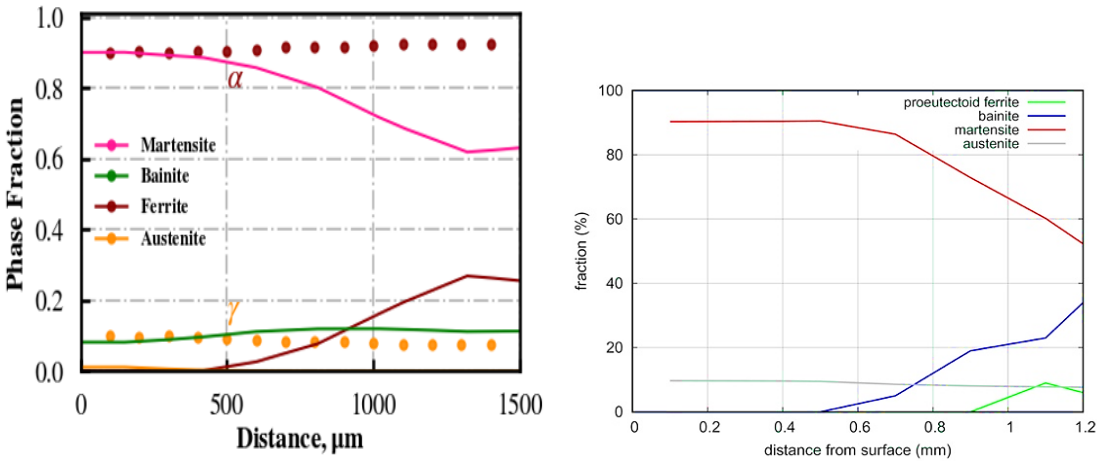

Figure IV.29: Carburized specimen, in situ HEXRD experiment. Profiles of: a) Microstructural constituents fraction (ferrite, bainite, martensite, and austenite) according to the simulation and α/α', γ phases according to HEXRD; b) Microstructural constituents according to HEXRD experiments (figure reproduced from chapter 3).

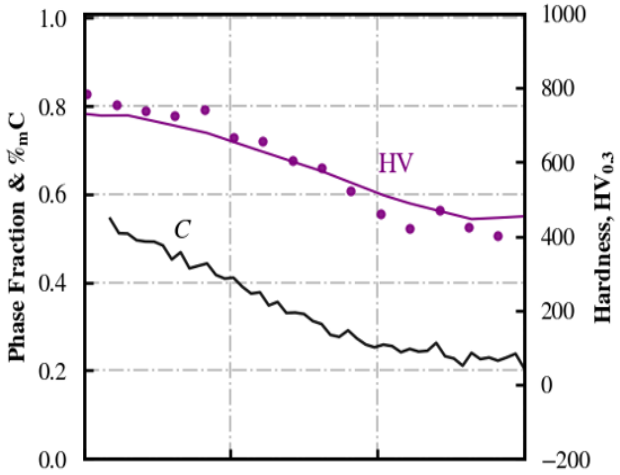

Figure IV.30: Carburized sample, in situ HEXRD experiment: a) experimental (dots) and calculated (lines) final phase fraction and hardness distributions.

center. Comparing with the previous investigated case (*in situ* HEXRD experiment), the obvious difference is that the austenite decomposes faster (see Figure IV.26). But another difference regards the fact that the kinetics at the surface and the center are fully uncorrelated for the quench into oil: there is no more the overlap which was observed for the *in situ* HEXRD experiment. This is also visible by plotting profiles of austenite phase fraction at different temperature (Figure IV.32). The profiles for the quench into oil are steeper than for the *in situ* experiment (Figure IV.28). The whole thickness of the sample never fully transforms simultaneously, whereas it was the case for the *in situ* experiment. Hence, the chronology of phase transformations (center followed by surface) is better defined and more sequential for the quench into oil than for the *in situ* experiment with slower cooling, according to the simulation. This may have consequences on the formation of internal stresses, as will be discussed later on.

Figure IV.33 shows the profiles of hardness and α/α' or γ phase fractions at the end of the oil quench, according to the simulation and the experiment. The hardness is well predicted throughout the sample thickness, and this confirms the accuracy of the empirical relationship used to calculate the hardness of martensite as a function of the carbon concentration (Eqn. 32 in [106]). The main discrepancy regards the fraction of austenite, which is underestimated by the model. The latter predicts the presence of austenite only near the edges, whereas the HEXRD experiment shows a fraction of

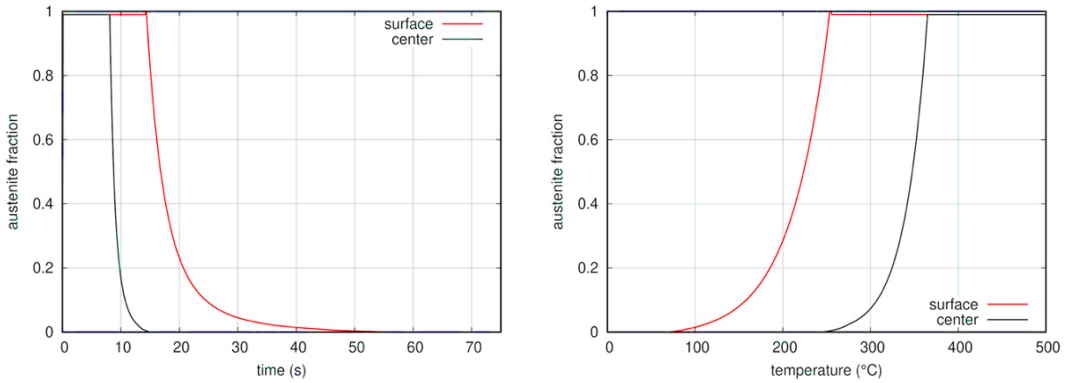

Figure IV.31: Carburized sample, quench into oil. Fraction of austenite as a function of time (left) and temperature (right) at the surface and in the center, according to the simulation.

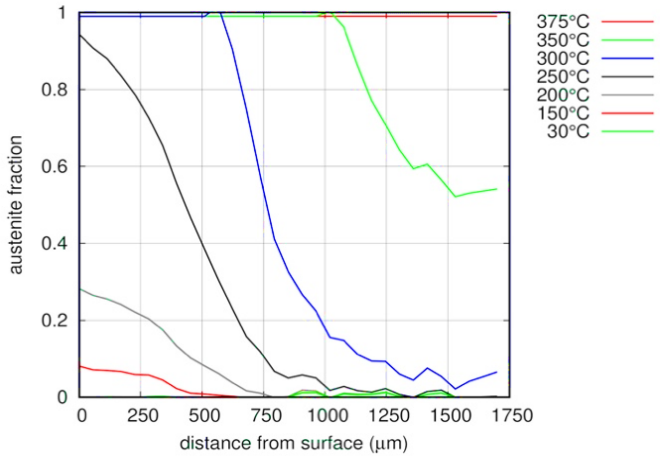

Figure IV.32: Carburized gradient sample, quench into oil. Profiles of austenite fraction, according to the simulation and at different temperatures.

austenite ranging between 5% in the center and 10% at the surface. Hence, like for the *in situ* experiment, the fraction of austenite is underestimated. This may be ascribed again to the stabilization of the austenite upon cooling, but one would expect these effects to be weaker for the oil-quenched sample, as the cooling is faster. As mentioned above, we did not measure the fraction of austenite inside the dilatometry samples, which served to establish the martensitic transformation kinetics. The latter may be less complete than suggested by the dilatometry experiments.

IV.4.2.2 Internal stresses

Figure IV.34a shows the evolutions of the tangential stress at the cylinder axis as a function of time, predicted by the simulation at the surface and in the center of the carburized gradient sample, considering the temperature evolutions during the *in situ* experiment. As mentioned previously, the temperature gradients are small because of the small sample size. As a result, no plastic strains occur during the cooling. Therefore, according to the simulations, the internal stresses only come from the phase transformation strains (volume expansion, phase transformation plasticity strain).

After 100 s, the proeutectoid ferrite transformation starts in the center. Because of the volume expansion, the center undergoes compression (negative) stress, whereas the surface, which has not started to transform, goes in tension by the reaction. The start of the bainite and martensitic transformations is also visible in the curve related to the center, as well as the bainite transformation at the surface. After 100 s, complex evolutions occur at the surface and in the center because the whole thickness of the sample

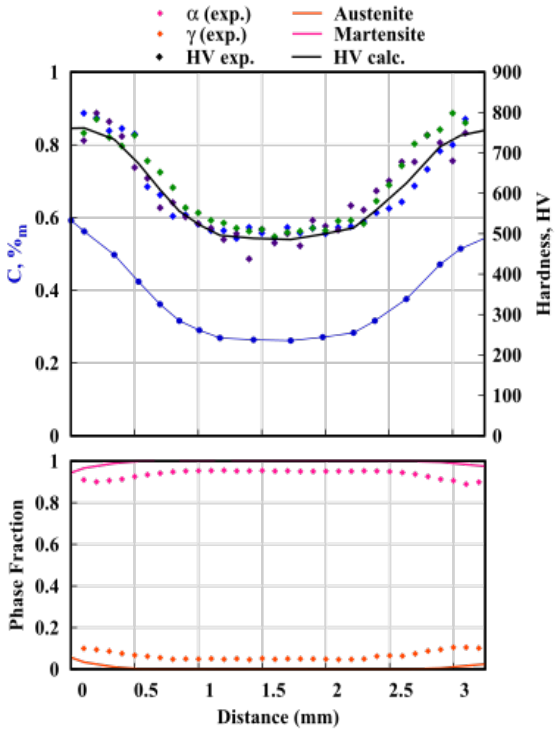

Figure IV.33: Carburized - oil quenched gradient sample. Profile of carbon concentration and hardness (dots: measurements (blue: center of the sample; green and purple: at 7 mm on each side from the center), line: calculated); Calculated profiles of phase/constituent fraction according to the simulation (lines); dots: α/α' and γ mass fraction according to HEXRD (ex situ).

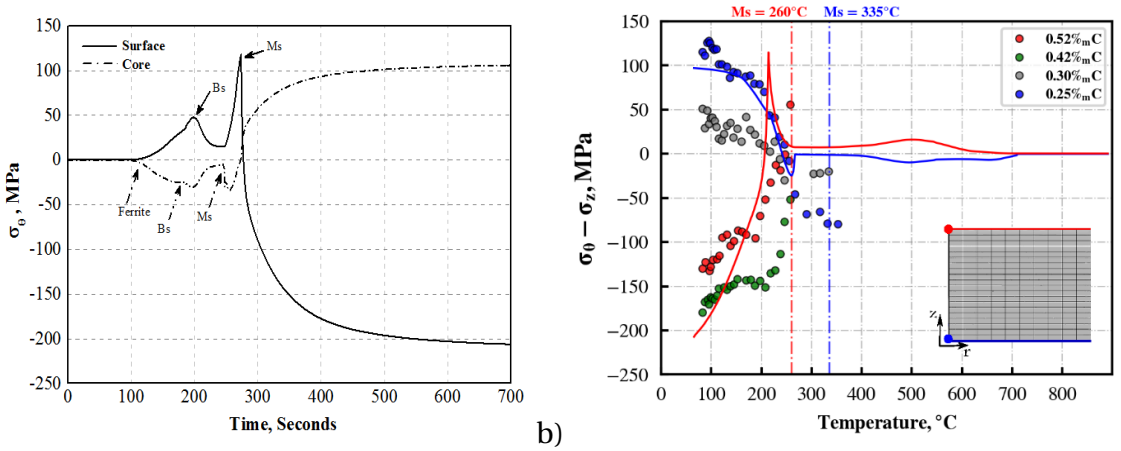

Figure IV.34: Carburized gradient sample, in situ experiment. a) Time evolutions of the tangential stress, σ_θ according to simulation, at the surface and in the centre; b) Temperature evolution of the stress difference (σ_θ-σ_z) averaged along the radius according to the simulation, at the surface and in the centre (red and blue continuous lines) and according to the experiment at four different positions.

simultaneously undergoes austenite decomposition, but at a different rate depending on the local carbon concentration (see the previous Section). Despite these evolutions, the center and the surface keep undergoing compression and tensile stress, respectively, until the start of the martensitic transformation at the surface, at about 275 s. At this stage, only the regions close to the surface undergo phase transformations, as seen before, whereas there is no evolution of the microstructure in the regions beneath anymore. This is one reason why large compression stresses form at the surface and, by reaction, compression stress in the center. About 20 s before the start of the martensitic transformation at the surface, the stress undergoes a sharp increase at this position in the sample. This is ascribed to the fact that the martensitic transformation has started in regions underneath.

The evolutions of the stress difference (σ_θ-σ_z) as a function of temperature as predicted by the simulation at the surface and the center are plotted in Figure IV.34b. It highlights again that the stresses undergo strong increase (above ca. 50 MPa) only when the martensitic transformation starts near the surface. The simulations are compared to the experiment, showing the stress evolutions determined *in situ* by HEXRD at the surface, in the center, and two intermediate positions (same curves as presented in Chapter III). Let us recall that the stresses were determined experimentally in α/α' phases but could not be established *in situ* in the γ phase. As the simulation predicts the average stress related to the mixture of α, α' and γ phases, the comparison between simulation and experiments is meaningful only when the austenite fraction starts to be negligible. In the center, this condition starts to be verified at about 250°C. At the surface, it is also the case at about 150°C. By taking this precaution, the prediction of the stress evolution in the center is satisfactory, except at the end of the cooling, where the stress is underestimated by about 25 MPa that lies in the experimental error. The discrepancies are higher at the surface (75MPa).

Figure IV.35 shows the profile of stress along the half-thickness of the sample predicted by the simulation at different temperatures. At 330°C, the stress predicted is nearly zero throughout the thickness. For decreasing temperature, the regions near the surface go to compression and the regions near the center go to tension. In the profiles at 80°C, 230°C and 330°C, a local minimum is observable (at about 500 µm depth at 230°C, for instance). This is due to the more advanced stage of the transformation at lower depth (mostly controlled by the carbon composition profile), which tends to induce compressive stress, because of the phase transformation strain.

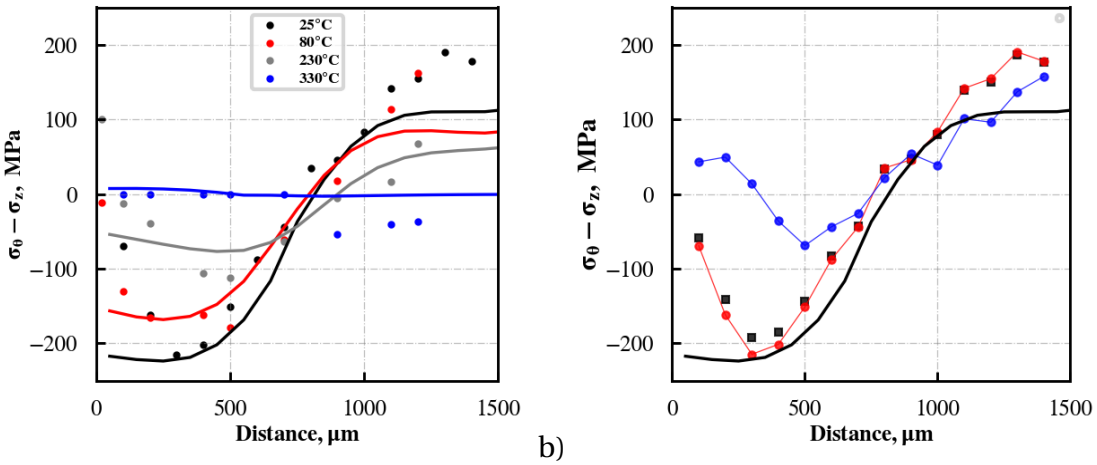

Figure IV.35: Carburized gradient sample, in situ experiment: a) Internal stress profiles along the depth of the sample at different temperatures, according to HEXRD experiments (α/α' phase, dots) and simulation (lines). b) Residual stress at room temperature, at the end of the cooling, according to HEXRD (dots: red: α/α', blue:γ, black: average) and according to the simulation (black line).

Experiments are also plotted in Figure IV.35a (dots). As mentioned above, comparison with simulation throughout the whole thickness is relevant only below about 150°C,

because of the austenite. The shape of the stress profile according to both experiments and simulation is the one expected for carburizing: compression at the surface, tension in the center. At 25°C, the stresses could be determined (*ex situ*) by HEXRD in both α/α' and γ phases. This allowed to calculate an experimental average (black dots) which can be compared to the calculated stress. At 25°C, the simulation underestimates the residual tensile stress in the center (by about 50 MPa) and it does not capture the decrease (in magnitude) of the stress when approaching the surface. This important discrepancy will be commented further later on. Apart from these discrepancies, the agreement between simulations and experiment is satisfactory. The precision of the simulations is based on the accurate knowledge of the phase transformation strains (volume change, and transformation induced plasticity). Their determination was presented in Section IV.2. Let us mention that these predictions are also based on mechanical models dedicated to the formation of stresses during treatment of carburized steels [12, 14]. The present study represents the first assessment of this model on the basis of *in situ* experiments.

We also considered a similar carburized gradient sample, but which underwent a quench into oil after enrichment and thus a faster cooling than during the *in situ* HEXRD experiment. Figure IV.36 shows the time evolutions of the radial stress at the surface and in the center of the sample, according to the simulation. Before the start of the martensitic transformation at the surface (see Figure IV.31), the low stresses are due to the temperature gradient. (Note that these stresses remained too small to induce plastic strain in austenite). The start of the martensitic transformation in the center is visible by the formation of compression stress at this point and, by reaction, tensile stress at the surface. When the martensitic transformation eventually takes place at the surface, this leads to the formation of compression stress at this point and tensile stress in the center. Hence, the same stages of stress evolutions as observed during the *in situ* HEXRD experiment are observed. However, an important difference regards the magnitude of the stress predicted, which is higher for the quench into oil than for the *in situ* experiment. This is confirmed by plotting profiles of the radial stress at different temperatures (Figure IV.37). The latter show the same evolutions as for the *in situ* experiment (Figure IV.35), but with higher magnitude of the calculated stresses.

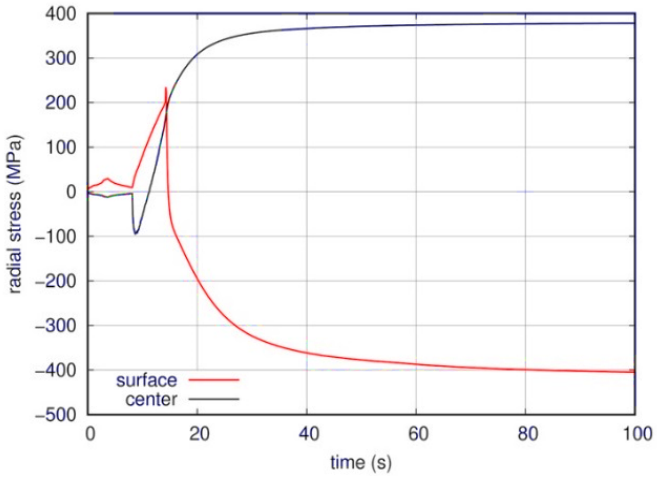

Figure IV.36: Carburized gradient sample, quench into oil. Time evolutions of the radial stress at the cylinder axis, at the surface, and in the center, according to the simulation.

Figure IV.38 shows residual stresses profiles in a carburized gradient sample that underwent quench into oil after enrichment. The simulation predicts the same shape of the residual stress profile as for the *in situ* experiment. The difference regards the magnitude of the stresses which is much higher after the faster cooling according to the simulation (for instance, -350 MPa instead of -225 MPa near the surface). However, the HEXRD (*ex situ*) experiments do not show that the residual stresses are significantly higher after the oil quench than after the *in situ* experiment. These are even slightly lower

after the oil quench, especially in the center (100 MPa instead of 150 MPa). As a result, the calculated residual stress is overestimated in the center, by the simulation of the oil quench. Near the surface, the lower magnitude of the stress is again not captured by the simulation, like for the simulation of the *in situ* experiment. At this stage, it is not possible to interpret the prediction of higher stresses upon faster cooling (oil quench vs. *in situ* experiment). One can postulate two origins: the higher phase transformation strains associated with martensitic transformation; the more sequential phase transformations in center then at surface, which may have consequences on the phase transformation plasticity strains. This will be analyzed further later on.

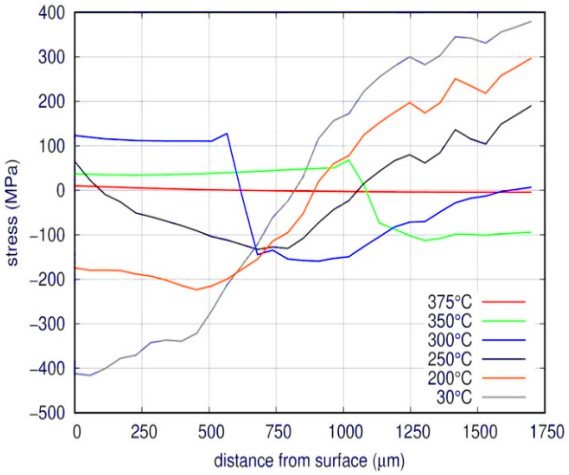

Figure IV.37: Carburized gradient sample, quench into oil. Profiles of radial stress along the cylinder axis, according to the simulation and at different temperatures.

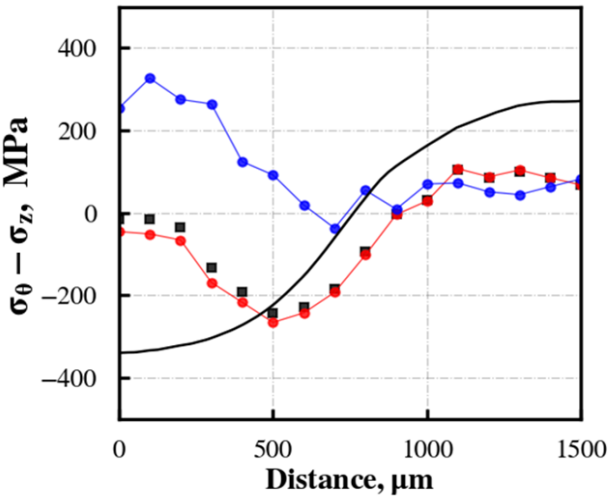

Figure IV.38: Carburized gradient sample oil quenched after enrichment. Residual stress at room temperature, according to HEXRD (dots: red: α/α', blue:γ, and black: average) and according to the simulation (black line).

IV.4.3 Nitrided gradient samples

IV.4.3.1 Phase transformations

Figure IV.39 shows the predictions by the simulation of the phase/constituent fractions time evolutions, considering the nitrided gradient sample and the *in situ* HEXRD experiment. Let us recall that in the presence of nitrogen, the austenite decomposes to

a complex microstructure which was termed as "High Temperature Constituent" HTC in previous works (See Section IV.1.1.1). The evolutions are represented at two points: the surface (which is enriched in nitrogen and slightly depleted in carbon) and the center, which kept the initial carbon composition of the steel. The evolutions of the austenite fraction show that the austenite decomposes much faster at the surface (in less than 150 s) than in the center (about 360 s). The overlap between both kinetics is also limited. This simulation result is expected from the experiments presented in Chapter III, as well as previous works: the enrichment in nitrogen induces a drastic loss of hardenability. The simulation predicts that the austenite fully decomposes to HTC (continuous green line) at the surface, whereas the center follows a usual sequence: proeutectoid ferrite followed by bainite and martensite.

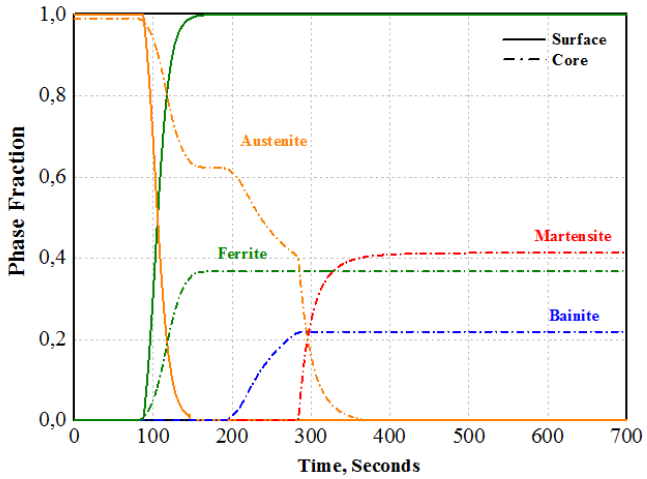

Figure IV.39: Nitrided gradient sample, simulation of in situ experiment. Evolution of the phase/constituent fractions predicted by the simulation, at the surface and in the center of the sample.

Figure IV.40 shows profiles of austenite fraction at different temperatures, according to the simulation. Two regions are visible: the nitrogen-enriched case (down to ca. 400 µm) and the interior. The former decomposes faster to the HTC, and the latter transforms more slowly and at a uniform rate because of the homogeneous carbon concentration. Inside the nitrogen-enriched case, the faster decomposition of austenite near the surface is due to the higher nitrogen concentration (see Figure IV.40), which makes decreases the Ae_3 temperature, as accounted for by the metallurgical model. (Note that a flat profile of carbon is considered for simplicity, despite the slight depletion measured experimentally, see Figure IV.40). At the end of the cooling, the nitrogen-enriched case is fully decomposed in HTC.

Figure IV.41 shows the fraction of decomposed austenite as a function of temperature, considering the surface and the center. The faster decomposition at the nitrogen-enriched surface is again highlighted, as well as the limited overlap between respective kinetics. The fraction of α/α' phase according to *in situ* HEXRD experiment is also plotted in Figure IV.41 (same curves as in chapter III). Despite the limited temperature range which could be examined experimentally (below 275°C), simulation and experiment are in agreement in the sense that the austenite decomposition is more advanced at the surface than in the center. However, the simulation does not predict the slow-down of the phase transformation kinetics at both points and at the end of the cooling. In the center, this corresponds to the martensitic transformation, which is not complete, and this was discussed when considering the carburized gradient sample. At the surface, the metallurgical model predicts a full decomposition of the austenite. This is because the HTC is assumed to contain no austenite on the basis of previous experiments [3, 4], in which the formation of the HTC was studied during isothermal treatments. One possible origin of the discrepancy between the simulation and experiment at the surface is that the

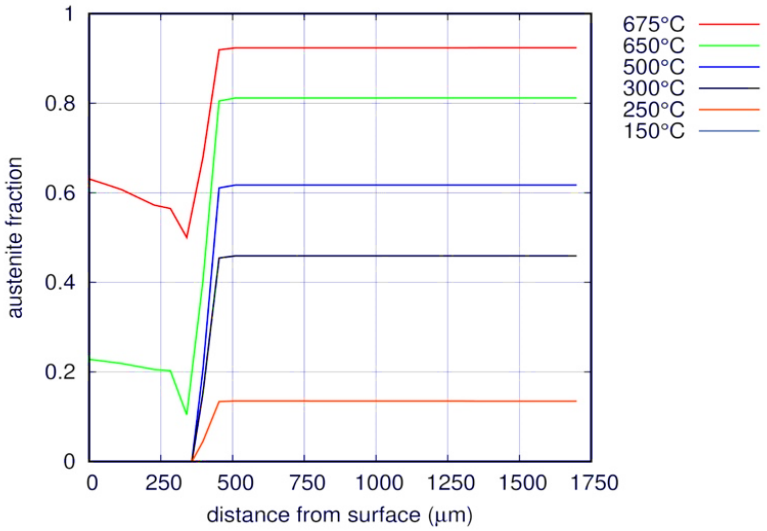

Figure IV.40: Nitrided gradient sample, in situ experiment. Profiles of austenite fraction, according to the simulation and at different temperatures.

austenite actually did not fully decompose above the Bs temperature, letting some bainite and martensite form. The latter phase transformations are more likely to be incomplete. Let us mention, though, that in prior work [106], the simulation of continuous cooling at 2°C/s showed very good agreement with the experiment when considering a nitrided dilatometry sample with similar homogeneous composition in C, N. But from previous work on the simulation of phase transformation kinetics in the presence of nitrogen [3], it is known that the austenite decomposition kinetics is highly sensitive to the nitrogen concentration. This effect of nitrogen concentration is not predicted with precision for the moment by our metallurgical model (contrary to the effect of carbon).

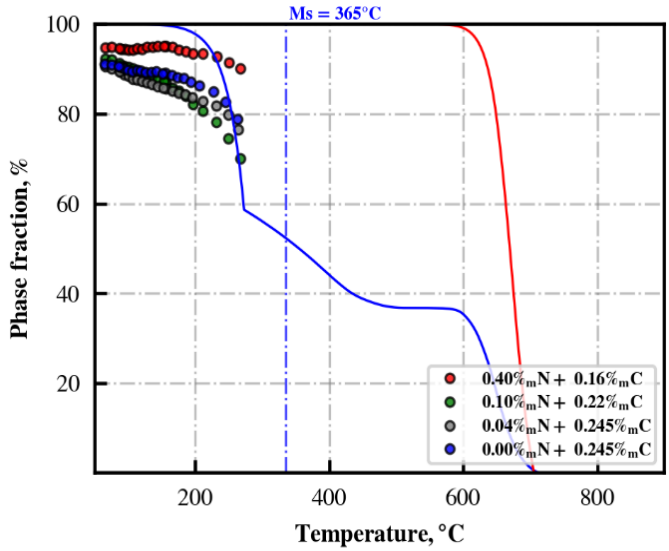

Figure IV.41: Nitrided gradient sample, in situ HEXRD experiment. Evolution, as a function of temperature, of α/α' mass fraction according to HEXRD (dots) and according to simulation (lines).

Concerning the final microstructure distribution (Figure IV.42), the simulation predicts a simple profile: 100% of HTC inside the N-enriched case (down to 400 µm) and, underneath, a mixture of proeutectoid ferrite (26.8%), bainite (36.2%), and martensite (36.8%). In the latter region, the fractions of each constituent show flat profiles, as expected because of the flat profile of carbon concentration. (Let us recall that no effects of stresses on phase transformation kinetics were accounted for). In both regions, the fraction of austenite is underestimated, for the reasons mentioned above. However,

one can see that the underestimation of the austenite fraction is less significant inside the nitrogen-enriched case (especially when approaching the surface) than underneath. This probably means that most of the austenite decomposition actually occurred above the Bs temperature, especially in the regions richest in nitrogen. Below the nitrogen-enriched case, a significant fraction of proeutectoid ferrite is predicted. This result is in disagreement with the profile of microstructure which had been envisaged in Chapter III: a mixture of bainite formed at low temperature and martensite. Despite this contradiction, the hardness profile, according to the simulation is in good agreement with the measurements (Figure IV.42), throughout the sample thickness.

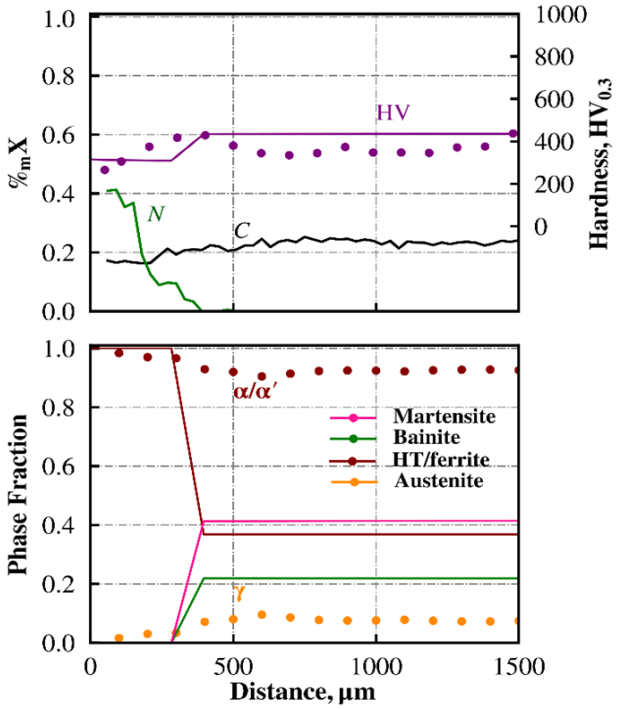

Figure IV.42: Nitrided sample, in situ experiment. a) experimental (dots) and calculated (lines) final phase fraction and hardness distributions along with the carbon and nitrogen profiles b) residual stress difference profiles: experimental (austenite, γ (blue), α/α' (red), macrostress (black squares) and calculated (black line).

We also considered a nitrided gradient sample enriched in nitrogen in similar conditions, but which underwent a quench into oil, and thus a faster cooling than during the *in situ* HEXRD experiment presented above. In this sample and for the quench into oil, the simulation predicts that the whole thickness of the sample will undergo martensitic transformation, and at a similar rate at each point. This is because the current metallurgical model assumes that the parameters of the Koistinen Marburger law have no dependence on the nitrogen concentration (see Section IV.1.1). There is a dependence of the carbon concentration, but a flat composition profile was assumed for the calculations on this sample. The only difference in martensitic transformation kinetics between the surface and the center comes from the small temperature gradient. Because of the similar kinetics inside the whole sample thickness, the corresponding simulations are not plotted.

At the end of the cooling, the simulation predicts a full-martensite microstructure throughout the sample thickness (Figure IV.43). The hardness profile calculated is in good agreement with the measurements, which validates the empirical formula (Eqn. 32 in [106]) used to calculate the hardness of martensite as a function of carbon and nitrogen concentrations. Note that this sample was not examined *ex situ* by HEXRD; experimental data for α/α' and γ phase fractions are thus not available.

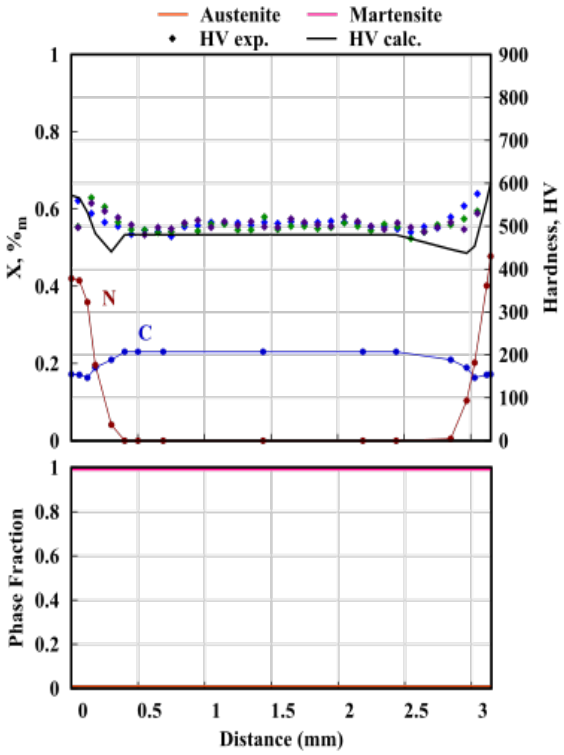

Figure IV.43: Nitrided oil quenched gradient sample. Profile of carbon/nitrogen concentrations and hardness (dots: measurements (blue: center of the sample, green and purple: at 7 mm on each side of the centre); line: calculated), line: calculated); Calculated profiles of microstructures.

IV.4.3.2 Internal stresses

Figure IV.44 shows the evolutions of the tangential stress σ_θ and axial stress σ_z at three representative points: the surface, the center, and an intermediate position (mid) located under the nitrogen enriched case (depth 400 µm), considering the nitrided gradient sample and the temperature evolutions during the *in situ* experiment. Like for the carburized specimen, three stages can be identified. Before about 80 s, no phase transformations have occurred yet, and the thermal stresses are negligible. Until about 300 s, complex evolutions occur, as a result of the phase transformation strains generated throughout the sample thickness. The arrows highlight that when new phase/constituents (ferrite, bainite, martensite) start to form, the phase transformation strain induces a decrease of the local stress. However, the stress evolutions depend on the evolutions which occur throughout the whole thickness of the sample. After 300 s the austenite decomposition mostly occurs below the nitrogen-enriched case, which undergoes a martensitic transformation. As a result, this region is put into compression, while the other parts of the sample go in tension, by reaction. In particular, the surface ends up with tensile stresses. This unusual evolution is already in agreement with the experimental HEXRD *in situ* study.

Figure IV.45 shows profiles of the radial stress at the cylinder axis and at different temperatures, according to the simulation. The effect of the simple phase transformations sequence (N-enriched case followed by the center) is visible: the N-enriched case goes first in compression, due to the faster phase transformation, whereas the inner regions go into tension. When the phase transformation takes place below the N-enriched case, compression stresses are generated, with decreasing stress when approaching the center. By reaction, the N-enriched case goes into tension. The high tensile stress eventually generated near the surface (350 MPa) may come, in part, from the fact that it equilibrates the compression stresses generated over a larger depth, below the N-enriched case.

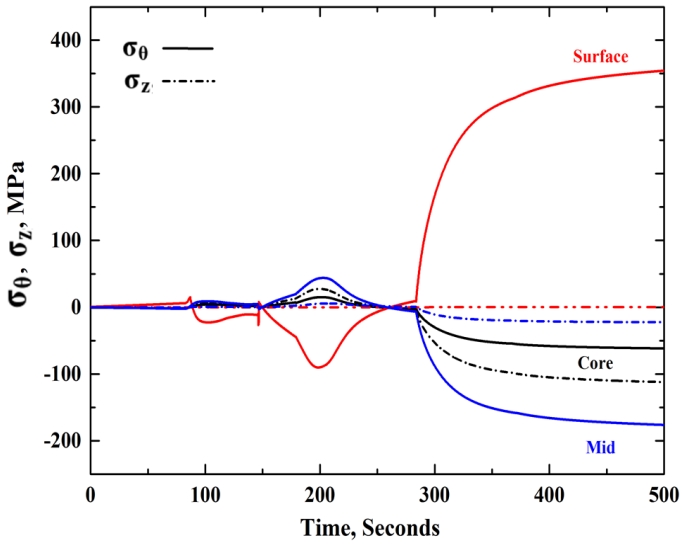

Figure IV.44: Nitrided gradient sample, simulation of in situ experiment. Time evolutions of the tangential stress σ_θ and axial stress σ_z at the cylinder axis, at the surface, in the center, and an intermediate position (mid) located under the nitrogen enriched case (depth 400 µm).

Figure IV.46 shows the calculated evolutions of the stress difference (σ_θ-σ_z), as a function of temperature and averaged over the cylinder radius, at the surface and in the center. One identifies again the three stages of the stresses evolutions, which were mentioned above. The stresses determined experimentally *in situ* by HEXRD are also plotted (same curves as in Chapter III). The simulation achieves to predict the most characteristic feature of stresses evolutions in nitrogen-enriched samples (see Chapter III): the build-up of tensile internal stresses inside the nitrogen-enriched case. Besides, the stress in the center is nearly equal to zero, in agreement with the experiment. However, the tensile residual stress calculated at the surface at the end of the cooling, 275 MPa, is underestimated, compared to the experiment, 500 MPa.

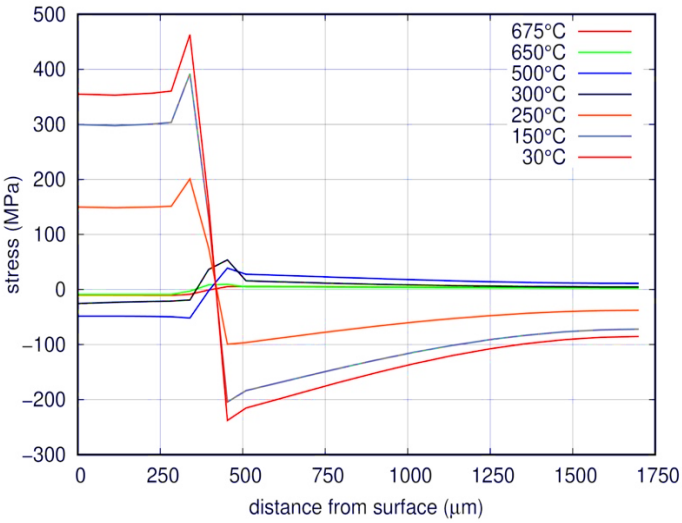

Figure IV.45: Nitrided gradient sample, in situ HEXRD experiment. Profiles of radial stress along the cylinder axis, according to the simulation and at different temperatures.

The profile of residual stresses difference according to the simulation (Figure IV.47, black line) shows tensile stresses over a depth of ca. 400 µm, compression stresses between 400 µm and 1250 µm, and stresses close to zero in the center. It is in agreement with the experimental profile main feature: the presence of tensile stresses in the nitrogen-enriched layer. However, it can be seen again that the residual stresses are

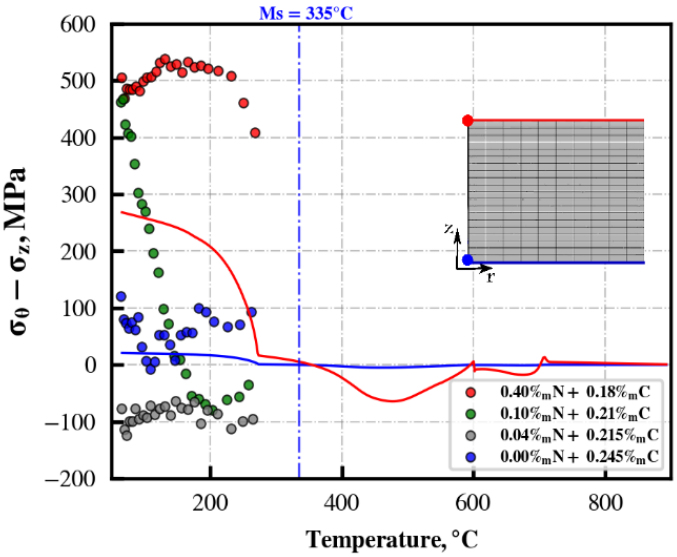

Figure IV.46: Nitrided gradient sample, simulation of in situ experiment. Evolution as a function of temperature of the stress difference (σ_θ-σ_z), averaged over the cylinder radius, at the surface and in the center.

underestimated in the nitrogen-enriched case. Let us point out that the profile of stress below the N-enriched case (compression at ca. 400 µm, close to zero in the center) does not come from any effect of phase transformations chronology. Indeed, the simulations presented above showed that all this region of the sample transforms simultaneously upon cooling, because of the uniform carbon concentration.

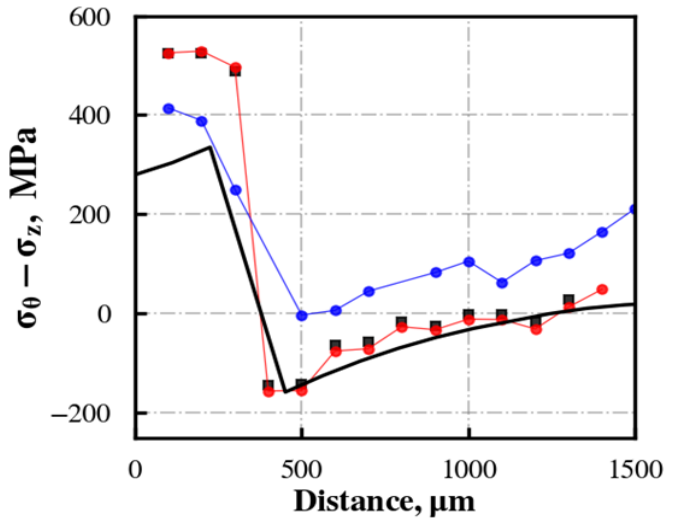

Figure IV.47: Nitrided gradient specimen, HEXRD in situ experiment. Profile of residual stress difference (σ_θ-σ_z) averaged over the cylinder radius according to the simulation (black line) and the HEXRD experiment (black dots: average, red dots: α/α' phase, blue dots: γ phase).

We also considered a nitrided gradient sample enriched in the same conditions and quenched into the oil. The simulation predicts low residual stresses, and these are not presented here for the sake of brevity. For instance, the radial stress remains lower than 60 MPa (tension or compression) throughout the sample thickness and in the cylinder axis. The reason is that the whole thickness of the sample undergoes a nearly simultaneous martensitic transformation and that the transformation strain (volumic variation) shows only a relatively small variation due to the (C+N) content. Let us mention that the residual stresses were not determined by HEXRD for this sample. At this point, one can notice

that single nitriding has limited strengthening potential compared to carburizing and carbonitriding. This regards the hardness and the residual stress at the surface.

IV.4.4 Carbonitrided gradient samples

IV.4.4.1 Phase transformations

Figure IV.48 shows the evolutions of phase/constituent fractions predicted in the carbonitrided gradient sample, considering the *in situ* HEXRD experiments, at the surface of the sample, in the center and at an intermediate position (labeled "mid," at 250µm depth, located below the nitrogen-enriched case). Let us recall that *in situ* tracking of the phase transformations by HEXRD could not be achieved for this sample. The evolutions of austenite fraction at the three positions give an overview of the chronology of phase transformations. The surface transforms at first due to the enrichment in nitrogen. The "midpoint" (right beneath the nitrogen-enriched case), which has a higher carbon concentration than in the center (see Chapter III), transforms at last. The center shows intermediate kinetics of austenite decomposition. There is limited overlap between the kinetics at the surface and underneath. But below the nitrogen-enriched case, the kinetics are more overlapped. The surface fully transforms to High Temperature Constituent (HTC), the center to a mixture of ferrite, bainite and martensite, and the midpoint to a mixture of bainite and martensite.

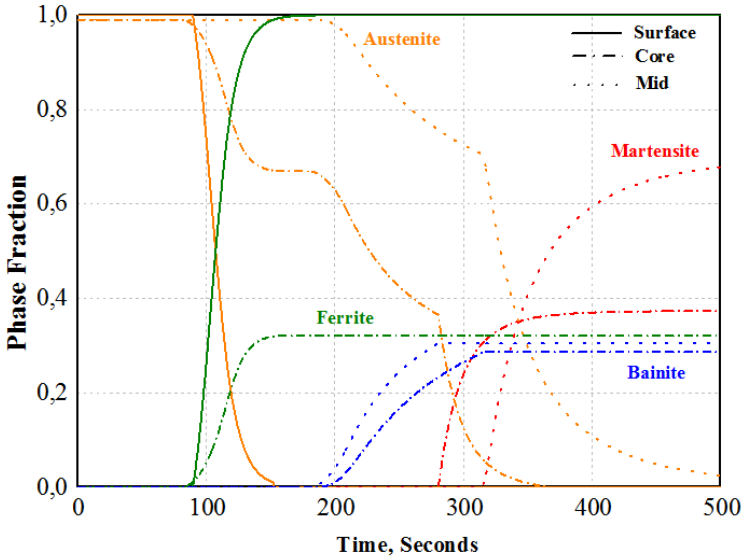

Figure IV.48: Carbonitrided gradient sample, simulation of in situ experiment. Evolution of the phase/constituent fractions predicted by the simulation, at the surface of the sample, in the center and at an intermediated position (labelled "mid," at 250µm depth, located below the nitrogen-enriched case).

Figure IV.49 shows profiles of austenite fraction at different temperatures, according to the simulation. Like for the nitrided specimen and the *in situ* experiment, main characteristic feature is the faster austenite decomposition inside the nitrogen-enriched case. But the difference is that there is now a gradient of austenite decomposition kinetics below this case, with faster kinetics when approaching the center, as imposed by the carbon concentration gradient. Hence, the carbonitrided sample exhibits three regions: the surface, the center and an intermediate region under the N-enriched case. It is not enriched in nitrogen, but it is enriched in carbon, and it thus undergoes the slowest phase transformations. This was different for the carburized and the nitrided gradient samples, inside which only two regions could be identified (the surface and the center),

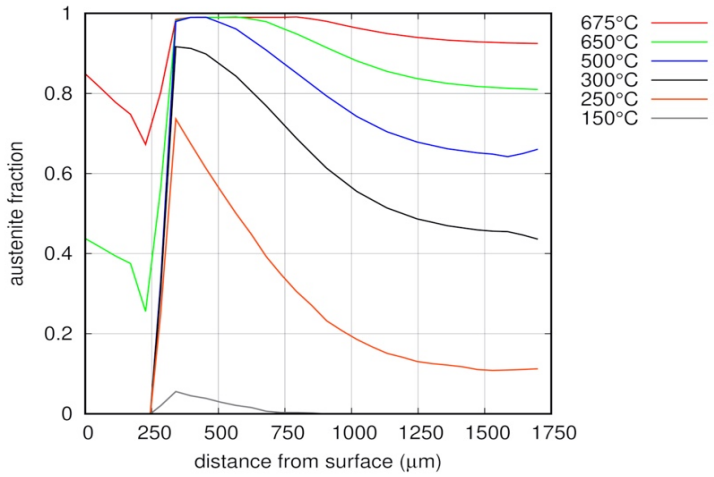

Figure IV.49: Carbonitrided gradient sample, in situ experiment. Profiles of austenite fraction, according to the simulation, at different temperatures.

Figure IV.50 shows the profiles of phases/constituents fractions predicted by the simulation at the end of the *in situ* HEXRD experiment. The nitrogen-enriched case (down to 400 µm) is almost fully transformed to the HTC with a few bainite and martensite, whereas the regions underneath present a gradient of microstructure with decreasing fraction of martensite when approaching the center, to the benefit of bainite and proeutectoid ferrite. The latter phase is present only in the innermost region of the sample (below depth ca. 750 µm). In the whole thickness of the sample, there is no significant fraction of austenite, according to the simulation, except a few percent near 600 µm depth.

However, a large amount of residual austenite is present in the sample according to the HEXRD experiment, with the lowest fraction (5%) in the center and the highest fraction in the nitrogen-enriched case (17%). The possible origins for the austenite fraction underestimation in the regions below the nitrogen-enriched case have already been mentioned in the Section on the carburized gradient sample. Inside the nitrogen-enriched case, the simulation predicts the formation of almost 100% HT Constituent. As evoked for the nitrided specimen, the kinetics of austenite decomposition in the nitrogen-enriched case may have been overestimated by the simulation, and more significant part may actually have occurred below the Bs temperature. One can also notice that the fraction of austenite in the nitrogen-enriched case measured by HEXRD is higher in the carbonitrided than in the nitrided sample. This may be related to the higher carbon concentration, which stabilizes the austenite. The metallurgical model can actually predict empirically the slower formation of HTC when the carbon concentration is increased (see Figure IV.3a). But the mitigation by the carbon of the HTC formation kinetics is stronger than predicted, according to this experiment.

The calculated profile of hardness shows a good agreement with the measurements below the nitrogen-enriched case, but higher discrepancies are found in the latter. In the outermost region, the hardness is correctly predicted. Between about 250 µm and 400 µm, the hardness is underestimated. This may be ascribed to the fact that significant part of the austenite may have decomposed below Bs, contrary to model's prediction. The model may also underestimate the hardness of the HTC when it forms under anisothermal conditions: empirical hardness laws are based on isothermal experiments. This is more developed in [106].

We also considered a carbonitrided gradient sample quenched into oil, hence which underwent faster cooling than during the *in situ* HEXRD experiment. In this sample, the simulation predicts a full martensitic transformation throughout the whole thickness of the sample, and negligible fraction of retained austenite. Figure IV.51 shows the evolutions of the austenite fraction as a function of time and temperature, at the surface

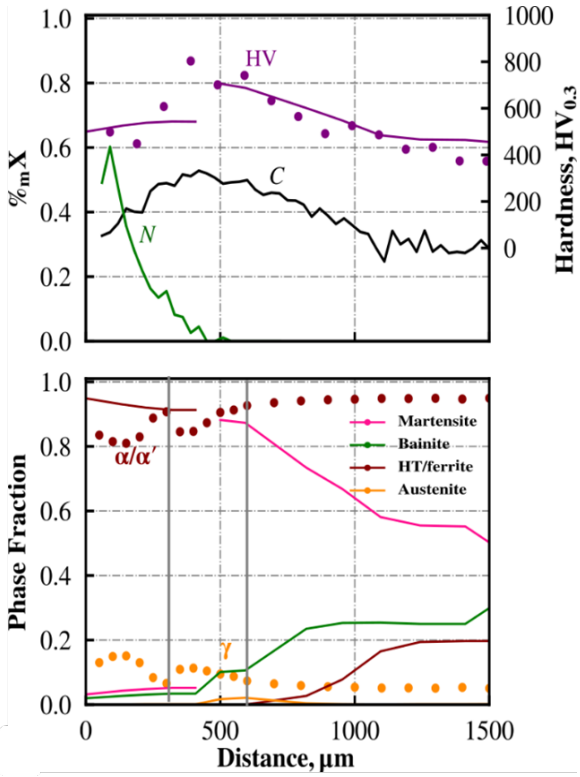

Figure IV.50: Carbonitrided gradient sample, in situ experiment, at the end of the cooling: profiles of hardness according to simulation (line) and experiment (dots), of carbon and nitrogen concentration, of phase/constituent fraction according to the simulation (lines), of α/α' and γ phases according to HEXRD (dots).

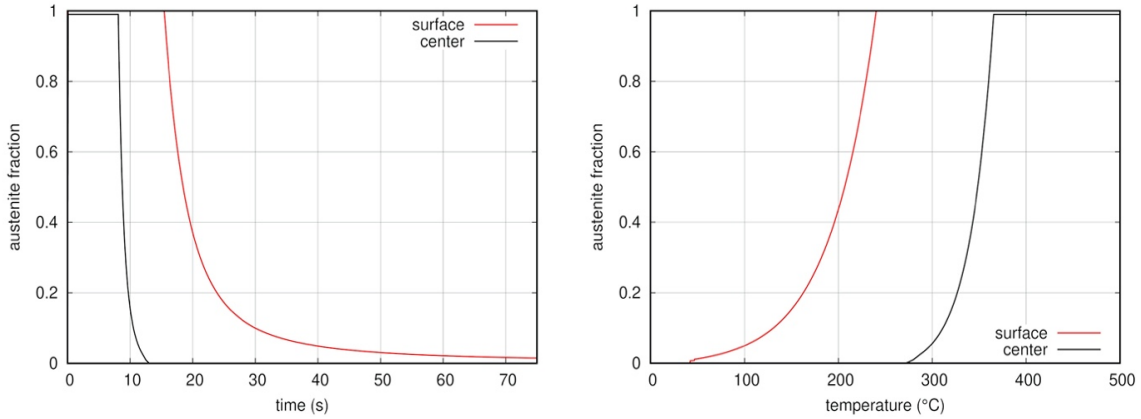

Figure IV.51: Carbonitrided sample, quench into oil. Fraction of austenite as a function of time (left) and temperature (right) at the surface and in the center, according to the simulation.

and in the center of the sample, according to the simulation. The evolutions are similar to those encountered with the carburized sample quenched into oil, with fully uncorrelated kinetics. Figure IV.52 shows profiles of austenite fraction at different temperatures. The chronology of the phase transformations conforms to the usual one: the transformations start in the center, followed by the surface. Like for the carburized, oil quenched sample (Figure IV.32), steep profiles of austenite fraction are obtained, whereas smoother profiles were obtained when considering the *in situ* experiment.

Figure IV.53a compares the profiles of hardness according to the simulations and the measurements. These show a good agreement, except near the surface, where the hardness is overestimated, in presence of nitrogen. The phase transformation model also underestimates the fraction of residual austenite, which goes up to about 10% according to the measurements by HEXRD. As mentioned when considering the carburized and nitrided samples, it is thought that the phase transformations model underestimates the stabilization of the austenite upon the martensitic transformation.

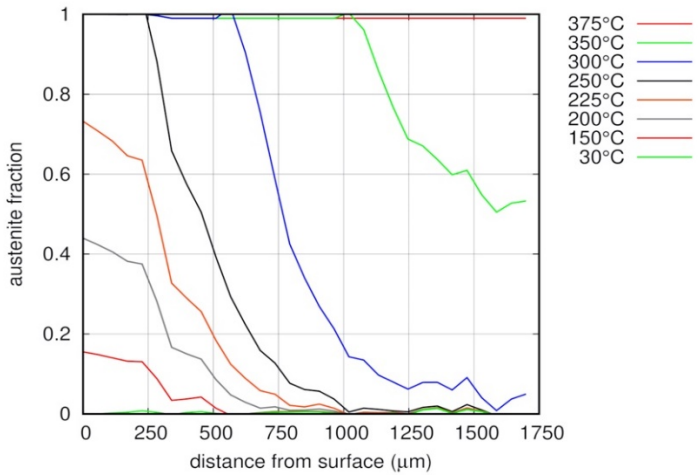

Figure IV.52: Carbonitrided sample, quench into oil. Profiles of austenite fraction, according to the simulation and at different temperatures.

We also considered a carbonitrided gradient sample which underwent a cooling in air. As shown in Figure IV.25, this corresponds to an intermediate cooling rate between the quench into oil (fastest cooling) and the *in situ* experiment (slowest cooling). Figure IV.54 shows the evolutions with time and temperature of the austenite fraction, according to the simulations and at three representative points: the surface, the center and an intermediate point (mid) located just below the nitrogen-enriched case, at 500 µm depth. The evolutions are similar as for the *in situ* experiment (Figure IV.48), as the cooling rate remains slow enough to allow phase transformations above the Ms temperature. The surface still undergoes the fastest austenite decomposition kinetics, due to the enrichment in nitrogen, the center, intermediate kinetics, while the mid point has the slowest kinetics, because of the high local carbon concentration. Most significant difference with the *in situ* experiment is that the kinetics at the surface and in the center are more overlapped.

Figure IV.55 shows the corresponding evolutions of phase/constituents fractions (HTC, bainite, martensite). The formation of HTC is incomplete because of the relatively fast cooling (faster than for *in situ* experiment), and some fraction of bainite and martensite is formed at the end of the cooling. In the center, bainite is formed in majority (whereas a mixture of proeutectoid ferrite and bainite was obtained for the *in situ* experiment, with slower cooling). At the intermediate point (mid), the model predicts the formation of a mixture of bainite and martensite (with more martensite than for the simulation of *in situ* experiment). All these evolutions are consistent with the local concentrations in carbon and nitrogen.

Figure IV.56 shows profiles of austenite fraction predicted by the simulation at

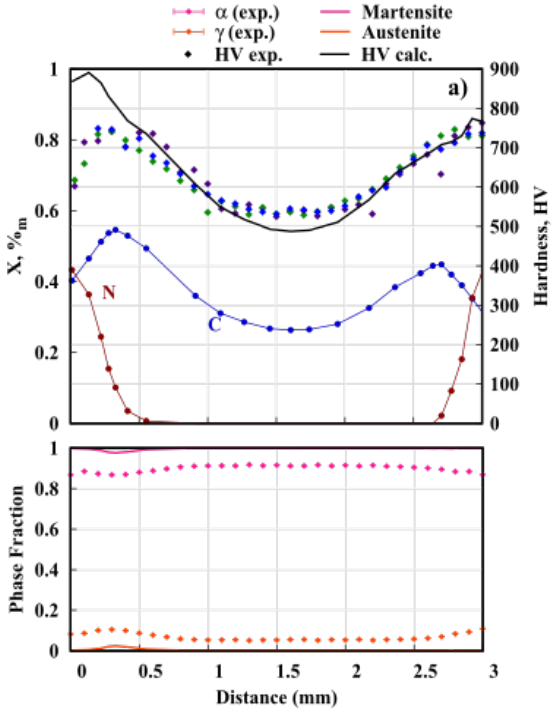

Figure IV.53: Carbonitrided gradient sample, oil quench: profiles of carbon concentration and hardness (dots: measurements (blue: center of the sample, green and purple: 7 mm on each side of the centre), line: calculated). Fractions of phase/constituent according to the simulation (lines) and of α/α' or γ phases according to the experiment.

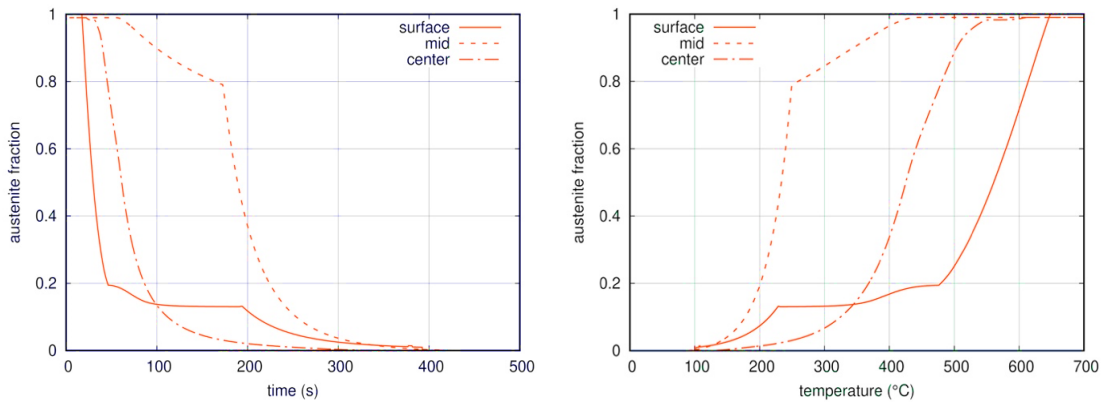

Figure IV.54: Carbonitrided gradient sample, cooling in air. Austenite fraction predicted by the simulation, as a function of time (left) and temperature (right), at the surface, in the center and at an intermediate point (mid) located just below the nitrogen-enriched case (depth 500 µm).

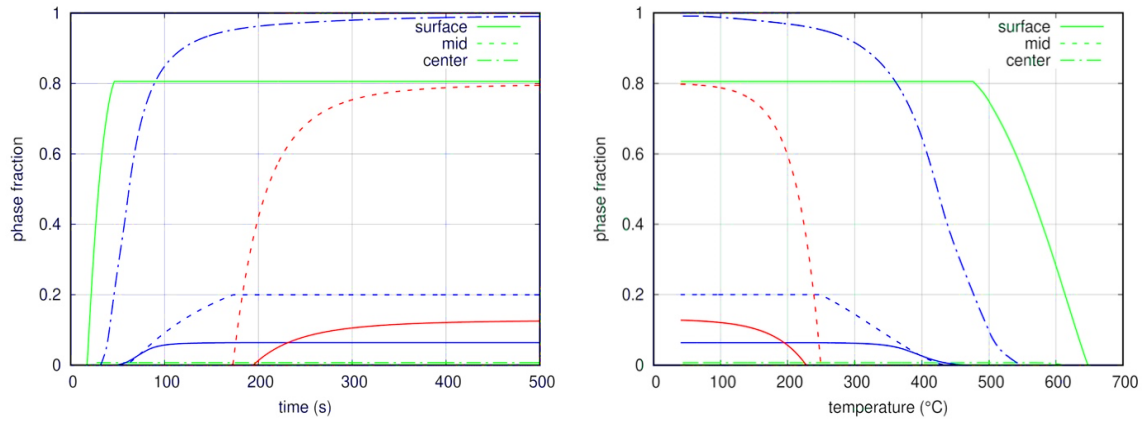

Figure IV.55: Carbonitrided gradient sample, cooling in air. Fractions of ferrite or HTC (green), bainite (blue), martensite (red) predicted by the simulation, as a function of time (left) and temperature (right), at the surface, in the center and at an intermediate point (mid) located just below the nitrogen-enriched case (depth 500 µm).

different temperatures. The profile at 300°C shows that three regions can be identified, in agreement with the time and temperature evolutions presented above. The nitrogen-enriched case undergoes the fastest kinetics of austenite decomposition. The center undergoes similar kinetics, while the region just below the nitrogen-enriched case decomposes more slowly, because of the high carbon concentration. However, the profile at 200°C is more complex, as it shows a local maximum of austenite fraction, at depth ca. 950 µm. This is due to the formation of bainite which stabilized the austenite against the martensitic transformation. These complex evolutions of the microstructural profile had no visible consequences on the formation of internal stresses and these will, therefore, not be discussed further. Nevertheless, let us point out a difference in phase transformations chronology between the *in situ* experiment and the cooling in air. In former experiment, a three-stages chronology was visible: the N-enriched surface, followed by the center, and then the intermediate region. For the cooling in air, the N-enriched surface still undergoes fastest pahse transformations, but its kinetics is not far from the one of the center. The possible consequences on internal stresses will be seen below.

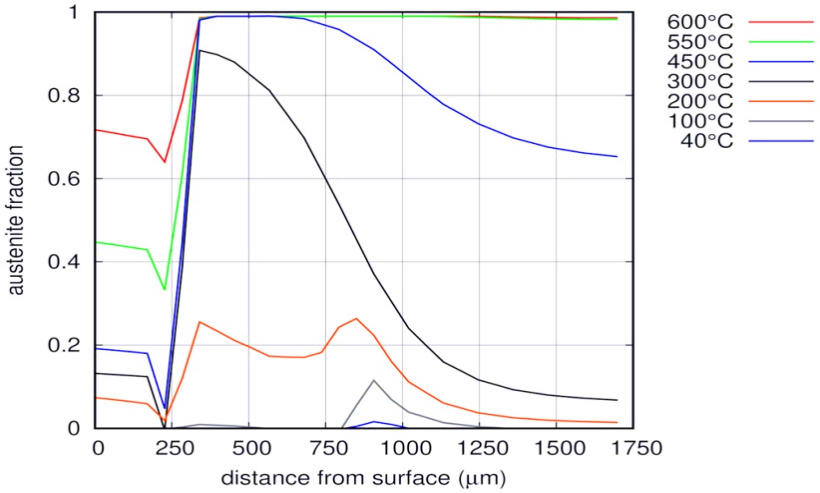

Figure IV.56: Carbonitrided gradient sample, air cooling. Profiles of austenite fraction predicted by the simulation at different temperatures.

Figure IV.57 shows the profile of phase/constituents fractions according to the simulation regarding the carbonitrided air-cooled sample, and at the end of the cooling. In agreement with the above, three regions are identified: the nitrogen-enriched case with a majority of HTC, the center with a majority of bainite and an intermediate region

with a mixture of bainite and martensite, the fraction of the latter phase increasing when approaching the nitrogen-enriched case. This microstructural profile is similar to the one of the *in situ* experiment. The main difference in the *in situ* experiment was the presence of ferrite in the center, because of the slower cooling rate. Microstructural observations were done for the carbonitrided, air-cooled sample, as presented in Chapter III, and these were in exact agreement with the identification of these three regions. However, the simulation predicts the absence of austenite (except at depth ca. 1 mm, with less than 2%), whereas, according to HEXRD measurements, the fraction of austenite goes up to 30% at the surface and is about 10% in the center. This discrepancy was already discussed in previous sections: it was ascribed to the non-accounting by the model of the stabilization of austenite upon bainite and martensitic transformations.

For this sample, the comparison of hardness profiles from simulation and experiment is satisfactory, despite the discrepancies regarding the microstructural profile. In particular, the calculations achieve to predict the "peak" of hardness just below the nitrogen-enriched case. It is due to the higher local carbon concentration and to the formation of bainite and martensite.

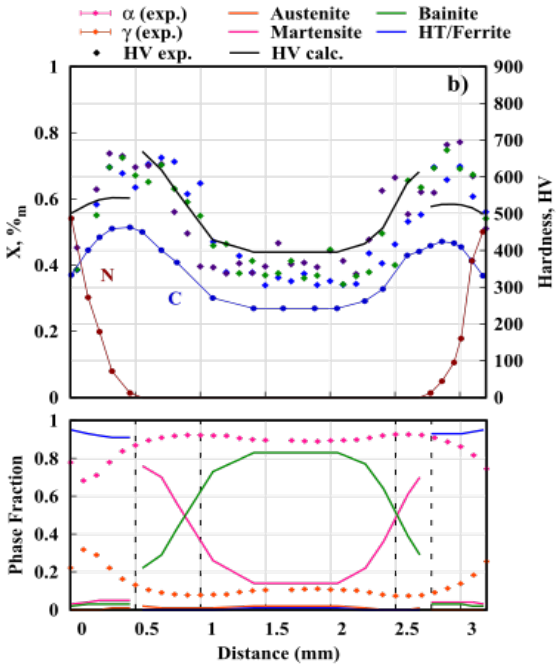

Figure IV.57: Carbonitrided gradient sample, air cooling: profiles of carbon concentration and hardness (dots: measurements (blue: center of the sample, green and purple: 7 mm on each side of the centre), line: calculated). Fractions of phase/constituent according to the simulation (lines) and of α/α' or γ phases according to the experiment.

IV.4.4.2 Internal stresses

Figure IV.58 shows the evolutions, according to the simulations, of the axial (σ_{22}) and radial (σ_{11}) stress in the axis of the cylinder and at three positions: surface, center, and intermediate (mid) position, below the nitrogen-enriched case, considering the temperature evolutions related to the HEXRD *in situ* experiment. Like for the nitrided specimen (Figure IV.44), the evolutions of the stresses show three main stages. Until about 100 s, there are only small thermal stresses. Until 300 s, phase transformations occur throughout the sample thickness, leading to complex evolutions of the stresses. After 300 s, the "mid point", which transforms, at last, undergoes strong compression stresses and the inner and outer regions go into tension, by reaction.

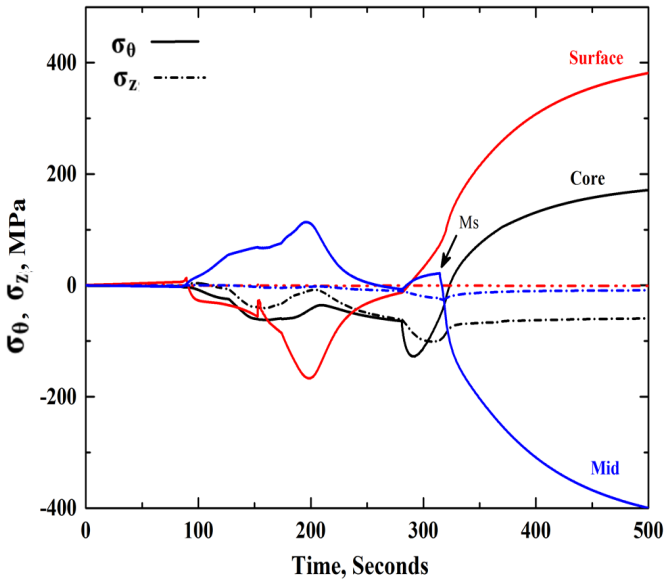

Figure IV.58: Carbonitrided gradient sample, simulation of in situ experiment. tangential stress σ_θ and axial stress σ_z in the axis of the cylinder and three positions: surface, center, and intermediate (mid) position, below the nitrogen-enriched case.

Figure IV.59 shows profiles of radial stress at the cylinder axis along the sample thickness. In the first stage, down to 300°C, the nitrogen-enriched case goes into compression, because of its faster decomposition, mostly into HTC, while the inner regions go into tension, by reaction. As seen before (Figure IV.48), phase transformations then occur in the center (between about 500°C and 250°C), but it has no visible consequences on the evolutions of the stress profile. When phase transformations eventually occur in the last region (just beneath the nitrogen-enriched case), this region goes into compression and the remaining of sample goes into tension, by the reaction.

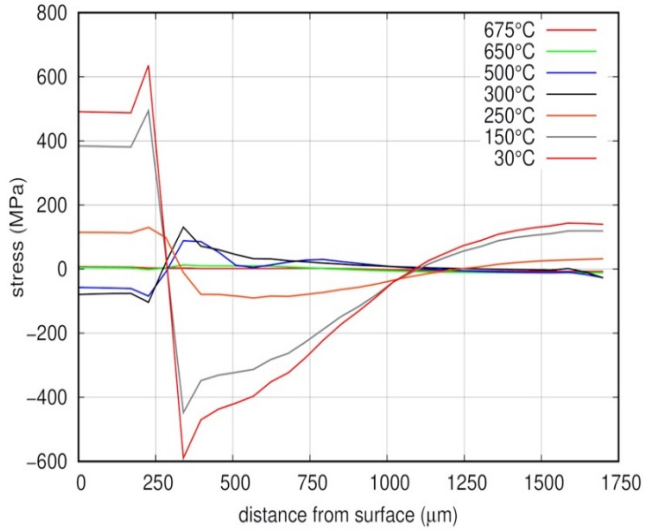

Figure IV.59: Carbonitrided gradient sample, in situ HEXRD experiment. Profiles of radial stress along the cylinder axis, according to the simulation and at different temperatures.

Figure IV.60 shows the profile of residual stress predicted by the simulation (black line) in the carbonitrided gradient sample after HEXRD *in situ* experiment, considering the stress difference, (σ_θ-σ_z) averaged over the radius of the sample. Like for the nitrided gradient sample, tensile stress is predicted in the nitrogen-enriched case, compression stress underneath and tensile stress in the center. compared to the simulation on the nitrided sample, higher compression stresses are predicted below the nitrogen-enriched

case and tensile stresses are predicted in the center instead of nearly zero stress. Two origins can be postulated for these differences between nitrided and carbonitrided gradient samples: (i) the higher phase transformation strains related to higher carbon concentration in the latter sample. (ii) The chronology of austenite decomposition below the nitrogen-enriched case: in carbonitrided sample, the last region to transform is concentrated just below the N-enriched case. Conversely in nitrided sample, all the region below the N-enriched case transforms simultaneously, because of the flat carbon concentration profile. Although the shape of the calculated stress profile is in good agreement with the experiment, it overestimates the tensile stress in the nitrogen-enriched layer, whereas it overestimates it, in magnitude, in the regions underneath.

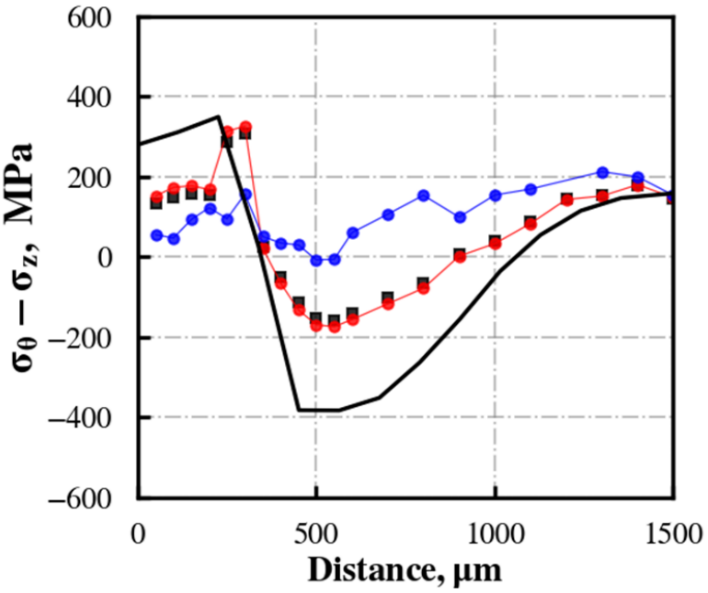

Figure IV.60: Carbonitrided gradient specimen, HEXRD in situ experiment. Profile of residual stress difference (σ_θ-σ_z) averaged over the cylinder radius according to the simulation (black line) and the HEXRD experiment (black dots: average, red dots: α/α' phase, blue dots: γ phase).

A similar carbonitrided gradient sample with same conditions of enrichment was also considered, but which underwent quench into oil. As shown in previous section, under these conditions, this sample underwent full martensitic transformation throughout its thickness. Therefore, it underwent the usual chronology of phase transformation, directly related to the profiles of concentration in carbon and nitrogen: the center followed by the surface. Figure IV.61 shows the resulting evolutions of the profile of radial stress at the cylinder axis, predicted at different temperatures by the simulation. These are consistent with the mentioned chronology, with the surface and the center being in tension and in compression respectively in a first stage, and a final inversion of this stress profile.

Figure IV.62 compares the profiles of stress difference (σ_θ-σ_z) averaged over the radius of the sample according to the simulation and the experiment. Although the shape of the stress profile is correctly predicted, the simulation overestimates the stresses, like in several simulations presented above.

A carbonitrided sample enriched in the same conditions as both previous ones was cooled in air. The cooling rate was intermediate between the *in situ* HEXRD experiment and the quench into oil. However, the evolutions of stresses inside this sample were similar to those of the *in situ* experiment. Figure IV.63 shows profiles of radial stress along the axis of the cylinder predicted by the simulation and at different temperatures. Three regions can be identified in this sample, like for the *in situ* experiment: the nitrogen-enriched surface, an intermediate region, and the center, which eventually undergo tensile, compression, and tensile stress, respectively.

As mentioned above, the chronology of phase transformations is not exactly the

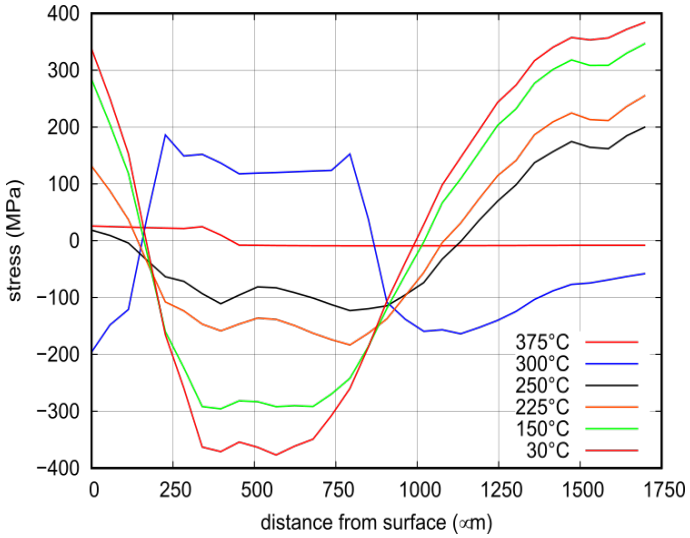

Figure IV.61: Carbonitrided gradient sample, quench into oil. Profiles of radial stress along the cylinder axis, according to the simulation and at different temperatures.

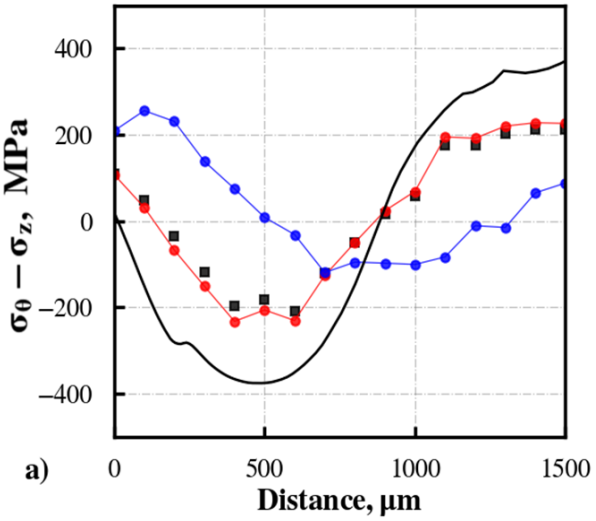

Figure IV.62: Carbonitrided gradient specimen, oil quench. Profile of residual stress difference (σ_θ-σ_z) averaged over the cylinder radius according to the simulation (black line) and the HEXRD experiment (black dots: average, red dots: α/α' phase, blue dots: γ phase).

same as the air cooling and the *in situ* experiment. During the former experiment, the N-enriched case and the center tend to undergo austenite decomposition with similar kinetics. Conversely, the *in situ* experiment shows a three-stage chronology (N-enriched case, center, intermediate region). This may have consequences on the formation of internal stresses. As shown in Figure IV.63, after the cooling in air, the intermediate region shows compression stress because it was the last to transform. There is a sharp transition to tension stress when approaching the center. For the *in situ* experiments (Figure IV.59), this transition is smoother, and this may be related to the kinetics of the intermediate region and of the center, which are more overlapped.

Hence, in carbonitrided gradient samples, the evolutions of the stresses may not be simply governed by the respective kinetics inside the N-enriched case and below. The precise chronology of phase transformation throughout the whole thickness below the N-enriched case should also be considered, as highlighted by the difference between samples cooled in air and which underwent the *in situ* experiment.

Figure IV.64 shows the profiles of the residual stress difference (σ_θ-σ_z) averaged over the cylinder radius, according to the simulation and to the HEXRD (*ex situ*) experiment

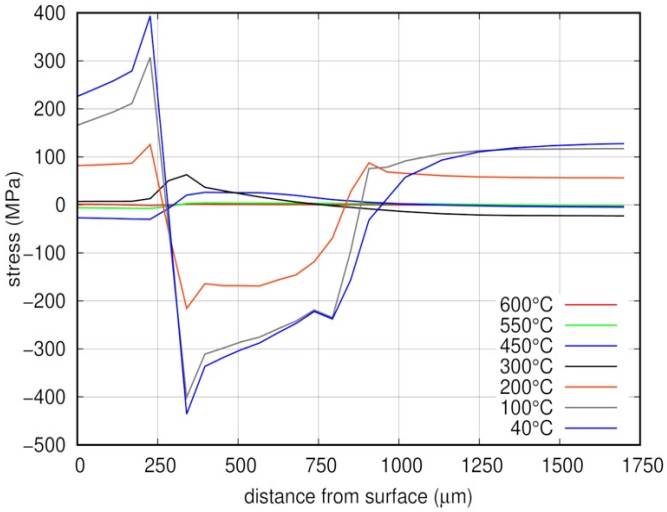

Figure IV.63: Carbonitrided gradient sample, cooling in air. Profiles of radial stress along the cylinder axis, according to the simulation and at different temperatures.

(black dots). The shape of the stress profile predicted by the simulation is in good agreement with the experiment, with the identification of the three regions identified above (N-enriched case, C-rich intermediate region, center). The stress predicted below the nitrogen-enriched case is in good agreement with the experiment, with a discrepancy lower than about 100 MPa. However, the tensile stress in the nitrogen-enriched case is underestimated by more than 300 MPa.

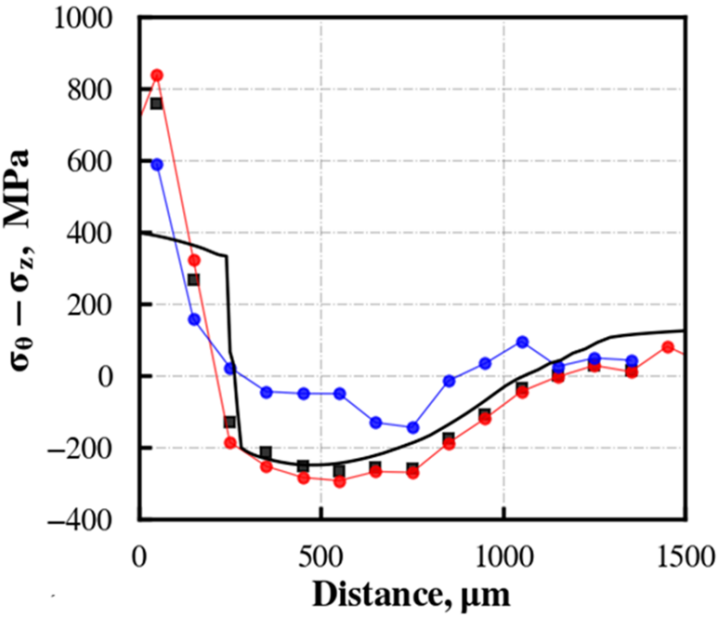

Figure IV.64: Carbonitrided gradient specimen, cooling in air. Profile of residual stress difference (σ_θ-σ_z) averaged over the cylinder radius according to the simulation (black line) and the HEXRD experiment (black dots: average, red dots: α/α' phase, blue dots: γ phase).

IV.4.5 Synthesis and discussion

A coupled simulation of thermal, mechanical, and phase transformations evolutions upon thermal treatment of carbon/nitrogen-enriched low alloyed steels has been established and assessed by comparing the predictions of the simulations to the

experiments presented in Chapter III. Although the coupled model includes a calculation of the temperature evolutions, this part of the model was not assessed by our experiments because the gradients samples thickness (3 mm) was too small to induce significant gradients of temperature. Hence, these are mostly the metallurgical model (phase transformations) and the mechanical model, which have been assessed in this Chapter.

IV.4.5.1 Metallurgical model (phase transformations)

This simulation study allowed to assess the phase transformations model by considering the cooling, at different rates, of laboratory samples with carbon and nitrogen composition gradients. It also allowed to investigate the microstructural evolutions by considering experimental conditions beyond those achieved experimentally (cf. experimental issues regarding *in situ* HEXRD experiments on nitrided samples).

The assessment carried out in the present study is in continuity with previous assessments of the same model [82, 106], but which considered laboratory samples with homogeneous composition. In these previous works, the kinetics model parameters (JMAK) were established mostly empirically by considering the base steel composition, on the basis of phase transformation kinetics established in isothermal conditions. Then, it was verified that the model is able to take account of the carbon concentration of the steel (with Kirkaldy's model) and to predict phase transformation kinetics during cooling (Scheil's sum, additivity rule).

The present work represents a further assessment of the model, because the gradients samples (carburized, nitrided, carbonitrided) provide a larger range of C and N compositions than selected before, when considering homogeneous samples (base steel, carburized, nitrided and carbonitrided). Three cooling schedules have also been considered (with increasing cooling rate: the thermal schedule of the *in situ* experiments, cooling in air and quench into cold oil). Also, the simulations were compared to measurements of kinetics by HEXRD. The main outcome of this method, apart from the precision of the recorded kinetics, is to provide the amount of austenite, especially at the last stages of the cooling. However, as seen in Chapter III, the austenite decomposition kinetics could really be tracked only in the carburized specimen, whereas only partial observations could be achieved in nitrogen-enriched gradient specimens.

In carburized gradient specimen, the predicted kinetics was in good agreement with the experiment, as well as the predicted final profiles of microstructure (fractions of constituents and hardness). The simulations conform to the usual analysis for this type of enrichments: the center transforms before the surface because of the effect of the carbon. Changing the cooling rate does not change this chronology. At the end of the cooling the hardness is higher near the surface. The discrepancies were commented in detail above. These good predictions come from the knowledge of phase transformations mechanisms in these steels, especially regarding the effect of carbon. This provided physical grounds to the model, which is not only empirical (e.g. [106], thereby ensuring its adaptability to different conditions (temperature evolutions, local carbon concentration).

As for the nitrogen-enriched gradient samples (nitrided, carbonitrided) the HEXRD *in situ* experiments combined with the metallurgical model allowed to investigate the effects of the nitrogen enrichment, which has been little studied so far in the literature. More important discrepancies between simulation and experiments (kinetics, final profiles of microstructure and hardness) occurred, has it has been detailed above. This is due to the fact that the model is based on more empirical grounds, regarding the effects of nitrogen, contrary to the effect of carbon.

Nevertheless, the metallurgical model was able to capture two important features of austenite decomposition in nitrogen-enriched gradient specimens (nitrided, carbonitrided). First, upon "slow" cooling (*in situ* experiment, in the present study), the nitrogen-enriched case transforms before the inner parts of the sample, because of the loss of hardenability in the presence of nitrogen, that we had been established before [3].

The model is able to predict this reversed chronology (compared to the more usual case of carburizing), even if it is on an empirical basis. Second, the model is able to predict that the usual chronology (center followed by surface) is re-established if the cooling is fast enough (quench into oil). In this case, all the sample transforms to martensite. As the usual effects of carbon and nitrogen are observed for this transformation (decrease of Ms, transformation shifted to low temperature), the surface of the gradient sample transforms at last. The model is also able to predict complex profiles of hardness, for instance, in carbonitrided samples cooled slowly (air, *in situ*), as a result of the microstructural profile, inside which three regions were identified (surface, intermediate, center), instead of two classically (surface, center).

Put together the model predictions give an overview of the phase transformations chronology inside the gradient specimens, which is essential to understand the formation of the internal stresses. The effects of composition and cooling rate can be summarized as follows:

- Carburized samples, whatever the cooling rate: center followed by surface.
- Nitrided sample, slow cooling (*in situ* exp.): surface followed by center.
- Nitrided sample, fast cooling (oil quench): center followed by surface.
- Carbonitrided sample, slow cooling (*in situ* exp.): surface, then center, then intermediate region.
- Carbonitrided sample, fast cooling (oil quench): center followed by surface. (In nitrogen-enriched samples, "surface" means the nitrogen-enriched case.)

Let us recall that this overview on the phase transformation chronology could be fully established experimentally only in the carburized specimen, for the *in situ* experiment.

The main limitation of the model predictions regards the underestimation of non-transformed austenite fraction and retained austenite. This happened whatever the local composition in carbon and/or nitrogen and whatever the cooling rate. This is ascribed to the absence of accounting of the austenite stabilization (chemical, mechanical) upon last stages of the cooling (bainitic and martensitic transformations). It could also be related to a too fast kinetics of the HTC (High temperature constituent) in the presence of nitrogen. This discrepancy between simulation and experiment was put into evidence thanks to the HEXRD experiments, which allowed to measure with precision the actual mass fraction of austenite inside the samples. Obvious improvement also regards the effects of nitrogen, which have still to be predicted by knowing better the related phase transformation mechanisms. Finally, let us mention that no effects of stress on phase transformation kinetics were accounted for. This did not seem to induce strong discrepancies between simulations and experiments, but this could be investigated further.

IV.4.5.2 Mechanical model

Before discussing the outcomes of the mechanical model, let us remind that only one part of the latter has been assessed in the present simulation and experimental study. Indeed, the temperature gradients were too small in the considered samples (3 mm thickness) to induce significant thermal stress and plastic strains. Hence, in the whole study, the internal stresses only came from the phase transformations strains: the volume changes and the phase transformation plasticity strain. One can separate the results in two parts: on the carburized samples and on the nitrogen-enriched samples (nitrided, carbonitrided).

Regarding the carburized samples, this study represented the first assessment by *in situ* HEXRD experiments of multiphysics models which had already been established in previous works [12, 14]. The model predicts the usual shape of the stress profile

(compression at the surface, tension in the center). The agreement between the simulation and experiment was satisfactory and the discrepancies were detailed in previous sections. The model was able to predict three stages in the stress evolutions. In the first stage, thermal stress are generated as the sample is fully in austenite state. These thermal stresses were significant only when considering the faster quench, into oil. In a second stage, the austenite decomposes at different rates throughout the sample thickness, leading to complex evolutions of the stress. In the last stage, the last region to transform in martensite undergoes high compressive stress and the remaining of the sample tends to go into tension, by reaction.

Regarding nitrogen-enriched samples, the model can predict the consequences on stress evolutions, of the drastic acceleration of the phase transformation kinetics in the nitrogen-enriched case. For slow cooling (*in situ* experiment), the formation of HTC in the nitrogen-enriched case leads to the formation of tensile residual stresses. The latter are almost exactly correlated with the depth of the nitrogen enriched case (ca. 400-500 µm), according to both simulation and stress determinations by HEXRD. But if the cooling is faster, the nitrogen-enriched samples "behave" more usually as mostly martensite forms, in the whole thickness of the gradient sample. The residual stresses formation then conforms, in this case, to the classical analysis related to carburizing.

In the following, the origins of the residual stresses in these treatments is further analyzed by simulation. As mentioned, for the investigated treatments, the residual stresses come from the phase transformation strains (volume variation associated with the phase change, and the phase transformation plasticity strain). One could also consider the thermal strains generated upon cooling because of the thermal contraction. The associated strain is different a priori throughout the sample thickness. Indeed, the austenite and its decomposition products have different coefficients of thermal expansion (about two times larger for austenite than e.g. for ferrite). Hence, the later the austenite will decompose, the larger the thermal strain will be. However, we investigated numerically the influence of the thermal strain on the residual stresses, and it was found to be negligible. It will thus not be discussed further here.

Regarding the phase transformation strain, its value will be different at each position inside the gradient samples. It depends on the local concentration in carbon and nitrogen and on the nature of the austenite decomposition products (ferrite, HTC, bainite, martensite), as each of these has a specific phase transformation strain. As for the phase transformation plasticity strains, they also depend on the local stress evolutions upon cooling, and thus on the evolution of the stresses occurring in the whole thickness of the sample. As a result, both phase transformation strains strongly depend on the chronology of the phase transformations, throughout the thickness of the gradient samples.

As the two preponderant factors controlling the internal and residual stresses are the volume change associated with the phase transformation and the phase transformation plasticity strain, their respective contributions were estimated separately by the simulation. To this aim, simulations were performed by suppressing the phase transformation plasticity strain, but letting the volume change occur. We consider first the carburized gradient sample submitted to the thermal schedule of the *in situ* experiment. Figure IV.65 compares the profile of residual stress (radial stress, along the cylinder axis) obtained by this simulation with the same simulation including the phase transformation plasticity strain (the one already shown in Section IV.4.2).

It can be seen that both profiles exhibit similar shape (compression at the surface, tension in the center). At the surface, the accounting of the phase transformation plasticity strain leads to the prediction of lower compressive residual stress as shown previously in literature (Figure I.9). With and without accounting of the phase transformation plasticity strain, the residual radial stress at the surface is equal to 350 MPa and 475 MPa respectively. Indeed, as martensitic transformation occurs at the surface, the austenite is under tension and the volumic variation induces a strong decrease of the stress that goes to compression (Figure IV.66). It has been shown in previous studies that transformation plasticity induces stress relaxation in comparison with the case without

transformation plasticity [24].

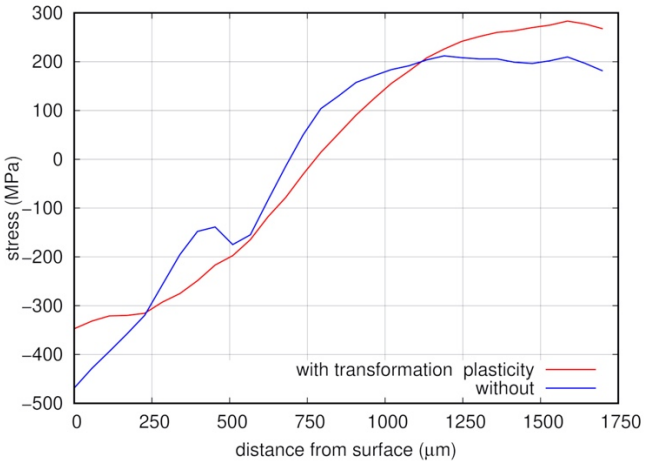

Figure IV.65: Carburized gradient sample, thermal schedule related to in situ experiment. Profile of the radial residual stress, along the half-thickness and the cylinder axis, according to simulation and by considering all phase transformation strains (red) or by suppressing the phase transformation plasticity strain (blue).

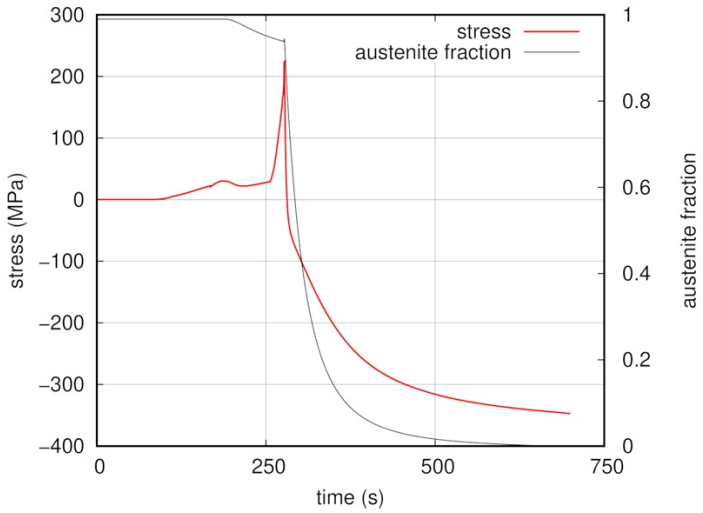

Figure IV.66: Carburized gradient sample, thermal schedule related to in situ experiment. Evolution of the radial stress and the austenite fraction at the surface, according to the simulation, with accounting of the phase transformation plasticity strain.

The same analysis was performed for the carbonitrided gradient sample submitted to the temperature evolutions related to the *in situ* HEXRD experiment. In line with the previous simulation, neglecting the phase transformation plasticity strain conducts to overestimate significantly the residual stress at the surface (about 800 MPa instead of 500 MPa). This trend is also clearly explained by looking at the evolution of stress upon austenite decomposition (Figure IV.68). One stresses that this comparison shows that the phase transformation plasticity strains have to be predicted with precision inside the nitrogen-enriched case. But as shown before, the simulation predicts the formation of the HTC in the nitrogen-enriched case, for this thermal treatment. Experimental determination of the phase transformation plasticity strain is difficult for the HTC, because of its fast kinetics of formation.

Put together, the simulations carried out on carburized, and carbonitrided samples show that the preponderant factor controlling the internal stress evolutions is the volume change associated with the phase transformation. Carburized specimen has

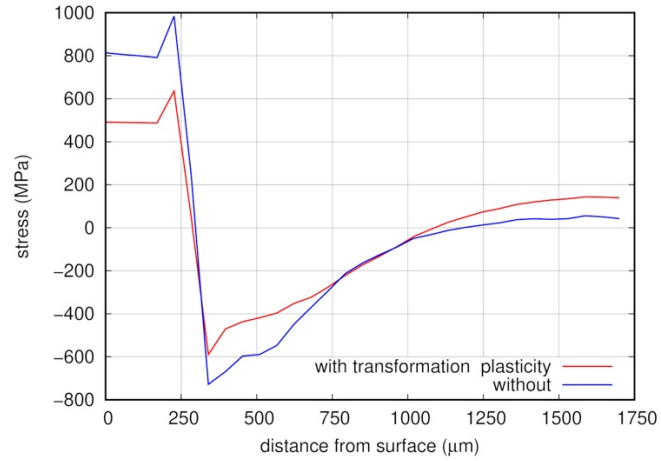

Figure IV.67: Carbonitrided gradient sample, thermal schedule related to in situ experiment. Profile of the radial residual stress, along the half-thickness and the cylinder axis, according to simulation and by considering all phase transformation strains (red) or by suppressing the phase transformation plasticity strain (blue).

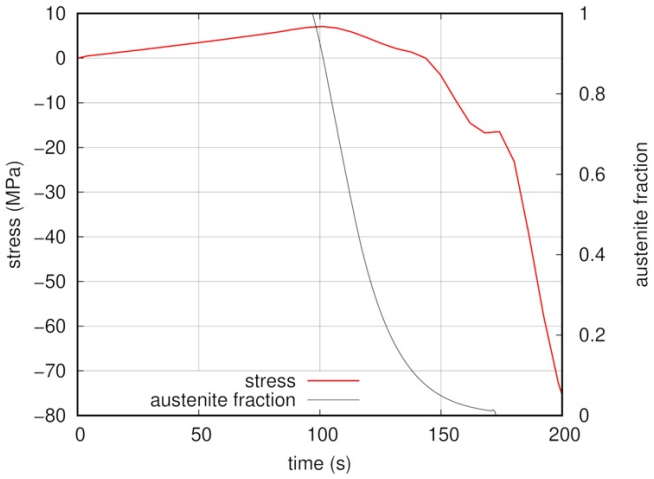

Figure IV.68: Carbonitrided gradient sample, thermal schedule related to in situ experiment. Evolution of the radial stress and the austenite fraction at the surface, according to the simulation, with the accounting of the phase transformation plasticity strain.

compression stress at the surface because of the high transformation strain associated with martensitic transformation and to the higher carbon concentration, as it is well-known. In carbonitrided specimen, tensile residual stresses are predicted by the simulation at the surface, in agreement with the experiment, because the nitrogen-enriched case transforms mostly to the High Temperature Constituent, which has a lower transformation strain than the products formed in inner parts of the sample, mostly bainite and martensite. However, the phase transformation plasticity strain cannot be neglected without overestimating the residual stress at the surface (for the *in situ* experiment: compression in carburized specimen, tension in carbonitrided specimen).

These conclusions had been reached in previous works regarding carburizing [12, 25], but only by the simulation. The present study confirmed these previous analyses for the first time by *in situ* tracking of phase transformation kinetics and stress evolutions, by HEXRD experiments on a synchrotron beamline. Thanks to this new combination of simulations and experiments, the unusual behavior of nitrogen-enriched specimens could be rationalized, particularly the atypical shape of the residual stress profile, if the cooling rate is slow enough.

Besides these satisfactory prediction, one important discrepancy between simulation

and experiment regards the decrease of the residual stress when approaching the surface of the sample, which occurred in almost all investigated cases (composition, thermal treatment). Usually, this is ascribed to the increasing fraction or retained austenite. However, the HEXRD experiments do not indicate that the fraction of austenite actually increases close to the surface. In most cases, the fraction of austenite is actually lower than ca. 10%. As the metallurgical model's current version does not consider any stabilization of austenite, this will be probably a way to improve the predictions, at least in part.

Conclusion and perspectives

The aim of this thesis was to investigate the formation of microstructures and internal stresses during thermal treatments of carburized and carbonitrided low-alloyed steel.

If carburizing treatments have been largely studied in the literature, fewer investigations have been conducted on carbonitriding, although this type of treatment has been developed for several years in parallel to carburizing. Promising results have been obtained regarding residual stress profiles and mechanical properties. However, a thorough analysis is lacking regarding the mechanisms controlling the formation of microstructure and stress profiles inside the enriched cases, especially after enrichment in nitrogen. Also, most previous experimental works consider "post mortem" characterizations, while *in situ* techniques in large scale facilities take more and more importance. As for the metallurgical models, few of them take into account explicitly the nitrogen concentration in the equations. Most models do not detail their assumptions and experimental basis, and mechanical models do not consider the nitrogen effect so far.

In this framework, this study combined innovative experiments and simulations to get a new insight on these thermal treatments. New methodologies to track *in situ* phase/stress evolutions by HEXRD experiments were exploited and adapted, in order to obtain these evolutions all along the cooling. The coupled thermal-mechanical model was developed by using approaches previously introduced in this laboratory, but with particular emphasis on the effects of nitrogen on the phenomena.

The experimental approach was based on the study of one single low-alloyed steel (23MnCrMo5), for which the effects of carbon and nitrogen enrichment of austenite on its decomposition had already been studied thoroughly in previous works, in the same research group. 3 mm-thick laboratory samples with carbon and/or nitrogen composition gradients representative of usual thermochemical treatments were investigated. Enrichments by carburizing, nitriding and carbonitriding were carried out in the laboratory with in-house thermobalance and by designing specific thermochemical treatments. The influence of the cooling rate from the austenite field at 900°C was investigated by considering a quench into cold oil or an air cooling after the enrichment treatment.

The most innovative part of the experimental study consisted in developing an original methodology to track *in situ* the stresses and the phase transformation kinetics during the cooling of the laboratory samples. This was achieved by using a portable lamp furnace designed in our research group to be placed at synchrotron beamlines. During the experiment, the sample is submitted to the thermal treatment and it is crossed by a high-energy X-Ray beam. A vertical motion is applied in order to scan the sample thickness and the composition gradient. The Debye-Scherrer rings produced by the diffracted beams are recorded by a 2D detector. During the post-treatment, the evolutions of phase fractions can be obtained by Rietveld analysis, whereas the stresses are determined in α/α' and γphases separately, with the $\sin^2\psi$ method. Besides, more conventional techniques were also employed (microscopies, hardness measurements, laboratory X-Rays) to characterize (*ex situ*) the stresses and microstructures.

The development of a multi-physics model was at the center of the simulation part, in order to predict the coupled evolutions of temperature, stresses, and microstructure inside nitrogen and/or carbon-enriched cases, and the coupling between these phenomena (particularly effects of phase transformations on stresses evolutions). The metallurgical model had been developed in previous studies mentioned above. It predicts the phase transformation kinetics, the amount of each product of austenite decomposition (ferrite, pearlite,bainite martensite), the resulting hardness, as a function of the temperature evolutions and the local carbon/nitrogen composition.

In present study, a campaign of experimental characterizations was undertaken to establish the thermal and the thermomechanical behavior as function of temperature, phase/constituent and carbon/nitrogen concentration. If some data were available in literature, some new experiments were necessary, especially regarding the effects of nitrogen. The thermomechanical behavior was established in temperature, in order to establish the thermo-elasto-viscoplastic behavior with phase transformation (volumic variations, transformation plasticity). To this aim, a tensile-testing machine designed in our research group to perform tensile tests at high temperature and controlled atmosphere, was used. Tensile samples with specific geometry (small thickness 1 mm, to achieve homogeneous enrichments) were designed for this purpose. Thermophysical parameters (diffusivity, density, specific heat) as well as latent heat were determined both experimentally and from thermodynamic data.
The two main outcomes of this dissertation study are the following.

First, the new introduced experimental methodology, based on *in situ* HEXRD experiments, has proven to be effective to track *in situ* the microstructural evolutions and the stresses inside gradient samples and during cooling. The study of carburized specimens served as a reference case, as it had been studied previously, in particular in this research group. As detailed previously, the evolutions of stresses and phase transformations obtained experimentally were in good agreement with previous analyses of the literature, thereby validating the new experimental method. compared to previous works, the evolutions of stress and phase transformation kinetics are now accessible during the cooling, whereas it was only possible before by the numerical simulation. In this work, this also allowed to assess more comprehensively the coupled thermal-mechanical-metallurgical model mentioned above, by considering the cooling stage and not only the final microstructures and residual stresses. Although the predictions are satisfactory, this new and more critical assessment revealed the current limitations of the models and axes of further improvement, that will be evoked later on.

Second original outcome of this study regards the nitrogen-enriched specimens (nitrided, carbonitrided). The fast austenite decomposition of austenite inside the nitrogen-enriched case can completely modify the chronology of phase transformations inside the gradient specimens (if cooling is slow enough), and this leads to unusual profiles of residual stresses, with tensile stresses at the surface. The new HEXRD experimental method has proven effective to establish firmly the formation of these unusual stress profiles, showing for instance that the tensile stresses are exactly correlated with the presence of nitrogen. However, *in situ* tracking of phase/stress evolutions by HEXRD upon cooling could not be fully achieved in nitrogen-enriched specimens, probably because of austenite grain size issues. Hence, the newly-developed coupled model was essential to analyze the evolutions at high temperature. It showed its ability to predict the effects of nitrogen (whereas effects of carbon were already well-established). In particular, it achieved to predict the reversed chronology and, consequently, the tensile stresses at the surface.

From all investigated cases, experiments and simulations, a comprehensive overview comes out regarding the formation of stresses during cooling after thermochemical enrichment treatments of low-alloy steels. The residual stresses profiles are determined by the chronology of phase transformation throughout the enriched specimen. First and last regions to transform tend to end up with tensile and compression stresses respectively. Key parameters to predict the stresses accurately are the phase transformation strains (volume change, phase transformation plasticity). It should be recognized that these conclusions had been reached in previous works on carburizing. However, present study goes towards more accurate experimental characterizations and model predictions including carbonitriding which are at the basis of better control and optimization of these treatments, in the future.

Practical outcomes of this study mostly concern nitriding and carbonitriding treatments, as carburizing treatments are already well-known and mastered. After carbonitriding, the enriched case ”behaves” in a way similar to carburizing (formation

or compression residual stress at the surface, higher hardness), provided the cooling rate is fast enough. However, there exists a critical cooling rate below which undesired microstructural and stress evolutions will occur in the N-enriched case. Let us mention, though, that this laboratory study involved the re-austenitizing the samples before the *in situ* experiments, which does not happen in industrial process. Recent works seem to indicate that this re-austenitization step is not without consequences on the loss of hardenability in the case, as it may change the austenite grain size. As for nitriding (without carbon enrichment), it does not seem interesting for application purposes: either the cooling is too slow, leading to an unfavorable stress profile, or it is fast enough, but all the enriched case will transform nearly simultaneously and with nearly uniform phase transformation strain, leading to low residual stresses.
This study opens the way for future work:

Obvious future work regards the improvement of the models, on the one hand, regarding the effects of nitrogen on phase transformations and stress evolutions. The comparison between simulation and experiments highlighted which parameters are critical to describing precisely the phenomena (especially phase transformation strains). Currently, the effects of nitrogen are mostly accounted for on an empirical basis, and the mechanisms have to be further understood. On the other hand, one should also take into account the interactions between the internal stresses and the kinetics of phase transformations and analyze their impact on the residual stresses.

Thanks to the accuracy of the HEXRD experiments, it was found that a significant fraction of retained austenite is present at the end of the cooling, for almost all investigated cases (enrichment, thermal schedule). This could not be predicted by the current metallurgical model. Besides the retained austenite being an important microstructural parameter, it has consequences on the evolutions of stresses. Definitely, the stabilization of austenite (chemical, mechanical) should be understood and then implemented in future models. Phenomena of martensite self tempering should also be considered.

The current simulation does not capture the decrease of the residual stress when approaching the surface of the sample. This issue is related to the previous one, as it may, in part, come from the underestimation of the retained austenite fraction. But other origins of these discrepancies should probably be looked after, as elaborated before.

The new HEXRD method gives, in theory, the possibility to track the stresses inside the α/α' and γ phases separately. (Even if in the present study, *in situ* tracking of stresses in γ phase could not be achieved). Mechanical models considering the biphasic material could be developed on this basis.

From the experimental point of view, the *in situ* HEXRD results have been analysed for deriving phase fractions and phase internal stresses. But, from our experiments, the lattice parameter evolutions and FWMH (Full width and Half Maximum) evolutions can also be further analyzed.

The *in situ* HEXRD experiments have been performed for slow cooling rates. In the near future, the new high energy synchrotron sources and the high speed detectors will allow to track phase transformations and internal stresses for much faster cooling rates and validate too our models.

On the applications side, several developments can be envisaged:

The multiphysics model can be used to consider conditions closer to industrial treatments, especially larger parts inside which thermal stresses and plastic strains will occur (whereas in the present work, only phase transformation strains were significant). It can also be used to study the effect of key parameters for these treatments, such as the concentration of C/N, the depth of enrichment or the cooling rate. Some preliminary study has already been done but has not been presented here.

The new combined experimental/simulation approach provides a powerful tool to investigate the tempering treatment that generally follows quenching in carburizing and carbonitriding treatments. A dissertation work has already started in that field. On the other hand, due to the necessary restrictions in energy consumptions, new innovative

heat treatment routes like interrupted quenching (that could substitute tempering) are interesting to investigate.

References

[1] P.S.A. Impact resistance and fatigue resistance of enriched gears with the different processes. Technical report, Citroën, Peugeot, 2010. xiv, 23

[2] W.Dal'Maz Silva. *Mise au point de la carbonitruration gazeuse des alliages 16NiCrMo13 et 23MnCrMo5: modélisation et procédés*. PhD thesis, Thèse Université de Lorraine, 2017. xiv, 19, 20, 21, 22, 24, 25, 26, 28, 30

[3] S.D. Catteau. *Effets du Carbone et de l'Azote sur les Cinétiques de Décomposition de l'Austénite dans un Acier Faiblement Allié - Étude Expérimentale et Modélisation*. PhD thesis, Thèse Université de Lorraine, 2017. xiv, xv, 18, 19, 20, 21, 22, 23, 24, 25, 26, 28, 32, 38, 40, 55, 57, 60, 62, 66, 67, 77, 78, 80, 81, 86, 90, 91, 98, 100, 104, 111, 112, 128

[4] V. Landeghem, S.D. Catteau, M.H.P. Dehmas, J. Dulcy, A. Redjaïmia, J. Teixeira, S. Denis, and M. Courteaux. Isothermal decomposition of carbon and nitrogen-enriched austenite in 23MnCrMo5 low-alloy steel. *Acta Mater.*, 148:363–373, 2018. xv, 26, 38, 55, 57, 67, 78, 86, 111

[5] E.H.S.H. Buhler and H. Buchholz. Eigenspannungen bei der Warmebehandlung von Stahl. *Fur Das Eisenhuttewes*, 5:413–418, 1932. 1, 5, I

[6] T. Ericsson and B. Hildenwall. Thermal and Transformation Stresses, in: Residual Stress. *Stress Relax., Springer US, Boston, MA*, pages 19–38, 1982. 1, 5, 8

[7] L. J. Ebert. The role of residual stresses in the mechanical performance of case carburized steels. *Metall. Trans. A.*, 9:1537–1551, 1978. 1, 5

[8] S. Sjostrom. *Dissertation n°84*. PhD thesis, Linkoping studies in Science and Technology, Sweden, 1982. 1, 5, 7, 8, 96

[9] O. V. E. Macherauch. Residual Stresses After Quenching:. *Residual Stress*, 1992. 1

[10] D. P. Koistinen. The Distribution of Residual Stresses in Carburized Cases and Their Origin. *Trans. ASM.*, 50:92–97, 1958. 1, 5

[11] J. C. Genzel, W. Reimers, O. Schwarz, and Grosch. *Development Of the residual stress state in carburized steels due to austenite transformation by deep cooling*. Residual Stress. (V) DGM Informations Gmbh, Oberursel, 1993. 1

[12] A. Mey. *Prévision par Calcul des Cinétiques de Transformation de Phases et des Contraintes Internes lors du Traitement Thermique d'Aciers Cémentés*. PhD thesis, Thèse Institut National Polytechnique de Lorraine,, 1997. 1, 8, 10, 11, 79, 83, 87, 88, 94, 109, 129, 132

[13] J. A. Burnett. Prediction of stress history in carburized and quenched steel cylinders. *Mater. Sci. Technol.*, 1:863–871, 1985. 1, 9, 10

[14] C. Aubry. *Modélisation et étude expérimentale des cinétiques de revenu/autorevenu d'aciers trempés: prévision des contraintes résiduelles de trempe dans un acier cémenté en incluant l'autorevenu.* PhD thesis, Thèse Institut National Polytechnique de Lorraine, 1998. 2, 8, 10, 11, 54, 87, 88, 89, 109, 129

[15] I. Y. Arkhipov and V. A. Kanunnikova. Residual stresses in the teeth of quenched gears. *Met. Sci. Heat Treat*, 12:909–913, 1970. 2

[16] Maria Rita Chini al. Influence of nitrogen enrichment on microstructures and mechanical properties of a carbonitrided low alloyed steel. In *48ème Congrès Des Trait*, Nantes, 2022. Therm. Trait. Surface. 2

[17] R. J. Katemi, J. Epp, F. Hoffmann, and M. Steinbacher. Investigations of Residual Stress Distributions in Retained Austenite and Martensite after Carbonitriding of a Low Alloy Steel. *Adv. Mater. Res.*, 996:550–555, 2014. 2, 3

[18] R. J. Katemi. *Influence of Carbonitriding Process on Phase Transformation during Case Hardening, Retained Austenite and Residual Stresses.* PhD thesis, Universität Bremen, 2019. 2

[19] R. J. Katemi and J. Epp. Influence of Tempering and Cryogenic Treatment on Retained Austenite and Residual Stresses in Carbonitrided 18CrNiMo7-6 Low Alloy Steel. *Tanzania J. Eng. Technol*, 38:71–82, 2019. 2

[20] R. Katemi and J. Epp. In-situ Observation of Retained Austenite and Residual Stress Evolutions during Tempering of carbonitrided DIN 1.6587 Alloy Steel. *Tanzania J. Eng. Technol*, 41:121–130, 2022. 4

[21] T. Ericsson. Residual Stresses Produced by Quenching of Martensitic Steels. *Compr. Mater. Process*, page 271–298, 2014. 5, 6

[22] R. Buhler. Representation of the formation of residual stresses in steel workpieces by means of their transformation diagrams. *Arch Eisenhuttenwes.*, 40:411–423, 1969. 5, 6

[23] J. P. Josserand. *Etude expérimentale de la genèse des contraintes résiduelles lors de la trempe martensitique d'un acier allié.* PhD thesis, Diplôme de thèse I.N.P.L, 1982. 6

[24] S. Denis, E. Gautier, A. Simon, and G. Beck. Stress–phase-transformation interactions – basic principles, modelling, and calculation of internal stresses. *Mater. Sci. Technology*, 1:805–814, 1985. 6, 7, 131

[25] C. Aubry, S. Denis, P. Archambault, A. Simon, F. Ruckstuhl, and B. Miege. Prediction of microstructures and quenching residual stresses in case hardened pieces including selftempering effects. *Metall. Ital.*, 91:33–38, 1999. 6, 10, 11, 59, 63, 82, 94, 132

[26] S. Denis, P. Archambault, E. Gautier, A. Simon, and G. Beck. Prediction of Residual Stress and Distortion of Ferrous and Non-Ferrous Metals: Current Status and Future Developments. *J. Mater. Eng. Performance*, 11:92–102, 2002. 7, 77, 82, 99

[27] S. Denis. Prévision des contraintes résiduelles induites par traitement thermique et thermochimique. *La Rev. Métallurgie - CIT/Sci. Génie Des Matériaux.*, page 157–176, 1997. 7, 10

[28] S. Denis, P. Archambault, and E. Gautier. Models for Stress-Phase Transformation Couplings in Metallic Alloys. *Handbook Mater. Behav. Model*, page 896–904, 2001. 7

[29] T. Inoue and K. Arimoto. Development and Implementation of CAE System "HEARTS" for Heat Treatment Simulation Based on Metallo-Thermo-Mechanics. *J. Soc. Mater. Sci. Japan*, 44:103–109, 1995. 7

[30] T. Reti, Z. Fried, and I. Felde. Computer simulation of steel quenching process using a multi-phase transformation model. *Comput. Mater. Sci.*, 22:261–278, 2001. 7

[31] J.B. Leblond, G. Mottet, and J.C. Devaux. A theoretical and numerical approach to the plastic behaviour of steels during phase transformations—I. Derivation of general relations. *J. Mech. Phys. Solids*, 34:395–409, 1986. 7

[32] S. Denis, D. Farias, and A. Simon. Mathematical Model Coupling Phase Transformations and Temperature Evolutions in Steels. *ISIJ Int.*, 32:316–325, 2008. 7

[33] J.B. Leblond. A new kinetic model for anisothermal metallurgical transformation in steels including effect of austenite grain size. *Acta Metall.*, 32:137–146, 1984. 7

[34] S. Denis, E. Gautier, S. Sjöström, and A. Simon. Influence of stresses on the kinetics of pearlitic transformation during continuous cooling. *Acta Metall.*, 35:1621–1632, 1987. 7, 93

[35] Y. Wang, B. Appolaire, S. Denis, P. Archambault, and B. Dussoubs. Study and modelling of microstructural evolutions and thermomechanical behaviour during the tempering of steel. *Int. J. Microstruct. Mater. Prop.*, 1:197–207, 2006. 7

[36] S. Sjöström. Interactions and constitutive models for calculating quench stresses in steel. *Mater. Sci. Technol. (United Kingdom)*, 1:823–829, 1985. 7, 8, 9, 96

[37] J.B. Leblond. Mathematical modelling of transformation plasticity in steels II: Coupling with strain hardening phenomena. *Int. J. Plast.*, 5:573–591, 1989. 7, 92

[38] F. Colonna, E. Massoni, S. Denis, J.L. Chenot, J. Wendenbaum, and E. Gauthier. On thermo-elastic-viscoplastic analysis of cooling processes including phases changes. *J. Mater. Process. Techology*, 34:525–532, 1992. 7

[39] Y. Vincent, J.M. Bergheau, and J.B. Leblond. Viscoplastic behaviour of steels during phase transformations. *Comptes Rendus - Mec.*, 331:587–594, 2003. 7

[40] S. Denis-Judlin. *Influence du comportement d'un acier pendant la transformation martensitique sur la genèse des contraintes au cours de la trempe.* PhD thesis, Institut National Polytechnique de Lorraine,, 1980. 7

[41] B. Hildenwall and T. Ericsson, Residual Stresses in the Soft Pearlite Layer of Carburized Steel. *J. Heat Treatment*, 1:3–13, 1980. 7, 8, 9

[42] T. Inoue and Z. Wang. Coupling between stress, temperature, and metallic structures during processes involving phase transformations. *Mater. Sci. Technol. (United Kingdom*, 1:845–850, 1985. 7, 11

[43] S.N. Lingamanaik and B.K. Chen. The effects of carburising and quenching process on the formation of residual stresses in automotive gears. *Comput. Mater. Sci*, 62:99–104, 2012. 8, 11

[44] A. Sugianto, M. Narazaki, M. Kogawara, A. Shirayori, S.Y. Kim, and S. Kubota. Numerical simulation and experimental verification of carburizing-quenching process of SCr420H steel helical gear. *J. Mater. Process. Technol.*, 209:3597–3609, 2009. 8, 11

[45] A. Sugianto, M. Narazaki, M. Kogawara, S.Y. Kim, and S. Kubota. Distortion analysis of axial contraction of carburized-quenched helical gear. *J. Mater. Eng. Perform.*, 19:194–206, 2010. 8, 11, 12

[46] V.C. Prantil, M.L. Callabresi, J.F. Lathrop, G.S. Ramaswamy, and M.T. Lusk. Simulating Distortion and Residual Stresses in Carburized Thin Strips. *J. Eng. Mater. Technol.*, 125:116, 2003. 8

[47] Z. Li and B.L. Ferguson. Controlling gear distortion and residual stresses during induction hardening. *Am. Gear Manuf. Assoc. Fall Tech. Meet*, 2011:370–381, 2011. 8, 11

[48] J. Besson, R. Leriche, R. Foerch, and G. Cailletaud. Object-Oriented Programming Applied to the Finite Element Method Part II. *Application to Material Behaviors, Rev. Eur. Des Éléments Finis*, 7:567–588, 1998. 8, 86, 99

[49] Douce. Coupled fluid flow, heat transfer, phase transformation, stress and deformation numerical model for gas quenching. *Int. J. Microstruct. Mater. Prop.*, 3:150–161, 2008. 8

[50] F. Convert and A. Turbat. Estimation Experimental determination of residual stresses distortion in quenched bars. *Eig. Karlsruhe*, 1983. 8

[51] T. Kreis, J. Müller, C. Kopylow, and W.Jüptner Von. Noncontacting Measurement of Distortion by Digital Holographic Interferometry. *IDE, Bremen*, page 115–121, 2005. 8

[52] B Hildenwall. *Dissertationsn°39.* PhD thesis, Linköping studies in Science and Technology, Linköping Suède, 1979. 8

[53] T. Ericsson. *Residual Stresses Caused By Thermal and Thermochemical Surface Treatments.* Pergamon Books Ltd, 1987. 8

[54] T. Inoue and K. Tanaka. An elastic-plastic stress analysis of quenching when considering a transformation. *Int. J. Mech. Sci.*, 17:361–367, 1975. 8

[55] M. Hoferer, H. Mueller, and E. Macherauch. Calculation of residual stresses in case-hardened SAE5115 steel cylinders. *Steel Res*, 66:31–34, 1995. 8

[56] T. Inoue, T. Yamaguchi, and Z. Wang. Stresses and phase transformations occurring in quenching of carburized steel gear wheel. *Mater. Sci. Technol. (United Kingdom)*, 1:872–876, 1985. 9, 82

[57] S. Denis, S. Sjöström, and A. Simon. Coupled temperature, stress, phase transformation calculation Model Numerical Illustration of the Internal Stresses Evolution during Cooling of a Eutectoid Carbon Steel Cylinder. *Metall. Mater. Trans. A*, 18:1203–1212, 1987. 10

[58] F. Fernandes, S. Denis, and A. Simon. Prévision de l'évolution thermique et structurale des aciers au cours de leur refroidissement continu. *Mémoires Etudes Sci. Rev. Métallurgie*, page 355–365, 1986. 10

[59] S. Denis, P. Archambault, C. Aubry, A. Mey, J.C. Louin, and A. Simon. Modelling of Phase Transformation Kinetics in Steels and Coupling with Heat Treatment Residual Stress Predictions. *J. Phys. IV*, 9:323–332, 1999. 10, 77, 79, 82, 84, 93

[60] A. Freborg, B. Ferguson, and Z. Li. Predicting Distortion and Residual Stress in a Vacuum Carburized and Gas Quenched Steel Coupon. In *Proc. from 6th Int. Quenching Control Distortion Conf.*, page 22–33, 2012. 11

[61] D. Kim, H. Cho, W. Lee, K. Taek, Y. Cho, S. Kim, and H. Nam. A finite element simulation for carburizing heat treatment of automotive gear ring incorporating transformation plasticity. *JMADE*, 99:243–253, 2016. 11

[62] K. Decroos and M. Seefeldt. Modeling of distortions after carburization and quenching processes of large gears. *Model. Simul. Mater. Sci. Eng.*, 21, 2013. 11, 12

[63] G.Sheng SONG, X. LIU, G. WANG, and X. XU. Numerical Simulation on Carburizing and Quenching of Gear Ring. *J. Iron Steel Res. Int.*, 14:47–52, 2007. 12

[64] T. Inoue. Metallo-Thermo-Mechanical Coupling in Quenching. *Compr. Mater. Process*, page 177–251, 2014. 12

[65] J. Lesage. Simplified Model of Prediction for Residual Stresses in Superficially Treated Layers. *Mem. Etudes Sci. Rev. Metall.*, 87(2):113–122, 1990. 12

[66] D.Y. Ju, C. Liu, and T. Inoue. Numerical modeling and simulation of carburized and nitrided quenching process. *J. Mater. Process. Technol*, 143–144:880–885, 2003. 12, 13, 15

[67] C.C. Liu, D.Y. Ju, and T. Inoue. A numerical modeling of metallo-thermo-mechanical behavior in both carburized and carbonitrided quenching processes. *Isij Int.*, 42:1125–1134, 2002. 12, 15

[68] H.S.R. Mukai, T. Matsumoto, D. Ju, and T. Suzuki. Modeling of numerical simulation and experimental verification for carburizing-nitriding quenching process. *Trans. Nonferrous Met. Soc. China*, 16:566– 571, 2006. 12, 14, 15

[69] G. Geandier, L. Vautrot, B. Denand, and S. Denis. In situ stress tensor determination during phase transformation of a metal matrix composite by high-energy X-ray diffraction. *Materials (Basel)*, 11:1–19, 2018. 15, 51

[70] T. Gladman. Aluminium for Grain Size Control. *Met. Heat Treat.*, 21:11–14, 1994. 17

[71] J. Dulcy and M. Gantois. Formation et durcissement de la couche de diffusion en nitruration et nitrocarburation - Systèmes fer-chrome-azote et fer-chrome-azote-carbone. *Tech. ingénieur*, M1223:1–44, 2013. 18, 21, 24, 25, 29

[72] J. Dulcy and M. Gantois. Théorie des traitements thermochimiques - Cémentation. *Carburation., Tech. ingénieur Trait. Therm. Superf. Thermochim.*, 33:1–23, 2013. 18, 20, 21, 22, 24, 26, 28

[73] H.A. Wriedt, N.A. Gokcen, and R.H. Nafziger. The Fe-N (Iron-Nitrogen) system. *Bin. Alloy Phase Diagrams*, 8:355–377, 1987. 19

[74] H. Du. A reevaluation of the Fe-N and Fe-C-N systems. *J. Phase Equilibria*, 14:682–693, 1993. 19

[75] M.S. Yahia. *Contribution A l'etude de l'influence de l'azote dans les traitement thermochimiques de surface des aciers en phase austenite*. PhD thesis, Thèse Institut National Polytechnique de Lorraine,, 1995. 20

[76] C. Ginter, L. Torchane, J. Dulcy, M. Gantois, A. Malchère, C. Esnouf, and T. Turpin. A new approach to hardening mechanisms in the diffusion layer of gas nitrided alpha-alloyed steels. *Metall. Ital.*, 98:29–35, 2006. 20

[77] J. Slycke and T. Ericsson. A study of reactions occurring during the carbonitriding process part I. *J. Heat Treat.*, 2:97–112, 1981. 21, 24, 25, 26

[78] J. Slycke and T. Ericsson. A study of reactions occurring during the carbonitriding process part II. *J. Heat Treat.*, 2:97–112, 1981. 21, 26

[79] D. Xu, C. Ji, H. Zhao, D. Ju, and M. Zhu. A new study on the growth behavior of austenite grains during heating processes. *Sci. Rep.*, 7:1–13, 2017. 23

[80] T. Gladman. Abnormal Grain Growth during the Heat Treatment of Steel. *Material Sci. Forum*, 94–96:113–128, 1992. 23

[81] O. Karabelchtchikova and R.D. Sisson. Carbon Diffusion in Steels: A Numerical Analysis Based on Direct Integration of the Flux. *J. Phase Equilibria Diffusion*, 27:598–604, 2006. 24

[82] S.D. Catteau, H.P. Landeghem, J. Teixeira, J. Dulcy, M. Dehmas, S. Denis, A. Redjaïmia, and M. Courteaux. Experimental Study and Modelling of Phase Transformation Kinetics During Austenite Decomposition in Carbonitrided Low Alloyed Steel. In *24th IFHTSE Congress*, 2017. 26, 77, 128

[83] J.O. Andersson, T. Helander, L. Hoglund, P. Shi, and B. Sundman. Thermo-Calc and DICTRA, computational tools for materials science. *Calphad Comput. Phase Diagrams*, 26:273–312, 2002. 29

[84] A. Borgenstam, L. Hoglund, J. Agren, and A.Engstrom. DICTRA, a tool for simulation of diffusional transformations in alloys. *J. Phase Equilibria*, 21:269–280, 2000. 29

[85] M. Gantois. Mechanisms and Modelling of Mass Transfer during Gas- Solid Thermochemical Surface Treatment. New Process and New Process Control for Carburizing and Nitriding. *Mater. Sci. Forum*, 163–165:37–50, 2009. 29

[86] Michaël VEAUX. *Etude expérimentale et prévisions par le calcul des cinétiques de transformation de phases, des contraintes résiduelles et des déformations lors de la transformation bainitique*. PhD thesis, Thèse Institut National Polytechnique de Lorraine, 2003. 32, 40, 83, 86, 89, 92, 94, 95

[87] Jean-Charles LOUIN. *Effets d'hétérogénéités de teneur en carbone sur les cinétiques de transformations de phase et sur la genèse des contraintes internes lors du refroidissement d'aciers*. PhD thesis, Thèse Institut National Polytechnique de Lorraine, 2003. 32, 89, 92, 94, 96

[88] C. Liebaut. *Rhéologie de la déformation plastique d'un acier Fe-C durant sa transformation de phase austenite–>ferrite + perlite*. PhD thesis, INPL Nancy, 1988. 32, 88

[89] ASTM International. A370 Standard Test Methods and Definitions for Mechanical Testing of Steel Products, 2003. 34

[90] ASTM International. E8/E8M 15a Standard Test Methods for Tension Testing of Metallic Materials, 2009. 34

[91] Quentin Le Bihan. Étude du comportement thermomécanique de l'acier BAE75 iNat. Technical report, IJL, 2013. 36

[92] S.D. Catteau, H.P. Landeghem, J. Teixeira, J. Dulcy, M. Dehmas, S. Denis, A. Redjaïmia, and M. Courteaux, Carbon and nitrogen effects on microstructure and kinetics associated with bainitic transformation in a low-alloyed steel. *J. Alloys Compd.*, 658:832–838, 2016. 38, 57, 63, 77, 78, 86

[93] A. Mey. *Prévision par Calcul des Cinétiques de Transformation de Phases et des Contraintes Internes lors du Traitement Thermique d'Aciers Cémentés*. PhD thesis, Thèse Institut National Polytechnique de Lorraine, 1997. 40, 54

[94] W.J. Parker, R.J. Jenkins, C.P. Butler, and G.L. Abbott. Flash Method of Determining Thermal Diffusivity, Heat Capacity, and Thermal Conductivity. *J. Appl. Phys.*, 32:1679–1684, 1961. 42

[95] L.J. Ebert. The role of residual stresses in the mechanical performance of case carburized steels. *Metall. Trans. A*, 9:1537–1551, 1978. 44

[96] M.E. Fitzpatrick and A. Lodini. Analysis of Residual Stress by Diffraction Using Neutron and Synchrotron Radiation. *Meas. Sci. Technology*, 14:1739–1740, 2003. 44

[97] L. Vautrot, G. Geandier, M. Mourot, M. Dehmas, E. Aeby-Gautier, B. Denand, and S. Denis. Internal Stresses in Metal Matrix Composites in Relation with Matrix Phase Transformations. *Adv. Mater. Res.*, 996:944–950, 2014. 45, 52

[98] B. Denand, M. Dehmas, E. Gautier, C. Bonnet, and G. Geandier. Four d'analyse portable pour ligne de rayonnement. *International patent deposed with reference number:WO2019081266A1*, 2019. 45

[99] J.P. Hammersley, A. P., S.O. Svensson, A. Thompson, H. Graafsma, A. Kvick, and Moy. Calibration and correction of distortions in two dimensional detector systems. *Rev. Sci. Instrum*, 66:2729–2733, 1995. 48

[100] G. Ashiotis, A. Deschildre, Z. Nawaz, J.P. Wright, D. Karkoulis, F.E. Picca, and J. Kieffer. The fast azimuthal integration Python library: PyFAI. *J. Appl. Crystallography*, 48:510–519, 2015. 48

[101] J. Rodriguez-Carvajal. FullProf. *Phys. B*, 192:55–59, 1993. 48

[102] J. Rodríguez-Carvajal. Recent advances in magnetic structure determination by neutron powder diffraction. *Phys. B Condens. Matter*, 192:55–69, 1993. 48

[103] J. Macchi, G. Geandier, J. Teixeira, S. Denis, F. Bonnet, and S.Y.P. Allain. Time-resolved in-situ dislocation density evolution during martensitic transformation by high-energy-XRD experiments: A study of C content and cooling rate effects. *Materialia*, 26:101577, 2022. 48

[104] I.C. Noyan and J.B. Cohen. *Residual Stress*. Springer New York, NY, 1987. 49, 54

[105] J.F. Nye et al. *Physical properties of crystals: their representation by tensors and matrices*. Oxford university press, 1985. 49

[106] K. Jeyabalan, S. D. Catteau, J. Teixeira, G. Geandier, B. Denand, J. Dulcy, S. Denis, G. Michel, and M. Courteaux. Modeling of the austenite decomposition kinetics in a low-alloyed steel enriched in carbon and nitrogen. *Materialia*, 9(10058):2, 2020. 55, 67, 77, 78, 79, 80, 81, 98, 103, 104, 105, 112, 113, 118, 128

[107] S. D. Catteau, S. Denis, J. Teixeira, J. Dulcy, M. Dehmas, A. Redja'ımia, and M. Courteaux. Effects of Carbon and Nitrogen on Isothermal Transformations of Austenite in a Low Alloyed Steel. *European Conf. Heat Treatment IFHTSE*, 21:153–161, 2014. 55, 78

[108] A Mehl A. Johnson, William. Reaction kinetics in processes of nucleation and growth. *Trans. Aime.*, 135:396–415, 1939. 78

[109] M. Avrami. Kinetics of phase change I: General theory. *J. Chem. Phys.*, 7:1103–1112, 1939. 78

[110] M. Avrami. Kinetics of phase change II: Transformation-time relations for random distribution of nuclei. *J. Chem. Phys.*, 8:212–224, 1940. 78

[111] M. Avrami. Kinetics of Phase Change III: Granulation, Phase Change and Microstructure. *J. Chem. Phys.*, 9:177–184, 1941. 78

[112] A. N. Kolmogorov. On the statistical theory of metal solidification. *Izv Akad. Nauk SSSR. Math. Ser.*, 3:355–359, 1937. 78

[113] J. S. Kirkaldy and D. Venugopalan. Prediction Of Microstructure And Hardenability In Low Alloy Steels. *Phase Transform. Ferr. Alloy*, pages 125–148, 1983. 79

[114] G. Krauss. Martensite in steel: strength and structure. *Mater. Sci. Eng A.*, 273-275:40–57, 2002. 80, 89

[115] F. Colonna. *Modélisation numérique du refroidissement des rails.* PhD thesis, Thèse Dr. l'Ecole Des Mines Paris, 1992. 83

[116] R. H. Greenwood, G. W., and Johnson. *The deformation of metals under small stresses during phase transformations.* Proc R. Soc. A Math. Phys. Eng. Sci, London, 1965. 84, 92

[117] C. L. Magee. Transformation kinetics, microplasticity and aging of martensite in Fe-31Ni. *Pittsburgh, PA Carnegie Inst Technol.*, 227, 1966. 84

[118] S. Zhang, K. Liu, H. Chen, X. Xiao, Q. Wang, and F. Zhang. Effect of increased N content on microstructure and tensile properties of low-C V-microalloyed steels. *Mater. Sci. Eng A*, 651:951–960, 2016. 86

[119] H. P. Van Landeghem, M. Véron, S. D. Catteau, J. Teixeira, J. Dulcy, A. Redjaimia, and S. Denis. Nitrogen-induced nanotwinning of bainitic ferrite in low-alloy steel. *Mater Scr*, 155:63–67, 2018. 86

[120] Y. Wang, S. Denis, and P. Archambault. *Synthèse des paramètres des aciers utilisés couramment pour la simulation du traitement thermique.* PhD thesis, Institut National Polytechnique de Lorraine, 2005. 87, 98, III

[121] S. B. Singh and H. K. D. H. Bhadeshia. Estimation of bainite plate-thickness in low-alloy steels. *Mater. Sci. Eng A*, 245:72–79, 1998. 88

[122] E. Gautier, A. Simon, and G. Beck. Deformation of Eutectoid Steel During Pearlitic Transformation Under Tensile Stress. *Pergamon Press Ltd*, 1980. 92

[123] M. Dalgic and G. L"owisch. Transformation plasticity at different phase transformations of bearing steel. *Materwiss Werksttech.*, 37:122–127, 2006. 92

[124] P. R. Woodard, S. Chandrasekar, and H. T. Y. Yang. Analysis of temperature and microstructure in the quenching of steel cylinders. *Metallurgical and materials transactions B*, 30:815–822, 1999. 93

[125] S. Sjostrom. Physical, mathematical and numerical modelling for calculation of residual stress- Fundamentals and applications. *Conf. Residual Stress*, ICRS-4 Proc. 4th Int.:484–497, 1994. 93

[126] J. Miettinen and S. Louhenkilpi. Calculation of thermophysical properties of carbon and low alloyed steels for modeling of solidification processes. *Metall. Mater. Trans. B*, 25:909–916, 1994. 96

[127] C. Basso. *Modélisation thermique et métallurgique de la transformation perlitique d'un acier eutecto"ıde, application au refroidissement STELMOR*. PhD thesis, Thèse d'ingénieur C.N.A.M, Nancy, 1984. 96

[128] Y. L. R. Desalos. Déformation d'aciers de traitement thermique. *Rev. Métallurgie*, 1979. 96

[129] J. Da Costa Teixeira, B. Appolaire, E. Aeby-Gautier, S. Denis, and L. Héricher. Modeling of the phase transformations in near-beta titanium alloys during the cooling after forging. *Comput. Mater. Sci.*, 42:266–280, 2008. 98

[130] P. Archambault, S. Denis, and A. Azim. Inverse resolution of the heat transfer equation with internal heat source. Application to the quenching of steels with phase transformations. *J Mater Eng. Perform*, 6(2):240–246, 1997. 99

[131] H. M. Rietveld. Profile Refinement Method for Nuclear and Magnetic Structures. *Journal of Applied Crystallography*, 2:65–71, 1969. V

Appendix A

Recall on residual stress scales

Residual stress is self-equilibrating arising from the elastic response of the material to an inhomogeneous distribution of nonelastic strains such as plastic, phase transformation, thermal expansion, and transformation plasticity strains. The contribution of the residual stresses can be beneficial or harmful, dependent on the sign and location of the residual stresses. The residual stresses are generated during the manufacturing processes, such as rolling, forging, shot peening, carburizing, etc. The residual stresses remain inside a material after the processes or the removal of all applied loads. Three kinds of internal stresses are generally defined depending on the scale, as shown below,

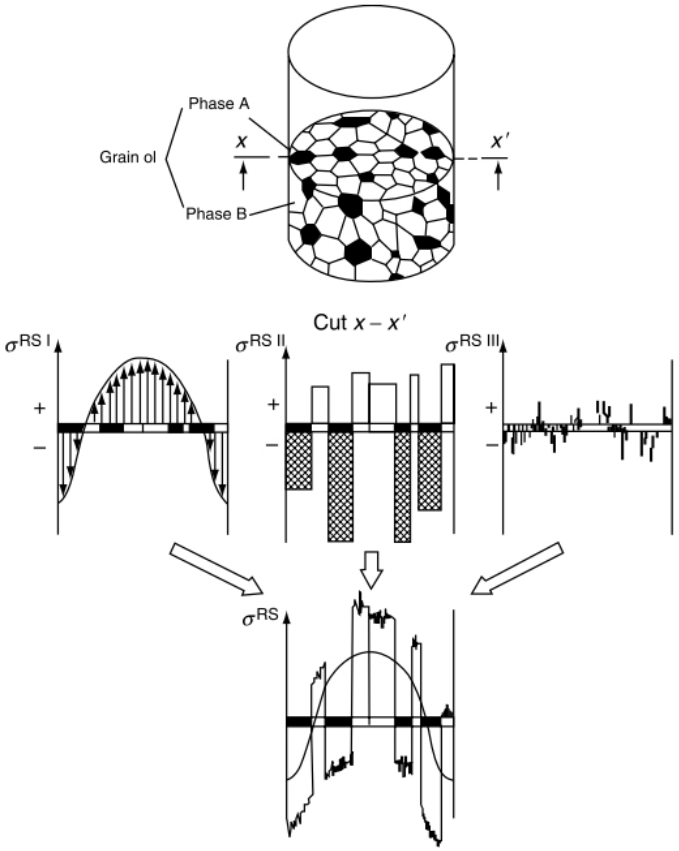

Figure A.1: Schematic illustration of different kinds of residual stresses and their superposition[5]

- **Type I:** Homogeneous across large areas, e.g., several grains of material, and are equilibrated with respect to the whole body.

- **Type II:** Homogeneous across microscopically small areas (one grain or sub-granular regions) and in equilibrium across grains.
- **Type III:** Across sub-microscopically small body areas (i.e., regions with dimensions of several atomic distances within single grains) and are in equilibrium across sub-granular areas.

All three kinds of residual stresses are superimposed to determine the total residual stress distribution in a material, as illustrated in Figure a. Here, we will consider only type I or macro residual stresses that could be either tensile or compressive in nature.

Appendix B

Test case: Martensitic quench simulation

First residual stress predictions using a coupled finite element thermo-mechanical-metallurgical model (Zebulon software) have been performed for a well-known test case developed at IJL, i.e., the martensitic quenching of a 60NiCrMo11 cylindrical steel specimen (diameter 35 mm and height 105 mm). The austenitization temperature of the cylinder is 900°C, quenched in water (25°C). The calculation considers a thermo-elastoplastic behavior of the steel with isotropic hardening and transformation strains (volumetric variation and transformation plasticity). A highly temperature dependent heat transfer coefficient, *h(T)*, is imposed in this simulation. Axial symmetry is assumed, and a 2D calculation is performed.

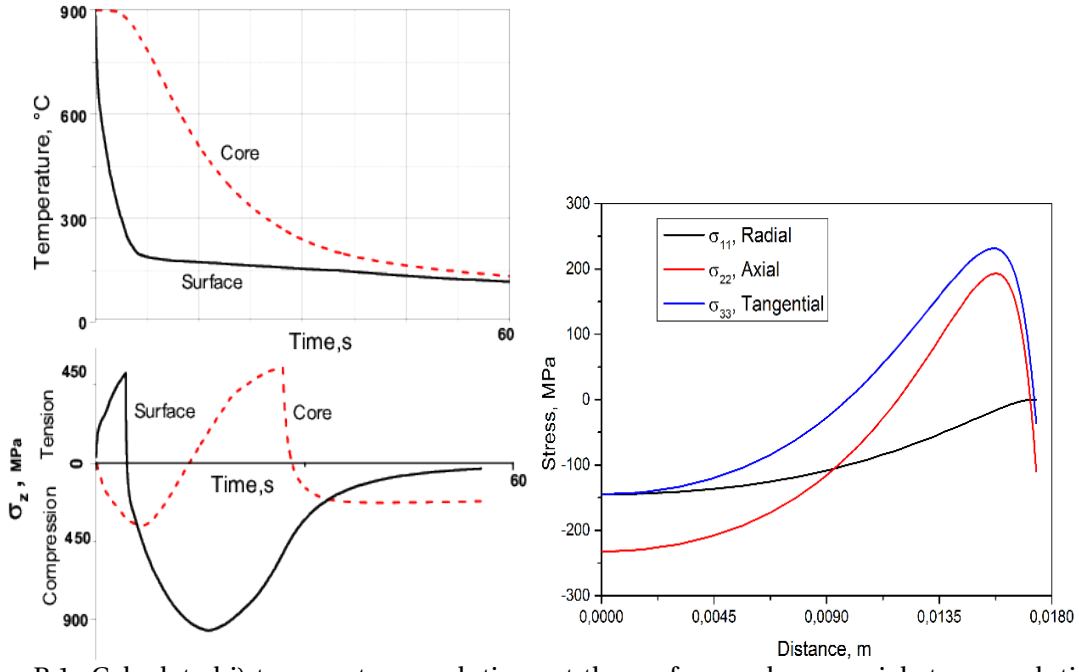

Figure B.1: Calculated i) temperature evolutions at the surface and core, axial stress evolutions versus time, and ii) residual stress distributions in the mid plane of a steel cylinder for martensitic quenching using Zebulon.

The results obtained can be compared with previous ones [120]. Axial stress evolutions during cooling at the surface and core (mid plane of the cylinder) can be followed parallel with the temperature evolutions in Figure B.1. As expected, tensile stresses and compressive stresses are produced at the surface and in the core at the beginning of quenching, respectively. When the surface reaches *Ms* temperature (245°C),

martensite phase transformation induces compressive stresses at the surface and a decrease of compressive stresses in the core. As the transformation progresses towards the core, compressive stresses increase at the surface generating tensile stresses in the core. As martensitic transformation occurs in the core, tensile stresses are relaxed, and compressive stresses form. At the end of the cooling process, the residual stress distributions (see Figure b) show compressive stresses in the core, tensile stresses beneath the surface, and relatively small compressive stresses at the surface.

Appendix C

X-ray diffraction method

C.1 Refinement of the structure by the Rietveld method

Rietveld's method [131] adjusts the calculated profile to the experimental profile by instrumental and structural parameters. Trying to minimize the mean of least squares the gaps between these profiles:

$$M = \sum_i w_i (y_i - y_{ci})^2$$

where w_i, is the weight assigned to the intensity of each reflection, y_i is the observed intensity for the angle $2\theta_i$, and y_{ci} is the calculated intensity for the angle $2\theta_i$. The Rietveld refinement simulates the diffraction peaks of the phases and their angular positions, sizes, and shapes. The model is used to refine experimental data, and much information can be extracted from the adjustment: lattice parameters, the proportion of phases, crystallite sizes, microstrains, occupations of sites, positions of atoms in the lattice, temperature factor, etc.

According to this method, the volume fraction of a phase is proportional to the sum of all its peak intensities I_{hkl} divided by the material scattering factors R_{hkl} divided by the number of peaks. The areas $I_{112/211}$ and I_{220} of the peaks obtained for the martensite and the austenite are proportional to the volume fractions y_{γ}' and y_{γ}, respectively, of these constituents:

$$I_{112/211_{\alpha'}} = kR_{112/211_{\alpha'}} y_{\alpha'}$$

$$I_{220_{\gamma}} = kR_{220_{\gamma}} y_{\gamma}$$

where $R_{112/211}$ and R_{220} are theoretical diffracted intensities and k is an instrument constant. However, the intensity at each angular position, 2θ on the diffractogram, interferes with the continuous background and the sum of the contributions of the Bragg reflections for all phases present. This intensity is described by:

$$I_i^{calc} = S_F \sum_{j=1}^{Nphases} f_j / V_j^2 \sum_{k=1}^{Npeaks} L_k |F_{k,j}|^2 \Omega_j (2\theta_i - 2\theta_{k,j}) P_{k,j} A_j + bkg_i$$

$S_F(2\theta_i - 2\theta_{k,j})$ line broadening parameters, $(hkl)_i$: the Miller indices of a Bragg reflection of phase i, S_F the scale factor of phase i, L_k the Lorentz-polarization factor, $F_{k,j}$ the structure factor, $P_{(k)j}$ the preferred orientation factor, A_j the asymmetry factor, bkg_i the intensity of the continuous background.

In our case, we have systematically adjusted the background intensity by a polynomial function of order 5. $\Omega_{(hkl)i}$ profile function in the case of powder X-ray diffraction is the Pseudo-Voigt function, $V(x)$:

Table C.1: The adjustable parameters to refining the calculated diffractogram profile.

Adjustable refinement	Structural settings	Crystalline parameters (a, b, c) Atomic positions (X, Y, Z) The occupancy rate of the sites (Occ) Thermal agitation factors (Bov)
	Parameters of shape profiles	Scale factor Offset at the originShape factor(η) Width at mid-height (U, V, W) Asymmetry of the lines
	Background settings	A polynomial of 5 in 2θ

$$\Omega_{(hkl)i}\,(2\theta) = pV(x) = \eta\, L(2\theta,H) + (1 - \eta)G(2\theta,H)$$

This Pseudo-Voigt function is calculated from the product of the convolution of a Lorentzian and a Gaussian. The fit of the shape function $\omega_{(hkl)i}$ is performed by two parameters: η, the linear adjustment parameter between the Lorentzian and the Gaussian, and $H_{(hkl)}$full width and half height. When the diffraction peaks show asymmetry, the pseudo-Voigt profile function is no longer suitable for adjusting the shape of the diffraction peaks for stress analysis.

To perform the diffractogram profile adjustment, we have used the Fullprof software, based on Rietveld's method. The grouped parameters in Table are used for refining the diffractogram profile.

Different confidence factors measure the quality of the adjustment *Rp* factor, *Rwp* weighted factor, expected factor *Rexp* and the "goodness of fit" χ or χ^2. These confidence factors make it possible to monitor the quality of the refinement after each cycle. Regarding our study, we chose to use the factor R_{wp} trustworthiness, the value of which is generally accepted for obtaining a satisfactory adjustment must be less than 10%. Nevertheless, the visual examination of the calculated diffractogram concerning the experimental diffractogram remains the best way to detect anomalies and suggest corrections.

The Fullprof software determines the uncertainties associated with determining lattice parameters and mass fractions for some diffractogram adjustments and considers the previously mentioned confidence factors. These uncertainties do not include those related to measurement errors (misalignment, detector correction) because they are difficult to estimate. The uncertainty associated with adjusting lattice parameters is a value absolute in angstrom, and it is high when the mass fraction of the phase analyzed is less than 10 (about 1.10^{-3} Å) and weak beyond (about 1.10^{-4} Å).

C.2 Diffraction evolution with the different beam sizes

The incident beam cross-section was 100 × 400 µm and 20 × 400 µm which define the small 'gauge volume' used to scan the sample. For example, first stress measurements on the carburized sample were performed with a beamwidth of 100 µm, which provides a satisfactory stress/strain resolution. However, the beam width was reduced to 20 µm to analyze the residual stresses in the enriched layers and with a concern of sufficient grains in a diffracting position However, this reduced beamwidth results in bad stress/strain resolution in the austenite domain, especially at high temperatures. Figure c shows a scatter measurement much larger than the normal statistical error ±50MPa.

For large-grained materials, the Debye Scherrer rings are dominated by some bright spots, and their peak position can be shifted according to the dominant diffracting spots originating from the front or the back of the sample. This introduces uncertainty into

the stress calculation (see Figure c). Despite the small gauge volume, the enriched layers with fine grain size have provided excellent continuous diffraction rings, and the resulting strain measurements along small nitrogen enriched layers.

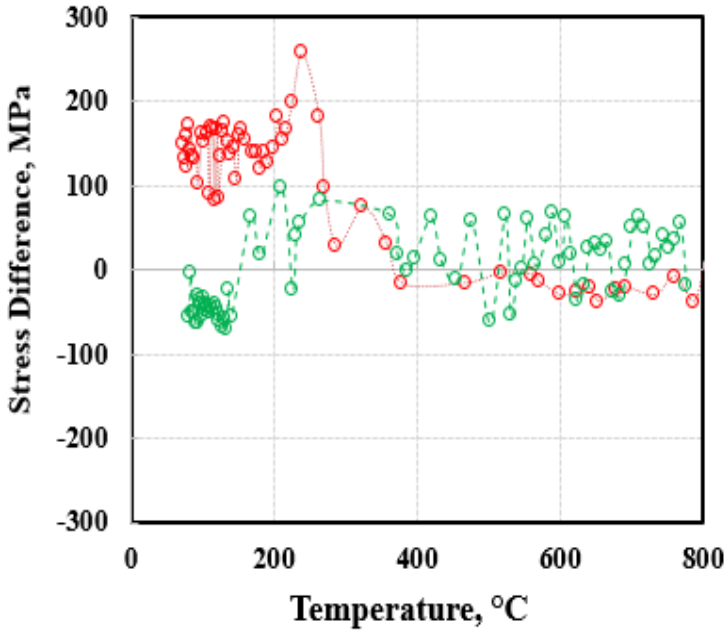

Figure C.1: The evolution of the austenite phase's stress difference was measured with different beamwidth (red) 100 X 400 µm and (green) 20 x 400 µm

During the *insitu* experiment on the nitrided and carbonitrided samples, the acquisition was interrupted between 900°C and 350°C due to the above-mentioned artifacts. Thus, the measuring points between this above temperature range are missing, and the inexistence of stress/strain results.

Appendix D

Thermomechanical system

D.1 Precautions measures

Before setting up the grips and specimen in the MTCC machine, the following steps should be done:

- PID (Proportional-Integral-Derivative) control loop tuning is a vital process undertaken before each test to control the system properly. PID tuning is performed to regulate the temperature, which minimizes the difference between the measured and recorded temperatures. It is also performed to compare the calculated strain signal to the demand waveform signal; the discrepancy signal is fed automatically to the system to eliminate the error.
- Load frame alignment was checked and adjusted using an appropriately strain-gauged small standard specimen linked to Instron's AlignPRO™ software and spherical adjustment fixture.

D.2 Fixing the grip system and specimens

By default, the MTCC starts up in the displacement channel with 'Sample protect' mode. Then, move into 'Medium pressure' mode to fix the specimen in the upper and lower grips, which are screwed on the pull-rods. The grip plates are placed over the specimen and tightened with two locking bolts, taking care of no bolt pretension loading the specimen. At the beginning of the test, in high-pressure mode, insert the pretension specimen of 5% yield stress on the material to ensure the machine clearances, alignment of the jaws, and limited straightening of the specimen. In addition, the test specimen must be positioned in the middle region of the furnace: to ensure a good homogeneity of temperature along the axial direction of the specimen and to ensure that the extensometer is impeded on the useful part of the specimen thickness face, as shown in Figure d. All the above adjustments have been considered, along with the placement of the extensometer, as shown in Figure d, to have correct tensile test curves at different temperatures. NB: Yield strength is more important for the simulations than Young's modulus.

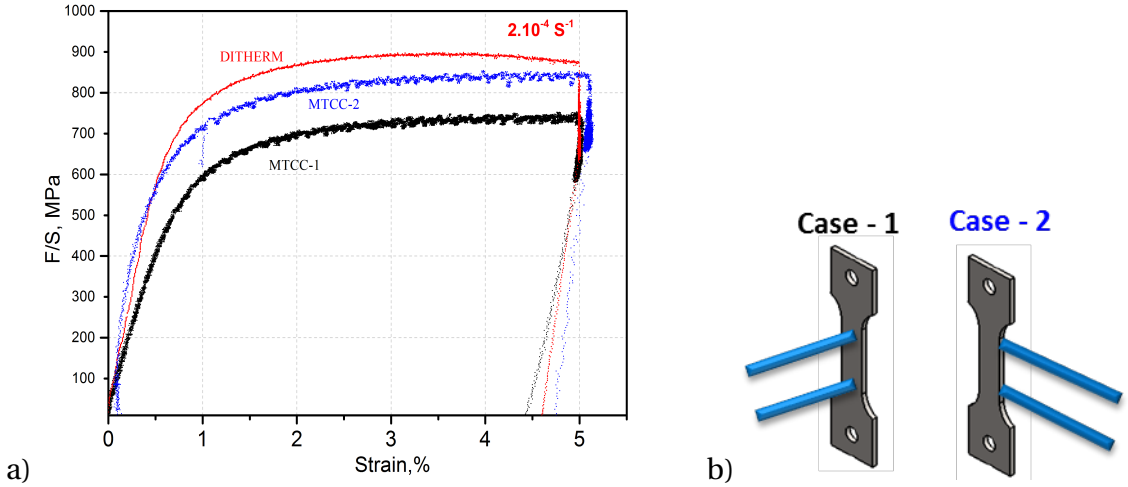

Figure D.1: a)The comparison of stress-strain curves obtained using different tensile test machines MTCC and DITHERM and b) the placement of MTCC extensometer on the width face and thickness face.

D.3 High temperature tensile testing

A test was carried out in a series of segments by defining the start and end temperatures, time duration, the amount of gas flow (percentage of valve opening), and the heating (input voltage). The helium/argon gas sweeps into the furnace with slight overpressure, reducing oxygen in the chamber and the oxidation of the alloys studied. The 'sample protect' function operates during the heating and cooling of test specimens before and after testing, respectively. This function will allow the actuator to change position to ensure the specimen is not subjected to an excessive load due to thermal expansion or contraction.

D.4 Data acquisition and unloading

The console software registers all the test settings and ensures the actuator position, applied load, and strain within the user-defined limits before, during, and after testing. During unloading, turn on 'sample protect' remove the pretension specimen and loosen the grip plate bolts on both pull-rods.

Experimental study and prediction of microstructures and internal stresses during heat treatment of carburized and carbonitrided low-alloyed steels

Abstract : Carbonitriding thermochemical treatments are used in automotive industry for improving fatigue and wear resistance of mechanical parts like gears. They consist in a carbon and nitrogen enrichment of the surface area of the parts at high temperature followed by quenching to get high mechanical properties and compressive residual stresses at the surface. The thesis work aims to better understand the role of nitrogen on the formation of stresses on cooling and their numerical simulation. The scientific approach consists in the elaboration of samples with carbon and nitrogen gradients which are representative of the gradients present in the surface area of the industrial parts. The originality of this study is to implement advanced characterization techniques to follow in situ on large instruments (synchrotron, ESRF Grenoble) the development of internal stresses during cooling in gradient samples that, as far as we know, has never been done before.

Keywords : Carbonitrided steels; Carburizing; Residual stresses; *in-situ* HEXRD; Numerical simulation.

Etude expérimentale et prédiction des microstructures et des contraintes internes lors du traitement thermique des aciers faiblement alliés cémentés et carbonitrurés

Résumé : Les traitements thermochimiques de carbonitruration sont utilisés dans l'industrie automobile pour conférer à des pièces (pignons…) des résistances à la fatigue et à l'usure élevées. Ils consistent à enrichir la surface des pièces en carbone et en azote à haute température et à les refroidir rapidement pour obtenir des propriétés mécaniques élevées et des contraintes résiduelles de compression en surface. Le travail de thèse porte sur une meilleure compréhension du rôle de l'azote sur la formation des contraintes au cours du refroidissement et leur simulation numérique. Le démarche scientifique consiste à travailler sur des éprouvettes à gradients de carbone et d'azote représentatives des zones superficielles des pignons. L'originalité de ce travail a été la mise en œuvre de technique de pointe pour suivre in situ sur grands instruments (ESRF Grenoble) la genèse des contraintes internes dans des éprouvettes à gradients ce qui à notre connaissance n'avait jamais été fait auparavant.

Mots-clefs : Carbonitrurés aciers; Cémentés; Contraintes résiduelles; *in-situ* Diffraction des rayons X haute énergie; Simulation numérique